KARLSRUHE INSTITUTE OF TECHNOLOGY (KIT)
INSTITUTE OF METEOROLOGY AND CLIMATE RESEARCH
DEPARTMENT TROPOSPHERE RESEARCH (IMKTRO)

The Land–Sea Breeze along the Guinea Coast and its Sensitivity to Sea-Surface Temperature Variations

Der Land–Seewind entlang der Guineaküste und seine Sensitivität gegenüber Schwankungen der Meeresoberflächentemperatur

Master's Thesis in Physics
by

Jasmin Haupt

17.05.2023 – 17.05.2024

Reviewer:	Prof. Dr. Peter Knippertz
Second Reviewer:	Prof. Dr. Andreas Fink
Advisor:	Dr. Bethany Jane Woodhams

Abstract

The land–sea breeze (LSB) is a local thermally-driven wind system which occurs all year-round at the densely populated Guinea Coast in West Africa. The LSB has a large impact on the living conditions of the local population and the economic resources of coastal countries by impacting for example wind, air quality, and precipitation. The characteristics of this wind system have a strong local dependency and are influenced among others by the sea surface temperatures (SSTs) of the adjacent ocean. This thesis is the first study, to the best of the author's knowledge, investigating in detail the impact of the SST on the LSB in the Gulf of Guinea.

Realistic simulations of the LSB are performed with the numerical weather prediction model ICON. The chosen research period from 13 to 17 December 2021 lies within the climatological beginning of the minor upwelling season, in which the near-coastal SSTs decrease. The satellite product OSTIA reveals additional short-time SST variations occurring within a few days in the Gulf of Guinea related to Saharan dust outbreaks. Sensitivity experiments with a uniform SST change of $\pm 1\,\mathrm{K}$ or $\pm 2\,\mathrm{K}$ are designed to model the response of the atmosphere, in particular any changes to the land–sea breeze, to SST variations. A sea breeze front (SBF) detection algorithm, relying on the universal sea breeze (SB) characteristics of horizontal wind and boundary layer depth gradients, was tuned and implemented to identify the position of the SBF along the whole Guinea Coast allowing for comparison between the different model runs.

A case study in West Nigeria reveals a high dependency of the LSB characteristics on the embedding flow, which changes from southwesterly monsoon winds (onshore) to a northerly Harmattan flow (offshore) within the research period. In all model runs, the sea breeze (SB) and the land breeze (LB) are weakened in wind speed, height and inland penetration distance when embedded in an opposing flow. The inland penetration distance of the SB depends on the large-scale flow characteristics of the West African monsoon (WAM) system and is limited by the position of the intertropical discontinuity (ITD). A transformation of the SB into a nocturnal low-level jet only occurs during monsoon days when the ITD is located relatively far inland. A change in the SSTs in the sensitivity experiments leads among other things to differences in the large-scale circulation of the WAM, influencing the LSB indirectly. Higher SSTs cause a weakening of the monsoon winds, a strengthening of the Harmattan flow and a southward (shoreward) shift in the ITD. Higher SSTs also directly influence the LSB by decreasing the atmospheric sea–land temperature gradient during daytime in the planetary boundary layer, leading among other effects to a lower mean SB wind speed. Increased atmospheric sea–land temperature differences during the nighttime strengthen the LB. The inland propagation velocity of the SBF is almost independent of the SST in contradiction to the inland penetration distance. Colder SSTs lead to a higher inland penetration distance, at least in part due to an earlier onset of the SB, experiments with warmer SSTs show a decreased inland penetration distance. The depth of the SB is independent of the SSTs. These relations between the SST and the SB found for the research period in the Gulf of Guinea are perturbed when convective precipitation forms cold pools at the SBF. The density currents of cold pools investigated in a case study have larger wind speeds, a smaller depth and a faster propagation speed than the SB. The outflow of cold pools formed at the SBF can merge with the SB and therefore change its circulation characteristics. Experiments with colder SSTs have a lower convective activity at the SBF suppressing cold pool formation.

This thesis demonstrates the multifaceted impact of SST changes on the SLB in the Gulf of Guinea. The results highlight the importance of applying realistic and updated SSTs to numerical weather simulations and in general taking the SSTs into account when investigating the SLB in the Gulf of Guinea.

Zusammenfassung

Der Land–Seewind ist ein thermisches Windsystem, das ganzjährig in der dicht besiedelten Küstenregion am Golf von Guinea auftritt. Das Windsystem hat unter anderem große Auswirkungen auf den Wind, die Luftqualität und auf den Niederschlag und beeinflusst daher die Lebensbedingungen der lokalen Bevölkerung und die Wirtschaftskraft der Küstenländer. Der Land–Seewind wird durch viele Faktoren beeinflusst und entwickelt sich abhängig von den lokalen Gegebenheiten. Die Meeresoberflächentemperatur ist einer dieser Faktoren. Diese Masterarbeit untersucht erstmals detailliert den Einfluss der Meeresoberflächentemperatur auf den Land–Seewind im Golf von Guinea.

Im Rahmen dieser Arbeit wird der Land–Seewind mit dem numerischen Wettervorhersagemodell ICON realitätsnah simuliert. Der gewählte Forschungszeitraum vom 13. bis zum 17. Dezember 2021 liegt am klimatologischen Beginn der Minor Upwelling–Saison, während der sich die küstennahen Meerestemperaturen vermindern. Satellitenbasierte Meeresoberflächentemperaturdaten zeigen zudem das Auftreten von mehrtägigen Temperaturschwankungen, die zeitgleich mit Saharastaub-Auswehungen über dem Golf von Guinea auftreten. In dieser Arbeit wurde der Einfluss unmittelbarer Meerestemperaturschwankungen auf den Land–Seewind mit Sensitivitätsexperimenten untersucht. Hierzu wurde die Meeresoberflächentemperatur um 1 K oder 2 K in den Simulationen gleichmäßig verringert oder erhöht. Die Simulationen geben Aufschluss über die Anpassung der atmosphärischen Zirkulationen, und im Besonderen des Land–Seewinds, auf eine Veränderung der Meeresoberflächentemperatur. Für die Identifizierung der Seewindfront wurde ein universell verwendbarer Erkennungsalgorithmus erfolgreich implementiert und auf den Küstenbereich zwischen der Elfenbeinküste und Westnigeria angewandt.

Eine Fallstudie in West Nigeria verdeutlichte den Einfluss des synoptischen Windes auf den Land–Seewind. Sowohl in der Referenzsimulation als auch in den Sensitivitätsexperimenten besitzen Seewind und Landwind eine geringere Windgeschwindigkeit und vertikale Ausdehnung in einem entgegengesetztem synoptischen Wind und dringen weniger weit in das Land ein. Die Tiefe, mit der der Seewind ins Land eindringt, zeigt zudem einen Zusammenhang mit dem Westafrikanischen Monsun: Die maximale Inlandvordringung des Seewindes ist durch die Innertropische Diskontinuität (ITD) begrenzt. Eine Transformation des Seewinds in einen Nocturnal Low-Level Jet wurde nur an Tagen beobachtet, an denen die Küstenzone unter Einfluss der Monsunwinde war und die ITD weit im Hinterland lag. Die Veränderung der Meeresoberflächentemperatur in den Sensitivitätsexperimenten beeinflusst die großräumige Zirkulation des Westafrikanischen Monsunsystems und damit indirekt den Land–Seewind. Eine Erhöhung der Meeresoberflächentemperatur führt zu einer Abschwächung der Monsunwinde, einer Verstärkung der Harmattan–Winde und einer südlichen (küstennäheren) Versetzung der ITD. Die Erhöhung der Meeresoberflächentemperatur führt zu einer kleineren Temperaturdifferenz in der atmosphärischen Grenzschicht über dem Land und dem Ozean am Tag und einer Erhöhung der Temperaturdifferenz in der Nacht, welche sich auf die Windgeschwindigkeit des Land–Seewindes auswirkt: Der Landwind verstärkt sich in der Nacht, der Seewind hingegen weist eine geringere mittlere Geschwindigkeit auf. Die Geschwindigkeit der Inlandspropagation des Seewinds bleibt ungefähr konstant, während die Tiefe der Inlandeindringung des Seewinds eine hohe Abhängigkeit von Änderungen der Meeresoberflächentemperatur zeigt. Niedrigere Meeresoberflächentemperaturen führen zu einer tieferen Inlandeindringung durch das frühere Einsetzen des Seewindes, in Sensitivitätsexperimenten mit erhöhten

Meeresoberflächentemperaturen zeigt sich eine geringere Inlandeindringung. Die vertikale Ausdehnung des Seewinds ist unabhängig von der Meeresoberflächentemperatur. Die bisher genannten Abhängigkeiten des Land–Seewindes von der Meeresoberflächentemperatur können ihre Gültigkeit verlieren, wenn Cold Pools durch konvektive Prozesse an der Seewindfront entstehen. Die in Fallstudien untersuchten Cold Pool–Dichteströme wiesen eine höhere Windgeschwindigkeit, eine geringere Höhe und eine schneller Inlandpropagation auf, verglichen mit dem Seewind. Dichteströme von Cold Pools, die an der Seewindfront entstehen, können sich mit dem Seewind vereinigen und daher die Eigenschaften des Seewinds ändern. Eine geringere konvektive Aktivität an der Seewindfront und eine damit einhergehende verminderte Cold-Pool-Bildung zeigte sich in Sensitivitätsexperimenten mit niedrigeren Meeresoberflächentemperaturen.

Eine Änderung der Meeresoberflächentemperatur hat somit einen vielfältigen Einfluss auf den Land–Seewind im Golf von Guinea. Diese Masterarbeit zeigt die Relevanz der Verwendung realistischer und aktualisierter Meeresoberflächentemperaturdaten, ins Besondere in numerischen Wettermodellen, für Untersuchenungen des Land–Seewinds im Golf von Guinea.

Erklärung

Ich, Jasmin Haupt, versichere wahrheitsgemäß, die Arbeit selbstständig verfasst, alle benutzten Hilfsmittel vollständig und genau angegeben und alles kenntlich gemacht zu haben, was aus Arbeiten anderer unverändert oder mit Abänderungen entnommen wurde sowie die Satzung des KIT zur Sicherung guter wissenschaftlicher Praxis in der jeweils gültigen Fassung beachtet zu haben.

Karlsruhe, den 17.05.2024

Jasmin Haupt

Contents

List of abbreviations

LB	land breeze
LSB	land–sea breeze
SB	sea breeze
SBC	sea breeze circulation
SBF	sea breeze front
SBG	sea breeze gravity current
SBH	sea breeze head
SST	sea surface temperature
UTC	coordinated universal time
WAM	West African monsoon

1 Introduction

The sea breeze circulation (SBC) is a meteorological phenomenon occurring along all major coastlines around the world, it is observed from the equator to polar regions (Flohn, 1969). The atmospheric temperature contrast over land and ocean initiates the sea breeze (SB) which is a local-scale onshore wind. At the leading edge of the SB, cumulus clouds can form due to low-level convergence (Miller et al., 2003). The subsidence behind the sea breeze front leads to clear sky conditions along the coast. The satellite image of the coastal regions in Ghana shows both characteristics on 14 December 2021 at 13:34 UTC in Figure 1.1c. The sea breeze has a major impact on wind, cloudiness, local thunderstorm development, fog formation, temperature changes, and air quality (Miller et al., 2003). This influences a large part of the human population living in major cities in the impact area of the sea breeze (SB) close to the coast (Figure 1.1a). More and more people move to the coasts and according to Crosman and Horel (2010), about 75% of the earth's population will live in coastal areas by 2030.

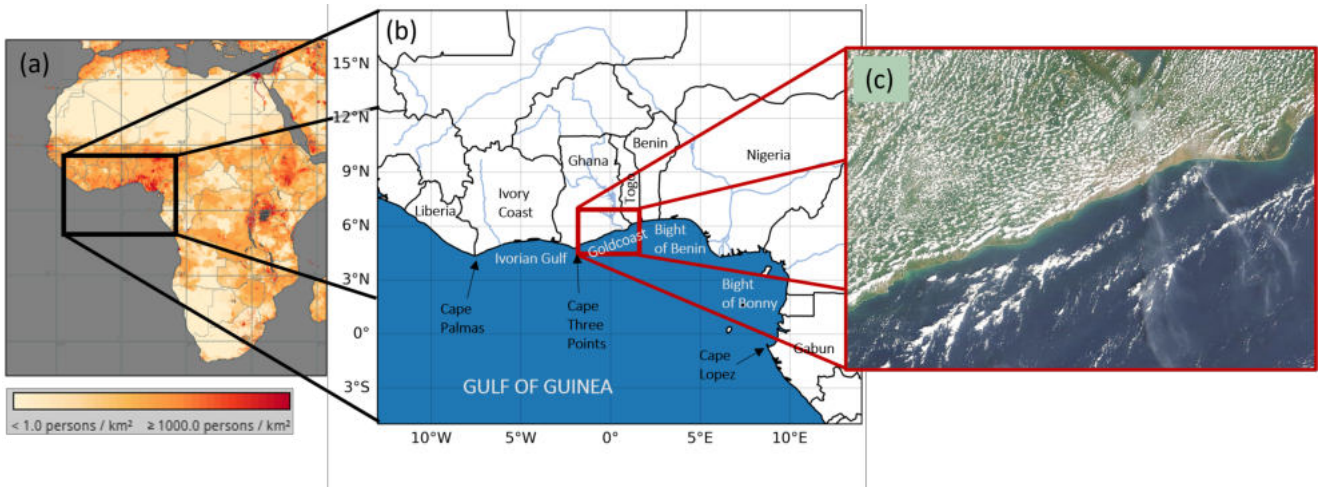

Figure 1.1: *(a) The population density in Africa in 2020 is high at (b) the Guinea Coast. (c) Satellite image showing the SB on 14 December 2021 at 13:34 UTC in Ghana, a band of clouds forms over land whereas a characteristic clearing occurs along the shoreline. Data from NASA Worldview https://worldview.earthdata.nasa.gov/.*

The Guinea Coast is a region in tropical West Africa. It is one of the most densely populated regions of Africa with a high urban agglomeration (Fink et al., 2017). The living conditions of a large majority of the local people depend on weather and climate since food production depends on the annual cycle of precipitation controlled by the West African Monsoon System as well as water resources. But also for health, and economic sectors like power generation and fisheries, the weather plays a critical role. The majority of the larger cities in the Guinea Coast lie close to the shoreline and thus in the impact region of the land–sea breeze. Fishers use the land breeze to sail out on the ocean with the off-shore land breeze in the early morning and head back with the onshore sea breeze during the day. Over the land, the SB is important for air quality, wind parks, and for a decrease in the near-surface temperatures (Miller et al., 2003). It is surprising how sparse the research of the SB characteristics is in this region. In addition, the availability of meteorological data relies mostly on satellite data, data from national weather services or amateur

observers due to the lack of data coverage of the region by the small number of weather stations (Fink et al., 2017). Weather models provide therefore valuable insights in regions where the data availability is low. Additionally, data originating from simulations provide the possibility to study atmospheric processes as a whole, which cannot be captured with station data. Most of the recently used earth science and global climate models have a too-coarse horizontal resolution to represent regional or local-scale phenomena like the SBC (Soares et al., 2024). Thus, the impact of the SBC in a changing climate is not captured adequately within these observational systems leading to a higher uncertainty for the coastal regions, out of all, where a majority of the earth's population lives.

This work shows that the SB winds can determine the near-surface winds in more than 200 km distance to the shoreline. In these regions, strong precipitation with flood events and landslides have occurred recently and with an increased frequency in the last decade (Maranan et al., 2018; Sanogo et al., 2015). Recent studies investigate the influence of the SB on these extreme events in littoral areas: Camberlin et al. (2020) classify a selection of intense rainfall days in West Africa and suggest that the SB plays a role in the formation of several convective storms in Ghana. Other studies presume not only the involvement of the SB in the initialization of storms but also in their development. Wissmeier et al. (2010) found a favourable environment for the development of multicell thunderstorms behind a sea breeze front in northern Australia. The large cities in coastal areas in the Gulf of Guinea are especially vulnerable to flooding resulting from strong precipitation: due to poor urban planning, a scarcity of drainage facilities and the rapid growth of cities, flooding causes human and economic losses (Camberlin et al., 2020). In the worldwide city rank of the population being exposed to coastal floodings in 2070, Abidjan (the economic capital of the Ivory Coast) and Lagos (the largest city in Nigeria) score at rank 16 and 15 (Nicholls et al., 2007). Both cities are located in the litoral area of the Gulf of Guinea. Camberlin et al. (2020) states that flooding in coastal cities in the Gulf of Guinea is mainly caused by heavy in-situ rainfall. Further investigations on the characteristics of the SB in the Gulf of Guinea are needed to gather an understanding of the role of the SB in this region in general and in such particular rainfall events.

The conditions under which an SB develops influence the occurrence, location, structure and strength of the circulation (Crosman and Horel, 2010). The sea surface temperature (SST) is a fundamental factor in SB development since the circulation is initialized by the atmospheric temperature gradient between the land and the adjacent ocean. The Tropical Atlantic Ocean in the Gulf of Guinea is known for a strong seasonal cycle in the coastal SSTs driven by coastal upwelling. Additionally, sudden SST variations exceeding 1 K are discovered in satellite data in the Gulf of Guinea in this thesis project. To the best of the author's knowledge, such events have not been discussed in the scientific literature. They appear in the near-coastal areas within a few days and disappear afterwards. It is very likely, that the SST variations in the near-coastal ocean affect the sea breeze circulation. The impact of the SST on the SB is sparsely investigated in case studies in other regions of the world, for example in Brazil, the US and South England. These studies show very different responses of the SB to SST changes for these different locations. This result is not surprising, as Crosman and Horel (2010) highlighted in their review paper the strong local dependency of the SB on its environment. Consequently, the response of the SB to the SST variability in the Gulf of Guinea cannot be assumed to be similar to other regions.

The impact of the SST on the SB has not yet been investigated in the Gulf of Guinea. This thesis aims to fill this gap by investigating the impact of the SST on the coastal near-surface winds with sensitivity experiments performed with the numerical weather prediction model ICON. Within a chosen research period from 13 to 17 December 2021, the atmosphere is modelled in the Gulf of Guinea. In Chapter 5.2, the development and characteristics of the LSB are analysed in the different wind conditions occurring within this period. The calculation of the inland extension of the SB requires an identification of the sea breeze front (SBF), which is the leading edge of the flow. Former studies have used filters, mainly based on wind variables, specific humidity or air temperature. Identifying the SBF on these criteria is unambiguous in the Guinea Coast, due to very dynamic atmospheric processes during the daytime. Therefore, an algorithm relying on the universal characteristic of the SB is adapted and implemented for the model data. It identifies the position of the SBF along the whole Guinea Coast. It is a useful new tool also for future studies of Sea Breezes. Chapter 5.1 identifies climatological SST variations in the Gulf of Guinea to achieve a better understanding of the intra-annual SST variability, the annual cycle of the SSTs and short-time SST variations. Chapter 5.3 investigates the sensitivity of the LSB to SST changes: In these simulations, the SST is uniformly increased or decreased about 1 K or 2 K while the atmospheric state and the land surface temperature are similar to the reference run. This SST shock aims to describe the observed sudden short-time cooling or warming events in the near-coastal ocean surface in the Gulf of Guinea. After a spin-up period, when the atmosphere is adjusted to the SST change, the results of the impact of the warmer or cooler ocean on the SB are valuable in the more general context of intra-annual variability. The focus of this thesis lies in the analysis of the LSB characteristics, however, cloud formation and precipitation processes are also examined in a case study. Gaining a fundamental understanding of these processes will be useful for future studies analysing the impact of the SB on precipitation events. This research project provides new insights into the LSB characteristics in the Gulf of Guinea, identifies short-time SST variations in the Gulf of Guinea, and presents for the first time a detailed analysis of the SST dependence of the land–sea breeze at the Guinea Coast.

2 Theoretical background

2.1 The land–sea breeze

The sea breeze circulation (SBC) is a local wind system driven by the atmospheric thermal gradient between land and ocean (Miller et al., 2003). It has been well-known for thousands of years and a common understanding of the processes is already developed. However, the appearance of the circulation and its impact on the environment depends strongly on local conditions (Crosman and Horel, 2010). Therefore, the characteristics of the land–sea breeze (LSB) must be investigated individually for each region. This section elaborates on the general structure and diurnal cycle of the SBC and gives an overview of the impact of external factors on the sea breeze (SB), which is investigated in the Gulf of Guinea. The relation of the LSB to convection, cloud formation and coastal precipitation is also discussed.

2.1.1 What is the land–sea breeze?

The sea breeze system is a local circulation occurring at coastlines around the world due to atmospheric temperature differences near the surface between the air masses over the water body and the land (Miller et al., 2003). A similar system can appear above sufficiently large lakes too. Sea breeze circulation systems have a common structure which is shown in Figure 2.1. In general, they occur in the daytime, intensify in the afternoon and vanish in the evening when the thermal gradient across the shore approaches zero. In the nighttime, a counter-rotating system might develop which is called land breeze circulation.

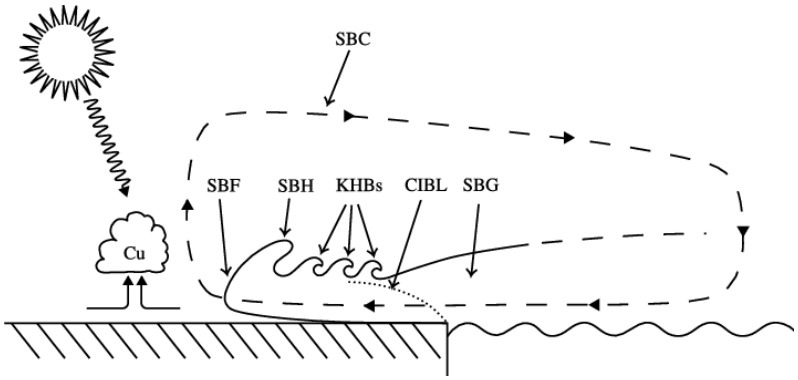

Figure 2.1: *Detailed structure of the sea breeze system, figure from Miller et al. (2003).*

The sea breeze circulation
The sea breeze circulation (SBC) is a cross-shore mesoscale rotation cell containing horizontal and vertical flow (Miller et al., 2003). The horizontal and vertical dimension shows a strong local dependency. In the Gulf of Guinea, Huaman et al. (2023) found an inland extension of the sea breeze (SB) exceeding 250 km distance to the shoreline. Vertical dimensions of the flow layers vary from 500 m to 1000 m for the lower layer (Parker et al., 2017) and reaches up to 2000 m for the upper-level return flow layer (Miller et al., 2003).

An atmospheric temperature difference between land and sea creates a local-scale pressure gradient force (PGF) directed towards the land (Miller et al., 2003). It induces movement of a shallow marine air layer across the shore, called the sea breeze (SB). The leading edge of this flow, the so-called sea breeze front (SBF), is characterized by sharp changes in temperature, moisture and wind. The SBF is defined as the boundary area occurring between the actual SB and the ambient flow, through which the SB propagates (Ji et al., 2013). The upper boundary of the SB has a wave structure (Miller et al., 2003). Updrafts behind the SBF shape the sea breeze head (SBH) which contains marine and continental air. It can reach twice the height of the SB. The subsequent waves forming on top of the SB are called Kelvin-Helmholtz billows (KHB). KHBs develop in an environment of low static stability during midday and dissipate in the late afternoon. Wexler (1946) defines the vertical extent of the Sea Breeze to where the horizontal velocity falls to zero above the SB. On top of the SB, a return flow forms (Miller et al., 2003). The circulation closes with a broad region of subsidence over the ocean.

The land breeze and katabatic winds

The land breeze (LB) develops due to the cross-shore atmospheric temperature gradient in the planetary boundary layer during night-time (Parker et al., 2017). The atmospheric temperature difference occurs due to the ocean's larger heat capacity compared to the land, leading to a stronger cooling of the atmosphere over the land than over the ocean during nighttime (Dragaud et al., 2019). The resulting circulation is shallower than the SBC due to the shallow nighttime boundary layer over land (Parker et al., 2017). The strength of the LB is weaker than the SB and depends on the local topography.

The simulations performed in this thesis indicate a potential superposition of the LB and katabatic winds during the night-time in a case study in Nigeria. The LB is often weaker than reverse flow down the mountains in the night (Simpson, 1994). These so-called katabatic winds develop when the near-surface atmosphere cools due to contact with a cooled slope by longwave cooling. This induces horizontal temperature and density gradients between the near-surface atmospheric layer above the slope and the atmosphere nearby (Hatchett et al., 2020). The cooled air layer above the slope achieves a higher density compared to the environment and accelerates down the slope by the time when gravity force exceeds buoyancy force (Parker et al., 2017).

2.1.2 Theoretical and empirical analysis of the sea breeze circulation

Bjerknes circulation theorem

A simple theoretical model describing the sea breeze circulation (SBC) is the Bjerknes circulation theorem (Miller et al., 2003). From a state of resting atmosphere, it describes an idealized sea breeze (SB) as part of a mesoscale rotation cell (Holton and Hakim, 2013). The calculation is based on angular momentum conservation. The sea breeze system appears in a baroclinic system, where a density gradient drives the circulation. A strong simplification of the system assumes friction to be zero, pressure to be constant at the surface and at the return flow layer, and a uniform temperature in each atmospheric column over land and sea (Holton and Hakim, 2013). Figure 2.2 illustrates the rotation cell for the example of the sea breeze circulation and demonstrates the assumed pressure and temperature distributions. The following calculation of the SB velocity follows the textbook of Holton and Hakim (2013).

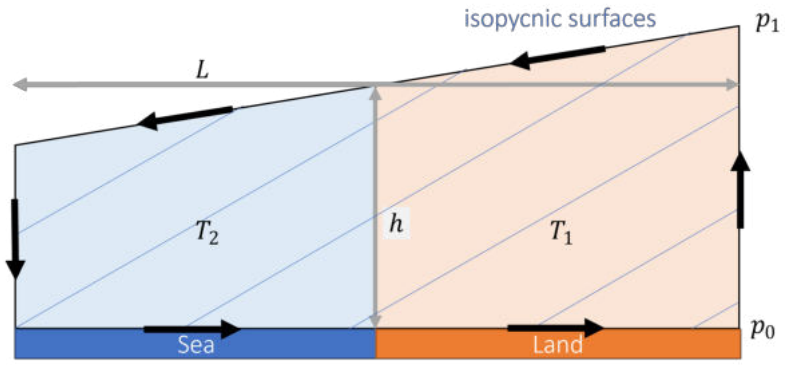

Figure 2.2: *Simplified model of the sea breeze circulation in analogy to Miller et al. (2003).*

The circulation C is a macroscopic variable, defined by the line integral over the tangential velocity component v along a contour of a closed path l:

$$C = \oint \mathbf{v} d\mathbf{l}.$$

For the sea breeze circulation example, the closed path is marked as a clack contour in Figure 2.2. C is a measure of the rotation in this defined area. The absolute circulation C_a is the sum of the circulation due to the rotation of the earth C_e and the relative circulation C measured from a frame of reference moving with the surface of the earth. Applying Newton's second law for a closed chain of fluid particles and neglecting viscous forces one finds the circulation theorem

$$\frac{DC_a}{Dt} = \frac{D}{Dt} \oint \mathbf{v}_a \cdot d\mathbf{l} = -\oint \frac{1}{\rho} dp, \tag{1}$$

with the time t, the density ρ and the pressure p. Applying the ideal gas law $\rho = RT/p$ with the gas constant R and the temperature T to the circulation theorem in equation 1 one finds for the simplified sea breeze system system

$$\frac{DC_a}{Dt} = -\oint \frac{RT}{p} dp = -R \oint T d \ln p = R \ln \left(\frac{p_0}{p_1} \right) (T_2 - T_1). \tag{2}$$

The mean wind velocity of all points along the defined path l can be defined by the absolute circulation C_a divided by the total path length. In the example of the sea breeze circulation, the total path length is composed of the sum of twice the mean height h and twice the horizontal cross-shore length L (Figure 2.2):

$$v_\mathrm{a} = \frac{C_\mathrm{a}}{2(h + L)}. \tag{3}$$

The change in the mean tangential velocity $\langle v_a \rangle$ over time can be found by taking the time derivative of equation 3 and substituting equation 2:

$$\frac{D\langle v_a \rangle}{Dt} = \frac{R}{2(h + L)} \ln \left(\frac{p_0}{p_1} \right) (T_2 - T_1). \tag{4}$$

This theoretical result overestimates the wind velocities due to the sea breeze circulation because it neglects friction, temperature advection and the alongshore component (Miller et al., 2003).

Theory of Rotunno - the impact of Coriolis force
Rotunno (1983) investigated the sea breeze from the perspective of linear motion theory. He assumes the atmosphere as a rotating, stratified fluid described by the Coriolis parameter and the Brunt-Väisälä-frequency N. The heat source is embodied by the diurnal cycle of heating by solar shortwave radiation. Without paying attention to the details of heat diffusion, he analyses the atmospheric response to the oscillating amplitude of the energy received at the land surface. The energy budget of a nearby ocean is kept constant.

He found a strong latitudinal dependence on the onset and maximum velocity of the sea breeze. While earlier studies neglected Coriolis force on the assumption that its impact will be negligible compared to the pressure gradient force and friction, Rotunno (1983) found a significantly different behaviour for a sea breeze developing in a location where the Coriolis parameter f is smaller, equal or larger than the angular frequency of the earth $\omega = \frac{2\pi}{\text{day}}$.

In this thesis, the sea breeze will be investigated in the Gulf of Guinea. The research area has a northern boundary of $\Phi = 19°\text{N}$, thus

$$f = 2\omega \sin\Phi \quad \Rightarrow \quad \frac{f}{\omega} \approx 0.68 \quad \Rightarrow \quad f \leq \omega.$$

According to Rotunno (1983) the extend of the inland penetration of the SBS in the Gulf of Guinea is thus mainly impeded by frictional forces and a delay between heating and the development of the circulation can be expected.

Empirical studies of density currents in water tank experiments
Gravity current, density current and buoyancy current are different names for the same meteorological phenomenon: a small density difference between two fluids causes a mostly horizontal current, where the denser fluids force its way through the less dense fluid. Due to the displacement of the less dense fluid, the main forces are gravity and inertia (Simpson, 1987).

Experimental studies of two fluids with different densities have been used to gain an understanding of the complex structure of the gravity flow dependence on different variables and environmental flow properties, slope angles etc. These experiments have been carried out in channels with salty water: a decreasing salinity from the bottom to the top of the channel depicts the stable stratification also found in the atmosphere under stable conditions. Then, the interaction with a liquid with higher salinity (and therefore higher density) can be investigated in the channel. Figure 2.3 shows a density current on a horizontal floor. Features like the Kelvin-Helmholtz billows can be nicely evaluated (Simpson, 1987).

The derived characteristics of the water channel density currents cannot be directly transferred to atmospheric gravity currents, one needs to take the compressibility of media into account. Water is in first-order incompressible while the atmosphere faces strong changes in volume due to pressure changes. Using the potential temperature instead of the temperature at every point diminishes the local effect of pressure in atmospheric density currents. The potential temperature is the temperature an air parcel brought down adiabatically to 1000 hPa (Simpson, 1987).

A simple approximation of the velocity can be derived under the assumption of energy conserva-

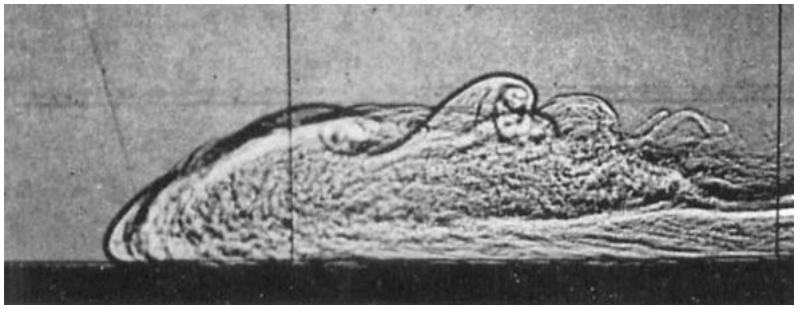

Figure 2.3: *Waterchannel experiments by Simpson and Britter (1980) analysing the impact of ambient flows.*

tion:

$$\frac{1}{2}mu^2 = mgh \Rightarrow u = \sqrt{gH}.$$

The left term describes the kinetic energy with the mass m and the velocity u, the term on the right side specifies the kinetic energy with the gravity constant g and the height of the denser fluid h. h can be replaced by the mean height of the centre of the gravity current $H/2$ in the case of no friction. The realistic acceleration will be extenuated by the interaction with the less dense media by the ratio of the density difference between the media divided by the density of the less dense fluid. When only driven by a density difference, a gravity current moves with the frontal velocity u of

$$u = k \cdot \left(\frac{\Delta\rho}{\rho} gH\right)^{\frac{1}{2}} \tag{5}$$

with the constant k to be determined in the individual gravity current environment (Simpson, 1987). Simpson (1969) adapted this relation and replaced the density relation by a temperature relation $\frac{\Delta T}{T}$. He determined the constant $k \approx 0.62$. And Simpson and Britter (1980) found a deviation from equation 5 in a prevailing geostrophic flow induced by a synoptic pressure gradient force: the flow velocity is modified by $-0.59 \cdot u_{\text{geostr}}$ of the opposing geostrophic wind velocity u_{geostr}.

Empirical studies of sea-breeze fronts in south-east England found a correlation between the speed of advance of the front u and the temperature drop ΔT across the front Simpson (1969):

$$\frac{u^2}{\Delta T} \approx \text{constant}. \tag{6}$$

This result supports equation 5 assuming similar depths and temperatures of the density currents compared in Simpson (1969) studies.

Various scale analysis studies of the SB investigate the dependence of the wind speed in the SB and the height of the circulation on other variables: Porson et al. (2007) found the sea breeze speed to be controlled by the surface heat flux. Steyn (1998) also states from a vertical scale analysis based on surface-layer turbulent fluxes of sensible heat and momentum, that the height of the SBC is independent of the temperature difference between land and ocean.

2.1.3 Lifecycle of a sea breeze system: five development stages

The development of all sea breeze systems can be described in a five-step model summarized by Miller et al. (2003).

In the first step, the immature stage, a local-scale pressure gradient force causes a divergence in the cross-shore wind component over the sea. This leads to an onshore gravity current which moves inland as a frontal-like structure. The sea breeze circulation (SBC) expands faster seawards than landwards. On land, a convergence zone evolves in the cross-shore wind component which causes an upward movement of the marine and continental air, forming the raised head.

The next stage, the early mature stage, starts with the decline in insolation. This leads to a decay in the Kelvin-Helmholtz billows (KHB). As KHB enhance friction on the upper boundary of the marine air layer, the SBC expands faster inland.

The late mature stage begins when the cross-shore temperature gradient drops to zero due to a decline in insolation. The inflow of marine air in the circulation is cut off. Still, the sea breeze moves inland with a sharp front. Radiative cooling limits convective activity after sunset and therefore confines the height of the sea breeze head (SBH) which still moves further inland.

In step four, the early degenerate stage, the SBH moves separated from the sea breeze gravity current inland. There can be some interaction with other night-time low-level features. A sea breeze cutoff vortex or undular bore might be formed.

In the last step, the late degenerate stage, the structure of the circulation breaks down. The leading edge of the flow flattens. Further inland penetration is limited by Coriolis force or frictional forces. Thus, on the equator, inland penetration of the sea breeze is only limited by friction.

2.1.4 Dependence of the land–sea breeze on external factors

Simpson (1994) summarised the most important impacts on sea breezes (SBs) which should be taken into account in more complex models. The formation of the SB requires a diurnal cycle in the ground temperature and the diffusion of heat. In the process of inland penetration, the static stability plays an important role. The diffusion of momentum slows the circulation down and prevents the predicted accelerating high wind speeds from the Bjerknes circulation theorem. It also forms the structure of the SB. Depending on the latitude, Coriolis force also plays an important role by producing a horizontal rotation of the sea breeze system. This also decreases the inland penetration distance. Two additional factors are the prevailing winds and the topography. Idealised studies mostly neglected the topography to gain more general results (Simpson, 1994). Still, the topography plays an important role, from channelling the sea breeze current, merging different convergent sea breeze systems or influencing the forcing factors by variations in the heating due to the orientation of mountain slopes.

(Lu et al., 2006) shows in a numerical study of the SB in coastal Alabama, that the SB development favours a weak shear environment. (Pearson et al., 1983) analysed the influence of shear on the SB in numerical simulations. He found a strong influence of the vertical shear on the structure

of the SB, whereas the inland penetration distance was not affected by wind shear in their studies.

Miller et al. (2003) states that higher ground temperature gradients over the day result in stronger wind speeds of the SB. These can occur due to higher land surface temperatures, for example, due to dunes which heat the lower atmosphere very efficiently or due to an increased cooling of the atmosphere over water bodies. Experimental studies in South Africa show that SBs are strongest over dune landscapes, where temperatures are exceptionally high over midday compared to the surrounding land (Schumann et al., 1991).

In a case study in south England, Sweeney et al. (2014) investigates the sea surface temperature (SST) impact on the SB with a convection-permitting Met Office Unified Model simulation. A reference run is compared to observations and two sensitivity experiments with a modified SST by $\pm 1\,\mathrm{K}$. A local geographic blocking effect due to an interaction of the SB with the orography builds a narrow zone of calm winds offshore. A decrease in the SSTs results in a higher stability in the marine boundary layer, which increases the blocking. This results in weaker onshore winds and a smaller inland penetration distance. This counter-intuitive result hints at the importance of secondary effects on the sea breeze circulation (SBC) caused by SST changes. A numerical SST-sensitivity study over coastal New England by Lombardo et al. (2018) finds only a small difference in the SB structure, speed and inland penetration distance due to SST variations. They found larger differences in surface sensible, latent heat and buoyancy fluxes. However, the authors point to the stable marine boundary conditions in the case study region and suggest testing the SB sensitivity to SST in other stability regimes. Studies from Franchito et al. (2008) in Brazil analyse the SB during and outside the upwelling season. Comparing observations to modelling results of the interaction between the SB and the upwelling in Cabo Frio, the study finds positive feedback between the upwelling and the SB. In coastal upwelling months, the occurrence of the SB is higher and higher wind speeds are observed, also related to the SB. Franchito et al. (2008) also found a stronger vertical motion over the continent. The coincidence of increased surface winds and increased upwelling in Capo Frio is related to the orientation of the wind to the coastline: Franchito et al. (2008) relate the increased upwelling to wind-driven Ekman pumping. The Ekman pumping intensifies the emergence of cold coastal surface waters which reinforces the cross-shore temperature gradient, resulting in stronger cross-shore winds. A climatological study by Perez and Dias (2017) of the near-surface winds in Sao Paulo (Brazil) finds no relation between the sea breeze arrival time and the thermal gradient between land and sea. This stands in contradiction to numerical studies from Sweeney et al. (2014) on the SST sensitivity of the SB in South England, who found a later onset of the SB in simulations with increased SSTs.

2.1.5 Rainfall related to the land–sea breeze

The vertical motion at the sea breeze front (SBF) can initiate or enhance convection (Miller et al., 2003). Sometimes the position of the SBF can be seen due to the development of Cumulus clouds in the convective area. Stronger convection can also lead to thunderstorm development. The onset time of rainfall related to the sea breeze (SB) depends on the location of the SBF (Fink et al., 2010). Theoretical and observational studies also found that a sea breeze circulation (SBC) can trigger the clustering of thunderstorm cells behind the SBF: Wissmeier et al. (2010) analyses the formation of a multicell thunderstorm behind an SBF in northern Australia with

numerical simulations. The strong low-level convergence ahead of the SBF allows the formation and preservation of the initial thunderstorm cell while enabling the formation of additional cells in the vicinity of the first one. Additional cold air can be supplied from a cold pool to the gust front of the cell if the initial updraft and the downdraught of the cold pool do not fall together. If the gust front opposes the flow direction of the SB, the increased low-level convergence can create new thunderstorms. Perez and Dias (2017) finds the SB to be important in the occurrence of coastal (extreme) precipitation in Sao Paulo, Brazil. An analysis of the climatology reveals that more than one-third of the annual total precipitation can be related to the SB. Also, the spatial distribution of the SB-related precipitation differs from the mean spatial precipitation distribution in this region. Fink et al. (2010) find the highest activity of convective rainfall in the Gulf of Guinea related to the land–sea breeze outside of the monsoon season. The land breeze can cause light convective showers in the early morning crossing the shoreline towards the ocean (Fink et al., 2010).

2.2 The meteorology of West Africa

Over the Gulf of Guinea and on the Guinea Coast, the land–sea breeze (LSB) is embedded in the complex monsoon system in West Africa. The following section describes the structure of the monsoon system and the seasonal cycle of rainfall. The seasonal cycle of occurrence of the near-surface winds is also discussed since they influence the LSB.

2.2.1 Climate zones in Tropical West Africa

Tropical West Africa includes the area from the West African Coast to 20°E and stretches from the equator to 30°N (Fink et al., 2017). It is one of the regions with the highest population density in Africa. Figure 2.4 gives an overview of the climate zones and countries at the Guinea Coast.

To the north of the region of interest lies the southern Sahara which is characterised by its arid desert climate (Fink et al., 2017). South of the Sahara is the semi-arid Sahel zone. Further south, a mixed wet and dry climate zone spans from the Soudanien zone to parts of the Guinea Coastal zones. In the coastal regions in the Gulf of Guinea, there are two zones of wet climate: in the western part of the Gulf of Guinea, one is located between Sierra Leone and Cape Palmas (Ivory Coast). The Niger Delta and the coastal regions in the Bight of Bonny also exhibit a wet climate. Between these zones of wet climate, two adjacent dry zones are located. From West Ghana to Togo lies the Ghana Dry Zone. From southwest Togo to West Nigeria the Dahomey Dry Gap joins.

2.2.2 The West African Monsoon System

The climate in tropical West Africa is determined by the West African Monsoon (WAM) (Fink et al., 2017). It belongs to the three major monsoon systems of our planet. The term ‘monsoon’ is defined by a reversal of the surface winds.

The zone schematic of the West African Monsoon System
Hamilton and Archbold (1945) structured the WAM in four zones, referring to the characteristic

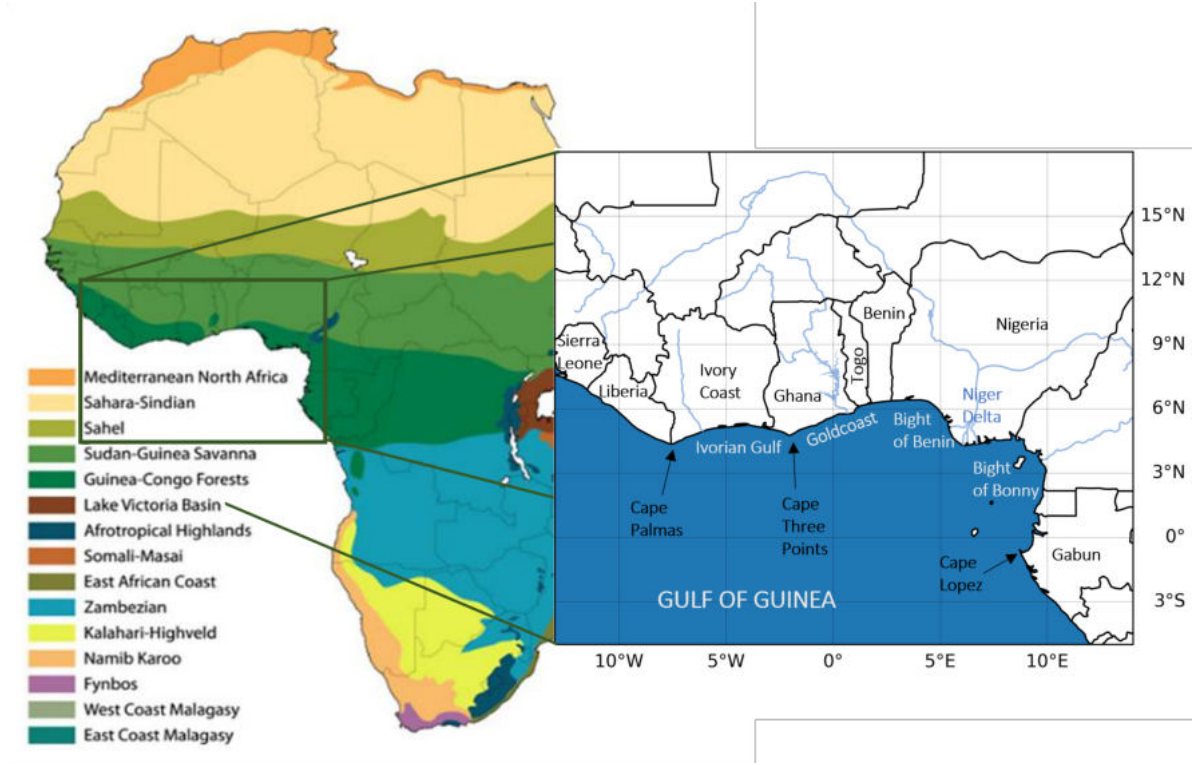

Figure 2.4: *Climate zones and terretories by environment facility (GEF). The Guinea Coast lies in Tropical West Africa. The box marks the area of research in this thesis.*

rainfall and wind structure of these areas. It is shown in Figure 2.5.

Zone A is most northwards (Fink et al., 2017). In this region lies the West African surface heat surface low. The daytime temperatures are very high and there is almost no precipitation. The southern boundary of zone A is the Intertropical Discontinuity (ITD). It is a small band of the maximal confluence of warm and dry air from the Sahara in the north and moist and cooler air from the monsoon layer coming from the southwest (Lafore et al., 2011). The dry northeasterly flow is called Harmattan wind and the moist southwesterly near-surface winds are the monsoon winds (Fink et al., 2017).

Zone B has the smallest latitudinal extension of the zones (Fink et al., 2017). Near the surface, it is characterised by a shallow monsoon layer with winds from the southwest. Aloft lies an equatorward return flow, originating from the converged Harmattan and monsoon winds. Zone B has some rainfall due to thunderstorms, which have a short duration of time. The southern boundary of this zone is the 'monsoon trough'. It can be visualised as a trough of low pressure on maps of geopotential height.

Zone C has the maximum shower activity, a high thunderstorm rate and thus high precipitation (Fink et al., 2017). The cloud structures are dominated by deep convective clouds. The term 'tropical rainbelt' describes this deep convective part with an associated rainfall maximum (Nicholson, 2009). The surface winds are dominated by the southwesterly monsoonal winds. Two jets are located in this zone: the African easterly jet (AEJ) and the tropical easterly jet (TEJ).

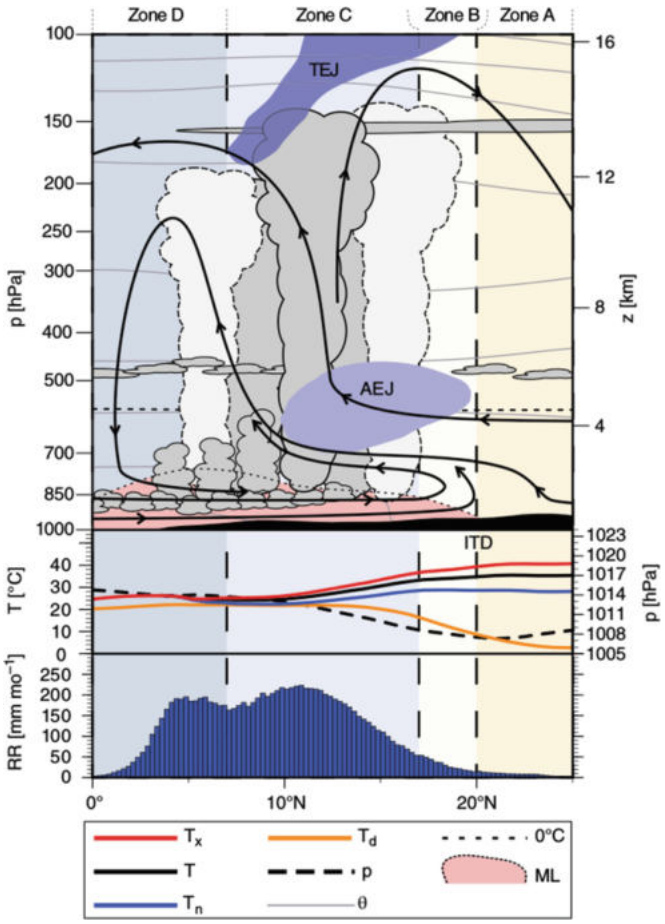

Figure 2.5: *Four zones of the West African Monsoon System after Hamilton and Archbold (1945), figure from Fink et al. (2017).*

The AEJ is a thermal wind, resulting from strong baroclinity due to meridional gradients in moisture and temperature between the Sahara and the moist tropical Atlantic (Fink et al., 2017). The highest velocities of the AEJ are observed around 600 hPa (Lafore et al., 2011). The TEJ is not a straight extension of the TEJ over the Indian Ocean but a consequence of the increasing geopotential gradient at the southern boundary of the upper-level high-pressure system over the Sahara (Fink et al., 2017). It is also influenced by the upper-level tropospheric outflow of the deep convective zone. The TEJ peaks at 100 hPa around 15°N and between 150 and 200 hPa at 8°N.

The coastal zone D is characterised by shallow stratus or mid-level stratus. The monsoon layer reaches its greatest depth at the Guinea Coast 4°–6°N (Fink et al., 2017).

The seasonal cycle of rainfall and surface winds in the different regions of West Africa can be understood by shifting the four-zone-structure northwards and southwards (Fink et al., 2017).

2.2.3 Seasonal cycle of rainfall over the Gulf of Guinea

Maximum precipitation depends on the location of the tropical rainbelt (Fink et al., 2017). The seasonal shift of the tropical rainbelt leads to a bimodal rain season along the coastline. Figure 2.6 shows a Hovmöller diagram of the climatological mean precipitation from 2007 to 2019 in the Gulf of Guinea (black box in Figure 2.6). The band of maximum rainfall shifts in DJF over the Gulf of Guinea, approaches in MA the coastline and moves in MJ northwards across the littoral areas. In JAS it is located in the Sahel region, leading to a dry season along the coast (Hamilton and Archbold, 1945). In ON the tropical rainbelt shifts back southward across the coastal areas which experience another rainy season. The Guinea Coast, from Cape Palmas to the eastern end of the Bight of Benin, therefore experiences a strong seasonal cycle with five different seasons (Hamilton and Archbold, 1945):

1. December to February: long dry season
2. March and April: the beginning of the long rainy season
3. May and June: long rainy season.
4. July to September: short dry season
5. October and November: short rainy season.

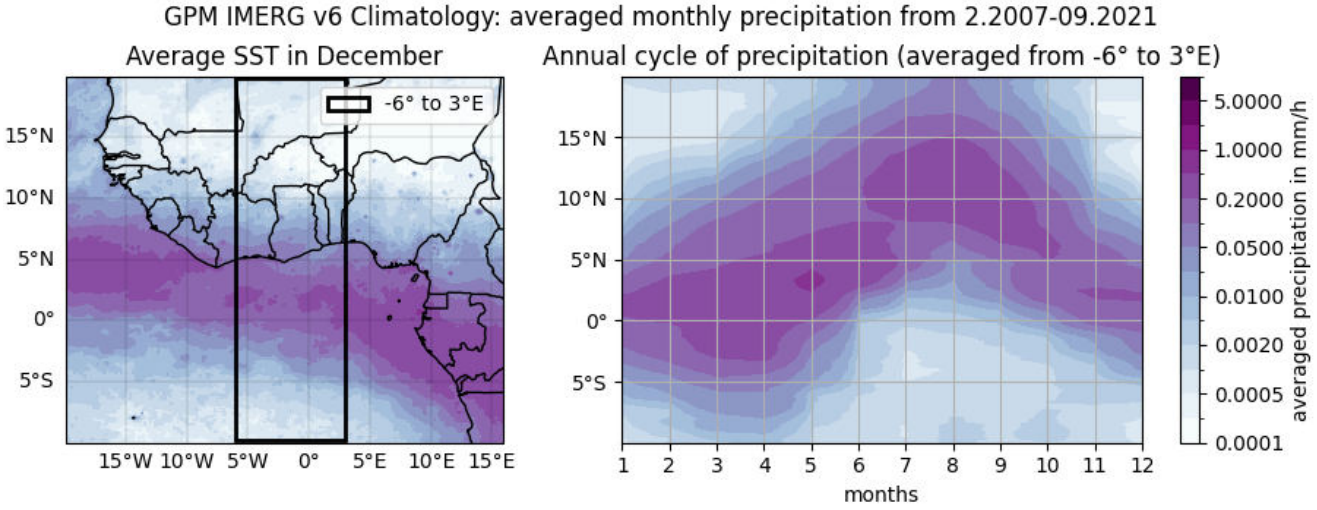

Figure 2.6: *Precipitation climatology: monthly averaged precipitation from February 2007 to November 2022 (GPM IMERG v6 Final data). Graphic on the left-hand side: Climatological precipitation distribution in December. The black box marks an area within a zonal mean is calculated. The graphic on the right-hand side shows the annual cycle of the meridional distribution of the mean monthly precipitation within this box.*

2.2.4 Seasonal occurrence of boundary layer wind regimes over the Gulf of Guinea

At the Guinea Coast, there are four dominant wind regimes observed in the lower troposphere: monsoon winds, Harmattan winds, the nocturnal low-level jet (NLLJ) and the land–sea breeze

(LSB). Within the seasons there is a variation in the occurrence frequency of the different wind regimes. (Guedje et al., 2019) depicts in Figure 2.7 the monthly climatology.

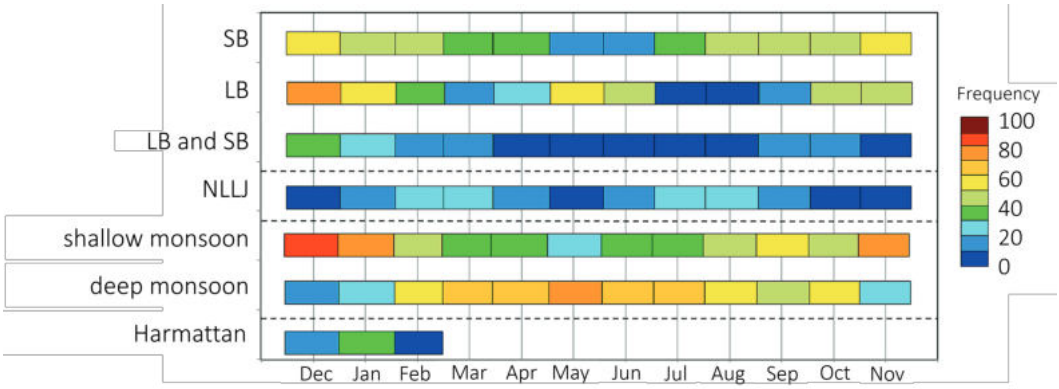

Figure 2.7: *Occurrence of the four dominant wind regimes at the Guinea Coast, adapted from Guedje et al. (2019).*

Monsoonal wind

The southwesterly monsoonal winds dictate the low-level winds nearly all year round at the Guinea Coast (Guedje et al., 2019). Cool and moist air flows from the ocean in the south towards the Intertropical Discontinuity (ITD) in the north. The strongest monsoon winds with the highest near-surface windspeeds of approximately $4\,\mathrm{m\,s^{-1}}$ are observed in the short dry season from June to September. The depth of the top of the monsoon layer varies between 850 and 700 hPa during the seasons. From December to February it is a shallow layer below 900 m depth. The depth of the monsoon layer also depends on the vertical structure and the location of the ITD.

Harmattan wind

Coastal weather stations observe during Harmattan periods a persistent northeasterly surface wind, very low humidities and higher 2 m temperatures (Guedje et al., 2019).The Harmattan wind occurs only in boreal winter when the ITD reaches its most southerly location at 8°N (which is just north of the Guinea Coast). Those winds recur in periods of a few days up to two weeks. The Harmattan wind regime mutually excludes the monsoon winds, therefore they cannot occur at the same time.

Nocturnal low-level jet

The nocturnal low-level jet (NLLJ) is a southwesterly wind occurring during the short dry season and from January to April (Guedje et al., 2019). It is widely observed at coastal, Soudanian and Sahelian stations. During the nighttime, air masses are accelerated towards the heat low and a jet is formed centred around 400 m height, sometimes in greater heights around 600 m as well (Guedje et al., 2019). The appearance in the late night and early morning can be explained by the decrease in friction due to the absence of convective turbulent mixing in the nighttime (Guedje et al., 2019). The nighttime inversion causes the decoupling from the surface layers and the aloft layer (Markowski and Richardson, 2010).

Land–sea breeze

The LSB is a local feature in contrast to the former wind systems (Miller et al., 2003). The

sea breeze (SB) has the highest occurrence frequency in November and December (Guedje et al., 2019). This is a period with a small but positive land–sea temperature difference and small precipitation amounts. Due to the high daytime temperatures and low nighttime temperatures (often clear-sky conditions), the LB and the SB are very likely to occur. The lowest occurrence frequency of the SB is during the long rainy season in May and June. The daytime land surface temperature decreases due to increased cloudiness, precipitation and evaporation whereas the sea surface temperatures (SSTs) remain high (details about the annual cycle of the SST can be found in Chapter 2.3.1). This increases the probability of an LB event, while the SB occurrence reaches its minimum. From July to September, the coastal SSTs drop to the annual minimum during the major upwelling season. The increased horizontal SST gradient strengthens the monsoon flow. In these conditions, the LB is barely observed, whereas the SB occurs on average on 50 % of the days.

2.2.5 Idealized daily atmospheric cycle over a dry continent

The atmosphere over landmasses and continents has a diurnal cycle driven by the cycle of heating from shortwave radiation and the atmospheric response (Rácz and Smith, 1999). Rácz and Smith (1999) discussed the dynamics of heat lows over arid landmasses in an idealized model over Australia. A squared land mass without elevation surrounded by the sea is used to filter the basic atmospheric oscillations from the complex interactions driven by topography, tilted shorelines, sea surface temperature gradients etc. The temperature in the model is only modified by a diurnal cycle of solar insolation. For maximal simplicity, there is no moisture, no direct atmospheric absorption of direct or indirect radiation in the atmosphere and an initialisation of the experiment in a resting state.

Two processes are found to be fundamental for the low-level circulation characteristics atmosphere: deep convective mixing and the formation of a nocturnal low-level jet (NLLJ) (Rácz and Smith, 1999). In the daytime, deep convective mixing occurs over the land due to the strong solar heating of the surface. Along the solar heating cycle, the surface pressure of the heat low decreases from its highest value at 9 LT in the morning until it reaches its daily minimum at 19 LT in the simulations of Rácz and Smith (1999). The surface winds respond to both the local-scale pressure gradient force (PGF) induced by the temperature gradient at the shoreline and to the large-scale pressure gradient force resulting from the heat low. The local PGF initialises a sea breeze, which penetrates slowly inland, slowed down by turbulence due to convective processes. In the nighttime, a surface inversion and the reduction of the atmospheric convection diminish the friction at the surface and in the atmosphere. The sea breeze transforms into an NLLJ. Rácz and Smith (1999) assume a close analogy from these diurnal atmospheric motions over other arid regions with analogous characteristics.

2.3 Sea surface temperature variability in the Gulf of Guinea

Tropical oceans are of major importance for our climate system (Brandt et al., 2023). Due to their latitude, they take a lot of energy from incoming shortwave radiation which is transported northwards and southwards by ocean currents. Over the interphase between the ocean and atmosphere trade gases like carbon dioxide and oxygen are exchanged. The oceans are a giant storage for carbon dioxide which is transported to large depths. On the other side, fisheries benefit from

the world's highest marine productivity in tropical oceans.

This work investigates the influence of the sea surface temperatures (SSTs) in the Gulf of Guinea on the sea breeze circulation. In this section, the seasonal variability of SSTs in the Gulf of Guinea is discussed. The different forcing processes are outlined. The impact of the SSTs on the atmosphere in general is also delineated. The impact of the SSTs on the land–sea breeze has not previously been investigated in the Gulf of Guinea, to the best of the author's knowledge. However, insights from other regions of the world are summarised in Chapter 2.1.4.

2.3.1 The seasonal cycle of sea surface temperatures in the Gulf of Guinea

The sea surface temperature (SST) depends both on atmospheric and oceanic processes (Deser et al., 2010). Wind speed, air temperature, cloudiness and humidity are the major atmospheric factors influencing the energy exchange at the sea surface. Within the ocean, the SSTs are impacted by vertical mixing, heat transport by currents and oceanic boundary layer depth.

The annual cycle of SSTs in the Gulf of Guinea is partly driven by upwelling (Moore et al., 1978). The ocean in the Gulf of Guinea has a strong stratification with warmer surface waters separated by a layer with a strong vertical temperature gradient (the thermocline) from the colder ocean water underneath. In an upwelling process, the thermocline is lifted isostatically, bringing cooler water to the surface Patrick et al. (2003). The upwelling seasons are therefore characterized by colder SSTs, higher surface salinities, a higher nutrient level and a lower dissolved oxygen level (Hardman-Mountford and McGlade, 2003).

Figure 2.8 shows the monthly climatological mean of the SST in the Gulf of Guinea. The most pronounced SST variation occurs at the equator: The so-called Atlantic cold tongue (ACT) emerges in the equatorial region between the African coast and 20° west (Mitchell and Wallace, 1991). The SSTs fall below 22°C when the ACT emerges from April to August, whereas SSTs take values between 27-29 °C in the warm seasons (Caniaux et al., 2011). A second cooling period occurs in November and December at the Equator. It is weaker in intensity and occurs on a smaller spatial extent (Jouanno et al., 2011).

The northern coasts in the Gulf of Guinea also experience a bimodal cycle in the SST variability. Two main upwelling cells can be defined east of Cape Three Points and east of Cape Palmas (Brandt et al., 2023). The major coastal upwelling season takes place from July to September (Sohou et al., 2020), sometimes also defined from June to October (Hardman-Mountford and McGlade, 2003). Besides the major upwelling season, a minor upwelling season occurs between January and March (Sohou et al., 2020). An earlier onset of the minor upwelling in December has been observed (Hardman-Mountford and McGlade, 2003). Figure 5.1 (in the result Section 5.1.1) shows the climatological mean SST along three sections of the northern coast in the Gulf of Guinea. The coastal upwelling in the Gulf of Guinea plays a key role in local fisheries and has, therefore, a high impact on the economics of the coastal countries (Amemou et al., 2020). The SST variability is also known to influence local climate for example by modulating the West African Monsoon

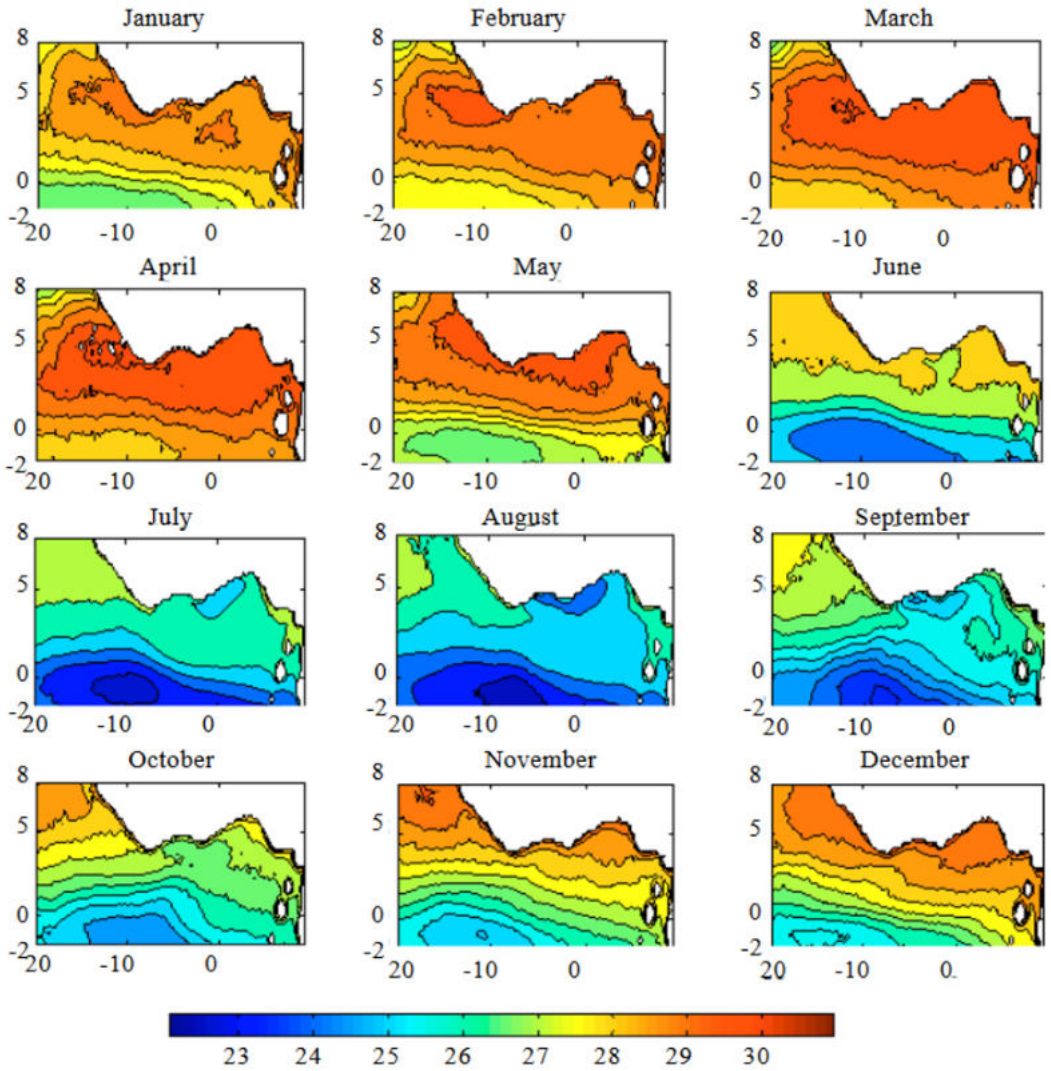

Figure 2.8: *Spatial evolution of the monthly SSTs in the Guinea Gulf from 1998-2007 from Ali et al. (2011).*

2.3.2 Reasons for upwelling events in the Gulf of Guinea

The seasonal cooling in the Atlantic cold tongue (ACT) results from a vertical displacement of the thermocline (Merle, 1980). The equatorial upwelling is an integral part of the subtropical cells, driven by Ekman transport due to forcing from the trade winds (Brandt et al., 2023). The strengthening of the equatorial upwelling results from increased wind stress divergence from increased easterlies and an increased monsoon flow (Patrick et al., 2003). Still, other oceanic processes also play an important role. Turbulent mixing, for example, is found to give a major contribution to the spatial distribution of the ACT (Jouanno et al., 2011). It contributes to the cooling by increasing the heat exchange between the mixed ocean layer and the deep ocean. Hummels et al. (2013) found the turbulent mixing in the equatorial Atlantic to be mainly driven by vertical shear between the westward south equatorial surface current and the eastward equatorial undercurrent.

The upwelling in the Gulf of Guinea is strongly connected to the equatorial upwelling by the propagation of equatorial Kelvin waves and coastally trapped waves: in the bimodal cycle of thermocline lifting in the ACT, equatorial Kelvin waves are induced (stronger effect in boreal summer) (Brandt et al., 2016). Equatorial waves are large-scale oceanographic features with wavelengths of 10 000 km and northward and southward extension of 350 km (Patrick et al., 2003). The vertical extension between the surface water and the thermocline is the amplitude of the wave. Due to the dimension of the wave, the Coriolis force cannot be neglected regarding the propagation of the wave. In the northern hemisphere, a parcel of water moving eastwards is deflected to the right with respect to the direction of motion and thus southwards. In the southern hemisphere, water masses moving eastward are deflected towards the left with respect to the direction of motion and thus to the north. An oceanic Kelvin wave moving towards the east will therefore be 'pushed' from north and south towards the equator and deepen exponentially. The Kelvin wave propagates with a velocity of $1\,\mathrm{m\,s^{-1}}$ toward the east and reaches Cape Lopez (Gabun) approximately one month later (Patrick et al., 2003). When the equatorial Kelvin wave reaches Cape Lopez, two effects happen: first, the equatorial Kelvin wave is reflected as a westward-moving Rossby wave (Brandt et al., 2023). Second, the equatorial Kelvin wave is transformed into a coastally trapped Kelvin wave, moving along the shoreline in the Gulf of Guinea. Coastal Kelvin waves affect only ocean areas 100 km south of the coastline. Similar to the equatorial Kelvin wave, the Coriolis force plays an important role: the westwards-moving coastal Kelvin wave experiences a deflection to the right and thus to the north due to Coriolis force. Therefore, the coastal Kelvin wave is pushed against the zonal coastline. Moore et al. (1978) observed the coastal temperature minima shift along the coastline of approximately $0.6\,\mathrm{m\,s^{-1}}$ to $0.7\,\mathrm{m\,s^{-1}}$ to the west. In the southeasterly aligned coastlines in the Ivory Coast and along the Gold Coast a large cooling effect was observed by Moore et al. (1978), whereas no cooling effect occurred in the Bight of Bonny (Nigeria). This is due to very deep thermocline in the Bight of Bonny (Patrick et al., 2003). The Niger River plume can limit the upwelling intensity at the Gold Coast and in the Bight of Benin: Souza et al. (2021) states, that the outflow of the Niger River plume reaches far east into the eastern upwelling cell and increases the SSTs about 1 K.

The remote forcing of the coastal upwelling by a wind-induced Kelvin wave formation at the equator is detected in the bimodal cycle. The resulting decrease in the thermocline depth along the Gulf of Guinea is additionally supported by the seasonal strengthening of the eastward-flowing Guinea current (Brandt et al., 2023). The Guinea current is the main surface current in the northern Gulf of Guinea from 10°W to 6°E is the eastward-flowing Guinea Current. It is present in the whole year except November. The two maxima in the Guinea Current coincide with the major and minor upwelling season (Bosson et al., 2023). Djakouré et al. (2017) found the link between the core location of the Guinea current and the coastal upwelling: Non-linear dynamics cause a detachment of the Guinea current down of Cape Palmas. In sensitivity experiments, they excluded non-linear terms in the momentum equations, finding the Guinea current trapped to the coast. Within these experiments, the cold coastal SST anomaly disappears. Djakouré et al. (2017) concluded that the detachment of the Guinea current plays an important role in the western upwelling cell. Bosson et al. (2023) found a similar detachment downstream of Cape Threepoint. They suggested an upwelling favouring effect similar to the one downstream of Cape Palmas.

Bosson et al. (2023) investigates the Ekman and geostrophic component in the Guinea surface cur-

rent. The Ekman current drives near-surface water currents all around the world by wind stress and Coriolis force (Ekman and Walfrid, 1905). The geostrophic current component originates from the balance of horizontal pressure gradient force and Coriolis force. In the Gulf of Guinea, the geostrophic component is maximum in the west and decreases eastward (Bosson et al., 2023). It originates from the sea level slope that increases towards the east, driven by density differences along the coast. East of Cape Three Points, cool and salty water comes to the surface in the upwelling core whereas warm and fresh water can be found in the Niger River plume (Brandt et al., 2023). Bosson et al. (2023) found the Guinea current to be predominantly geostrophic. However, they state, that the Ekman current cannot be neglected due to its contribution to the coastal upwelling dynamic. In summary, Bosson et al. (2023) state that the spatial variability and the variability in the contribution of the Ekman and geostrophic components favour convergence or divergence of water masses which are likely to impact the SSTs.

In summary, there are plenty of effects causing or preventing coastal upwelling in the northern Gulf of Guinea, reviewed by Brandt et al. (2023). They conclude the major contributions in the western upwelling cell to be determined by advection of momentum (inertial detachment of the Guinea current), whereas wind-induced divergence of coastal water masses is a major factor to the eastern upwelling cell. The details about the coastal upwelling in the Gulf of Guinea still remain unclear. Especially the minor upwelling season is poorly understood.

2.3.3 Cooling of the sea surface by Saharan dust on short time-scales

When the wind stress on the ocean surface is low, the absorbed solar shortwave radiation will result in a higher temperature of the sea surface. The increased vertical thermal gradient results in a stable stratification in the uppermost ocean layer. A diurnal warm layer forms which is also called the diurnal thermocline (Gentemann et al., 2009). Stronger near-surface winds induce increased vertical mixing which prevents the formation of this surface warm layer. The SST difference in clear-sky conditions in weak wind conditions and strong wind conditions can reach several Kelvin (Donlon et al., 2012; Minnett et al., 2011). The wind speed is therefore a determining factor for the SST variability. Studies of Foltz and McPhaden (2008); Lau and Kim (2007) show, that SST variations are weak under strong winds and well-mixed conditions.

In weak wind conditions, however, radiative effects are very important. A decreased downward shortwave radiation resulting from Saharan dust outbreaks can lead to a decreased SST (Avellaneda et al., 2010; Evan et al., 2009; Foltz and McPhaden, 2008; Lau and Kim, 2007; Luo et al., 2021). Dust aerosols can exceed a size of $10\,\mu$m and scatter or absorb short-wave radiation and emit longwave radiation (Kok et al., 2017). Luo et al. (2021) quantifies the dust scattering and absorbing effects on the surface radiative fluxes by using a measurement set from ship campaigns, reanalysis products and a model for atmospheric radiative transfer and thermal skin effect. Their study reveals both a small warming effect and a strong cooling effect of the SST which is induced by dust outbreaks. The warming effect can reach 0.06 K per day in their studies. It results from the reduced longwave flux from the sea surface to the atmosphere: the sea surface is nearly everywhere warmer than the atmosphere aloft. Thus, there is an outward longwave radiation flux. Dust aerosols in the atmosphere absorb shortwave and longwave radiation and emit longwave radiation in every direction, thus they also lead to an increased downward longwave radiation

flux. Therefore, the net longwave radiation flux from the ocean surface upwards is reduced by the downward longwave radiation flux of the aerosols. This effect is present during the daytime and the nighttime. The effect of the reduction of solar shortwave radiation due to absorption or scattering by dust aerosols exceeds the warming effect. Especially under light wind conditions, the reduced shortwave radiation flux at the ocean surface leads to a cooling of the SSTs (Luo et al., 2021). The skin SST can therefore be reduced by 0.24 K during daytime (Luo et al., 2021). Avellaneda et al. (2010) found a cooling effect of up to 0.4 K of the skin SST.

2.3.4 Feedback between sea surface temperatures and the near-surface atmosphere

The sea-surface temperatures strongly impact the near-surface atmosphere and vice versa. The atmospheric response of the interaction is most likely trapped due to the high stability of the atmosphere above the marine atmospheric boundary layer (MABL) (de Coëtlogon et al., 2010). de Coëtlogon et al. (2010) states, that the interaction between the ocean and the atmosphere occurs on short dynamical time scales on slower thermodynamic processes. Their studies on the ocean–atmosphere interaction in spring and summer in the Gulf of Guinea have revealed a bi-weekly variability in the SST anomaly, observed in the equatorial Atlantic cold tongue. They found a high correlation between wind stress and SST for a 5–day time lag when the wind leads the SST and a 3–day time lag when the SST leads the wind. de Coëtlogon et al. (2010) linked the variability in the SSTs to the variability in the surface winds which belong to stronger or weaker south easterlies. The strength of these south-easterlies depend on a large-scale circulation, spanning the southern basin of the Atlantic. It is driven by the variability of the St Helena anticyclone.

de Coëtlogon et al. (2010) also noted an effect of the strong zonal anomaly in the SST in the region of the northern front of the cold tongue on the near-surface winds. This effect is described by Lindzen and Nigam (1987): Differential heating northwards and southwards of the cold front initialises a pressure gradient force. Hsu (1984) found secondary thermally driven circulations due to this pressure gradient force.

The SSTs have a direct effect on the stability of the MABL. Wallace et al. (1989) found an increased stratification in the lower atmosphere above colder SSTs. The lower stability results from the colder air temperatures caused by cooling from the SSTs. Vertical mixing is suppressed in such a strongly stratified atmosphere due to decreased turbulence and convection. This effect leads to a decoupling of the surface winds from the winds aloft and therefore to an increase of wind shear near the surface. Wallace et al. (1989) found an effect in more than 100 m height above ground. A higher SST on the other hand destabilises the MABL, enhances vertical mixing and therefore supports downmixing of momentum. Statistical analysis from de Coëtlogon et al. (2010) indicates, that the SST-induced effect on vertical mixing of momentum exceeds the forcing from the change in sea level pressure due to the SST variation.

Large-scale cold anomalies in SST impact large-scale circulations like the Hadley cell in location and extension of the zonal rain band (Raymond, 1995). A local impact is the reduction of the convective available potential energy (CAPE) of air parcels close to the surface due to reduced evaporation, reduced sensible heat content and inversion layers. This lowers the energy content of air parcels originating from the equatorial upwelling region being transported in the monsoon flow towards the coast. Still, the motion across 350 km warm surface waters until the winds reach

the Guinea Coast destabilises the air.

3 Research questions and aims of this thesis

The literature review reveals that the Sea Land Breeze (LSB) has a frequent occurrence in the Gulf of Guinea and plays an important role in the West African coastal weather (Guedje et al., 2019; Miller et al., 2003). Still, the LSB circulation characteristics are only poorly investigated in this region. The analysis of the sea surface temperature (SST) impact on the land–sea breeze is yet unexplored in the Gulf of Guinea, to the best of the author's knowledge. In studies in other regions of the world, the literature review reveals large discrepancies between studies of the SST impact on the LSB. The climatology analysis of the SST variability in the Gulf of Guinea confirms a large intra-annual and seasonal SST variability and reveals SST variations in near-coastal areas appearing within a few days. To the best of the author's knowledge, such short-time SST cooling events have not been discussed in the scientific literature.

For investigating the influence of the SST on the LSB, SST sensitivity experiments are designed using the numerical weather prediction model ICON: In four of five identical atmospheric and land surface simulation setups, the SSTs in the whole region of the research area are uniformly increased or decreased by 1 K or 2 K. The remaining fifth simulation is treated as a reference run. For the data analysis, a sea breeze front (SBF) identification algorithm is adapted and implemented to allow the analysis of SB characteristics along large areas of the Guinea Coast. With this novel approach to explore the LSB characteristics, the research questions below are investigated:

1. Can the ICON model realistically reproduce the LSB in the chosen configuration?
2. How far does the SB penetrate inland and what atmospheric mechanisms control this distance?
3. How does the inland penetration distance of the SB depend on the SSTs?
4. How does the height of the LSB depend on the SSTs?
5. How do circulation characteristics (mean and maximum wind speed) of the SB depend on the SST?
6. Does the formation of convective clouds related to frontal processes at the Sea Breeze Front depend on the SST?

The chosen setup for the simulation is expected to give a detailed insight into the formation, development and characteristics of the LSB in this region. The novel approach of performing SST sensitivity experiments in the Gulf of Guinea allows the analysis of the SST impact on the large-scale circulation of the West African monsoon system and the LSB. This fundamental research can be expected to contribute to an understanding of the influence of SST changes on the whole atmosphere. The shock-like modification of the SSTs in the simulations allows an insight into the responses of the atmosphere to short-time SST variations, found in the satellite-based SST data. After a spinup time, the results are valuable in a more general context, for example, intra-annual SST variability. The results of this work are relevant for understanding the impact of the SST on the LSB in the Gulf of Guinea in general. This is relevant for future studies analysing the LSB in different SST conditions in the Gulf of Guinea and also for improving the

LSB forecasting in these regions. A clear dependence of the SLB on the SSTs would imply the requirement of implementing exact and updated SSTs in future numerical studies investigating the SLB in the Gulf of Guinea.

4 Methodology

4.1 Data

OSTIA

The Operational Sea Surface Temperature and Sea Ice Analysis (OSTIA) system provides a worldwide foundation surface temperature (SST) field combining satellite data and in situ measurements Good et al. (2020). The foundation surface temperature is the SST free of diurnal variations. The Copernicus Marine Environment Monitoring Service (CMEMS) provides the data for numerical weather prediction nearly in real-time. The SST data is available in daily timesteps with a horizontal resolution of 0.05°. The estimate of foundation SST with global coverage is based on microwave and infrared satellite measurements (Donlon et al., 2012). The passive microwave radiometry uses the 6 GHz to 10 GHz band, which estimates the temperature of the sea surface depending on the actual SST and the surface roughness of the ocean. An additional measurement of the brightness temperatures removes the roughness impact on the estimated temperature. Atmospheric water vapour and aerosols are almost transparent to the 6 to 10 GHz microwave radiation, therefore the microwave measurement works under all weather conditions except rainfall. Additionally, the received satellite data is corrected with in-situ measurements from drifting buoys and constantly validated to guarantee a zero mean bias. In the initial phase of the satellite-based SST estimate of OSTIA, bias errors of about 1 K were detected during Saharan dust outbreaks given that the infrared sensors are highly affected by dust in the atmosphere. Studies from Merchant et al. (2006) mention a bias of up to 3 K, depending on the SST retrieval algorithm and the brightness temperature effects. A Saharan dust index scheme applied by Merchant et al. (2006) limits this problem. An overestimation of SST variabilities during Saharan dust outbreaks is possible when the data is received from satellite data. Besides the possible measurement errors, an impact of the atmospheric dust on the SST is found in studies based on satellite data, simulations and in-situ measurements from ship campaigns.

TAHMO

The Trans-African Hydro-Meteorological Observatory (TAHMO) is an initiative which installs inexpensive (10 Euro) and robust weather stations in the Sub-Saharan region (van de Giesen et al., 2014). The data from these weather stations is used to improve the weather forecast and monitor and manage water and energy resources. The project targets to build a weather station every 30 km. By now, in the Gulf of Guinea Ghana, Togo a Benin are already well-covered by weather stations. The data availability and quality differ from station to station (correspondence with Kwame Duah for TAHMO data access). Schunke et al. (2021) show in a comparison of TAHMO stations to meteorological reference stations, that there is a good agreement in air temperature and relative humidity, while wind data shows high deviations.

GPM IMERG

The National Aeronautics and Space Administration (NASA) provides a Global Precipitation Measurement (GPM) Integrated Multi-SatellitE Retrievals for GPM (IMERG) product to monitor the precipitation worldwide Huffman et al. (2015). It combines the data from microwave spectra and infrared (IR) from satellites in the IMERG Early and Late datasets. The post-processed dataset IMERG Final includes the forward and backward analysis using rain gauge

data Sungmin et al. (2017). GPM IMERG has several important issues, including an overestimation of rainfall from frequently occurring weak convective events while underestimating strong mesoscale convective systems. Another problem is a low sensitivity to warm rain and oversensitivity to low-level cloudiness (Amekudzi et al., 2023). These issues also affect the measurement of low-level clouds and associated rainfall related to the land–sea breeze.
The data used in this thesis is the final precipitation product. It has a vertical resolution of 0.1° and time steps of 30 minutes.

ERA5
ERA5 is the fifth generation of an atmospheric reanalysis of the global climate from 1940 to the present, generated by ECMWF (European Centre for Medium-Range Weather Forecasts) (Hersbach et al., 2020). By combining observations ECMWF produces a detailed dataset of the global atmosphere, land surface and ocean waves with the Integrated Forecasting System (IFS) Cy41r2. It has a horizontal resolution of 0.25° and a time resolution of down to hourly steps.

4.2 The ICON model

The ICOsahedral Non-hydrostatic model (ICON) is a numerical weather modelling framework developed by the German Weather Service (DWD), Max Planck Institute for Meteorology, the German Climate Computing Center and KIT.

Numerical weather models calculate the state of the atmosphere by solving a set of seven basic equations numerically from an initial state of the atmosphere (Pu and Kalnay, 2018). These equations contain Newton's second law (conservation of momentum), the continuity equation (conservation of mass), the equation of state for ideal gases, the first law of thermodynamics (conservation of energy) and a conservation equation of water mass. The state of the atmosphere is calculated by integrating the spatial and temporal discretised equations.

This short introduction to the ICON model and the description of the relevant settings for the simulations within this project are based on the ICON tutorial of Prill et al. (2022) and the ICON user guide of (Rast, 2018). Zängl et al. (2015) gives an additional detailed description of the dynamics core of the ICON model.

4.3 Setup for the ICON reference run

Given the scarcity of observational data in this region, data from ICON simulations are analysed to address the research questions of this thesis. A reference run is used to investigate the characteristics of the LSB. In the next step, SSTs are adjusted in the initial conditions of the model and the corresponding simulations. The SST experiments are analysed to investigate the impact of the SST on the LSB. The characteristics of the circulations in these new settings are compared to the reference run.

4.3.1 Research area and grid parameters

The simulation is performed with a two-nested simulation in the area presented in Figure 4.1. The output data of the first nest is taken as the initial and boundary conditions for the second nest with higher horizontal resolution. The simulations have a resolution of 0.06° and 0.03° latitude. It is anticipated that this resolution is sufficient to resolve aspects of the sea breeze circulation. The resolution is too coarse to resolve the detailed structure of the SBF. Still, the resolution of the second nest is sufficient to assess the inland extension, height and dynamic properties of the SB.

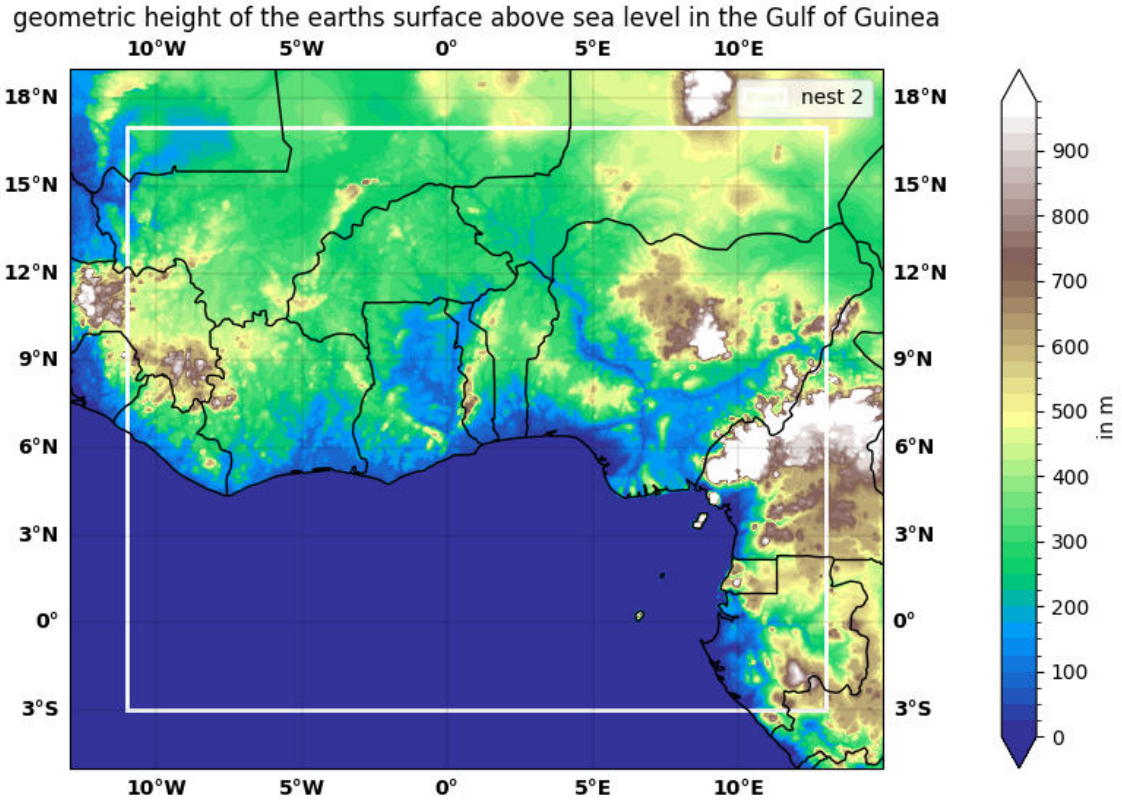

Figure 4.1: *Area of research: map of the first nest, the second nest is indicated as a white rectangle.*

Table 1 summarises the grid settings of the simulations in this thesis. They are based on the operational settings of DWD with additional changes suggested for tropical regions.

4.3.2 Period of the simulations

The period of the simulations has to fulfil four criteria:

1. The period is in the dry season to minimize the impact of cloud cover and precipitation on the LSB.

2. The period is during a season when the LSB is common.

Nest	1	2
Grid	R3B7	R3B8
Horizontal Resolution	0.06°	0.03°
Half width	12° lat 14° lon	10° lat 12° lon
Center	7° N 1° E	
Number of model levels (output)	top: 0, surface: 60 (42 to 60)	
Height at which all model levels are flat	16000 m	
Top height	75000 m	

Table 1: *Vertical and horizontal grid settings in my simulations.*

3. The period is within the minor upwelling season.

4. The period should contain a Harmattan wind event and the shallow monsoon flow across the coast.

All these criteria are fulfilled in December: Guedje et al. (2019) found the highest SB and LB combined occurrence in the Gulf of Guinea in December. Also, this month falls within the long dry season which takes place from December to February. Additionally, cooling events being classified in the minor upwelling season are observed during December (Hardman-Mountford and McGlade, 2003).

Finally, a simulation period of 5 days from 13.-18. December 2021 was chosen for a reference run. In a daily analysis of precipitation and SST, this period is particularly dry in the coastal areas of the Gulf of Guinea. Figure 4.2 shows the accumulated rainfall during the research period. The accumulated precipitation over 5 days stays below 2 mm in large areas in Ghana, Togo, Benin and West Nigeria. Precipitation in littoral areas occurred in West Ghana and in the Ivory Coast from 14. to 15.12.2021 (Figure 8.1 in the appendix: The graphic shows the daily accumulated precipitation).

During the research period, the SST from OSTIA data shows little variations on all length scales north of the equator. (Figure 8.5 in the appendix). The constraint of a constant SST in the ICON simulation is therefore reasonable.

4.3.3 Initial and boundary conditions and nudging

ICON global analysis data is used to initialise the model and as boundary conditions to nudge the model. This data type is recommended to run ICON-LAM (limited area model). It benefits from data assimilation. Still, the data quality is unknown due to the limited data availability in Africa.

The simulations are nudged within the outermost 10 grid-size steps with the boundary data. Nudging guides the simulation on the path of a realistic scenario evolution by controlling the boundary of the simulation.

For the SST experiments, the nudging of the first nest is also done with the same data as in the reference run. While the atmosphere in the centre of the research area adapts to the higher or lower SST, the air flowing into the first nest at the boundaries is not in equilibrium with the

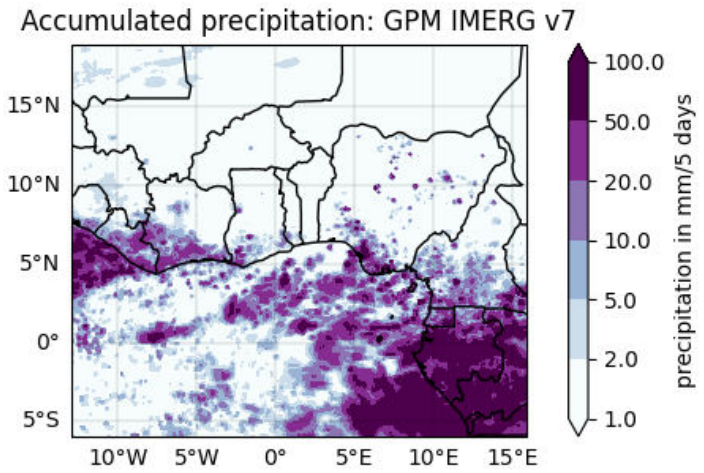

Figure 4.2: *Accumulated precipitation (GPM IMERG v7) from 13.-17. December 2021.*

surface below. This causes boundary effects due to the mismatch in temperature and moisture. The second nest is initialised and nudged with the data from the second nest. Therefore, the location of the second nest is chosen far enough inside the first nest to avoid these boundary effects.

4.3.4 Parametrization schemes

In tropical Africa, convection occurs on all length scales from large MCS to small convective updrafts during mid-day due to radiative heating in the lowest atmosphere.

Table 2 gives on overview over some of the important parametrization schemes. Most of the

	Parametrization scheme setting	
Microphysics (COSMO-EU)	inwp_gscp = 1	Single-moment scheme
Convection scheme	inwp_convection = 0	Explicit convection
Shallow convection scheme	lshallowconv_only = FALSE	Explicit convection
Surface scheme	inwp_surface = 1	TERRA
Vertical diffusion transfer	inwp_turb=1	COSMO
Cloud cover	inwp_cldcover=1	Diagnostic PDf
Radiation	inwp_radiation = 4	ecRad
Sub-grid scale orographic drag	inw_sso = 1	Lott and Miller scheme

Table 2: *Choosen parametrization scheme settings in the ICON simulations.*

parametrisation schemes are identical with the recommendations of the German weather service for tropical regions, they can be found in Prill et al. (2022) in section 'Tropical setup'. Based on test runs with the convection parameterisation (deep and shallow) turned on and off, it was determined that simulations without convective parametrisations best matched the observations.

4.4 SST experiments with ICON

4.4.1 Concept of the SST experiments

The annual mean cycle of the coastal SST is described in Chapter 2.3.1. Within the major and minor upwelling season, intraseasonal SST changes occur along the coast. Additionally, daily SST variations are observed. These SST variations are analysed in Chapter 5.1.3.

The thesis project aims to investigate the SST impact on the LSB. In the Gulf of Guinea, SST changes are found on different time scales, from seasonal up to diurnal SST variations. The theoretical background about the coastal SST changes and the oceanic forcing mechanisms in the Gulf of Guinea can be found in Section 2.3. The influence of the SST on the SBC will be analysed in SST experiments.

The SST experiments use the same data for initial conditions as the reference run except that the weighted ground temperature T_g is modified. The weighted ground temperature is a proxy for the SST, which cannot be directly accessed and modified in the input data for the simulations. For all water surface areas, a constant temperature anomaly ΔT is added or subtracted to the T_g-field. The new weighted ground temperature for each point in the grid can thus be calculated by:

$$T_{g,exp}(\text{lat,lon}) = T_{g,ref}(\text{lat,lon}) + \Delta T \tag{7}$$

for all ocean grid points.

The names of the ICON runs refer to the applied weighted ground temperature change. Table 3 gives an overview over the experiments.

Name of the ICON run	SSM2	SSTM1	reference run	SSTP1	SSTP2
ΔT	$-2\,K$	$-1\,K$	$0\,K$	$1\,K$	$2\,K$

Table 3: *Overview: SST experiments with ICON. The applied temperature anomalies relate to equation 7.*

The sudden modification of the SST in the SST experiments reflects the short time scale of the observed SST variations. It leads to an out-of-equilibrium-state at the boundary of the atmosphere and the ocean. The larger the magnitude of ΔT, the higher the shock to the system. Discontinuities lead to alignment processes, in the real world just as in the simulation. The atmosphere and the ocean are a coupled system, that approaches balance in different processes on different time scales. They are analysed in Section 5.3.1. A defined spinup time confines the analysis of the LSB to a period with quasi-equilibrium between the atmosphere and the ocean.

Within the SST experiments, the SST is again kept constant. This is, to avoid secondary adjustment processes within the simulation period. The SST variation is applied to the whole ocean area in the research area to keep the interpretation simple. Coastal upwelling events usually occur in the near-coastal areas. Still, it is valuable to apply a temperature change to the full domain. First, any applied gradient of SST will induce a pressure gradient force. This would lead to a change in the near-coastal shallow monsoon flow which would impact the SBC. Also, it remains unclear how far the oceanward extension of the impact region for the LSB reaches.

Gradients within this region might also lead to unknown side effects. To avoid changes in SST gradients, a uniform warming or cooling of the weighted ground temperature field is the solution. Details about how SST changes or SST gradients affect the marine boundary layer are explained in Chapter 2.3.4.

4.4.2 Spinup timescale

The SST experiments with ICON use the same initial and boundary conditions as the reference run with ICON, but the weighted ground temperature at all ocean grid points is consistently changed. The analysis of the SBC in the data analysis Section 5.3 differentiates between the spinup period and the quasi-equilibrium period.

Analysing the air temperature and the specific humidity over the land and the ocean, the spinup period can be restricted from 13 December 2021 1 UTC to 14 December 2021 10 UTC for SST experiments with lower weighted ground temperatures. SST experiments with higher weighted ground temperatures reach the quasi-equilibrium state already within 24 h. Details can be found in Section 5.3.1.

4.5 Sea breeze front detection

An automatic SBF detection algorithm was adapted and implemented to analyse changes in the position of the sea breeze front (SBF) and its speed of propagation. This detection method is based on universal criteria independent of the embedding wind field and the topography.

4.5.1 Criteria for the sea breeze front detection

Following the definition of Ji et al. (2013), the SBF is the boundary area between the SB and the ambient flow ahead of it. It is characterised by sharp changes in temperature, moisture and wind. The identification of the SBF in observational station data or model data requires identification criteria. The following universal criteria are used in different studies:

1. location where horizontal velocity u is zero (Ogawa et al., 2003)
2. location with the maximum horizontal temperature gradient (Miller et al., 2003)
3. location with the maximum vertical velocity (Ogawa et al., 2003)
4. location of maximum moisture gradient (Simpson et al., 1977)

Local peculiarities for example in terrain, shoreline curvature or ambient flow make these general criteria useless, since the land–sea breeze (LSB) responds to these local impact for example in changing wind speed or direction. Therefore, model studies adapt these general criteria to individually defined filters: In the framework of the almost year-round southwesterly monsoon winds in the Gulf of Guinea, Guedje et al. (2019) suggests, for example, three definitions:

1. Definition on the diurnal variation of u: A SB event shows a steady increase in the 10 m wind from 06 UTC to 12 UTC. From the afternoon until 21 UTC a gradual decrease is observed. Guedje et al. (2019) sets the arbitrary threshold of the change in the windspeed to $2\,\mathrm{m\,s^{-1}}$.

2. Definition on the change in wind direction: The wind direction changes from offshore to onshore flow after sunrise from 09 UTC to 15 UTC. In the study of Guedje et al. (2019) at Cotonnou (Benin), the 10 m wind direction is supposed to change from 100° to 260° using this definition.

3. Definition on the diurnal temperature differences: Comparing the daily mean of the 2 m air temperature over land from 06 - 18 UTC and the daily mean SST, an SB occurs if the first exceeds the later.

A first attempt of defining individual filters for the simulations in this thesis analogue to these studies failed. The main issue of the local application of filters in perpendicular cross-sections is the local ambiguity: Strong convection in the mid-day, eventually accompanied by precipitation, also causes sharp gradients in wind speed, humidity, and air temperature. Another problem is the spatial variation of the location of maximum change in the variables at the SBF. Especially in the evening, the location of the spatial change in wind occurs ahead of the location of the maximum gradient in humidity. Another particular difficulty includes the differentiation between other meteorological features with the same signature: the criteria which classify an SBF are not unique. Thus, these filters would have to be adapted depending on the location along the Guinea Coast, depending on the daytime and depending on the embedding flow. This approach was therefore rejected not only due to the high time and effort of adapting filters according to these criteria but also to avoid inconsistencies resulting from different definitions.

A robust SBF detection should therefore be based on the large-scale properties of the SB. The local-scale pressure gradient force due to the differential heating between the land and the ocean induces an SB all along the coastline between Cape Palmas and West Nigeria. Analysing 10 m wind maps in the Gulf of Guinea from 8 UTC to 23 UTC for each day of the simulation (exemplarily shown in Figure 4.5), a strong gradient in the wind is clearly visible parallel to the coast and can be seen to propagate inland. Note that other regions of a strong gradient are also seen due to orography and cold pools, therefore the criterion of a strong gradient in wind is not sufficient to locate the sea breeze front.

The boundary layer depth (BLD) is another important criterium for the SBF detection. Over the sea, the marine boundary layer has a depth of approximately 500 m in the reference run. The marine BLD shows little diurnal variations. Over land, the BLD has a strong diurnal cycle. A well-mixed layer develops and deepens due to solar heating after sunrise until sunset. In the late afternoon, the BLD extends vertically up to 2000 m over land. When the SBC sets in, the SB transports a layer of cool and moist marine air over the land in the region of the deep well-mixed layer. In areas where the SBF has passed, the BLD is therefore similar to the ocean, as the SB undercuts the warmer and less dense air over land. Therefore, a strong BLD gradient develops at the SBF.

A successful method for SBF detection is based on the intersection of regions with strong 2d-gradient in the BLD and wind speed. It was demonstrated by DeYoung and Evans (2024) at the American Meteorology Society (AMS) conference in January 2024 for an analysis at Lake Michigan. In this thesis project, this method was implemented and adapted for the Gulf of Guinea.

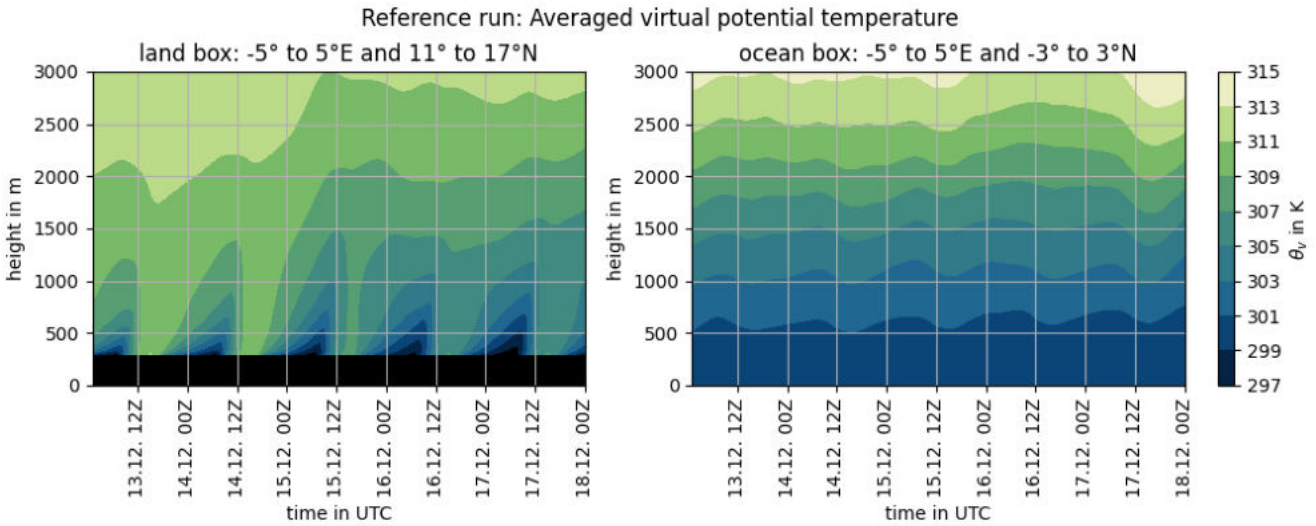

Figure 4.3: *Time series of the vertical virtual potential temperature profile over land and ocean. Horizontal average in defined boxes in the reference run.*

4.5.2 Calculation of the boundary layer depth

The BLD is not an output variable of the ICON model and therefore has to be calculated from model data. The BLD is defined here as the height which separates a well-mixed atmospheric layer close to the surface from a stably stratified layer on top. The virtual potential temperature characterizes the stability of an atmospheric layer. It is constant in the well-mixed layer above the surface and increases in a stably stratified layer on top of the boundary layer.

The virtual potential temperature is calculated with:

$$\theta_\mathrm{v} = \theta \cdot \frac{\omega + \epsilon}{\epsilon(1+\omega)}.$$

Here, the potential air temperature θ is calculated from the air temperature T, the air pressure P (P_0 at the surface) and $\kappa \approx 0.286$

$$\theta = T \cdot \left(\frac{P}{P_0}\right)^{\kappa}.$$

The mixing ratio ω is calculated from the specific humidity q of the variable using

$$\omega = \frac{q}{1-q}.$$

The molecular weight of the constituent gas is defined as the ratio of the water vapour to that assumed for dry air ($\epsilon \approx 0.622$).

The BLD analysis is done for each vertical column at all longitudes and latitudes individually. The vertical grid of the ICON output data on mode levels is unequally spaced (orange marker in Figure 4.4). Therefore, the data is first interpolated on a vertical grid with $\Delta z = 50\,\mathrm{m}$ (blue marker). On this grid, the vertical change in Θ_v between neighbouring steps is calculated. The BLD is

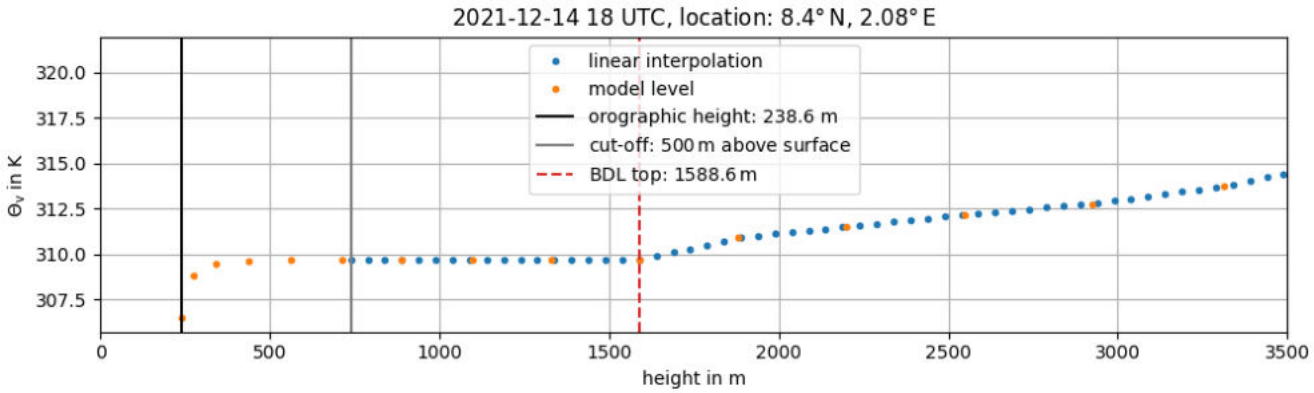

Figure 4.4: *BLD calculation (red dashed line) on 14 December 2021 at 18 UTC in central Benin in the ICON reference run: Linear interpolation of the virtual potential temperature of model level data (orange marker) on a* $\Delta z = 50\,\mathrm{m}$ *vertical grid (blue marker). The analysis starts* 500 m *above surface (surface height: black line, starting height: grey line).*

defined here as the lowest height where the vertical change of the virtual potential temperature exceeds a threshold of

$$\frac{\Delta T_\mathrm{v}}{\Delta z} \geqq \frac{0.1\,\mathrm{K}}{50\,\mathrm{m}},$$

marked as red dashed line in the figure. The orographic height of the location is indicated as a black line.

The linear interpolation and threshold analysis start at a vertical offset of $z = 500\,\mathrm{m}$ above the surface (grey line in Figure 4.4). This limits the impact of long-wave cooling in the evening and other disturbances on the lower parts of the BLD. Due to the long-wave cooling with decreasing solar radiation at 17 UTC, a strong positive virtual potential temperature difference emerges at the surface. Cut-off heights are tested at 300 m, 400 m, 500 m, 600 m and 800 m. A cut-off at values smaller than 500 m cannot shield the analysis from surface effects. The cut-off of 500 m gives the best results and allows an application of this method until 24 UTC.

4.5.3 Identification of the sea breeze front location

The two plots on the lefthand side of Figure 4.5 show the mean wind speed in the lowest four model levels starting a layer above the surface and the BLD in the reference run of the ICON simulation. The wind speed in the lowest level can be very noisy and is therefore excluded in this method. The mean height of the four lowest model levels lies between 30 m and 330 m above the lowest model level. Since the SB has a height of 450 m to 1400 m in the ICON reference run, this height average of the wind speed covers the wind characteristics in the lower part of the SB.

At the location of the SBF (approximately 1° north of the shoreline), the wind speed and the BLD change sharply. The horizontal gradients of both scalar fields are calculated with the function NumPy.gradient. The interest of this analysis lies in the absolute change of these variables at each point. Therefore, the absolute value of both gradients is calculated. The two plots on the right side of Figure 4.5 show the absolute value of these gradients. The SBF is visible in both of

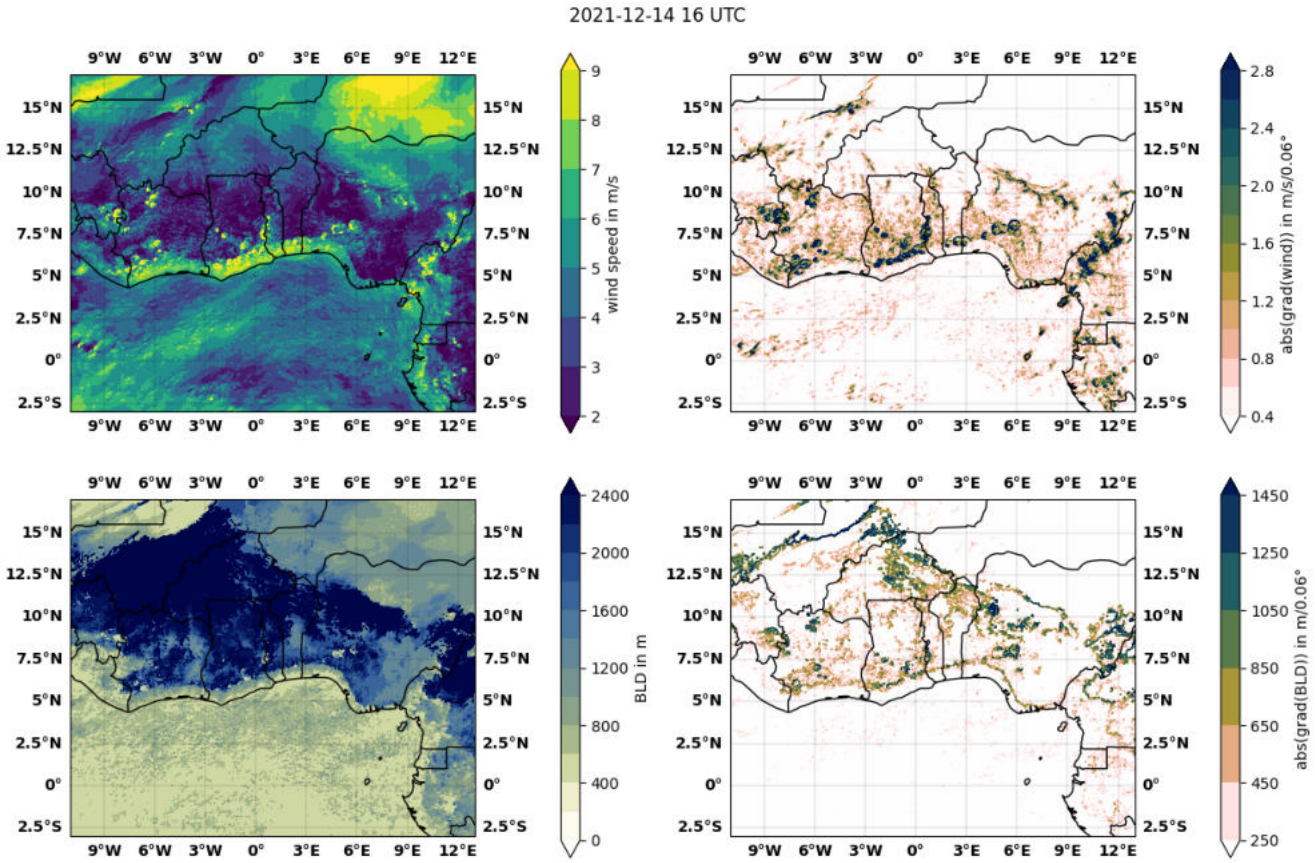

Figure 4.5: *Wind speed, BLD and 2d gradients of both variables at 16 UTC on day 14 December 2021.*

the right plots as a small band approximately 1° north of the shoreline. A threshold of

$$\frac{\Delta \text{abs(grad(BLD))}}{0.06^\circ} \geqq 250\,\text{m} \qquad \frac{\Delta \text{abs(grad(windspeed))}}{0.06^\circ} \geqq 0.4\,\text{m/s} \tag{8}$$

is applied to the gradients. The adapted colour bars in the plots leave areas with smaller spatial changes white. Still, many points over the land and fewer over the ocean fulfil these criteria.

In the next step, the closest landward location to the shoreline where both criteria of equation 8 are fulfilled is extracted for each longitude. The possible location of the SBF is restricted from the shoreline (blue line in Figure 4.7) to 4.5° north of it (orange line). The resulting location is very noisy and in some places a few degrees of latitude away from the true location. Considering the collective behaviour of the SB along the coastline, a large-scale local pressure gradient force forces the SB all along the coastline deeper into the land. To relate the resulting SBF location to this large-scale behaviour, the median of 10 points east and west (this corresponds to ±0.3° longitude is calculated at each longitude. Boundary values to the east and west have symmetrically fewer points included in the median. The resulting red line is the calculated location of the SBF.

The dataset with the SBF location is saved as a latitude-longitude map containing an SBF-index of 100 at positions of the median and zeros elsewhere.

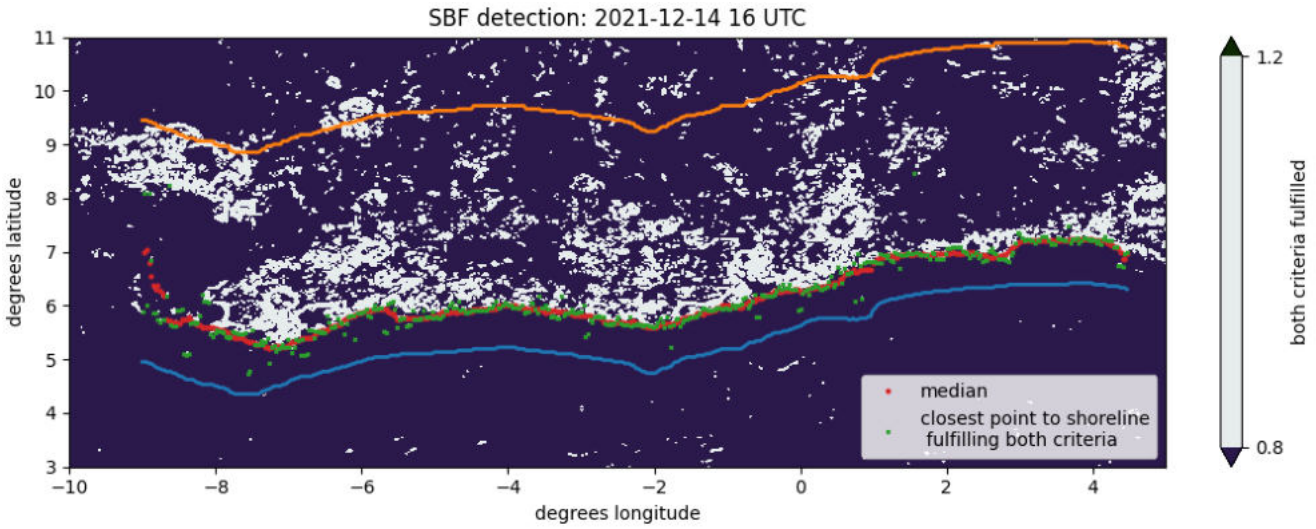

Figure 4.6: *SBF detection on 14 December 2021: Map of all the points, where the criteria of equation 8 are fulfilled are marked grey. The location of the SBF is restricted between the shoreline (blue line) and a line* 4.5° *north of it (orange). The green marker shows the landward location closest to the shoreline, where both criteria are fulfilled. The red marker shows the median of the location including green points* 0.3° *to the east and the west.*

This dataset is transferred into the rotated cross-section analysis (see Chapter 4.6). Along a chosen or several averaged cross-sections, the position of the SBF is defined by the distance to the shoreline, where the SBF-index is maximal. The spread occurs due to the linear interpolation along the cross-section and the averaging of several cross-sections.

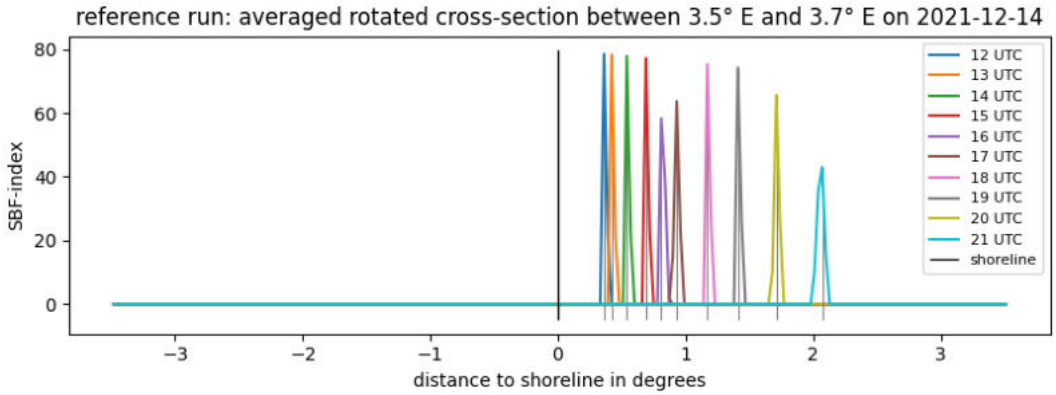

Figure 4.7: *SBF detection in the rotated cross-section: The maximum of the SBF-index indicates the location of the SBF. The plot shows the shift of the averaged SBF location between* 3.5°*E and* 3.7°*E in the reference run on 14 December 2021. The SB moves further away from the shoreline (black vertical line) with increasing time.*

This method can be used from 12 UTC to 20 UTC. In earlier times, only a few points along the coastline fulfil both criteria. The SBC initialisation time depends on many factors. Within the simulation period, it lies between 9 UTC and 12 UTC. Thus, in times before the SBC is initialized locations deeper in the land which are not related to the SBC are selected by the method. A

closed line along the coastline which is identified as the SBF can be seen from 12 UTC on. In the later evening, the signal tends to get weaker. Therefore, a location deeper inland is sometimes chosen. To restrict this error, the analysis should be limited from 12 UTC to 20 UTC since a coherent SBF signal can be observed in this period. Still, under some conditions, SBF detection works greatly from 10 UTC until 23 UTC. A careful analysis of a vertical cross-section arranged perpendicular to the shoreline reveals if the SBF detection was successful. Details about the data processing on the transects perpendicular to the coast can be found in the following Chapter 4.6.

4.6 Transects perpendicular to the coast

The SBC forms perpendicular to the shoreline as the pressure gradient force is initialized due to the air temperature difference over the ocean and the land. The analysis of the SBC in cross-sections should be therefore also arranged perpendicular to the shoreline. Within a chosen section along the coastline, these transects are averaged for the analysis of the LSB.

The first step in this method is the fitting of the shoreline. For a chosen longitude a linear fitting is done for the interval including 0.24° longitude which equals 8 points eastwards and westwards of the location. The number of points determines the sensitivity of the rotation to the curvature of the coastline.

The data along the perpendicular transect is interpolated linearly. The half length of the cross-section is set to 3.5 km, since the SB never exceeds this distance in the reference run. The number of steps along the cross-section is chosen to be 234, which gives a step spacing approximately equal to the grid spacing. An example for a rotated cross-section is depicted in Figure 4.8.

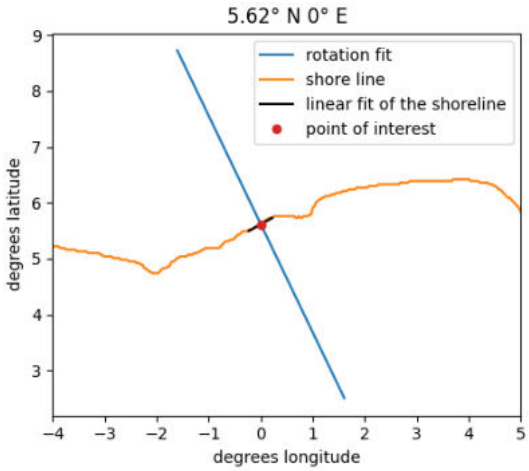

Figure 4.8: *Method: Linear interpolation of the data on a cross-section arranged perpendicular to the shoreline.*

The calculation of the location of the boundaries of the cross-section is automatized for any location, step number along the cross-section, half-length of the cross-section and number of neighbouring longitudes for the linear fit. It calculates the location of the boundaries by using the Theorem of Pythagoras and the Intercept theorem.

For the wind analysis, a normal wind and along-transect wind component are calculated. When averaging over several cross-sections, the orientation of the coastline should be taken into account to prevent an analysis based on intersecting or diverging cross-sections.

5 Results

5.1 Climatological context: sea surface temperature variability in the Gulf of Guinea

The coastal and equatorial sea surface temperatures (SST) in the Gulf of Guinea follow a bimodal cycle: during the minor and major upwelling season, the SSTs decrease in the near-coastal areas due to coastal upwelling. The upwelling seasons, the intra-annual SST variability and short-time SST variability are analysed in the following sections for the Gulf of Guinea.

5.1.1 Climatology in the Gulf of Guinea: the Annual Cycle of SST

Figure 5.1 shows the climatological mean SST along three sections of the northern coast in the Gulf of Guinea: the Ivorian Gulf (A: blue box), the Gold Coast (B: orange box) and the Bight of Benin (C: green box), all shown on the map in Figure 5.1. All three coast sections have a climatological mean SST of 301.5 K to 302.5 K outside of the upwelling seasons. The SST decrease related to the major upwelling season begins in June and persists until October. Thus, this climatological analysis shows similar results compared to the studies of Hardman-Mountford and McGlade (2003). The SST decreases stronger in the Ivorian Gulf and along the Gold Coast, where the two major upwelling cells are located (Brandt et al., 2023), than in the Bight of Benin. The minor upwelling season can be found between December and March at the Gold Coast and in the Bight of Benin. In the Ivorian Gulf, the SSTs fall one month later in the climatological mean. Also, the SSTs reach their minimum one month later. The research period for the land–sea breeze investigation is thus chosen at the beginning of the minor upwelling season.

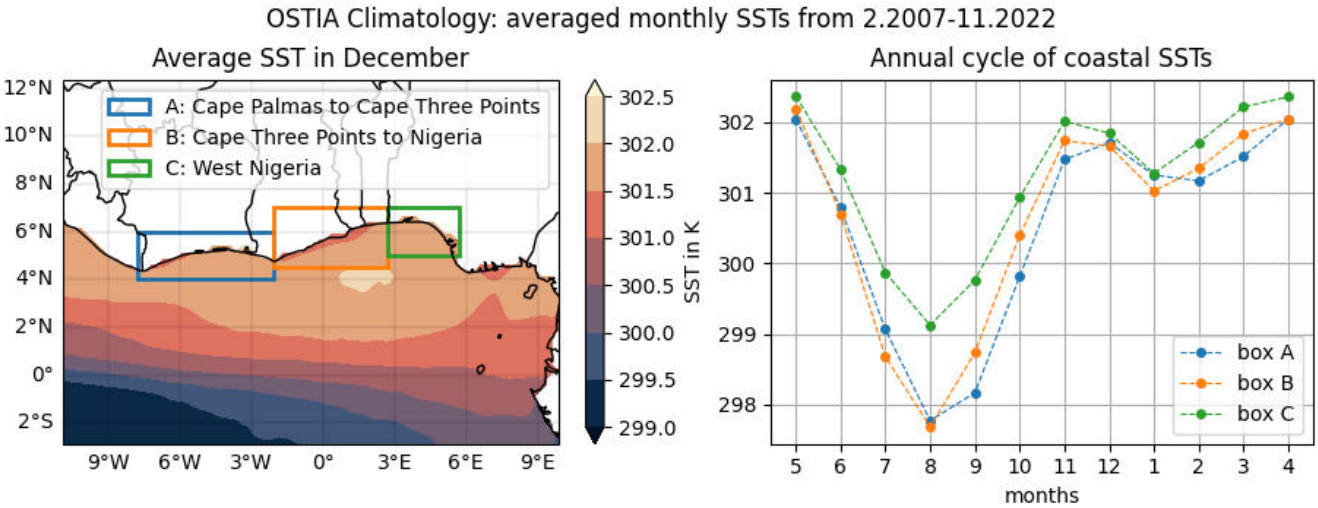

Figure 5.1: *SST climatology: monthly averaged SST from February 2007 to November 2022 (OSTIA analysis data). Graphic on the left-hand side: Climatological SST distribution in December. Three littoral areas are defined. The graphic on the right-hand side shows the annual cycle of the mean SST within these areas.*

5.1.2 Intra-annual SST variability in the Gulf of Guinea in December

The intra-annual SST variability is also not negligible in the Gulf of Guinea. Figure 5.2 shows the anomaly of the monthly averaged SST in December from the climatological mean calculated from December 2007 to 2020 with the OSTIA data. December 2021 belongs to the warmer De-

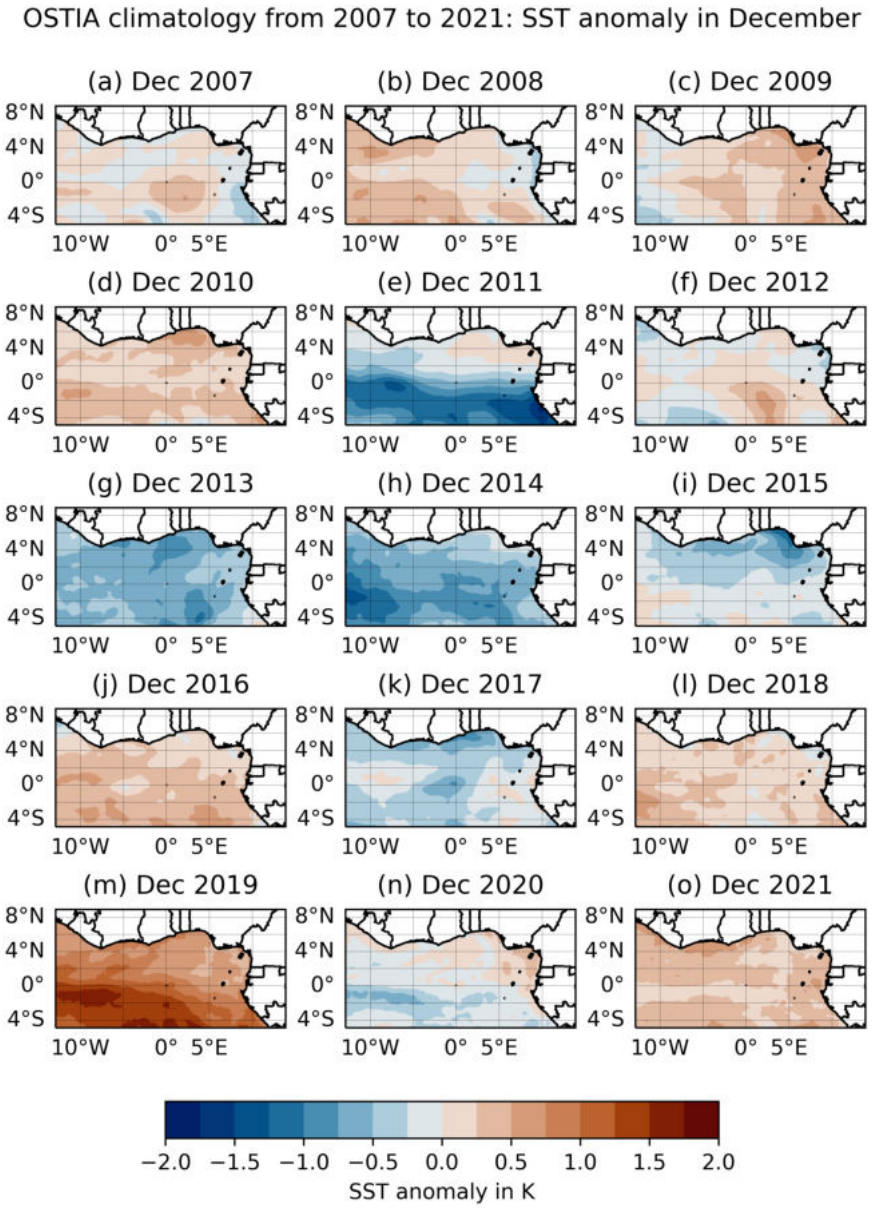

Figure 5.2: *OSTIA climatology: SST anomaly for every December from 2007 to 2021 (mean monthly SST in December minus climatological mean for December).*

cembers between 2007 and 2021 with slightly increased SSTs between 0 K to 0.75 K above the climatological mean (Figure 5.2o). December 2010, 2016, and 2018 show a very similar averaged SST distribution. However, the SSTs in December 2019 are increased by about 1 K whereas the December 2013 and 2014 show SSTs reaching values up to −2 K lower compared to December 2021. These SST variations can mainly be connected to long-term SST variability in the tropical

Atlantic. Figure 8.14 in the appendix shows the anomaly of the annual mean SSTs in the Gulf of Guinea. The previously named warmer or colder Decembers relate to equally higher or lower annual SST anomalies.

5.1.3 SST variability along the coastline (OSTIA data) in December 2015

In an analysis of the coastal sea surface temperatures (SSTs) in the Gulf of Guinea with the OSTIA dataset, peculiar SST variations on a short time-scale occur: the SST drops up to 1 K within one or two days and increases after a period of a few days again. The SSTs in the near-costal ocean are investigated in the area of the LSB, which is found to extend up to 3° offshore. Therefore, the coastal SST variability is analysed within this distance to the shoreline. Figure 5.3 shows a map with boxes of three sizes, in which the mean SST is calculated. The mean SST in the boxes is compared to the monthly mean SST of all the boxes of equal size. The different sizes of the boxes are defined to analyse if the cooling is stronger at the coastline than in the outer ocean.

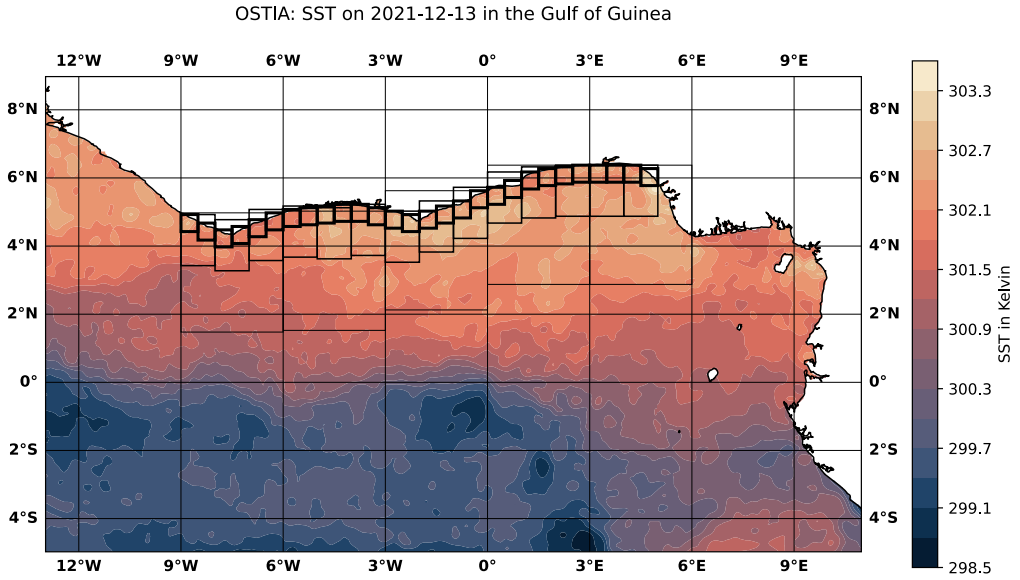

Figure 5.3: *The near-coastal daily SST changes are analysed on three lengths scales: small (0.5°×0.5°), middle (1.5°×1°), large (3.5°×3°). The contours show the SST on the first day of the simulation period (13 December 2021).*

A short-time cold anomaly occurring in December 2015 is analysed in the following. Figure 5.4a shows the SST anomalies in December 2015 in the smallest coastal boxes depicted in Figure 5.3. In December 2015 are two periods, where the near-coastal SSTs strongly decrease: from 3 to 6 December, the SST falls up to 2 K and increases slowly from 6 to 12 December back to SSTs before the cooling set in. Later in December 2015, the SSTs fall again in 4 days over 2.5 K with a minimum in the Bight of Benin and the east part of the Ivorian Gulf. Again, the SSTs increase in the following days. This behaviour is visible also in the boxes with middle and large sizes

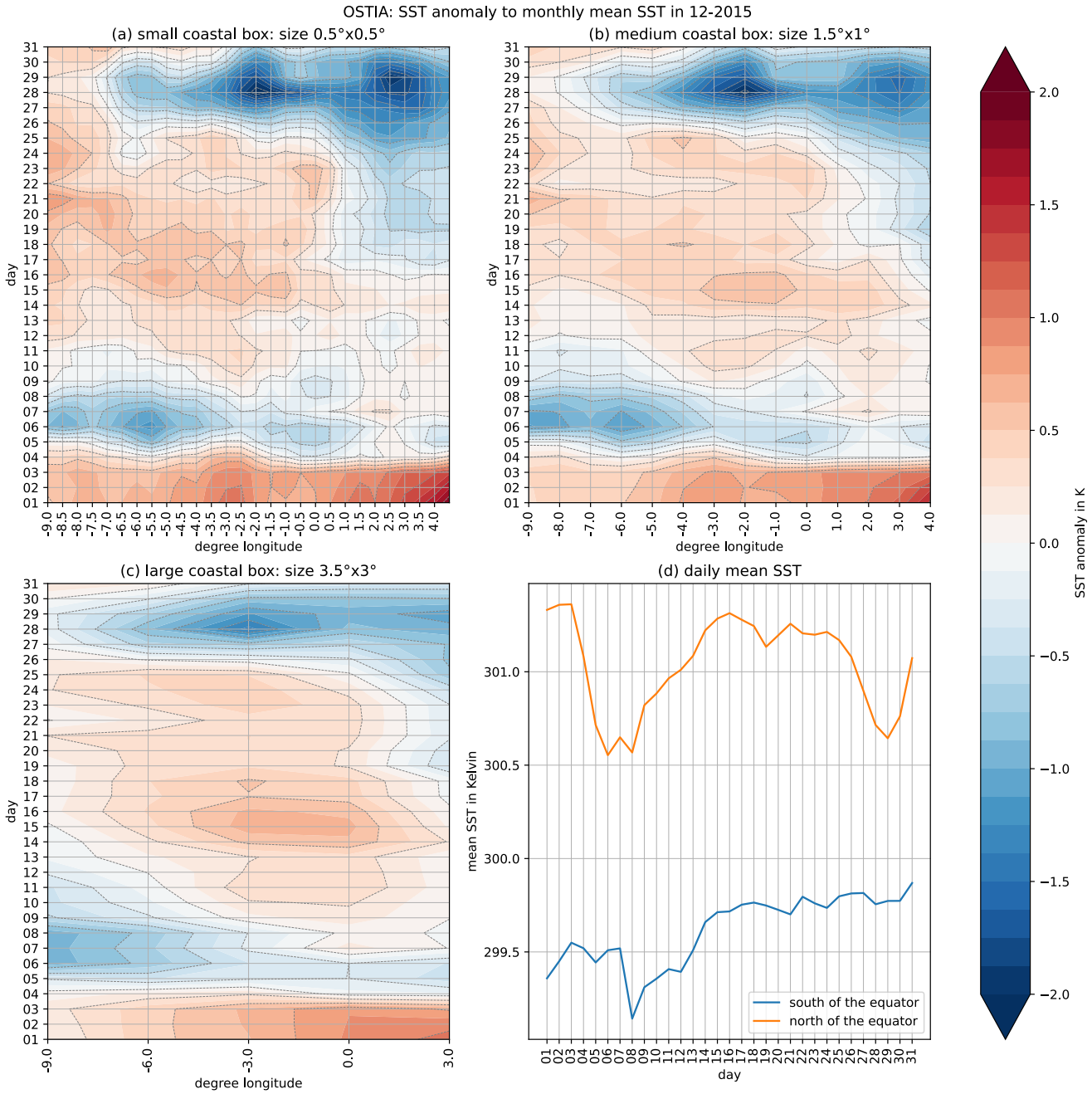

Figure 5.4: *Hovmöllerplots for the near-coastal daily SST changes are analysed on three lengths scales: small (0.5°×0.5°), middle (1.5°×1°), large (3.5°×3°). The boxes are presented in Figure 5.3. The contour lines in subplot a–c indicate SST anomalies in* 0.25 K *steps. Subplot d shows the larger-scale mean SST in the area of Figure 5.3: the blue curve depicts the mean SST of the whole research area while the orange curve takes only the ocean surface north of the equator within the research area.*

(Figures 5.4b and c). Notice the density of the grey SST isotherms on 3 December in the Gold Coast and the Bight of Benin in the Hovmöller diagram of the largest boxes (−2° to 3°E in Figure 5.4c). Figure 5.4d shows the time evolution of the averaged SST north (orange line) and south (blue line) of the equator in the research area. The SST variation during these short-time cold

periods affect the mean SST in the whole area north of the equator in the research area depicted in Figure 5.3. The mean SST south of the equator does not show a synchron SST decrease in these periods. Between 7 and 8 December, however, the SSTs south of the equator decrease also with a delay of 4 days compared to the coastal SST drop.

Figure 5.5 shows the maps of day-to-day SST difference in the first short-time cooling period in December 2015. The SSTs drop suddenly more than 1 K between 3 and 4 December 2015 at the Gold Coast and in the Bight of Benin (blue shading). On the following day, the SSTs do not exceed a day-to-day variability of ±0.3 K in these regions. Further west, in the Ivorian Gulf and coast sections between Guinea and Liberia, the near-coastal SSTs decrease by −0.3 K to −0.9 K within one day. Between 5 and 6 December the SSTs decrease again about −0.3 K to −1.3 K in the ocean between the coastline and 2° latitude offshore in those parts of the coast. In the following three days (6 to 8 December in Figure 5.5e and f), the SSTs increase again. The SST decrease in the southern part of the Gulf of Guinea depicted in Figure 5.4d is also clearly visible in Figure 5.5f.

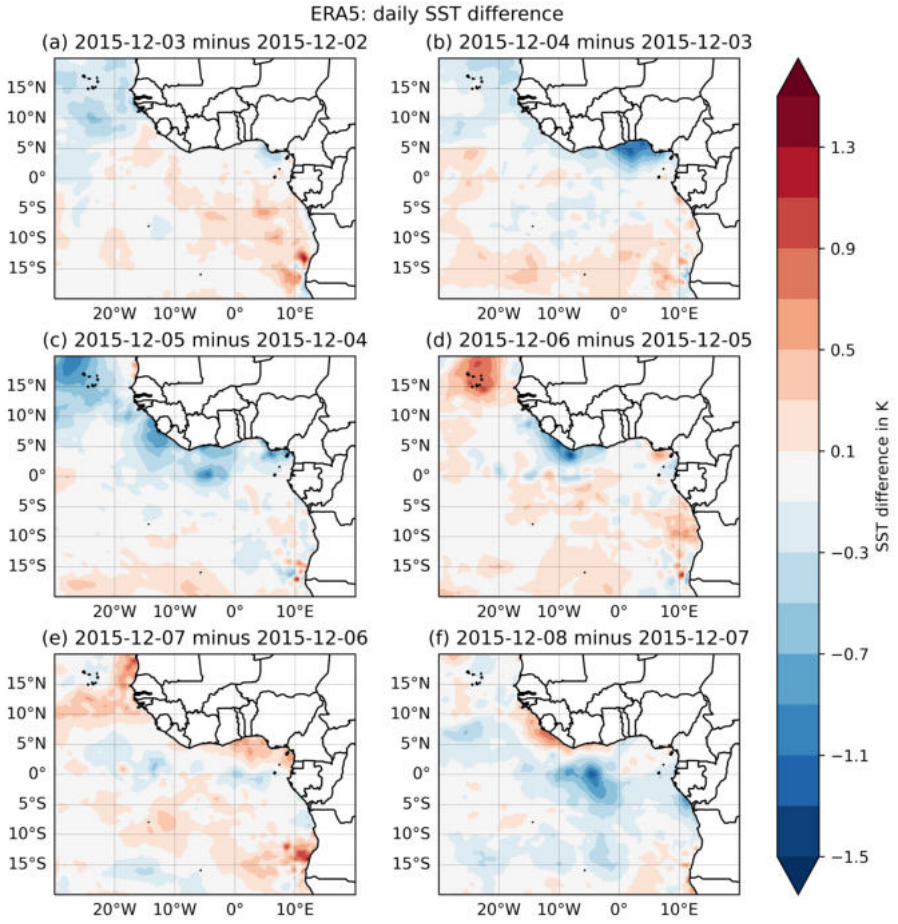

Figure 5.5: *ERA5 data: SST difference from day to day during the SST drop from 02.12.2015 to 08.12.2015.*

Table 4 summarises a similar analysis of the coastal SST variability in December from 2007 to 2023. In December 2021, the SSTs in the Gulf of Guinea show only little variation. Therefore,

December	period of strong coastal SST-decrease
2015	3 to 6 December and 24 to 28 December all along the coast
2016	21 to 24 December and 26 and 31 December all along the coast
2017	9 to 12 December all along the coast
	15 to 17 December at the Gold Coast
	22 to 24 December in the Ivorian Gulf
	25 to 29 December in the Bight of Benin
2018	2 to 4, 5 to 8, 10 to 12, 20 to 23 December in the Gold Coast and the Bight of Benin
	25 to 28 in the Ivorian Gulf
2019	no strong SST decreases
2020	no strong SST decreases
2021	3 to 5 December in the Bight of Benin
	19 to 21 in the Ivorian Gulf
2022	no strong SST decreases
2023	11 to 14 December, 16 to 17 December all along the coast

Table 4: *Periods in December 2015 to 2023 where the SST drop over* 0.5 K *in* 1° *latitude distance to the shoreline. Analyse with Hovmöller diagrams presented in Figure 5.4 from OSTIA data.*

this period is valuable for the simulation setup with constant SSTs.

5.1.4 Relation of the coastal SST variations to Saharan dust

These sudden coastal temperature drops shown in the previous Section 5.1.3 in the coastal regions in the Gulf of Guinea are not explained or mentioned in the literature to the best of the author's knowledge. However, various studies discuss the impact of Saharan dust storms on the SST variability in the northern parts of the tropical Atlantic (see Section 2.3.3). The following analysis describes the short-time cold event from 3 to 6 December 2015 analysed in Figure 5.5 and relates its appearance to a simultaneous Saharan dust outbreak over the Gulf of Guinea.

Figure 5.6 shows satellite images from 1 to 9 December 2015 over the Gulf of Guinea and the Guinea Coast. The satellites recording the data cross the Gulf of Guinea twice a day. The satellite images clearly show a dust cloud approaching the Gulf of Guinea on 1 and 2 December from the northeast (Figures 5.6a and b: beige shading in the upper-right corner of the images where Nigeria is located). The dust cloud crossed the shoreline on 3 December in the Bight of Benin (Figure 5.6c: the beige shading has expended and extends over the ocean. The markers of the coastline are displayed over the dust outbreak). From 3 to 4 December, the dust storm moves to the west, covering large areas over the ocean south of the Bight of Benin, the Gold Coast and extending over land over the Ivory Coast (compare Figure 5.6c and d). Between 3 and 4 December, the SSTs start falling in the Bight of Benin. The area coverage of the dust storm highly coincides with the location of the SST decrease (compare Figure 5.6c to Figure 5.5b). On 5 December, the dust storm moves further to the West and extends over the ocean between Senegal and Liberia while the Ivorian Gulf, the Gold Coast, the Bight of Benin, and the Bight of Bonny are still covered by the dust storm from the satellite perspective (Figure 5.6e). The satellite image on 6 December shows an alike behaviour. The day-to-day SST difference again resembles the area covered by

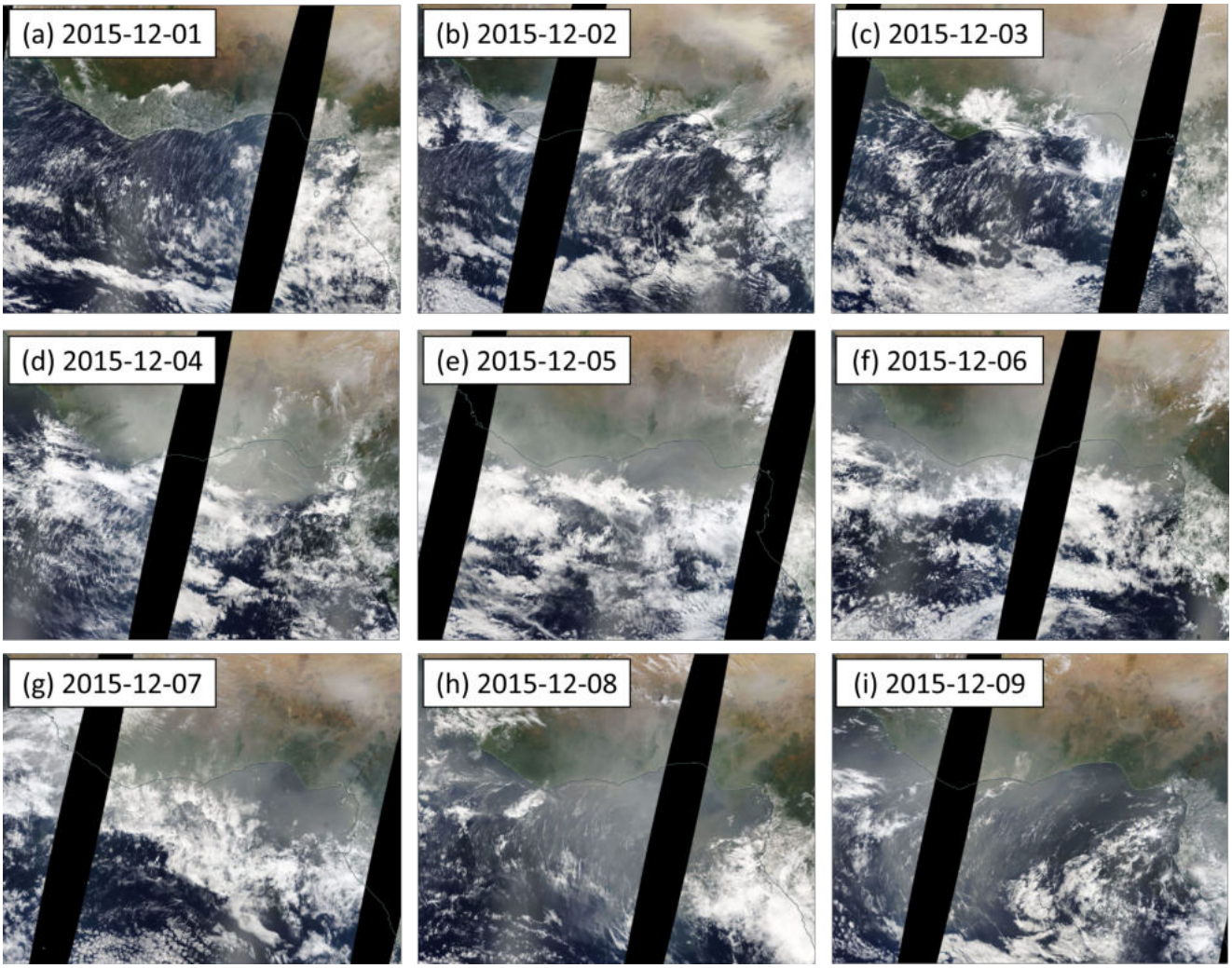

Figure 5.6: *Satellite images from 1 to 9 December 2015 over the Guinea Coast and the Gulf of Guinea provided by NASA Worldview https://worldview.earthdata.nasa.gov/.*

the dust region: between 4 and 5 December the SST decreases from the northern Bight of Bonny to the Atlantic Ocean west of Senegal (Figure 5.5c). On 6 December, the SSTs decrease in the Ivorian Gulf and in the near-coastal ocean west of Guinea, Sierra Leone and Liberia, whereas the SSTs in the Gold Coast and the Bight of Benin stay almost constant (Figure 5.5d). On 7 December, the satellite image shows higher visibility of the ocean surface in the Bight of Benin while the other near-coastal ocean parts are still covered by the dust storm (blue shading of the ocean surface emerges in the Bight of Benin in Figure 5.6g). On 8 December, the Saharan dust is transported further south over the tropical Atlantic, coinciding with the SST decrease over the outer ocean in the Gulf of Guinea in Figure 5.5f). Along the coastal areas, the dust intensity decreases. This coincides with positive SST changes along these coastal areas (red shading in Figure 5.5e and f coincides with the areas in 5.6g and h where the beige shading turns bluish). This qualitative analysis shows, that the day-to-day SST decrease coincides with the location of a Saharan dust outbreak, whereas an SST increase can be noticed in areas, where the dust storm retreats.

The cooling impact of Saharan dust outbreaks is known to be strongest in periods with small near-surface wind velocities over the ocean (Luo et al., 2021). Figure 8.15 in the appendix shows the 10 m wind and the total precipitation in the Gulf of Guinea in the period with the high SST variability. The accumulated precipitation rate is low in the areas of the SST cooling event, therefore it is unlikely that the satellite measurement of the SSTs are disturbed by precipitation (Donlon et al., 2012). Additionally, the 10 m winds are very weak in the areas where the SSTs during the period. A cooling effect in the SST from Saharan dust is more likely under weak wind conditions (Luo et al., 2021). Still, an overestimation of the SST variations can not be excluded since the day-to-day differences analysed in the Gulf of Guinea are higher than the dust-related variations found in the northern tropical Atlantic (Avellaneda et al., 2010).

5.1.5 Chapter summary

The Gulf of Guinea exhibits a high SST variability on different time scales. The climatological study of the OSTIA satellite data confirms an annual cycle with two upwelling seasons in near-coastal areas. Between December and January, the coastal SSTs decrease about 1 K in the climatological mean due to the beginning of the minor upwelling season. Short-time SST variations of up to 2 K are also found in the OSTIA data during December in the Gulf of Guinea. In an analysis of December 2015, these variations coincided with Saharan dust outbreaks over the Gulf of Guinea. The increased dust particle concentration can cause a cooling of the SST (Luo et al., 2021) as well as an overestimation of the sea surface cooling in the satellite data (Donlon et al., 2012). Therefore, the amplitudes of the short-time cooling events should be assumed to be attenuated. The intra-annual SST variability shows differences exceeding 3 K in the mean SST in December from 2007 to 2021 in the Gulf of Guinea. In summary, this analysis has shown near-coastal changes in the SST in December due to the onset of the minor upwelling season and short-time cooling events.

5.2 Realistic simulations of the SBC in the Gulf of Guinea

In the research period from 13 to 17 December 2021, the land–sea breeze (LSB) is investigated along the Guinea Coast with numerical simulations performed with ICON. This chapter investigates first the large-scale circulation characteristics of the West African monsoon system in the simulation, in which the LSB is embedded. A subsequent comparison of the simulation to reanalysis data and satellite-derived rainfall observations analyses the similarities between the ICON simulation and other available datasets for this region. The LSB is then first analysed in case studies in West Nigeria, to understand the formation and development of the wind system in different embedding wind fields. The results are compared to the characteristics of the LSB developing along the Guinean Coast from Ivory Coast to West Nigeria. This chapter lays the foundation for the following Section 5.3, which compares the here analysed ICON reference run to SST sensitivity experiments.

5.2.1 Large-scale circulation during the research period

Figure 5.7 shows the averaged 10 m wind during the first day of the simulation. The shallow monsoon flow advances the littoral regions from the Ivory Coast to Nigeria from a south-westerly direction. The southerly monsoon winds are steady in speed and direction over large parts of the ocean especially south of the equator during the research period (not shown). As the monsoon flow reaches land its velocity is decreased due to drag. Figure 5.7 shows the strong north-easterly Harmattan winds across the Sahel and Sudan. These winds are confined to the north of the ITD (purple line).

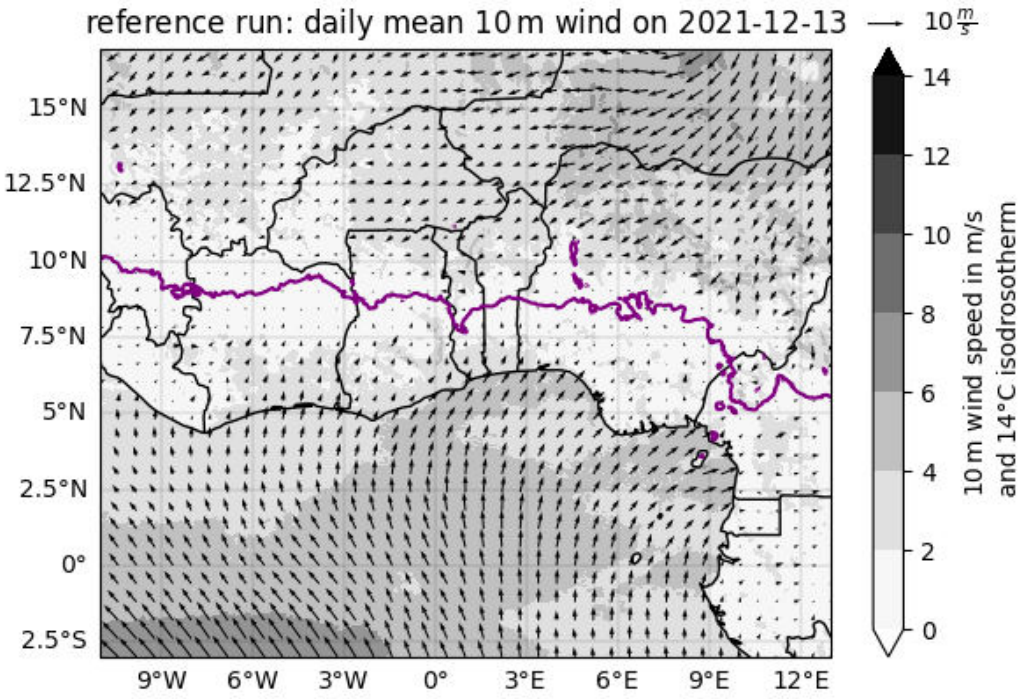

Figure 5.7: *Mean* 10 m *wind on 13 December 2021 in the reference run. The purple line represents the mean position of the* 14 °C *isodrosotherm on this day indicating the location of the ITD.*

date	coastal wind conditions
13.12.2021	monsoon winds
14.12.2021	monsoon winds
15.12.2021	monsoon winds at the Ivory Coast
	12 UTC: 10 m winds turn south in Ghana, Benin, Togo and West-Nigeria
16.12.2021	18 UTC: 10 m winds turn south at the Ivory Coast
17.12.2021	monsoon flow at the Ivory Coast
	16 UTC: Monsoon flow in Ghana, Benin, Togo and West-Nigeria

Table 5: *Coastal winds in the reference run.*

The atmospheric conditions at the start of the run are typical for December. However, December may also experience Harmattan surges when the Harmattan winds extend further south toward the coast. Such a transition happens between the simulation's third and fourth day in the eastern part of the Gulf of Guinea. Figure 5.8 shows the 10 m wind and specific humidity on the 15 and 16 December 2021 (the third and fourth day of the simulation period). The ITD shifts southwards towards the coast and the 10 m winds east of Ghana turn to northerlies over the ocean.

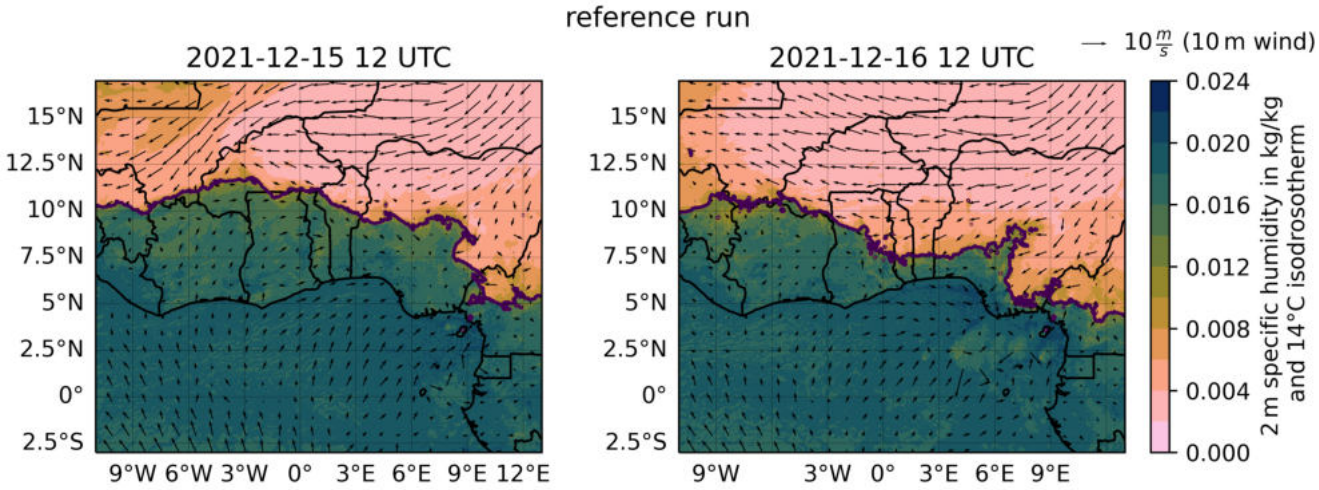

Figure 5.8: 10 m *wind and* 2 m *specific humidity on third and fourth days of the reference run at 12 UTC. The* 14 °C *isodrosotherm at* 2 m *height (purple line) indicates the zone of maximum convergence between the dry north-easterlies and the moist monsoon winds. On the 16.12.2021 east of Ghana the near-surface winds in the littoral area and over the ocean turn southwards.*

The sea breeze circulation (SBC) develops during the five days of the simulation period in different embedding wind fields, summarised in Table 5.

Figure 5.9 shows a meridional transect of wind averaged over −7.5° to 5°E between 13–17 December for the reference run. In the zonal winds, two maxima catch attention: The signature of the STJ is strong westerly winds. It persists over the land (latitudes north of the blue line in Figure 5.9) with a maximum in the height of 300 to 100 hPa. The AEJ shows a negative maximum between 800 and 600 hPa height south of 7.5°N. The mean peak velocities are between −8 and $-10\,\mathrm{m\,s^{-1}}$ matching values in the literature.

The wind arrows show the shallow monsoon winds from the south meeting the Harmattan flow from the north between 8° and 10° north at the ITD. Here, both air masses converge and are forced upwards. The air masses of the shallow monsoon layer overturn and merge with the upgliding dry air from the Saharan zone to form a southerly reverse flow on top of the monsoon winds.

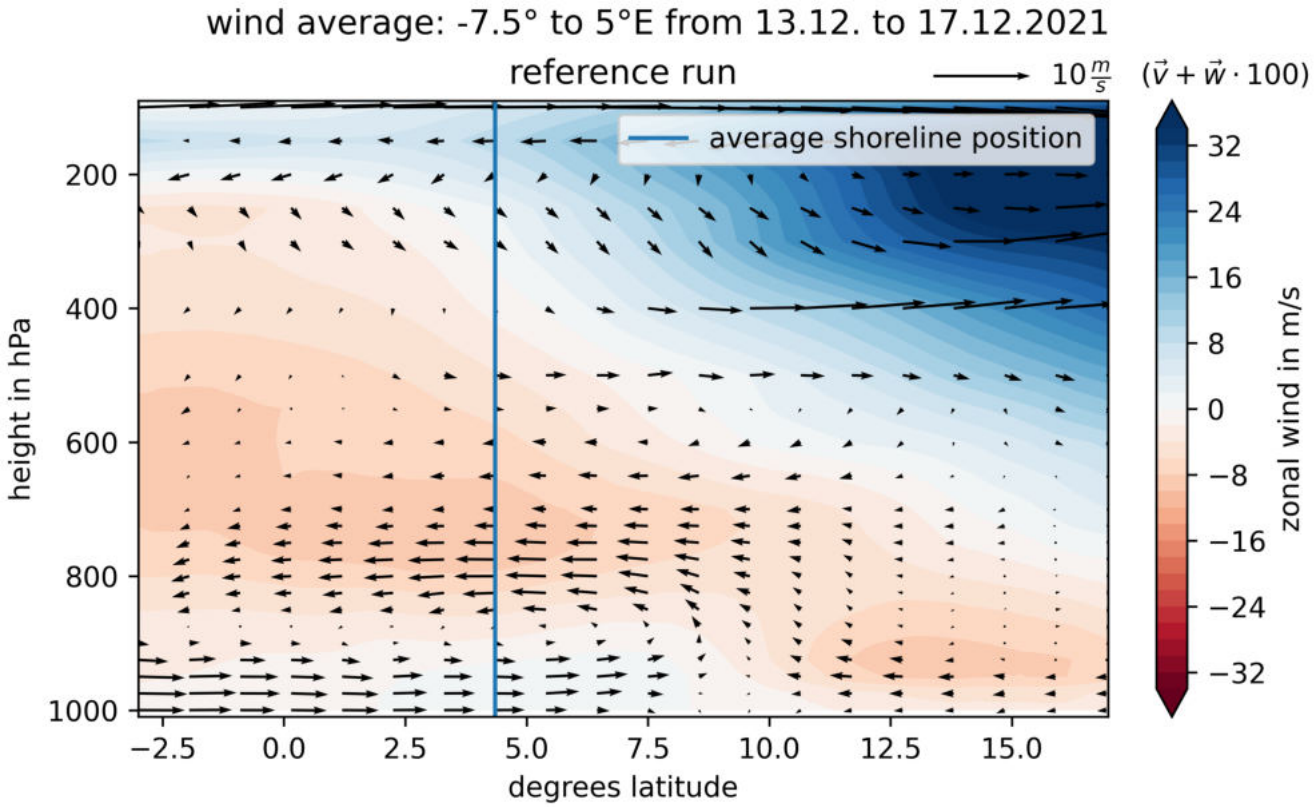

Figure 5.9: *Meridional vertical wind profile averaged from 13 to 17 December 2021 in the reference run. The zonal mean was performed between −7.5° and 5°E. The arrows indicate the meridional and vertical wind components, whereby the vertical velocity is multiplied by a factor of* 100. *The contours depict the mean zonal winds in this area. In this zonal average, the land lies on average north of the blue vertical line (averaged latitudinal shoreline position).*

5.2.2 Precipitation comparison between the ICON reference run and GPM IMERG v7

One criterion for the research period is the dryness in this period. The chosen period from 13 to 17 December 2021 shows only a few distributed precipitation cells in the satellite–derived rainfall product GPM IMERG v7. The comparison of the reference run with ICON and the observations shows strong similarities in precipitation rate and location.

Discrepancies between the precipitation rates are found in the first six hours of the ICON reference run. While the GPM IMERG v7 data shows isolated precipitation cells with more than $0.2\,\mathrm{mm\,h^{-1}}$ distributed over the ocean of the whole research area, the reference run shows no precipitation greater than $0.001\,\mathrm{mm\,h^{-1}}$ (except of a cell close to Gabun). After 6 hours, the ICON run

reproduces the GPM IMERG v7 data.

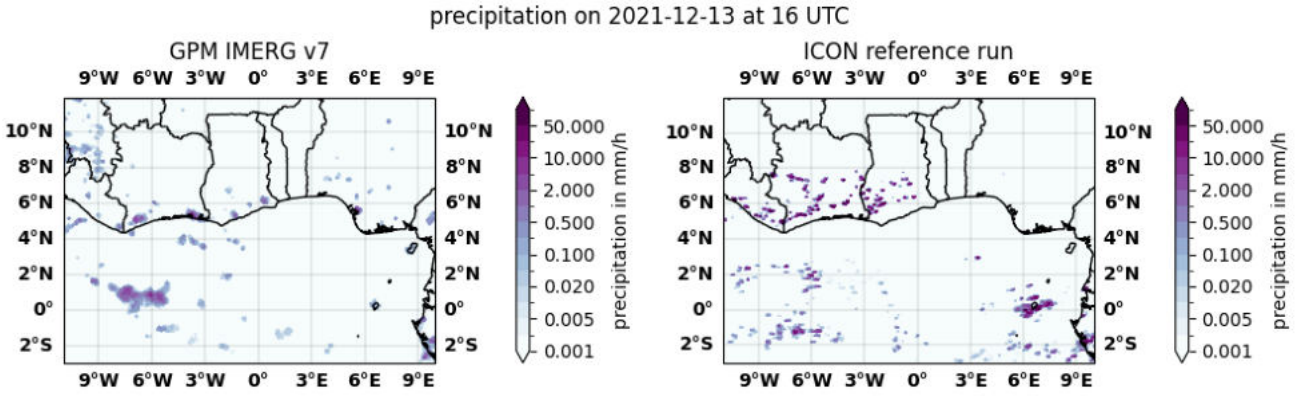

Figure 5.10: *Comparison of the precipitation: GPM IMERG data v7 (resolution:* $0.1° \times 0.1°$*) and ICON reference run (resolution:* $0.03° \times 0.03°$*) at 16 UTC on 13 December 2021.*

Another discrepancy is the location of the sea breeze–related coastal precipitation between both datasets. In the GPM IMERG v7 dataset, the precipitation appears close to the coastline. In the following hours, the precipitation strengthens at the coastline and extends lands inwards. In the ICON reference run, two scenarios are distinguished: eighter, the precipitation sets around the same time at the coast and propagates inland in the following hours leaving a precipitation-free zone along the shoreline. Or the precipitation appears at a later hour already about a degree north of the shoreline. Figure 5.10 compares the precipitation at 16 UTC on the first day in the research period between the simulation and the satellite product. The precipitation in the ICON reference run covers greater sections along the coastline and also is located deeper inland.

Although the detailed location cannot be represented exactly, the daily occurrence of precipitation in the ICON reference run resembles the precipitation in the GPM IMERG v7 dataset. For numerical simulations with ICON in the tropics, it is a well-known challenge to reproduce the satellite-estimated rainfall. Hereby, the reasonable distribution and occurrence of precipitation is more important than the exact representation.

5.2.3 Comparing the SBC in ERA5 data and the ICON reference run

The ICON reference run was compared to ERA5 reanalysis to ensure that the large-scale circulation during the simulation period is well-represented by the model. Although it is of interest to see how the sea breeze is depicted in ERA5 compared to the model, ERA5 should not be taken as ‘truth’ in this situation given its coarse resolution.

Figure 5.11 shows an example of the winds in 10 m height on 13 December at 14 UTC, 17 UTC and 23 UTC in the ERA5 data and the reference run. In a qualitative comparison of the winds in 10 m height and the location of the 14 °C isodrosotherm, the ICON reference run resembles the ERA5 data very well. Still, smaller differences can be identified in the wind direction over the eastern parts of the Gulf of Guinea during the Harmattan period, in the location of the ITD (especially over the Niger River and the Niger Delta) and due differences in the resolution of the

ERA5 data and the ICON simulation. Figure 8.4 in the appendix shows an example of the local wind differences over Lake Volta in Ghana and the differences in wind direction in the Harmattan winds. Even in this example, there is a high agreement in the 10 m winds and the location of the ITD in both datasets. Aside from the points mentioned above, the reference run of the ICON simulation has high similarities with the ERA5 dataset within the full research period, supporting the reliability of the ICON simulation.

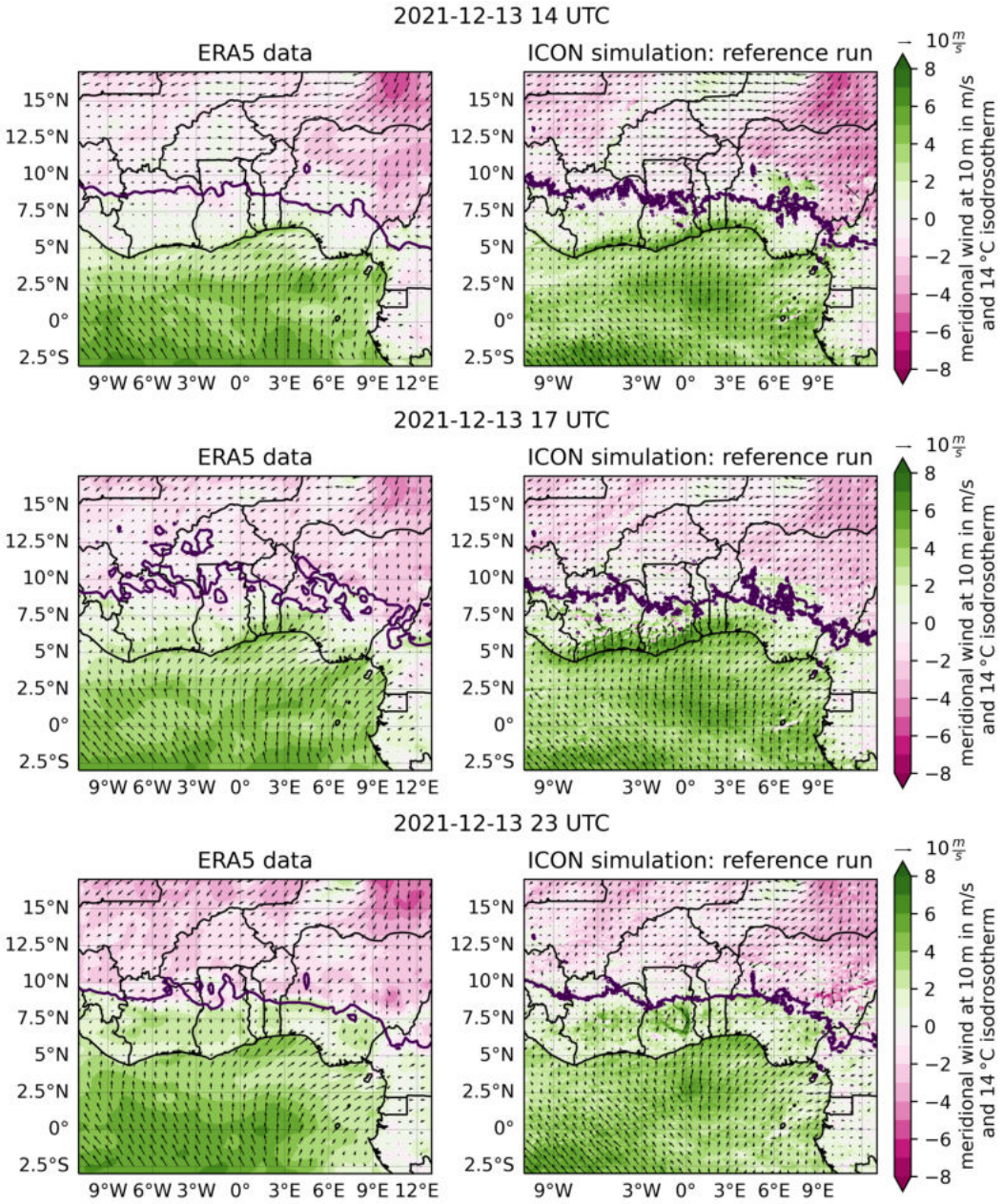

Figure 5.11: *Contourplot: meridional* 10 m *winds. Arrows:* 10 m *wind speed and direction. Different development stages of the SBC on 13 December 2021 in ERA5 and the ICON reference run. Upper plot: strengthening of the coastal* 10 m *winds at 14 UTC. Middle plot: inland penetration of the SB at 17 UTC. Lower plot: winds are accelerated towards the ITD at 23 UTC.*

The 10 m winds illustrate the sea breeze (SB) in the ERA5 dataset and the ICON reference run. Figure 5.11 shows maps of the 10 m winds on the first day of the simulation at 14, 17 and 23 UTC. In the almost zonal coast alignment in the Gulf of Guinea, the SB is strongly visible in the meridional wind. At 14 UTC, the onshore winds increase in the vicinity of the shoreline in the reference run due to the development of an SB (green shading at the shoreline). The SB develops all along the coastline from Cape Palmas (Ivory Coast) to the western part of Nigeria. At 14 UTC in the ERA5 dataset, an increased onshore wind can only be observed along the eastern part of the Gold Coast and in the Bight of Benin. Due to the coarser resolution of the ERA5 data, the SB cannot be resolved until it reaches a length scale of about seven times the grid size ($7 \cdot 0.25° = 1.75°$) (Milton et al., 2016). The two plots in the middle of Figure 5.11 show the near-surface winds three hours later. In both datasets, the SB extends far inland. The strength of SB wind speed is stronger in the ICON simulation. In ERA5 the SB-related near-surface winds are stronger east of Cape Three Points. An hour before midnight, the near-coastal 10 m winds over land are weak. Still, higher near-surface southerly winds are visible deeper inland both in the ERA5 data and the ICON simulation. The landward winds in the ERA5 penetrate faster inland compared to the reference run. Comparing the winds from 23 UTC in Figure 5.11 to later time steps, it is clearly visible that the inland penetration distance of the SB is limited by the location of the ITD (Figures are not shown, see analysis in Section 5.2.6). Overall, there is a good agreement in the representation of the SB in the 10 m wind maps of the reference run and the ERA5 dataset.

5.2.4 Case study 1: The LSB in a shallow monsoon flow in West Nigeria

Within the following three sections, the diurnal cycle of coastal winds for a case study in West Nigeria will be described. The analysis is based on transects perpendicular to the coastline, averaged from 3.5° to 3.9°E, corresponding to a zonal distance of 55.4 km.

Figure 5.12a shows a cross-section of the along-transect wind at 9 UTC on the second day, 14 December 2021, of the reference run. On 14 December, the near-surface winds up to 1500 m height are directed landwards (green shading). They are a part of the shallow monsoon flow. Above the monsoon winds, the flow is oceanward. At 9 UTC the boundary layer depth (BLD), defined as the height of the well-mixed layer of virtual potential temperature, over land is similar to the BLD over the ocean (black contours, figure 5.12a), with a height of approximately 800 m.

Two hours later, the BLD over the ocean is still around 800 m and the virtual potential temperature in the BL remains constant (Figure 5.12b). Over land, the virtual potential temperature is increased up to 3 K and the BLD has deepened, exceeding 1100 m. Figures 5.12b–5.12d show how the BL depth continues to grow over land throughout the day as the near-surface air over land warms faster than over the ocean. The difference in virtual potential temperature between the marine and land BL results in a density current moving from the shoreline inland. This density current is the sea breeze (SB). It is a part of the sea breeze circulation (SBC). Figure 5.12b shows the increased cross-shore wind speeds in the BL in the vicinity of the shoreline (darker green shading). The sea breeze front (SBF) is the zone between the sea breeze (SB) and the ambient flow where sharp changes in temperature, moisture and wind occur (Ji et al., 2013). The black line shows the automatically detected SBF from the algorithm introduced in Section 4.5.3.Ahead of the SBF, the surface air is forced upwards (the reddish contour indicates a vertical velocity

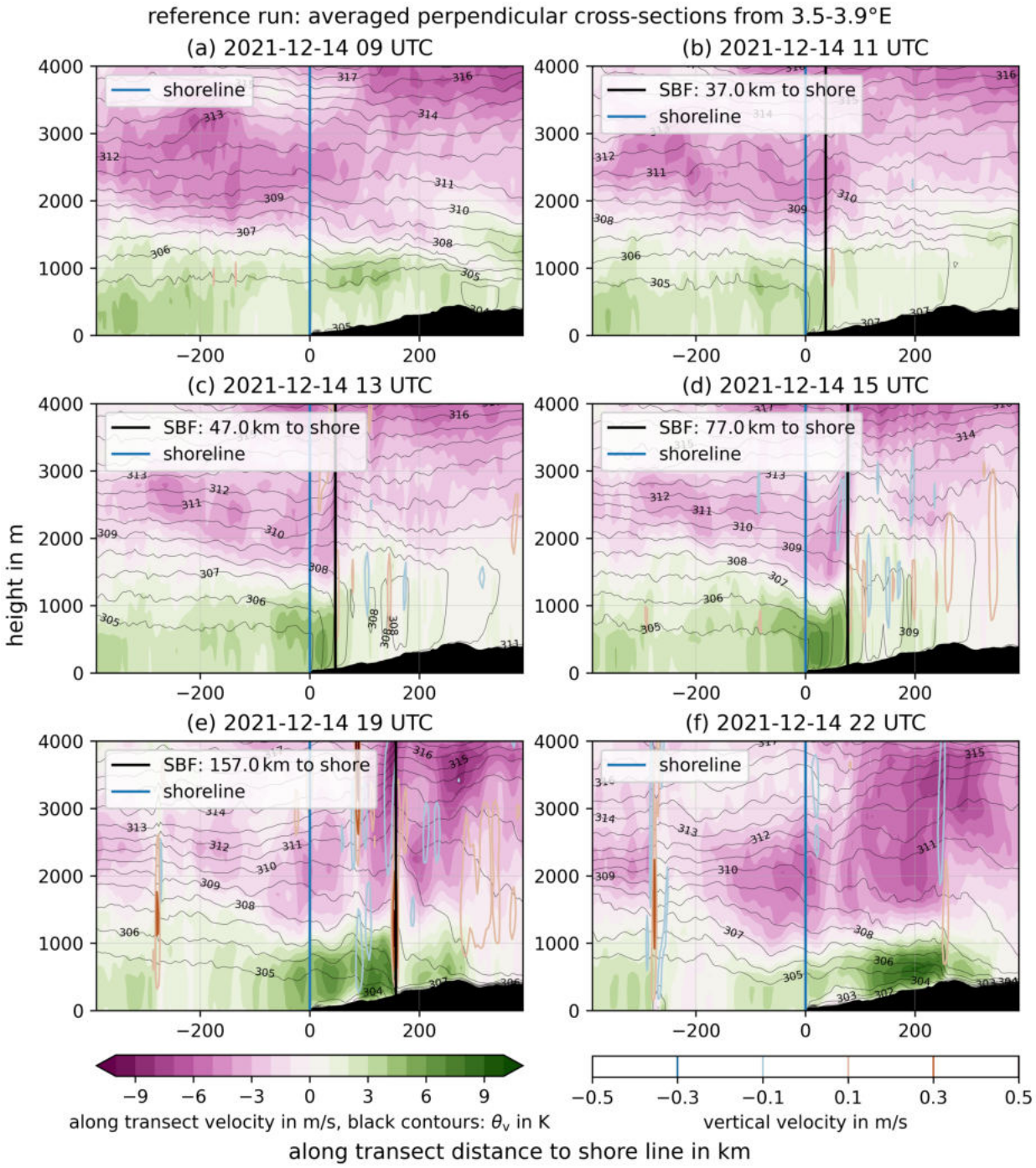

Figure 5.12: *Averaged perpendicular cross-section from* 3.5° *to* 3.9° *East on the 14 December 2021 of the reference run at 9, 11, 13, 15, 19, and 22 UTC. Green shaded areas mark along-transect winds from ocean to land, pink shaded areas a horizontal wind from land towards the ocean. The virtual potential temperature describes the density of an airmass and is, therefore, a proxy for the stability of the atmosphere. Lines of equal virtual potential temperature are visualised in black. The numbers on the lines indicate the values of the virtual potential temperature in Kelvin. The reddish and blueish contours depict the vertical velocity (positive upwards). In this figure, the vertical velocity exceeds the magnitude of* $0.1\,\mathrm{m\,s^{-1}}$ *in very few locations.*

exceeding $0.1\,\mathrm{m\,s^{-1}}$).

Figure 5.12c shows the cross-section at 13 UTC. Over land, the BLD has further extended vertically and daytime convection is initiated in the BL (ahead of the SBF, 'stripes' of up- and downdrafts appear (red and blue contours)). The onshore wind speed in the SB has further increased and the SBF has moved 10 km further inland.

At 15 UTC, the SBF reaches 77 km inland (Figure 5.12d). Between 15 and 16 UTC the BLD over the land reaches its greatest depth due to vertical mixing and convection (not shown). Convective updrafts extend in Figure 5.12d through the whole BL over land. Comparing the return flow of the SB at 15 UTC to 9, 11 and 13 UTC, a deformation of the flow patterns can be observed: The height of the SB over land is about 300 m lower than the shallow monsoon flow, which extends approximately up to 1500 m height at 9 UTC. Therefore, the return flow of the SB has a lower height than the oceanward return flow of the large-scale monsoon circulation. Additionally, the return flow increases the wind speed in the return flow of the large-scale circulation aloft of the SB. The schematic in Figure 5.13 illustrates how the SBC influences the embedding flow locally.

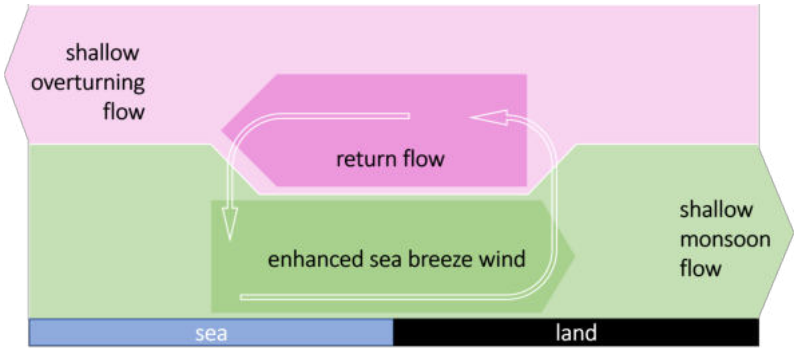

Figure 5.13: *Impact of the SBC on the height of the shallow monsoon flow and the shallow overturning circulation.*

Figure 5.12e shows the cross-section at 19 UTC, approximately 1.5 h after sunset, during the late-mature stage of the SBC. The SB wind weakens in the vicinity of the shoreline. At the SBF, the frontal structure of the virtual potential temperature remains. The virtual potential temperature profile reflects the longwave cooling at the land surface: A strong vertical gradient emerges in θ_v within the lowest 100 m to 200 m above the surface. The atmosphere above remains well-mixed up to 1500 m height.

Figure 5.12f shows the SBC at 22 UTC. The surface cooling is increased compared to the cross-section at 19 UTC. In the lowest 100 m of the atmosphere, where a strong vertical gradient of virtual potential temperature occurs, the surface winds are slowed down (white shading below the green-shaded SB). The SB detaches from the surface and moves on top of this inversion layer further inland. Still, it retains its frontal structure at the SBF. The low along-transect wind speed 100 km inland of the shoreline shows a decoupling of this flow from the shoreline. The high wind speed in the gravity current and the detachment from the surface indicate a transforma-

tion of the SB into a nocturnal low-level jet (NLLJ). This will be further analysed in Section 5.2.6.

The land breeze and katabatic winds

At 19 UTC, the effect of the surface cooling can already be noted in the strong vertical gradient in virtual potential temperature close to the land surface (Figure 5.12e). Within the following hours, the cooling extends vertically. At 22 UTC, this near-surface inversion layer has almost doubled its vertical extension and reaches approximately 200 m above the land surface (Figure 5.12f). The vertical profile of the virtual potential temperature above the ocean remains constant after sunset. At the shoreline, the near-surface virtual potential temperature gradient between land and ocean thus reverses compared to the daytime, generating a reversed rotation cell across the shoreline: the land breeze (LB).

Figure 5.14a shows the along-transect wind at 22 UTC again within the lowest 600 m height. Within 30 to 100 km landward from the shoreline, a shallow flow directed towards the ocean forms. The flow forms on a sloped terrain. The land–breeze circulation is reinforced by katabatic flow, shown by the horizontal gradient in the virtual potential temperature.

Two hours later at 0 UTC on 15 December 2021, the oceanward flow strengthens close to the shoreline (Figure 5.14b). The circulation is very shallow, reaching a vertical extent of just 200 m above the surface. The wind velocities are also weak with values up to $1\,\mathrm{m\,s^{-1}}$.

Between 1 UTC and 3 UTC on 15 December 2021 the monsoon flow in the vicinity of the shoreline strengthens. Figure 5.14c shows the along-transect winds at 3 UTC. Over land the inversion layer increases further in height and the virtual potential temperatures at the land surface decrease as well. The surface flow towards the ocean disappears. The weak LB and katabatic winds are replaced by the monsoon flow, which increases in strength. Still, the wind velocities stay low in the inversion layer.

Between 4 and 5 UTC, the surface flow in the inversion layer over the land again turns oceanward (not shown). It increases in windspeed until 6 to 7 UTC. Figure 5.14d shows the land breeze close to its maximum. The flow reaches again a height of 200 m and wind speeds up to $1.5\,\mathrm{m\,s^{-1}}$. The sun rises shortly before 6 UTC. With the increasing solar heating of the land surface, the temperature inversion over land reduces. At 8 UTC, the LB dissolves (not shown). At 9 UTC, the temperature inversion over land disappears and the BLD over the ocean equals the BLD over the land (not shown).

The occurrence of the LB thus highly depends on the embedding flow which can extinguish it. It can be observed as soon as the land surface and the lowest atmosphere on top have sufficiently cooled below the temperature of the atmosphere over the ocean. In this case study, the land breeze can first be observed 3.5 h after sunset. It dissipates two hours after sunrise.

5.2.5 Case study 2: The LSB in a Harmattan flow in West Nigeria

This case study analyses the daily development of the sea breeze circulation (SBC) in a strong opposing flow on 15 December 2021. The location is the same location analysed in the first case

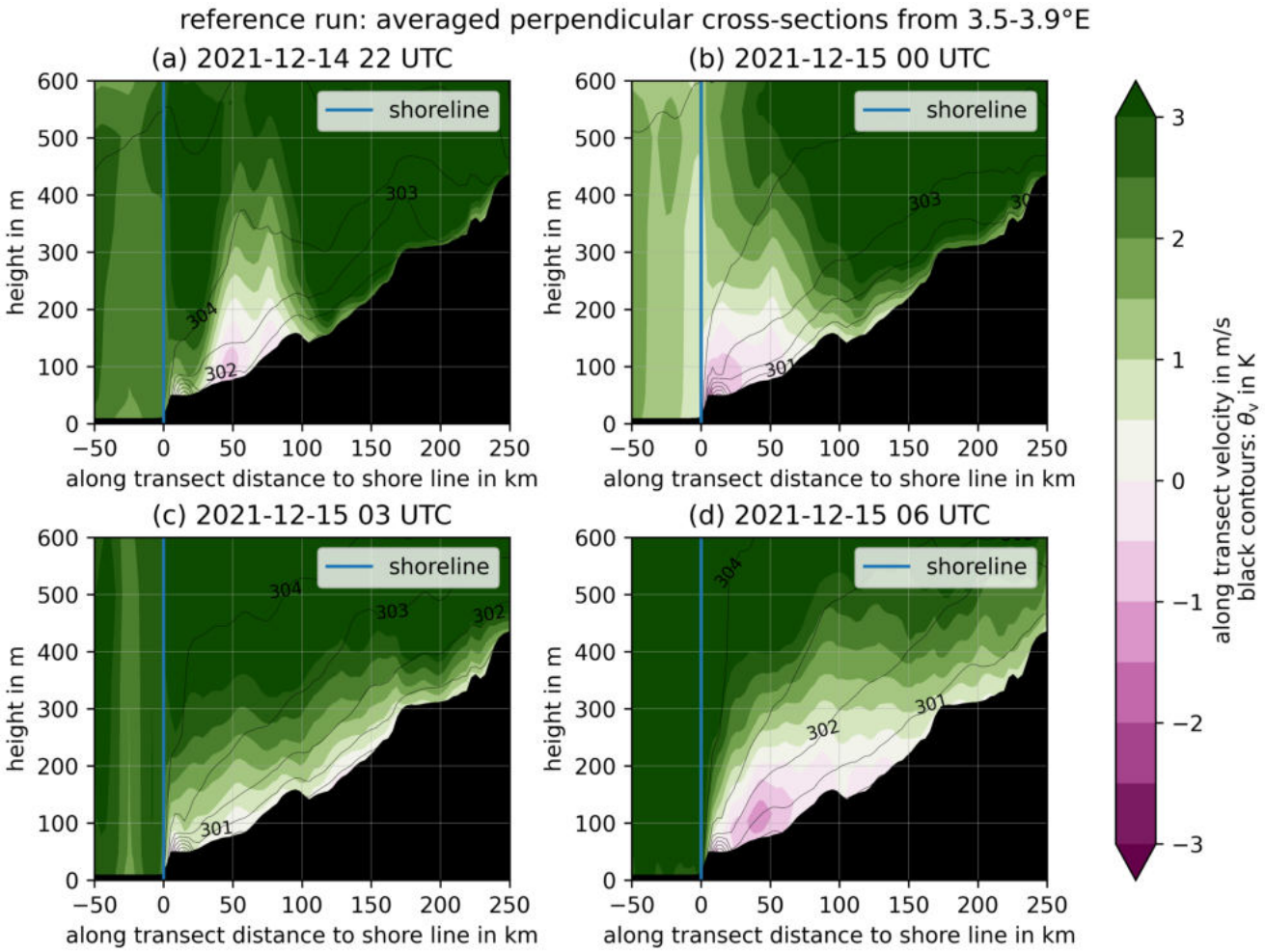

Figure 5.14: *Averaged perpendicular cross-section from 3.5° to 3.9° East on the 14 December 2021 of the reference run at 22 UTC and on 15 December 0 UTC, 3 UTC, and 6 UTC. Green shaded areas mark along-transect winds from ocean to land, pink shaded areas a horizontal wind from land towards the ocean. The virtual potential temperature describes the density of an airmass and is, therefore, a proxy for the stability of the atmosphere. Lines of equal virtual potential temperature are visualised in black. The numbers on the lines indicate the values of virtual potential temperature in Kelvin.*

study (West Nigeria, perpendicular cross-sections averaged between 3.5° and 3.9°E).

On 15 December 2021 at 11 UTC strong northerly winds replace the shallow monsoon flow over land in West Nigeria (not shown). The SBC forms before the embedding winds over land turn offshore (not shown). At 13 UTC, the northerly winds have already strengthened in between 60 to 140 km distance from the shoreline, thus directly ahead of the SBF (Figure 5.15). At the sea breeze front (SBF) the SB collides with the opposing northerly flow and a strong updraft forms (Figure 5.15: the reddish contour shows an upward vertical wind speed exceeding 0.1 $\mathrm{m\,s^{-1}}$).

Figure 5.16 shows the along-transect and vertical wind speed in the following four hours. At 14 UTC, the specific cloud water and rain content is increased at the SBF and at the position of the

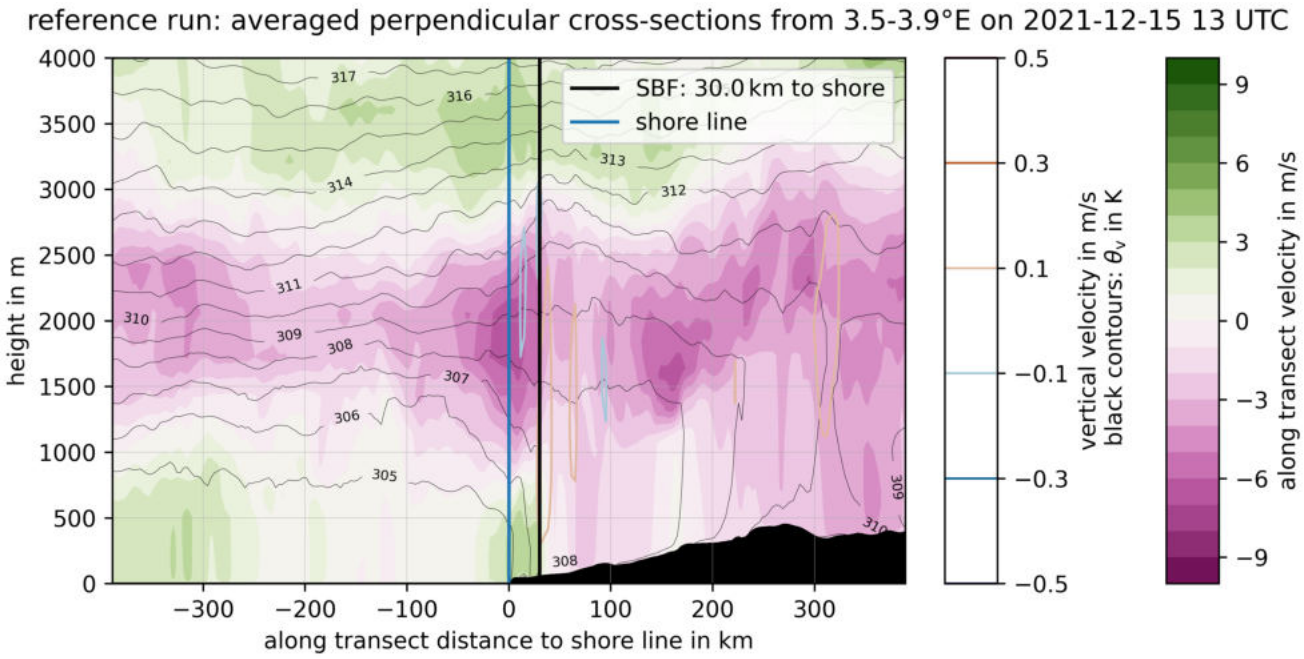

Figure 5.15: *Same as Figure 5.12c but for 15 December 2021 at 13 UTC.*

strong updraft about 10 km ahead of the SBF (Figure 5.17a). Between the surface and 400 hPa height, the water vapour content is also increased in these regions, compared to the atmosphere around (see the upward tilt in the contour lines of equal specific humidity in these regions). This visualizes the evaporation process of the rain and the water droplets. Evaporation takes energy from the atmosphere and thus cools the atmosphere locally. The cooler and denser air sinks (strongly visible at the SBF at 16 UTC in Figure 5.16c: the dark blue contours indicate a strong downward velocity exceeding 0.3 m s^{-1} in average). This downward motion is directly centred at the position of the shoreline at 16 UTC.

The near-surface divergence from the outflow of the cold pool is also visible in the green shading at the right of the circular virtual potential temperature profile pattern, indicating a southerly flow, whereas to the left, a pink shading indicates northerly winds from the cold pool outflow (Figure 5.16b). On the map of the horizontal surface winds, the cold pool shows a characteristic circular pattern due to its radial extension: figure 5.18 shows the development of the meridional wind component at 10 m height in hourly steps from 13 to 18 UTC. The area of the case study is indicated with a black box. At 15 UTC (Figure 5.18c) a circular pattern appears in the box between the areas of the SB (green shading) and the northerly Harmattan flow (pink shading). The wind vectors extend approximately radially from the centre of the circle. Comparing the 10 m wind maps from 13 to 18 UTC, the SBF position is not homogeneous along the shoreline. The cold pool density current shows a faster frontal inland propagation wind speed than the SBF.

At 16 UTC, two separate circulations can be identified in the cross-section in Figure 5.16c. The one circulation extends from over 75 km off-shore to 30 km inland. The horizontal density gradient caused by the cold pool develops a second circulation in this area from 40 km to 75 km distance to the shoreline: the strong horizontal gradient in virtual potential temperature between the cold pool region and the opposing Harmattan flow enhances the surface flow. The virtual potential

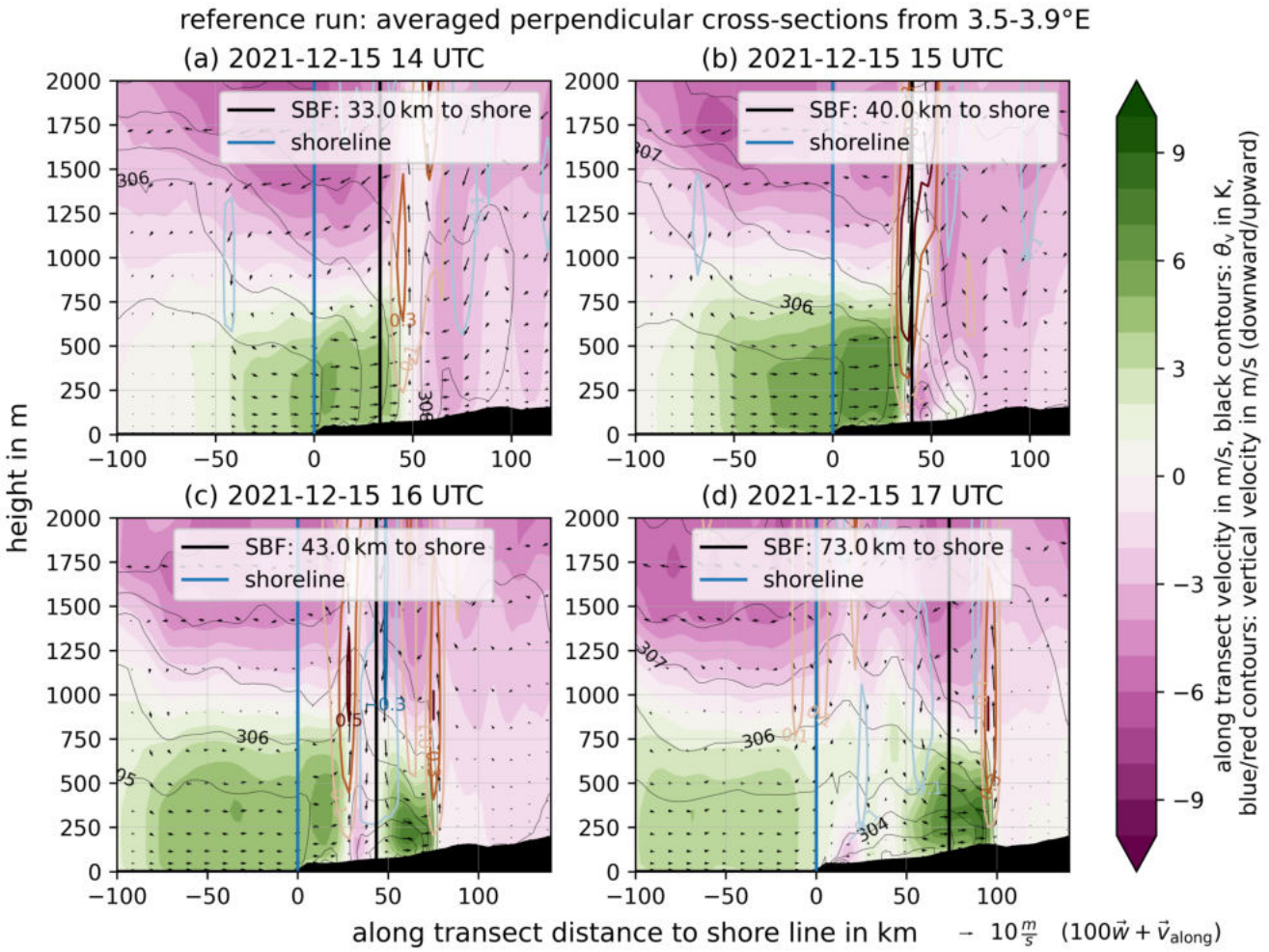

Figure 5.16: *Air temperature, lines of equal virtual potential temperature and wind vectors at 14, 15, 16, and 17 UTC on 15 December 2021. Averaged perpendicular cross-sections between* 3.5° *and* 3.9°*E in the case study in West Nigeria.*

temperature profile at the front of the circulation has strong similarities with the profile of the SB density current in case study 1, in fact, both wind systems are hard to distinguish from the perspective of the surface winds. The boundary layer depth, however, shows a decreased vertical extent over the cold pool outflow. The SBF detection algorithm identifies the SBF 73 km from shoreline at 17 UTC. A closer look at the virtual potential temperature profile reveals, that this SBF position is related to the position where the SBF and the cold pool merge.

The day-time analysis of the SBC in the second case shows:

1. Cold pools can form or strengthen at the SBF. The opposing embedding flow may enhance this by causing a stronger low-level convergence at the SBF.

2. The SB faces an opposing flow due to the seaward outflow of the cold pool. This can displace the SBF closer to the shoreline while a second SBC-like circulation forms at the front of the cold pool density current.

3. In the later evening this secondary circulation can move far inland.

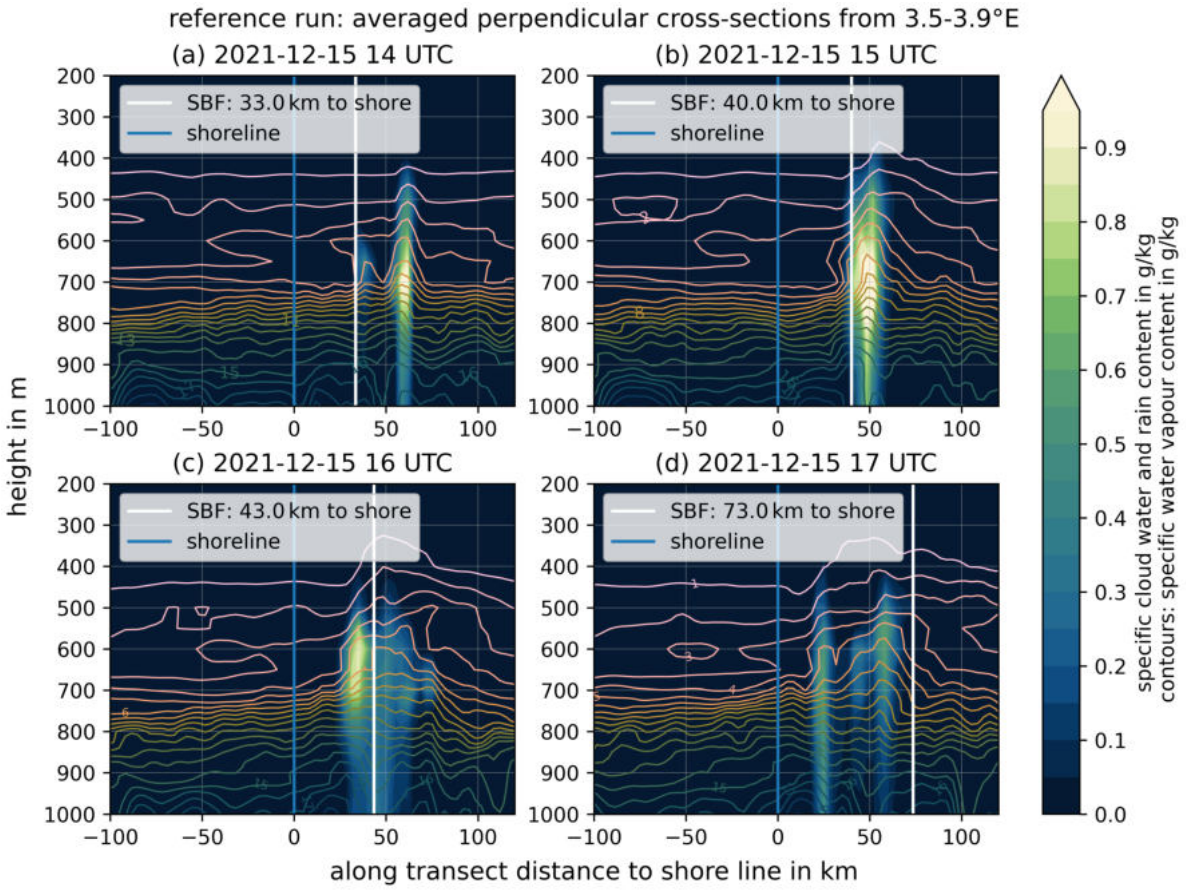

Figure 5.17: *Specific cloud water and rain content and contours of specific water vapour content on 15 December 2021 at 14, 15, 16, and 17 UTC in West Nigeria. Development of a cold pool at the SBF in the reference run.*

At 20 UTC the SB has moved 87 km inland (Figure 5.19a). This is approximately 26 km less than the day before (not shown), where the SBC is embedded in the shallow monsoon flow. Over the ocean, the winds have also turned north. The southward extension of the Harmattan flow exceeds 400 km over the ocean (not shown).

At 23 UTC, a land breeze has developed in the near-surface inversion layer (not shown). It increases in depth and strength and reaches UTC the shoreline at 2. Compared to the day before, the flow has a greater vertical extent (about 400 m) and a stronger wind velocity (3 to 4 $\mathrm{m\,s^{-1}}$) (compare Figure 5.14d and Figure 5.19b). This can lead back to the weaker embedding flow: The night before, the land breeze (LB) and the katabatic wind developed in an environment of a strong shallow monsoon flow. In the early morning of 16 December 2021, the wind speed of the onshore embedding flow is about 2 to 5 $\mathrm{m\,s^{-1}}$ lower compared to the day before. At 6 UTC, the LB merges with the Harmattan flow (Figure 5.19c). In the following hour, the northerlies replace the southerlies (remnants of the SB from the day before) over the land and extend more than 200 km off-shore (Figure 5.19d). The LB penetrates over 50 km off-shore. At 10 UTC, the solar heating has already dissolved the night-time surface inversion.

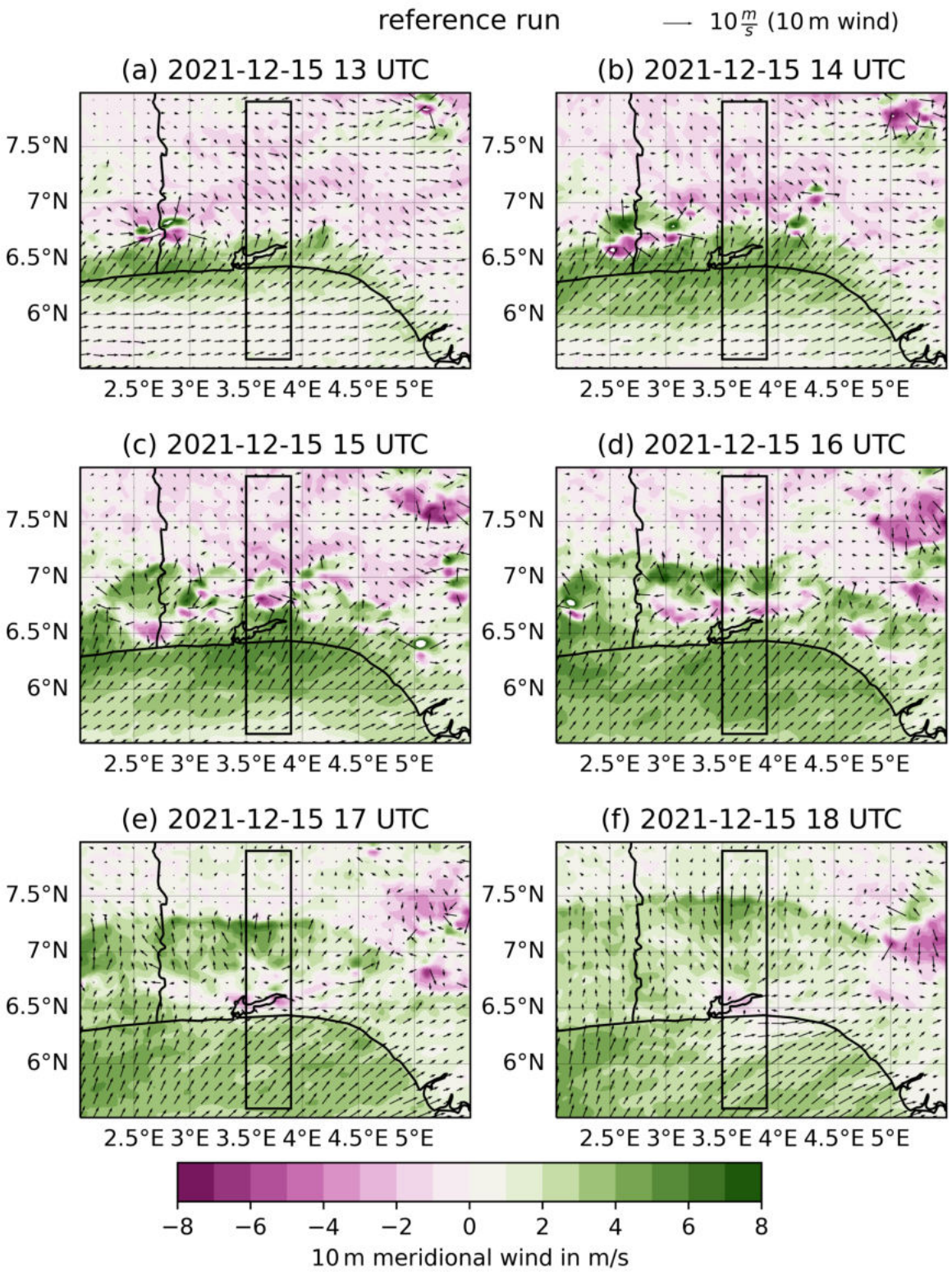

Figure 5.18: *Maps of* 10 m *meridional wind (contours) and horizontal* 10 m *wind vectors on 15 December 2021 between 13 UTC and 18 UTC. The black box indicates the location of the study area of case studies 1 and 2 (the cross-sections extend furth north and south).*

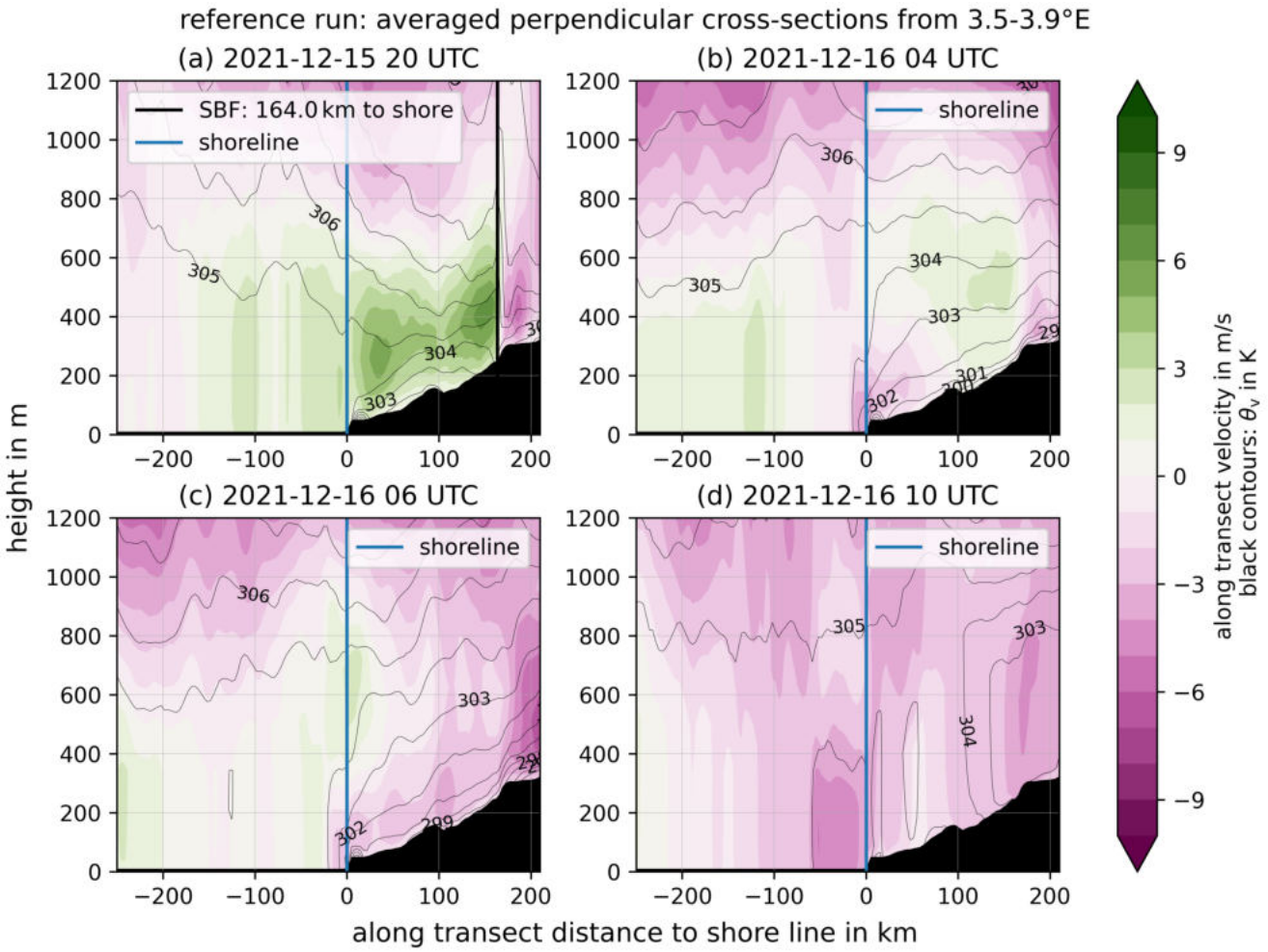

Figure 5.19: *Averaged perpendicular cross-section from* 3.5° *to* 3.9° *East on the 15 December 2021 of the reference run at 20 UTC and on 16 December 4 UTC, 6 UTC, and 10 UTC. Green shaded areas mark along-transect winds from ocean to land, pink shaded areas a horizontal wind from land towards the ocean. The virtual potential temperature describes the density of an airmass and is, therefore, a proxy for the stability of the atmosphere. Lines of equal virtual potential temperature (in* K*) are visualised in black.*

5.2.6 Case study 3: Transformation of the SB into a nocturnal low-level jet

In the late evening, the sea breeze (SB) can transform into a nocturnal low-level jet (NLLJ). On 14 December 2021 (monsoon flow period), this development occurs whereas the same transformation was not visible on 15 December 2021 (see case study 1 and 2 in Section 5.2.4 and 5.2.5).

Figure 5.20d shows the Hovmöller diagram of the 10 m along-transect wind speed averaged from 3.5° to 3.9 degree East (similar area as in case study 1 and 2) during the 5 days of the simulation period. This Hovmöller diagram confirms the wind conditions of the embedding wind field described in the sections before: The shallow monsoon flow (green shading) is replaced from 12 UTC on 15 December until 12 UTC on 17 December by the northerly Harmattan flow (pink shading) over the Guinea Coast (area with positive distances to the shoreline indicated as a horizontal blue line). Over the land, the embedding flow direction depends on the position of the

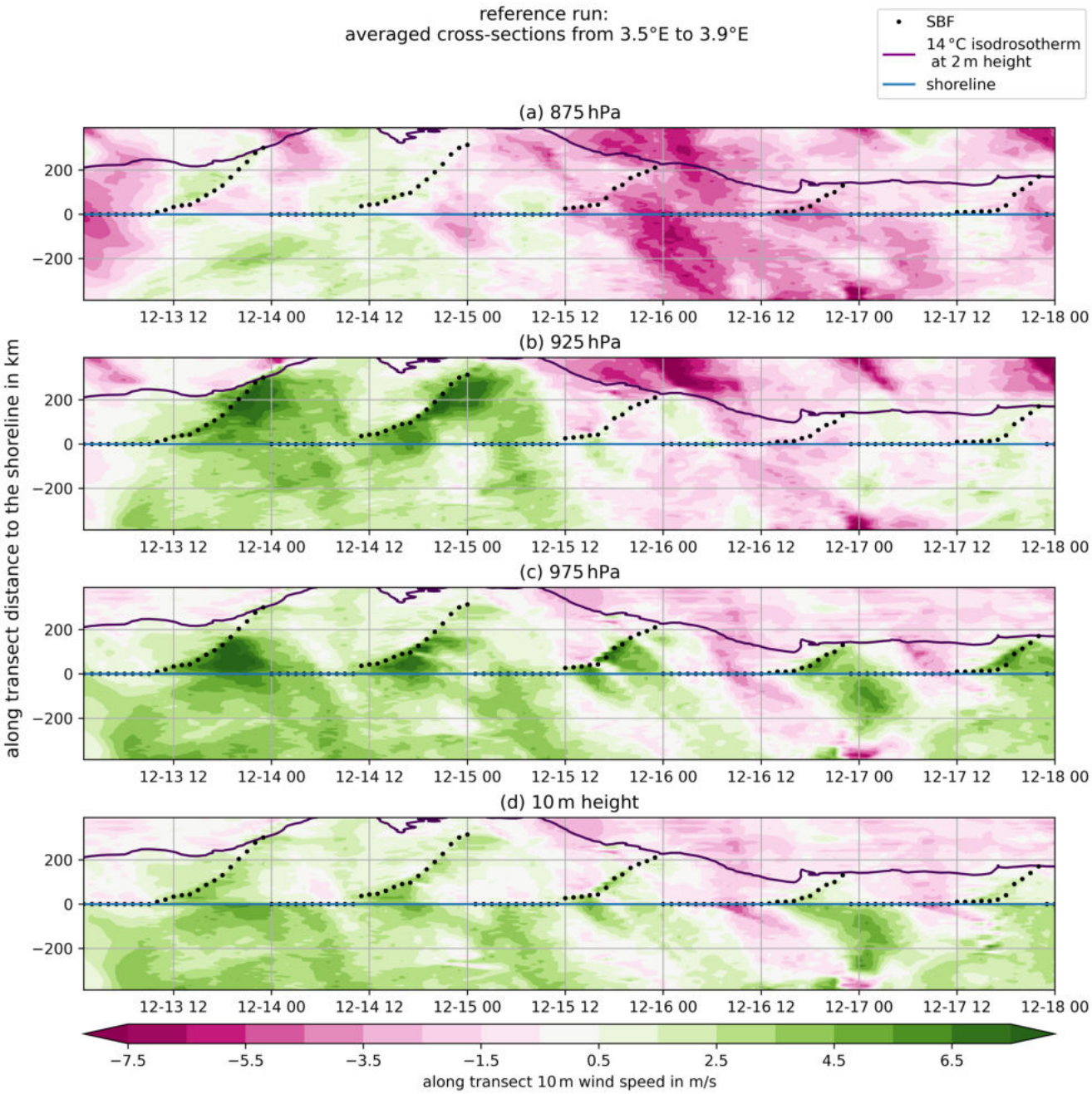

Figure 5.20: *Hovmöller diagram of the along-transect wind component in the averaged perpendicular cross-section in West Nigeria (3.5° to 3.9° E). The y-axis shows the along-transect distance to the shoreline. The x-axis shows the timestep within the five days of the simulation period. Green shading indicates an onshore wind and pink shading an offshore wind. The sea breeze front location is indicated with a black marker. The sea breeze extends during the daytime from the shoreline (blue line) inland towards the ITD (purple line: 14 °C isodrosotherm at 2 m height). Subplot (d) shows the 10 m along transect winds, the plots above the along transect winds at pressure levels of 975 hPa, 925 hPa and 875 hPa in the atmosphere above.*

ITD (purple line, indicated by the 14 °C isodrosotherm at 2 m height). North of the ITD, the surface winds usually have a northerly component (pink shading) whereas the winds south of the

ITD are southerlies (green shading). Over the ocean and in the vicinity of the coastline, the use of the 14 °C isodrosotherm to denote the ITD may not be appropriate closer to the coast, due to the enhanced moisture content in the maritime atmosphere. In these areas, the criteria for the ITD and the identification of the surface winds should be defined by the location of maximum confluence. Figure 5.20 shows the strong day-to-day variations of the ITD. A diurnal cycle is less clearly visible. Following the position of the purple line, the ITD is on average closest to the shoreline at around 18 UTC and furthest inland at 6 UTC.

The locations of the sea breeze front (SBF), calculated with the SBF detection algorithm, are indicated as black markers in Figure 5.20a. They fit the areas with the increased onshore wind speed (darker green shading) in the vicinity of the shoreline very well. Dividing the distance from the shoreline to the SBF into two halves, the half closer to the shoreline experiences lower 10 m wind speeds than the half closer to the SBF after 18 UTC on the first two days. At this time, the longwave cooling has already set in building a very shallow inversion layer. This decouples the near-surface atmosphere from the SB aloft.

The Hovmöller diagram at 975 hPa shows a different situation (Figure 5.20c). This level lies within the SB. During all days from the onset of the SBC (when the SBF location is north of the shoreline), the land- and seaward extension of the circulation is visible (darker green shading, extending land- and seaward from the shoreline). After around 20 UTC, the along-transect wind speed at and behind the SBF decreases.

The along-transect wind velocities at 925 hPa in the afternoon and evening differ strongly between Harmattan days and monsoon flow days (Figure 5.20b). In an embedding monsoon flow (first two days), the along-transect winds at 925 accelerate between 18 and 19 UTC in 100 to 300 km distance from the shoreline at once (also ahead of the SBF). These winds propagate north until they reach the ITD. In the early morning, they decrease in velocity but still show a strong signal until sunrise. These observations suggest the transformation of the SB into a NLLJ in the first two days.

The last three days show also a very interesting pattern in the 925 hPa winds in Figure 5.20b: between the shoreline and the SBF, the along-transect wind flows offshore. This supports the hypothesis, that the return flow of the SBC is located at a lower level than the overturning reverse flow of the WAM. Figure 5.20a shows the same patterns in the 875 hPa winds in the first two days. Here, the return flow is located at larger heights since the SB depth is also increased compared to the last three days of the simulation.

5.2.7 Inland penetration distance of the SB in the reference run

These three case studies show that the inland penetration distance of the sea breeze (SB) depends among others on the embedding wind field. Figure 5.21 compares the inland penetration distance of the SB in the case studies (West Nigeria, 3.5° to 3.9° E) for the 5 days of the simulation period.

In the first two days of the simulation, the SB extent increases with time. All days have in common that the SB extends faster inland after sunset than during the daytime. This can be seen in an increased inland propagation velocity (increased slope). Also, the slope of values, proportional

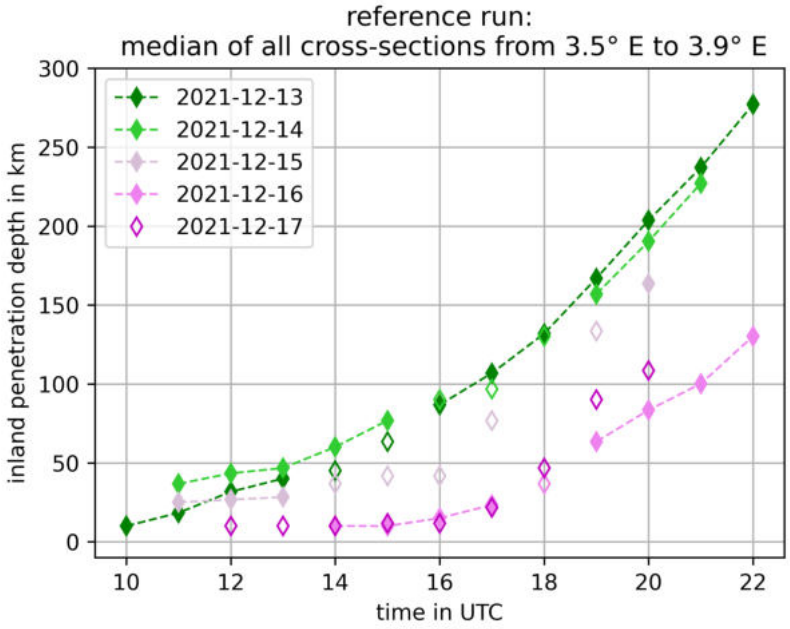

Figure 5.21: *Inland penetration distance for the five days in the research period of the reference run. The colours of the markers relate to the different days. The embedding wind conditions are either shallow monsoon winds (green) or a Harmattan flow (pink) (details in Table 5). The position of the SBF is determined for each cross-section with the SBF detection algorithm described in Chapter 4.5.3. The median of all determined positions is shown here. Filled markers indicate a good agreement in position with the location of a horizontal gradient in the virtual potential temperature and the wind speed in the lowest* 500 m *to* 1000 m *(the height depends on the environmental flow) compared to perpendicular cross-sections.*

to the speed of propagation, for the inland penetration distance in the evening is comparable. The inland penetration distance in the late morning and midday differs strongly with the wind conditions: In the first two days (shallow monsoon flow), the SB extends constantly inland over time. In the last two days, the SBC sets 2 h to 4 h later and SBF stays close to the shoreline until 16 UTC. In the strong opposing flow, the SBC extends mainly oceanward. On the third day, the SBF persists between 11 UTC and 16 UTC within a distance of 30 to 40 km to the shoreline. Due to the shallow monsoon embedding flow conditions in the morning, the SBC has already extended 30 km inland before a further extent is impeded by an opposing Harmattan flow.

Figure 5.21 shows that the embedding flow can result in differences of up to 150 km of the inland penetration distance. Also between 13 UTC and 16 UTC, where the development of deep convection is strongest, differences of approximately 40 to 70 km occur in this case study. These differences are important in respect to the local thunderstorm development and precipitation triggered at the SBF.

Figure 5.22 shows the median of the SBF location calculated in all cross-sections over nearly the whole Guinea Coast between −7.5° and 4.5° East. Figure 8.8 to 8.12 in the appendix show the spread of the inland penetration distance for each day for the simulation period.

The median of the SBF location reflects the behaviour described for the inland penetration dis-

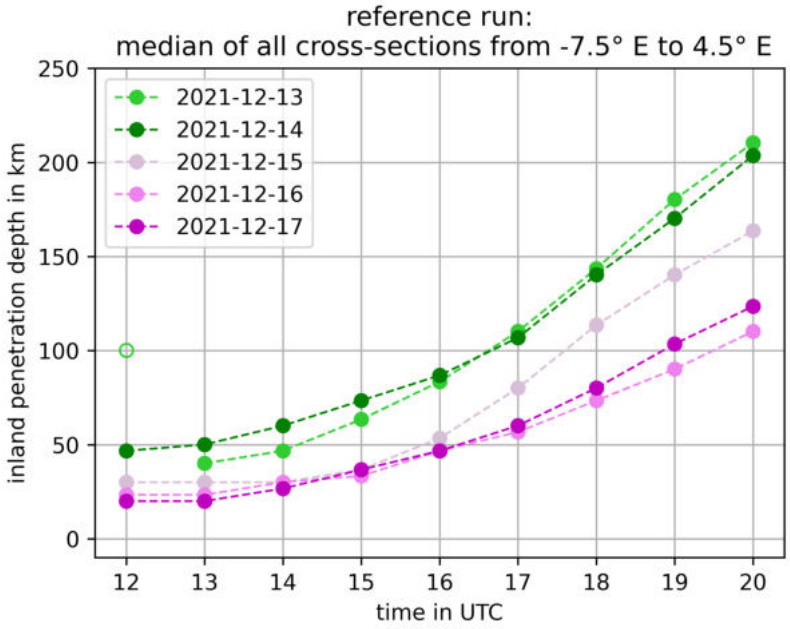

Figure 5.22: *Hourly median of the inland penetration distance of the SB along all cross-sections from −7.5° to 4.5° E. The colours indicate the day of the reference run.*

tance of the case study area for the first two days (compare Figure 5.22 to Figure 5.21). The last three days during the Harmattan period show a higher inland penetration in the daytime and a higher slope. These differences can emerge from the different wind conditions along the coast: The Harmattan surge is stronger east of Cape Palmas. Therefore the median of the whole region understates the impeding effect of the strong Harmattan winds in the east of the Gulf of Guinea. Thus, for meaningful prognoses of the SBC, the area should be divided according to the conditions of external factors like the embedding wind field.

5.2.8 Height of the SB in the reference run

The calculation of the height of the sea breeze (SB) is based on the wind reversal criteria from Wexler (1946): He defines the height of the SB to where the horizontal velocity falls to zero. Here, the SB height is defined as the mean of all the heights between 300 m and 1800 m above the surface where the wind changes from onshore to off-shore. Figure 5.23 shows a cross-section of the sea breeze circulation on 14 December at 19 UTC. The heights where the along-transect velocity changes sign are marked with contours. Between 80 and 100 km landwards of the shoreline (blue vertical line), the contour of wind reversal appears close to the surface and above 1000 m height whereas the height of the SB can be estimated by eye between 1000 m and 1200 m above the surface. The limitation between 300 m and 1800 m cuts out surface effects and effects of strong convective updrafts. The average takes into account, that the wind reverses direction in some locations several times between the SB and the return flow.

The two case studies (Sections 5.2.4 and 5.2.5) in West Nigeria show, that the height of the sea breeze depends strongly on the embedding flow. Figure 5.24a shows the mean land-ward height of the SB in the first four days in the case-study area of West Nigeria (3.5° to 3.9°E). On 13

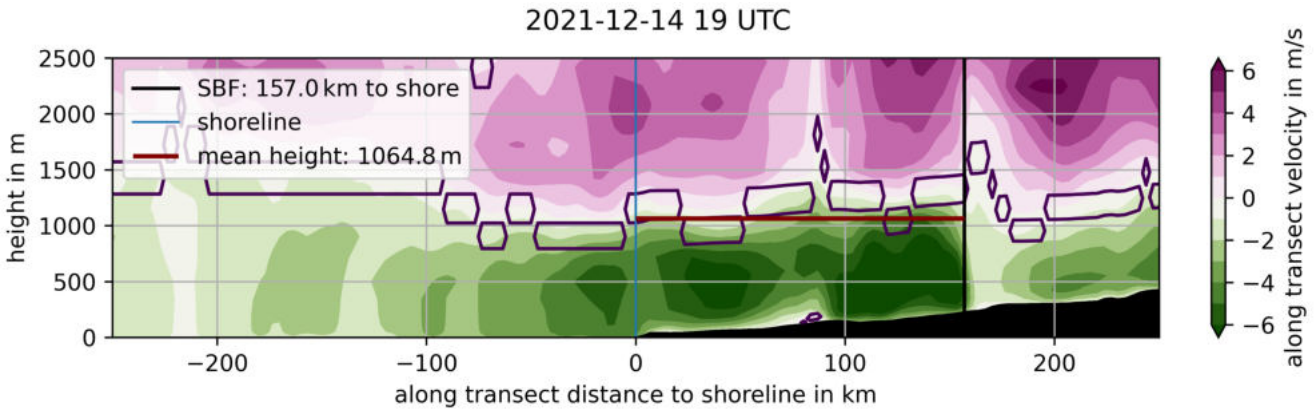

Figure 5.23: *Along-transect wind velocity in the averaged cross-sections between* 3.5° *and* 3.9° *E on 14 December 2021 at 19 UTC. The purple contours show areas where the wind reversal criteria of Wexler (1946) is fulfilled, thus areas with zero horizontal wind. The brown line shows the mean SB height calculated between the shoreline (blue vertical line) and the SBF (black vertical line) (orography is subtracted).*

and 14 December 2021 (green markers), when the SB is embedded in the shallow monsoon flow, the SB is about twice as high as during days with Harmattan flow (pink markers): on 13 and 14 December at 18 UTC, the SB extends 900 m to 1000 m vertically whereas it reaches 500 m to 600 m depth on 15 and 16 December at 18 UTC. Figure 5.24b shows the median of the SB height of the cross-sections all along the zonal coast from Cape Palmas (Ivory Coast) to West Nigeria. Comparing these result to the case study in West Nigeria, the SB height shows similar behaviour in the first two days. In both coastal zones the SB extends between 900 m and 1100 m vertically. Only in the Harmattan regime (pink markers), the median of the SB between Cape Palmas and West Nigeria shows higher values: on 16 and 17 December the SB height lies between 600 m and 900 m. This difference between Figure 5.24a and 5.24b can be explained by the stronger Harmattan flow in the eastern part of the Gulf of Guinea compared to the western part (not shown): West Nigeria experiences a stronger northerly flow compared to the averaged flow along the whole coastline which leads to a stronger decrease in the SB height.

5.2.9 Chapter summary

In the research period from 13 to 17 December 2021, the large-scale flow pattern of the WAM shows high variability in the near-surface winds along the Guinea Coast. The eastern part of the Guinea Coast experiences an onshore monsoon flow in the first two days, which reverses into a northerly Harmattan flow from the third day to the end of the research period. Case studies in West Nigeria show a large dependence of the LSB on the embedding flow: opposing ambient winds impede the LSB in wind velocity and inland penetration distance and decrease the depth of the circulations. The SB finds its maximum inland penetration distance at the position of the ITD. When the ITD is located far inland, the SB can transform into a NLLJ during the night. During the day, the SB can induce or strengthen convection, leading to the formation of cold pools at the SBF. The density current resulting from the outflow of these cold pools can merge with the SB and modify the SB characteristics.

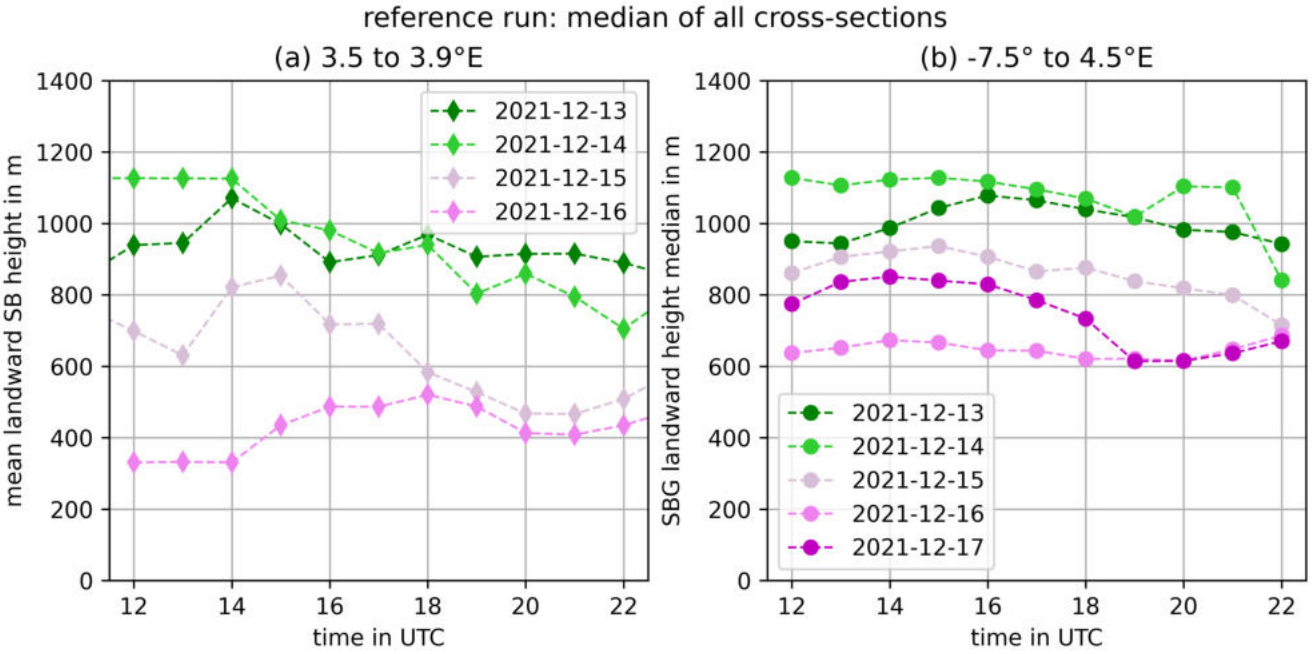

Figure 5.24: *Hourly mean of the SB height along all cross-sections from (a) 3.5° to 3.9°E and (b) −7.5° to 4.5°E. The SB height is calculated between the shoreline and the SBF. The colours indicate the days of the reference run (green markers: monsoon period, pink markers: Harmattan winds).*

5.3 Sensitivity of the LSB to SST

The impact of the sea surface temperatures (SSTs) on the sea breeze characteristics is analysed with SST sensitivity experiments. In the four SST experiments, the SST from the reference run is uniformly modified by ±1 K and ±2 K. The names of the SST experiments compose by the applied SST variation: The simulation with an SST variation by +1 K is called SSTP1 run ('P' stands for 'plus') and the SSTM2 experiment is a simulation with a uniformly decreased SST by −2 K ('M' stands for 'minus'). Details about the simulation setup can be found in Section 4.4.

5.3.1 Temperature and moisture adjustment processes during spinup

A change in the SST impacts the temperature and the moisture content in the atmosphere. Therefore, the adjustment processes of the atmosphere to the uniformly applied SST variation in the SST experiments are investigated. Two areas are defined: the box over the sea extends from −5° to 5°E and from −3° to 3°N. The box over the land covers an area from −5° to 5°E and from 11° to 17°N. The areas are chosen at a large distance from the coast to represent the adjustment processes in areas which are not directly affected by land-sea interactions.

Figure 5.25b shows the time series of the difference in air temperature between the SSTP2 experiment and the reference run. The warmer SSTs ($\Delta T = 2$ K) lead to a warmer marine boundary layer (depth around 500 m to 600 m) and warming in the atmosphere over the ocean up to 2000 m height. The term 'marine boundary layer' is here defined as the atmospheric boundary layer over the ocean. The strongest air temperature change occurs in the marine boundary layer. A higher cap layer above 2000 m impedes a deeper heat transport. A cap layer is defined here as a vertical

level with a higher virtual potential temperature than the levels below, which impedes vertical moisture and energy transport. The adjustment process takes about 12 h over the ocean. In the averaged area over land, the differences between the SSTP2 experiment and the reference run do not exceed ±0.4 K (Figure 5.25a). Moreover, no time-dependency is visible in Figure 5.25a.

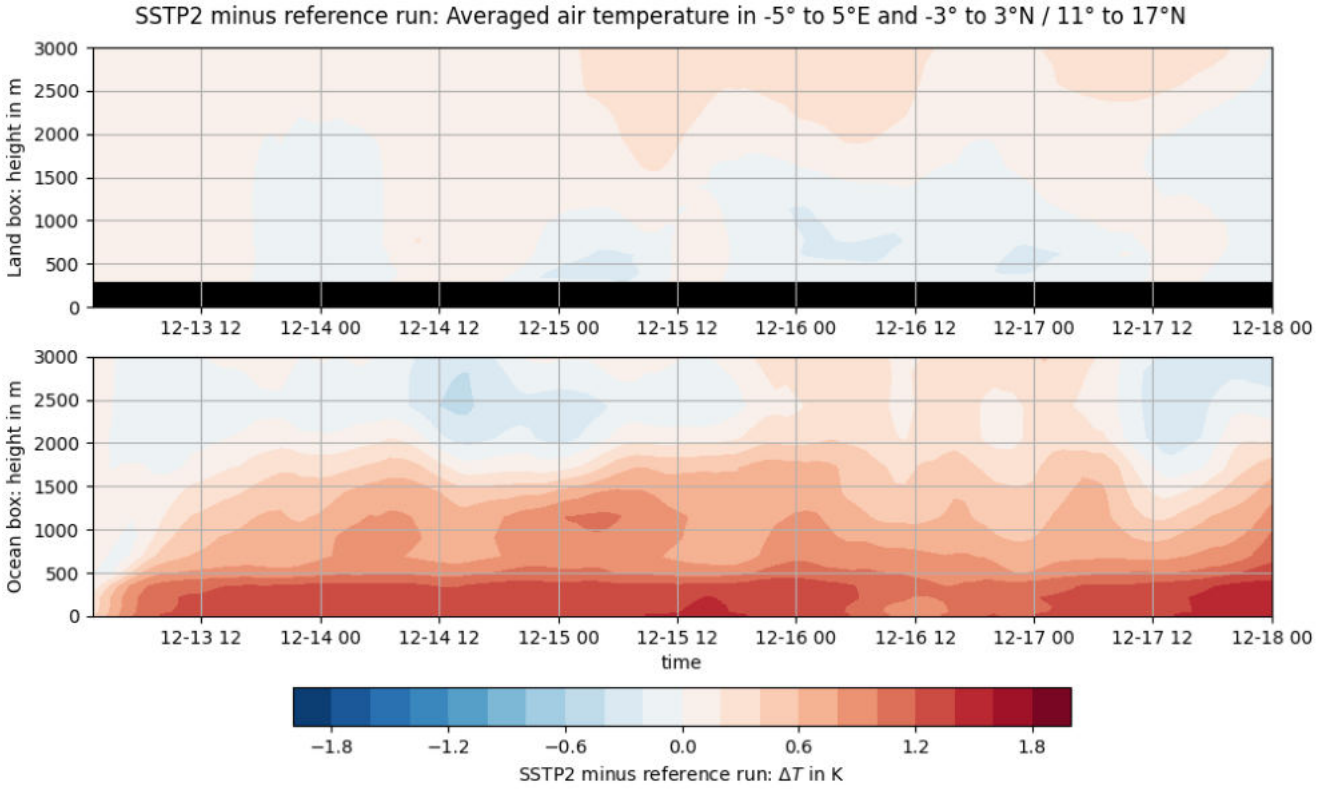

Figure 5.25: *Time series of the averaged air temperature anomaly (SSTP2 minus reference run) in the lowest* 3 km *of the atmosphere over land (upper plot, black area indicates the orographic height) and ocean (lower plot). The box over the sea extends from* $-5°$ *to* $5°E$ *and from* $-3°$ *to* $3°N$*. The box over the land covers an area from* $-5°$ *to* $5°E$ *and from* $11°$ *to* $17°N$*.*

Figure 5.26 shows the time series of the specific humidity difference between the SSTP2 experiment and the reference run. Here, the adjustment processes take between 12 h and 24 h over the ocean (Figure 5.26b). The increased SSTs lead to a higher humidity in the marine boundary layer and the atmosphere above. Highest specific humidity differences can be seen between 400 m and 1000 m and between 2000 m and 2700 m. The lower maximum follows from an increase in the marine boundary layer depth at higher SSTs. Due to the deepening of the well-mixed marine boundary layer, the water vapour concentration in height between the boundary layer top of the reference run and the SST experiments differs between the simulations. The marine atmosphere below 500 m height lies below the boundary layer top in the reference run and the positive SST experiments. The specific humidity in the increased SST experiments differs up to 3 % from the specific humidity in the reference run due to the SST change (not shown). The second maximum in specific humidity lies within a height where the air temperature of the SSTP2 run is similar or slightly decreased (up to −0.6 K) compared to the reference run. An increase in the height of the cap layer top could cause this difference.

Over land, the specific humidity decreases slightly (Figure 5.26a). A possible explanation would be a decreased moisture flux from the ocean to the land. During the first half of the research period, the specific humidity decreases at all heights in the lowest 3000 m of the atmosphere. After mid-day on 15 December 2021, the difference between the SSTP2 experiment and the reference run decreases again.

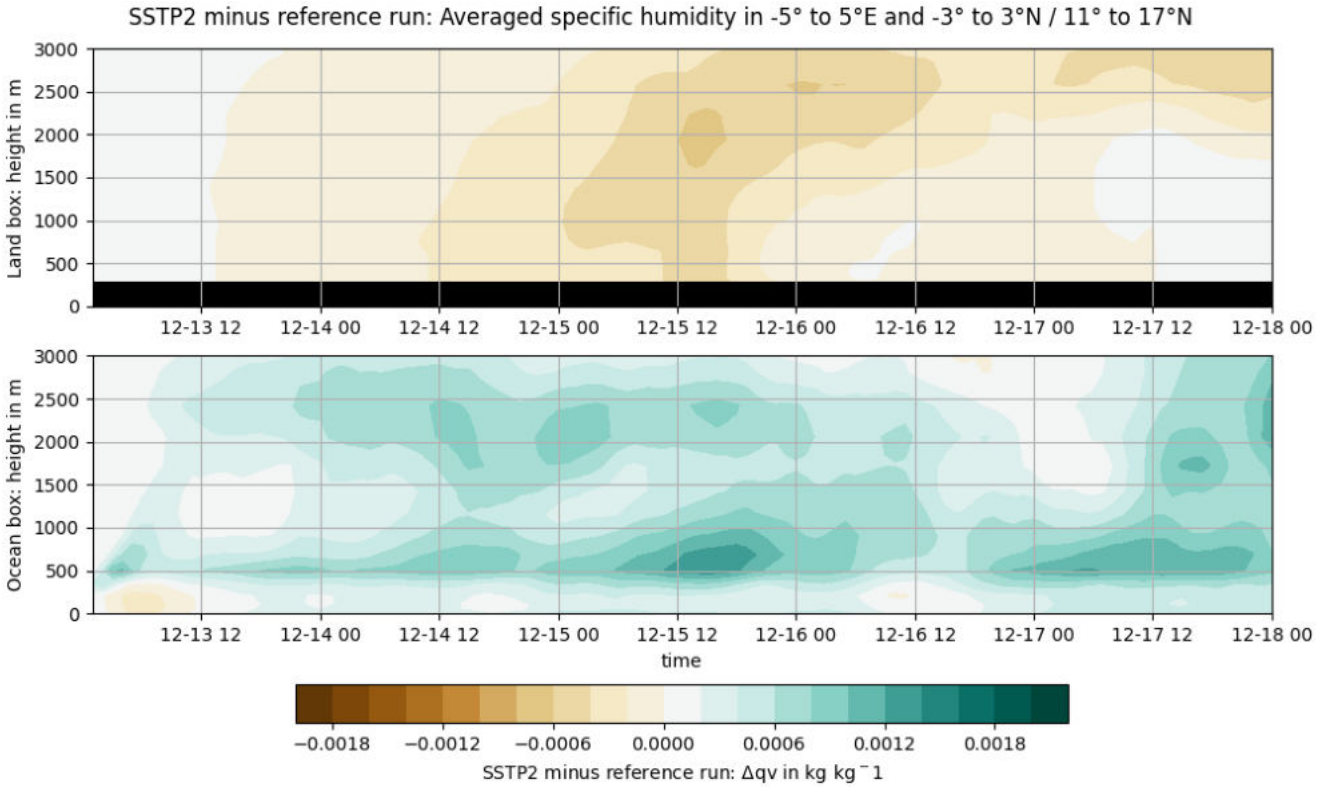

Figure 5.26: *Time series of the averaged specific humidity anomaly (SSTP2 run minus reference run) in the lowest* 3 km *of the atmosphere over land (upper plot, black area indicates the orographic height) and ocean (lower plot). The box over the sea extends from* $-5°$ *to* $5°E$ *and from* $-3°$ *to* $3°N$*. The box over the land covers an area from* $-5°$ *to* $5°E$ *and from* $11°$ *to* $17°N$*.*

The experiments with a decreased SST show the opposite behaviour. Figures 8.6 and 8.7 (in the appendix) show the time series of the averaged air temperature difference and specific humidity difference between the SSTM2 experiment and the reference run. Over the ocean, the temperature of the marine BL decreases during the first 10 h. In the lowest layer, there is a decrease of over -1.6 K in the first 18 h. The air temperature also decreases in the atmosphere below the marine cap layer. The positive temperature difference above shows the lowering of the height of the cap layer due to the SST decrease. In the box over land, the air temperature stays nearly constant during the simulation period. The air temperature adjustment processes in the lowest 300 m take one and a half days.

The averaged specific humidity shows a decrease over the ocean in the SSTM2 and the SSTM1 experiments compared to the reference run. The atmosphere over the ocean cools and less mois-

ture is evaporated at the ocean surface. Therefore, less moisture is transported into the higher atmosphere. Moreover, due to the decreased air temperatures, the air can hold less water vapour and condensation sets in. Another effect is the shift in height in the boundary and cap layer. Over land, the specific humidity increases slightly. A higher specific humidity is visible on the third day of the simulation. The humidity adjustment processes take about one day in the SSTM2 experiment.

The data for the SSTP1 and SSTM1 cases show a similar behaviour to the SSTP2 and the SSTM2 cases and are therefore not shown here. Overall, a spinup period can be defined from 13 December 2021 at 0 UTC to 14 December 2021 at 10 UTC for the experiments with decreased SST. For the experiments with increased SSTs, a spinup of 24 h is sufficient.

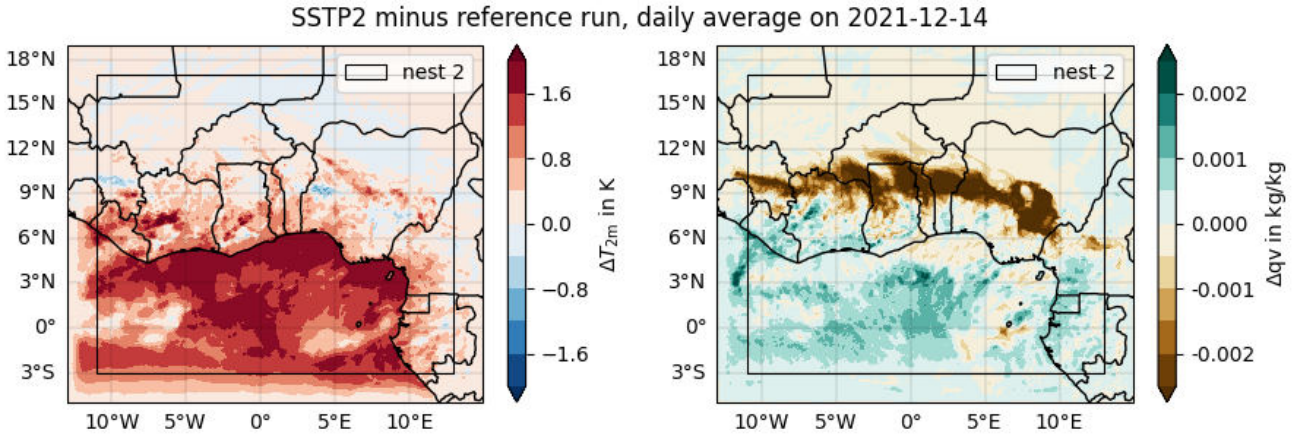

Figure 5.27: *Differences between the SSTP2 experiment and the reference run in the air temperature and the specific humidity at* 2 m *height on 14 December 2021.*

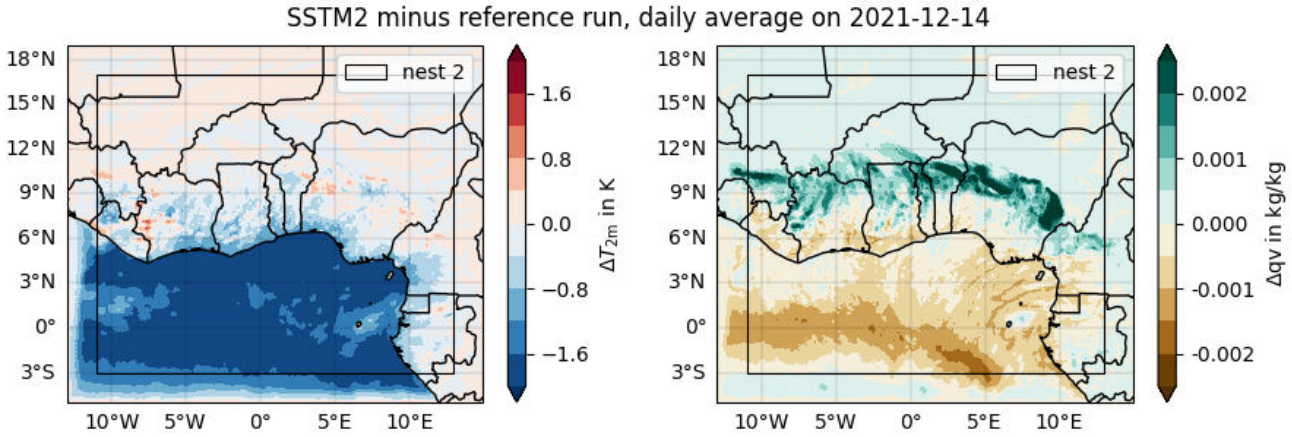

Figure 5.28: *Differences between the SSTM2 experiment and the reference run in the air temperature and the specific humidity at* 2 m *height on 14 December 2021.*

Figure 5.27 shows the difference in the daily averaged 2 m air temperature and specific humidity between the SSTP2 experiment and the reference run. The second day is representative of the following three days after the spinup period (see Chapter 4.4.2). The air temperature differences are strongest over the ocean and in near-coastal areas since only the weighted surface tempera-

ture for all ocean grid points is changed. At the southern and western boundary over the tropical Atlantic, a strong air temperature gradient emerges. The south-westerly monsoon flow transports colder air from the boundaries into the research area. When transported over the warmer ocean ocean in the SSTP2 experiment, the air warms and reaches a quasi-equilibrium state with the surface. This adjustment process takes time. Hence the distance to the boundary depends on the mass transport: The eastward wind component at the western boundary is smaller than the northward wind component at the southern boundary. Therefore the 2 m temperature reaches quasi-equilibrium with the ocean surface 2° east of the western boundary but 3° north of the southern boundary.

The difference in the daily averaged specific humidity at 2 m height between the SSTP2 experiment and the reference run shows a similar area over the ocean affected by the boundary conditions: The western boundary of the influence zone extends 2° east of the western boundary of the first nest. The southern boundary reaches even further northwards: The impact area of the boundary data reaches 5° north of the southern boundary. The strong signal over the land is analysed and explained in Chapter 5.3.2.

The boundary effect influence from the SST experiments with lower SST resembles the characteristics described above (compare Figure 5.28 for the difference in the daily averaged 2 m air temperature and specific humidity between the SSTM2 experiment and the reference run). The SSTP1 and SSTM1 experiments behave analogously (not shown).

The location of the second nest is chosen within or at the boundary to the area, where the lower atmosphere in the SST experiments is already adjusted to the ocean surface (black rectangle in Figure 5.27 and 5.28). Comparing the SSTP2 and the SSTM2 experiment on the second nest to the reference run, the boundary effects are negligible small (Figure 8.2 and 8.3 in the appendix).

5.3.2 Impact of the SST change on the atmospheric large-scale circulation

The change in the sea surface temperature (SST) affects the large-scale circulation. Figure 5.29 shows the difference between the meridional wind in the SST experiments and the reference run. It depicts the zonal mean from −7.5° to 5°E averaged over the period from 14 December to 17 December 2021 (thus after 1 day for spinup). The wind vectors show the averaged meridional and vertical wind velocity (factor 100 in the vertical wind component) for the experiment to visualise the large-scale circulation. The following analysis focuses on the differences in the near-surface winds between the simulations.

The location, where the surface winds meet over land (ITD) shifts between the experiments. The lower the SSTs the further the ITD moves inland: In Figure 5.29b, the SSTs are increased by 2 K with respect to the reference run. The blue vertical line indicates the average position of the shoreline dividing the atmosphere over the land to the right from the atmosphere over the ocean to the left. The surface wind vectors show the near-surface monsoon winds over the ocean. The monsoon flow crosses the shoreline (blue vertical line) and extends inland until it converges with the Harmattan flow (wind vectors pointing towards the shoreline in the lower right corner of the figure). In Figure 5.29b the winds converge between 7° and 9°N. Comparing this behaviour to the SST experiment with −2 K decreased SSTs compared to the reference run, the zone where

the monsoon flow and the Harmattan winds meet is located between 9° and 11°N (Figure 5.29d). Figure 5.29a and 5.29c present the differences between the SSTP1 and the SSTM1 experiment and the reference run. In both figures, the convergence zone of the monsoon flow and the Harmattan wind is located between the location found for the SSTP2 and the SSTM2 case.

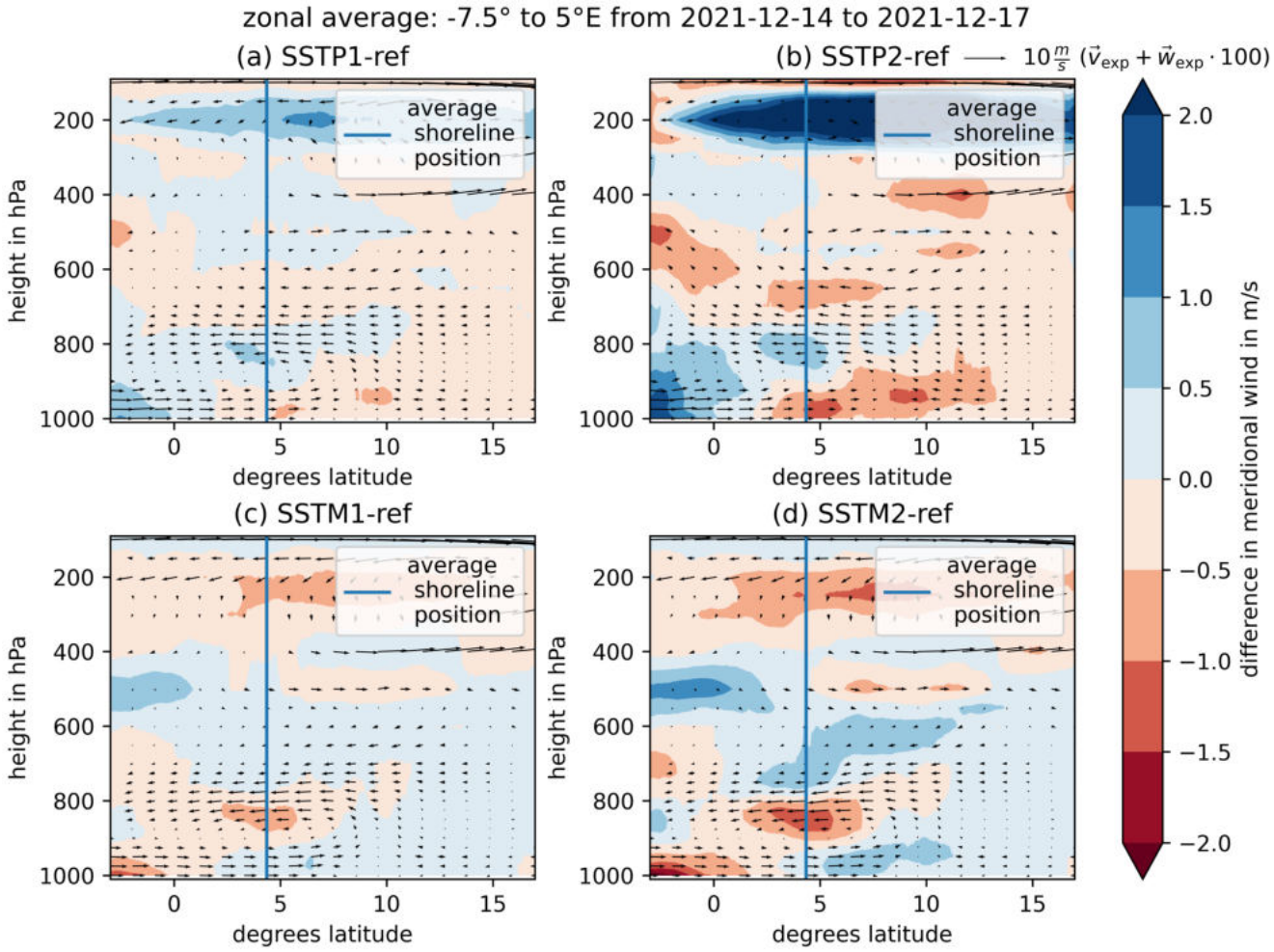

Figure 5.29: *Comparison of the meridional wind velocity of the SST experiments to the reference run. The graphic compares the mean meridional wind component from a zonal mean between −7.5° and 5° E averaged from 14 to 17 December 2021. Blue shading indicates increased onshore winds and red shading increased offshore wind velocity in the SST experiment.*

The time evolution of the location of the ITD during the simulation time for the zonal mean from −7.5° to 5°E is shown in Figure 5.30. The black line shows the ITD position in the reference run calculated from the 2 m 14 °C isodrosotherm. The orange and red line show the ITD position in the experiments with 1 K and 2 K increased SST and the blue and deep blue line show the same for the SST experiments with −1 K and −2 K decreased SST. After the defined spinup time of 34 h (grey dashed line), Figure 5.30 supports this finding: The higher the SSTs, the closer the ITD shifts towards the shoreline.

The Harmattan winds over the land are stronger in the SST experiments with higher SSTs (red

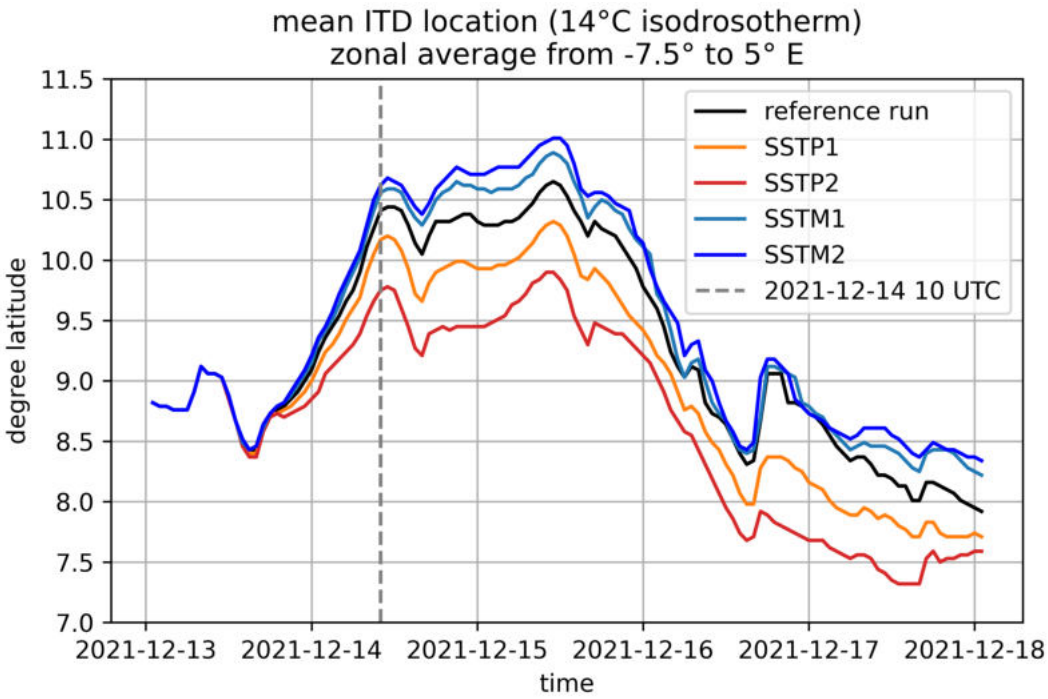

Figure 5.30: *Comparison of the ITD position of the SST experiments to the reference run in the zonal mean between* $-7.5°$ *and* $5°E$*. The ITD position is calculated from the* 14 °C *isodrosotherm in* 2 m *height. The dashed grey line marks the end of the spinup period.*

shading indicating stronger northerly near-surface flow north of 10°N in the experiments SSTP1 and SSTP2 in Figure 5.29a and 5.29b). The near-coastal monsoon winds (±3° north and south of the blue indicated shoreline) are weaker in higher SST experiments (red shading in the near-surface area 3° north and south of the shoreline). This is a reasonable result: The monsoon winds are driven by the temperature and humidity gradient between the tropical Atlantic Ocean and North Africa. An increased SST in the experiments decreases this temperature difference and thus leads to a weaker monsoon flow.

The opposite behaviour in the shallow monsoon flow in the southern end of the cross-sections in Figure 5.29a to d can result from boundary effects: the SST is only modified in the research area whereas the air temperature is not changed. Due to nudging at the boundaries, an incoming air parcel at the southern boundary of the simulation area is not in equilibrium with the modified ocean surface temperature. The modified increased or decreased SSTs within the simulation area introduce a temperature gradient at the boundary, accelerating the monsoon flow towards the higher SSTs. This boundary effect occurs in all simulations only south of 3°N. The research area of the land–sea breeze (LSB) extends 3.5° from the shoreline along a perpendicular transect to the coast. The case study area in West Nigeria has a coastline north of 6°N and is thus not affected by boundary effects. In the regions with a more southerly shoreline, only the southernmost part of the ocean of the transect can be affected. Hence the sea breeze (SB) develops at the shoreline and moves inland, this development takes place in winds adjusted to the modified SSTs.

The SB signal is also embedded in the time mean of the cross-sections in Figure 5.29. Interestingly, the shallow overturning circulation increases its velocity in the vicinity of the shoreline in

the SSTM2 case in Figure 5.29d (darker red shading between 900 hPa and 800 hPa across the blue vertical line indicating the shoreline). The location indicates an increased return flow from an increased sea breeze circulation (SBC). The increased surface onshore winds can correspond to an increased SB, an increased monsoon flow or both.

The shallow overturning flow is also locally increased in the vicinity of the shoreline in the SSTM1 experiment but not as strongly as in the SSTM2 run. In the experiments with the increased SSTs, the shallow overturning flow is locally weakened and also appears 25 hPa higher (see darker blue shading in the vicinity of the shoreline around 800 hPa in figure 5.29a and 5.29b).

Overall, the differences in the mean meridional wind speed are below $2\,\mathrm{m\,s^{-1}}$ except for the strongly increased meridional winds above 300 hPa. The difference in the averaged zonal wind speed between the SST experiments and the reference run is also small (Figure 8.13 in the appendix). Two distinct differences can be seen in the zonal wind: First, the easterly wind velocity increases between 600 hPa and 500 hPa over the ocean in the SST experiments with decreased SSTs and decrease for the runs with increased SST. This can be related to the African Easterly Jet (AEJ), which forms due to the temperature and moisture contrast between the tropical Atlantic Ocean and the dry Saharan Desert. Increased SSTs strengthen the AEJ.

Figure 5.31 shows the differences in specific humidity between each of the SST experiments and the reference run. Both experiments with increased SSTs show similar behaviour (Figure 5.31a and 5.31b): The specific humidity is stronger increased in the lowest 100 hPa over the ocean than in the atmosphere above. This can result from the increased moisture flux from the warmer ocean surface into the atmosphere and from the vertical extension of the warmed atmosphere. When the atmosphere extends, it transports moisture to former dryer layers. Over the land, the atmosphere is drier in the experiments with higher SSTs. Except for the vicinity of the shoreline, here, the monsoon winds bring in moister air than in the reference run. The shallow overturning circulation takes drier air out towards the ocean between 900 hPa and 700 hPa. A very clear signal appears between 7° and 12°N: Here, the atmosphere shows an increased dryness in experiments with increased SSTs. This signal is also visible in the specific humidity maps (Figure 8.13) in section 5.3.1. The SST experiments with decreased SST show a moist anomaly in the same location. The anomaly region changes its location between the experiments: Its centre is closer to the shoreline in the SSTP2 run compared to the SSTM2 experiment (compare Figure 5.31b and 5.31d). The moisture anomaly can have several reasons, for example, increased or decreased moisture advection by the increased or weakened monsoon and Harmattan winds. However, a very clear correlation can be found between the location of this anomaly and the ITD location. The location of the ITD in the SSTP2 experiment is always closer to the shoreline after the spinup period compared to the reference run (Figure 5.30). This leads to a strongly decreased specific humidity in the latitudes between the positions of the ITD in the SSTP2 run and the reference run. The ITD location can be found in a northernmost position exceeding 10.5°N in the reference run and a southernmost position below 7.5°N in the SSTP2 experiment. In the height-latitude cross-sections shown in Figure 5.31, the clear specific humidity anomaly occurs between these latitudes (7.5° and 10.5°N). The two minima in the moisture anomaly occurring around 7.5° and 9.5°N (dark brown shading close to the surface in the anomaly) can also be explained with the ITD location: The ITD location stays almost constant from 14 December 6 UTC to 16 December 0 UTC and from 16 December 12 UTC until the end of the simulation period. The time-mean of

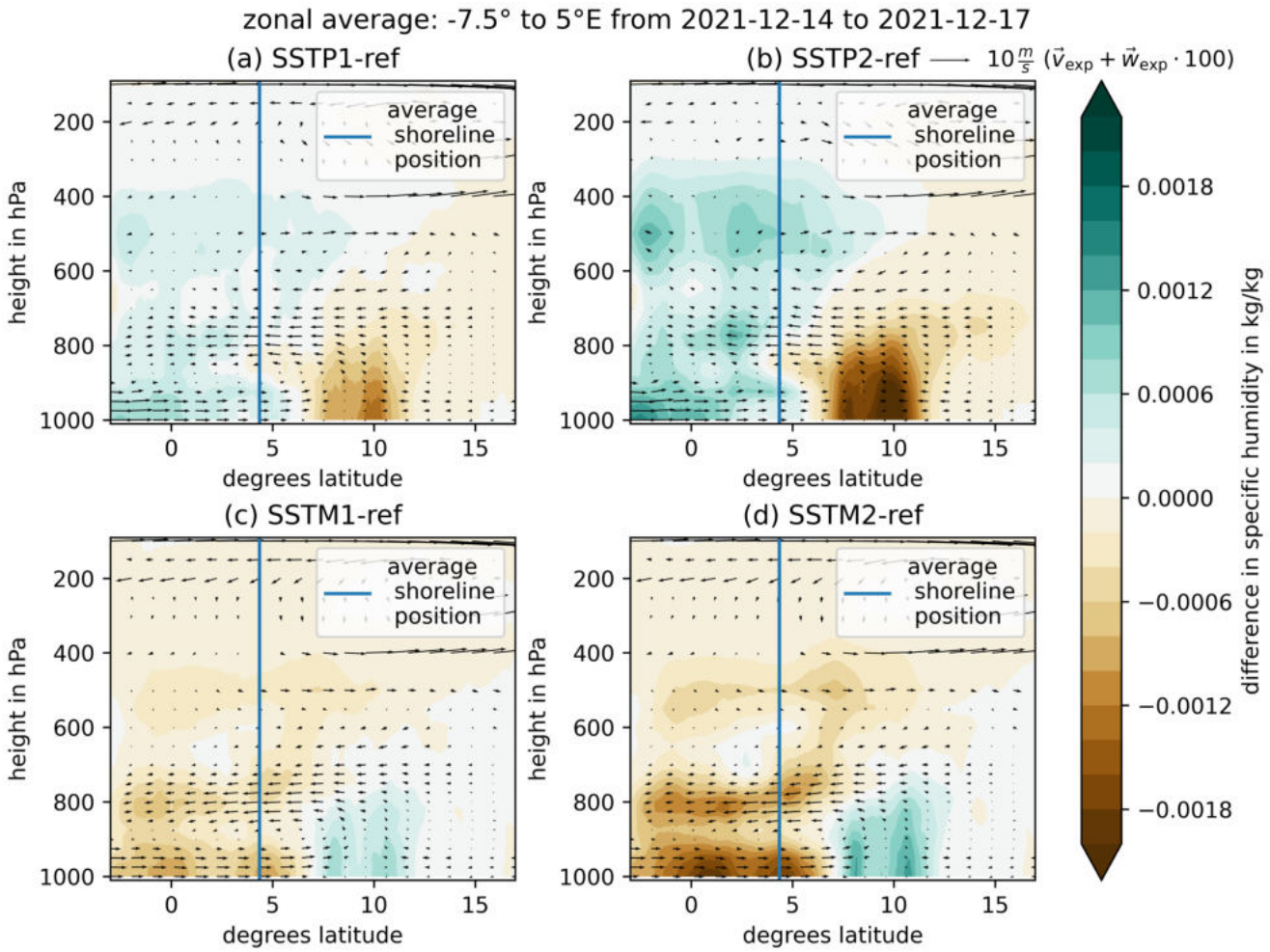

Figure 5.31: *Comparison of the specific humidity of the SST experiments and the reference run. The graphic compares the mean specific humidity from a zonal mean between 7.5° and 5°E averaged from 14 to 17 December 2021. Yellow shading indicates decreased specific humidity in the SST experiment compared to the reference run.*

latitude-height cross-sections of the specific humidity depicted in Figure 5.31 shows thus a large difference in moisture in the latitudes between the ITD position in the reference run and SSTP2 in this first period and this second period. The small northern shift in Figure 5.31a, c and d for the SST experiments SSTP1, SSTM1 and SSTM2 follows from the displacement of the ITD to the reference run in these experiments.

In summary, the change in the SSTs does affect the large-scale circulation: on average, the near-surface monsoon flow weakens, the Harmattan flow strengthens and the moisture is transported less far inland due to a shoreward, thus southward, shift of the ITD when the SSTs are increased in the experiments. The opposite behaviour is observed in this zonal mean for decreased SSTs.

5.3.3 Case study in West Nigeria: Hovmöller diagrams in the SST experiments

Figures 5.32 to 5.35 show Hovmöller diagrams of mean along-transect winds averaged in the area from 3.5° to 3.9°E (West Nigeria) for the SST experiments. The comparison shows again, that the ITD-position is shifted closer to the shoreline for increased SSTs (compared to the previous section). The along-transect wind speeds in the sea breeze (SB) show higher values in the experiments with decreased SSTs (compare the green shading between the shoreline (blue horizontal line) and the sea breeze front (SBF)). The difference in the velocities is analysed in detail in Chapter 5.3.6.

Another strong difference can be seen in the Land Breeze (LB) development on 16 and 17 December 2021. The LB is visible from 0 UTC until the late morning in the SSTP1 and SSTP2 experiments. Compared to the SSTM1 and SSTM2 runs the LB formation is strongly increased.

Differences can also be seen in the inland penetration distance (compare the position of the black markers in the four figures): In West Nigeria, the SB moves further inland in the experiments with lower SSTs. This is analysed in detail in Chapter 5.3.4.

5.3.4 Influence of the SST on the inland penetration distance

Figure 5.36 compares the mean inland penetration distance of the sea breeze circulation (SBC) along the perpendicular transects averaged between 3.5° and 3.9°E (West Nigeria) in the reference run and the SST experiments. Subfigures 5.36a to e show day one to day five of the research period.

A general trend is present in all five days of the simulation period: experiments with lower SSTs (blue lines) show a greater inland penetration distance than the runs with higher SSTs (red lines). The deeper inland penetration distance for simulations with lower SSTs can have many reasons. Possible hypotheses are:

1. A higher atmospheric land–sea temperature gradient results in faster inland penetration propagation of the Sea Breeze Front (SBF). Thus, a decrease in SSTs causes a deeper inland penetration distance.

2. Figures 5.29a and b show that, on average, higher SSTs weaken the shallow monsoon winds, whereas the monsoon winds are increased for lower SSTs. Assuming that the embedding flow supports the inland penetration distance, the weaker monsoon winds in the increased SST experiments could lead to a slower inland penetration distance.

3. The SST controls the onset time of the sea breeze circulation (SBC). The atmospheric temperature gradient from the ocean to the land initialised the SBC. For higher SSTs, the atmospheric temperature over the land exceeds the near-surface atmosphere temperature over the ocean at a later time of the day compared to the reference run. A later onset time results in a time-shifted inland movement of the SBF between the experiments.

Table 6 shows the onset times of the SBC in the reference run and the SST experiments in the case study area in West Nigeria (3.5° to 3.9°E). For most of the days and experiments, the onset

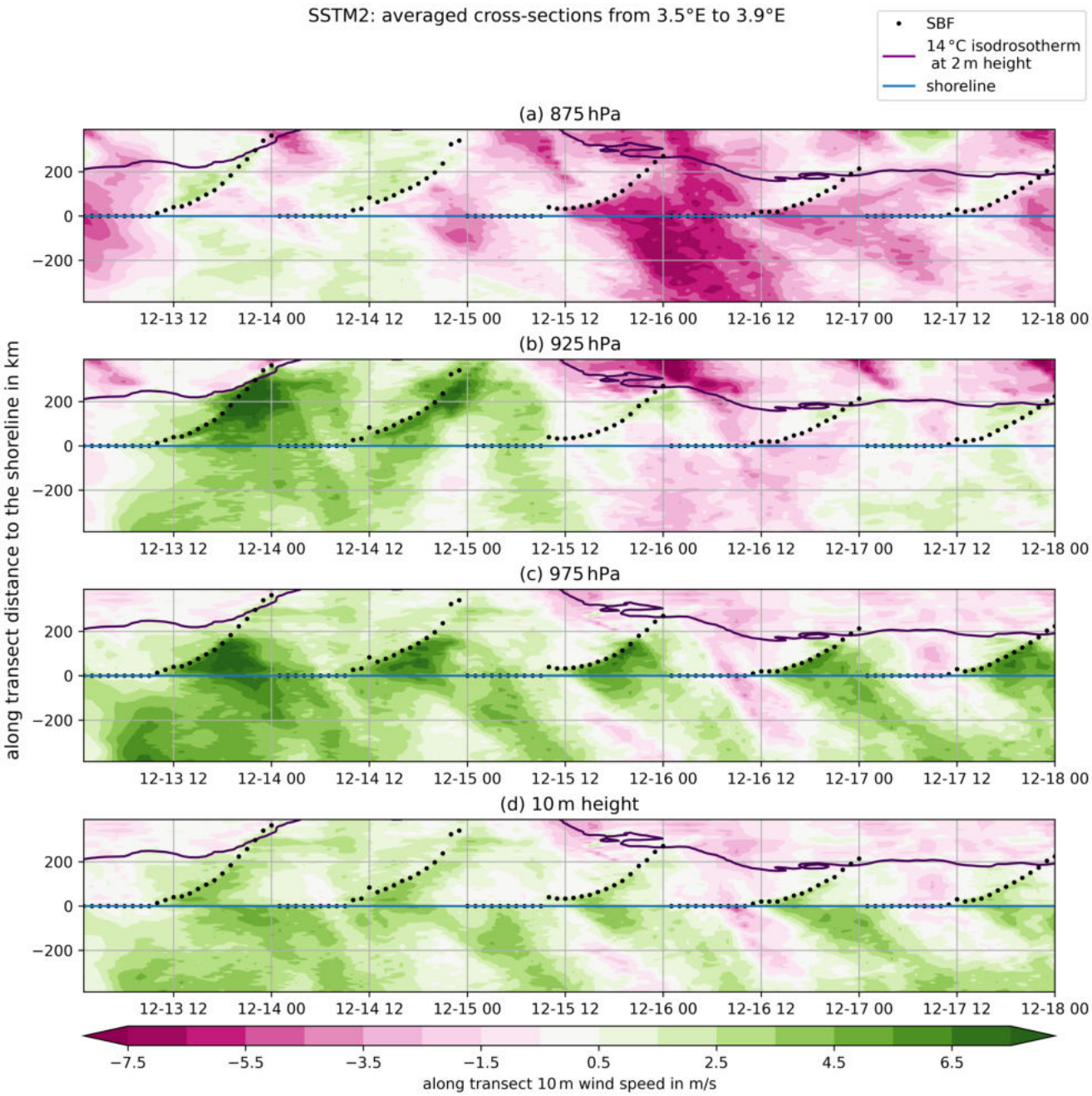

Figure 5.32: *Same as Hovmoeller diagram in Figure 5.20 but for the SSTM2 experiment.*

time is postponed to later daytimes for higher SSTs, supporting hypothesis 3.

On the first day of the simulation period, the SBF in the reference run and the SST experiments have almost the same inland propagation speed (Figure 5.36a). During the day, the spread of the graphs increases slightly, meaning a slightly higher inland propagation velocity in the SSTM2 experiment (dark blue curve) than the SSTP2 experiment (red curve). This difference in the inland propagation velocity of the SBF could result from a stronger atmospheric temperature gradient between the land and the ocean.

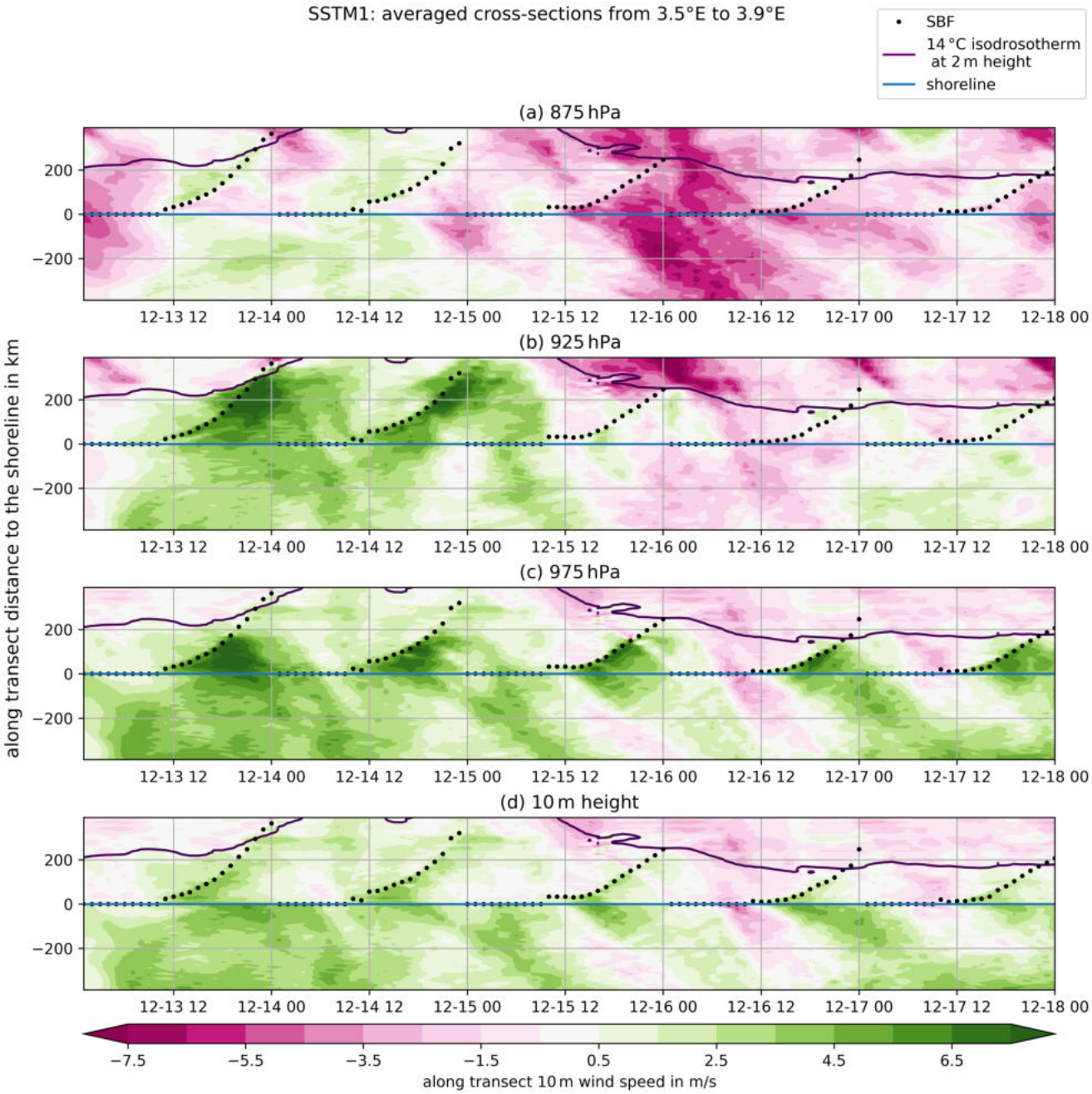

Figure 5.33: *Same as Hovmoeller diagram in Figure 5.20 but for the SSTM1 experiment.*

On the second day of the research period, 14 December 2021, the simulations behave similarly to the first day until 15 to 16 UTC (compare Figure 5.36a and 5.36b). Whereas the inland penetration distance of the SSTM1 and SSTM2 experiment increases constantly until 19 UTC, the inland penetration distance of the reference run and the SSTP1 and SSTP2 experiment increases suddenly at 16 UTC. This difference results from the formation of density currents related to the formation of cold pools at the SBF (not shown). The rate of propagation of the cold pool density currents is higher than the inland propagation speed of the SB (on the surface wind maps in Figure 5.18a, b and c the typical circular outflow of cold pools is visible between 6.5° and 7°N and 2.5° and 3°E. Identifying the SBF with the wind reversal in 10 m height, it is clearly visible,

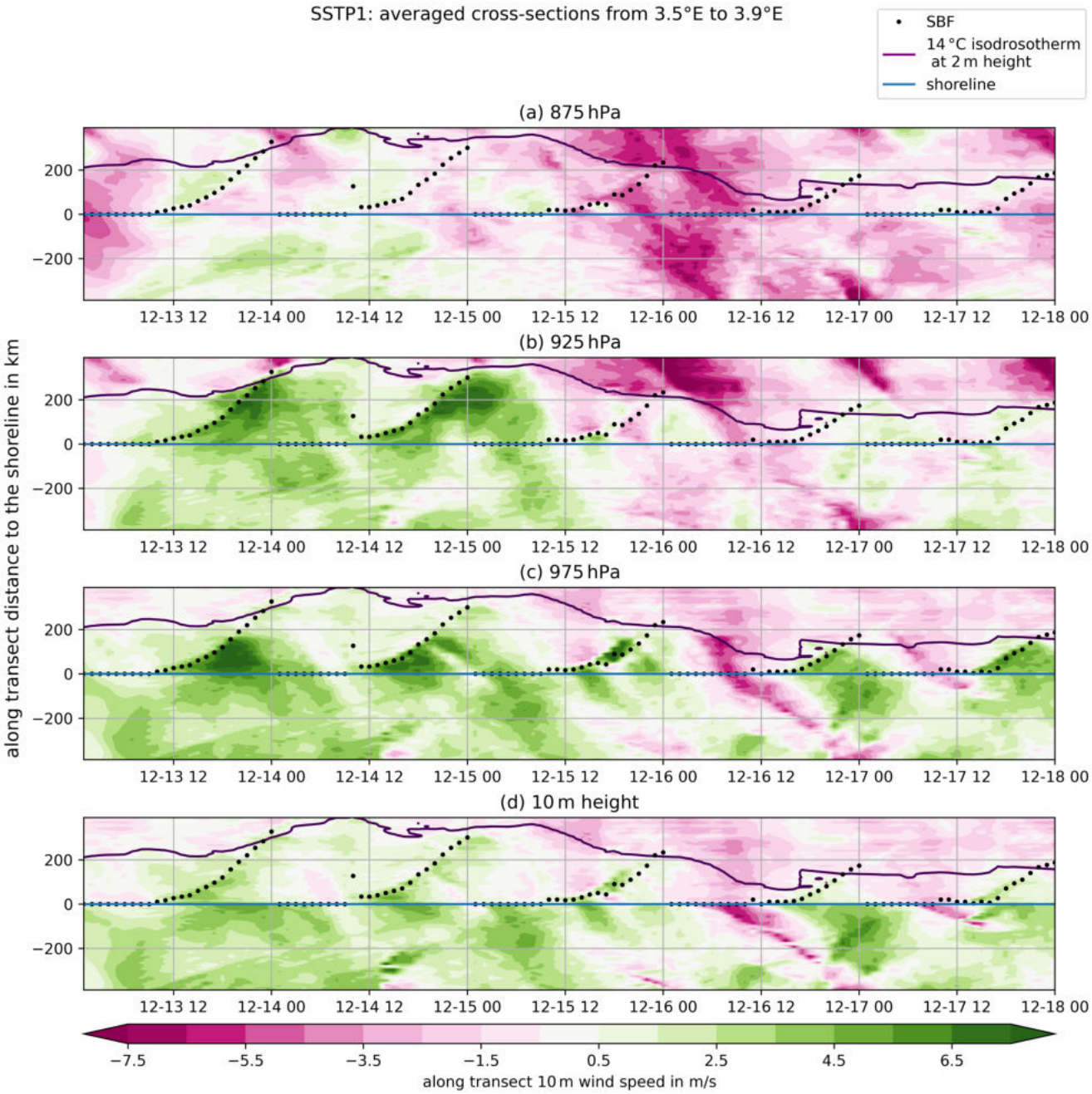

Figure 5.34: *Same as Hovmoeller diagram in Figure 5.20 but for the SSTP1 experiment.*

that the SBF (for example at 2.1° East) moves slower inland than these cold pools). Whenever both structures merge, the front of the combined cold pool and sea breeze propagates fast inland.

On 15 December 2021, the inland penetration distance between 16 and 21 UTC again shows a very different behaviour to the SST experiments on 13 December (compare Figure 5.36a to Figure 5.36c). In the SSTM2 experiment, the SB forms in a weak embedding southerly flow. In the SSTM1 experiment, the embedding wind field shows on average a weak northerly component (below $3\,\mathrm{m\,s^{-1}}$). In the reference run, the SSTP1- and the SSTP2-experiment, the SB develops in a stronger opposing northerly flow. Here, cold pools develop at the SBF. In all three cases, the

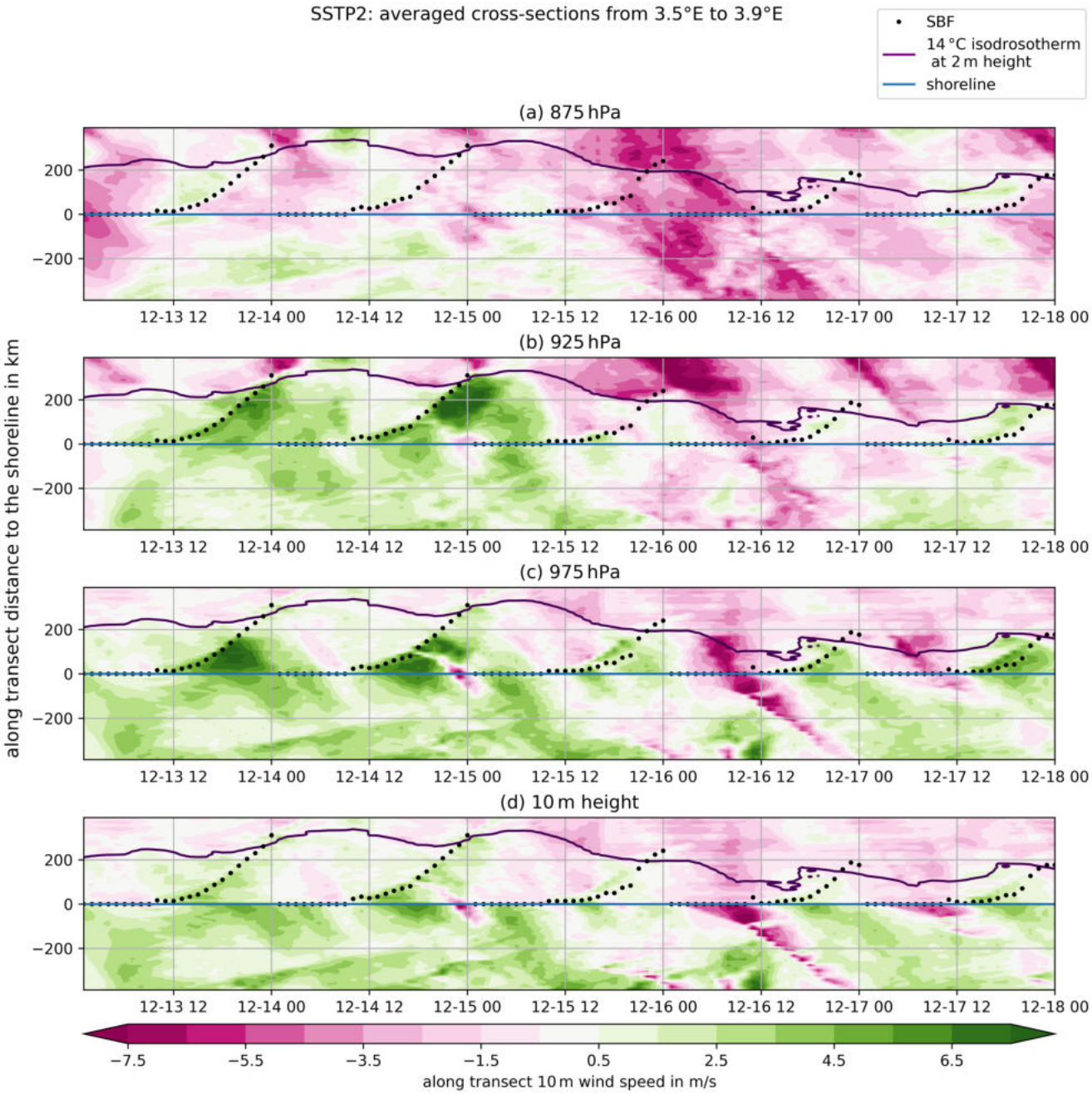

Figure 5.35: *Same as Hovmoeller diagram in Figure 5.20 but for the SSTP2 experiment.*

SBF detection algorithm first detects the boundary between the SB and the outflow of the cold pool towards the shoreline as the SBF (see sketch in Figure 5.37a: the SBF is marked as a vertical black line). Later in the evening, the wind speed of the cold pool density currents decreases. The cold pool outflow opposing the SB reduces to an area with decreased onshore velocities within the SB (compare the shoreward outflow of the cold pool in the Schematic 5.37: (a) after formation the outflow is strong and causes an offshore wind opposing the SB (pink shading near the surface). With time, the intensity of the cold pool outflow density current decreases, leaving an area with weak onshore winds (bright green shading) in (b)). The SBF detecting algorithm finds now the front of the onshore density current at the front of the cold pool (see Schematic 5.37b: the SBF

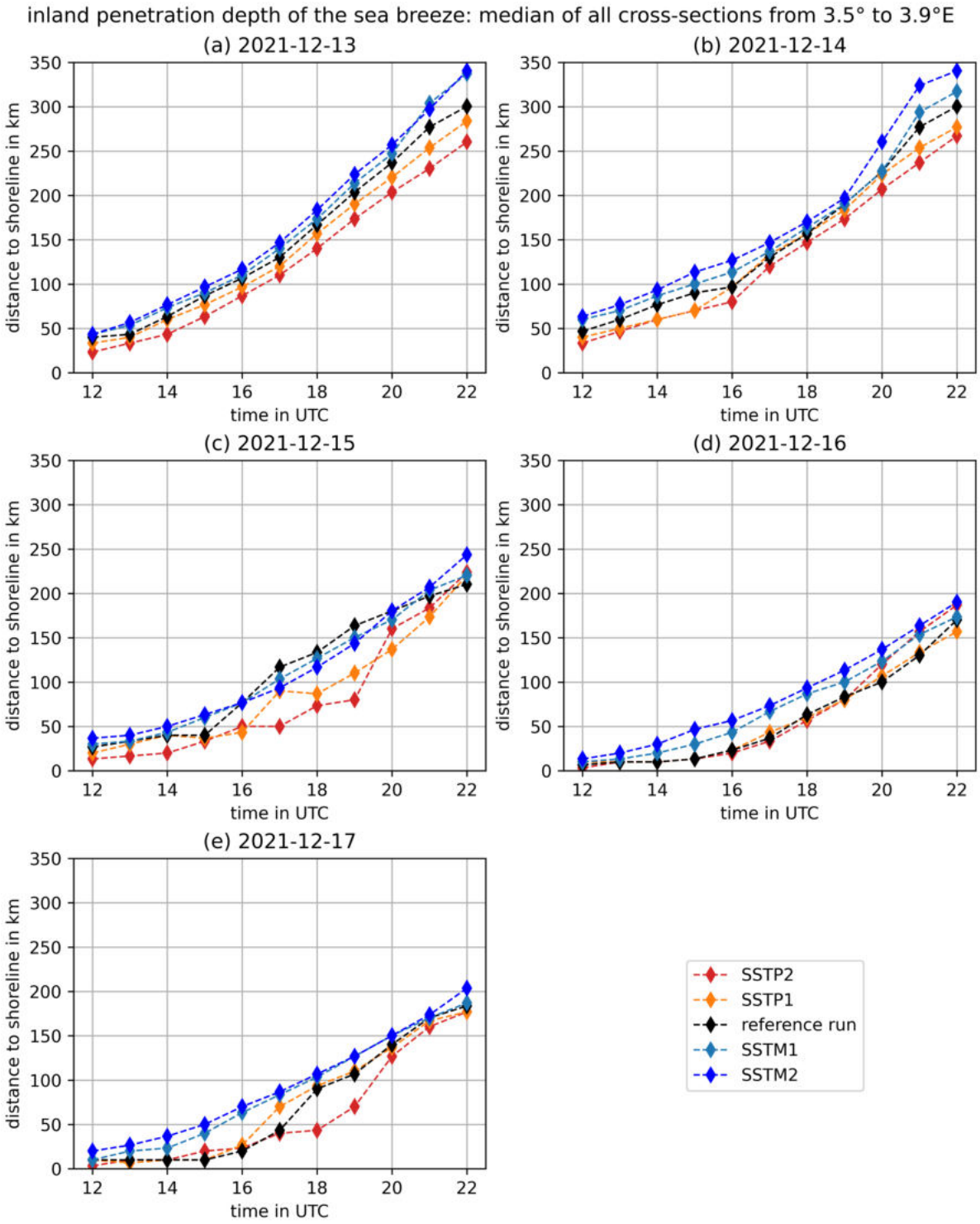

Figure 5.36: *Median inland penetration distance of the SBF between 3.5–3.9°E (West Nigeria) for each day of the case study and for the reference run and the different SST experiments.*

is marked at the northernmost front of the combined density current).

In the evening of 16 December, the inland penetration distance for all runs is shorter compared to

	13 Dec 2021	14 Dec 2021	15 Dec 2021	16 Dec 2021	17 Dec 2021
SSTP2	11 to 12 UTC	11 UTC	11 UTC	13 to 14 UTC	12 to 14 UTC
SSTP1	11 UTC	10 UTC	10 UTC	13 UTC	12 to 13 UTC
reference run	10 to 11 UTC	10 UTC	10 to 11 UTC	11 to 12 UTC	13 to 14 UTC
SSTM1	10 to 11 UTC	10 UTC	10 to 11 UTC	11 to 12 UTC	11 to 12 UTC
SSTM2	9 to 10 UTC	9 to 10 UTC	10 to 11 UTC	10 to 11 UTC	10 to 11 UTC

Table 6: *Onset time of the SBC in the case study in West Nigeria (3.5° to 3.9°E). The onset time corresponds with the onset of an (increased) onshore wind in the vicinity of the coastline in addition to the formation of a density current (visible in the virtual potential temperature profile).*

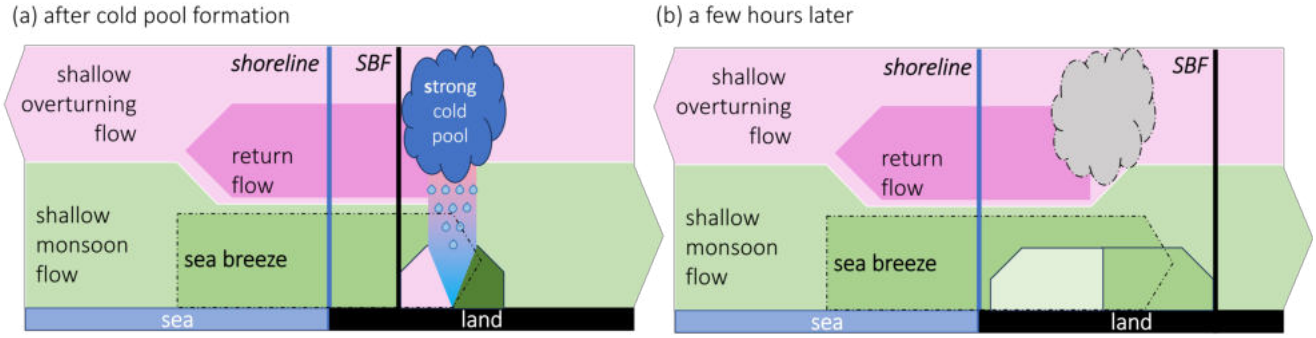

Figure 5.37: *SBF tracking algorithm: when strong cold pools develop at the SBF.*

the previous days: in Figure 5.36d the inland penetration distance lies above 150 and below 200 km distance to the shoreline whereas the inland penetration distance exceeds 250 km for all the simulations at 22 UTC on the first two days (Figure 5.36a and b). In all runs, the SBC develops in an opposing northerly flow which reaches far offshore. While the SBC is limited to the shoreline until 16 UTC in the reference run and the increased SST experiment, the SB extends earlier inland in the runs with decreased SSTs. Comparing the cross-sections of the simulations at 12 UTC, there is no horizontal cross-shore gradient in virtual potential temperature in the reference run and the increased SST experiments, whereas, in the SSTM1 and SSTM2 run a gradient can be observed (not shown). This again supports the theory, that the onset time of the SBC is related to the SST.

The collective behaviour of the median of the inland penetration distance for all the cross-sections along the coastline from the Ivory Coast to West Nigeria resembles the behaviour described in the case study in West Nigeria (compare Figure 5.36 to 5.38): to almost all times except after 16 UTC on 15 December 2021 (Figure 5.38c), the inland penetration distance of the SB in the experiments with lower SSTs exceed the one in the experiments with higher SSTs. In the afternoon of 15 December 2021, the inland penetration distance jumps in the reference run and the experiments with increased SSTs analogous to the case study in West Nigeria.

Figure 5.39 shows maps of the meridional wind in 10 m height at 14 UTC and 19 UTC to shed light on the anomalous behaviour of the inland penetration distance in the afternoon and evening on 15 December 2021 (Figure 5.38c). The inland penetration distance in the SSTM1 case shows at 19 UTC a homogeneous distance to the shoreline along the whole coastline (compare the position of the SBF (purple marker) with the position of the coastline (black line) in Figure 5.39f). In the

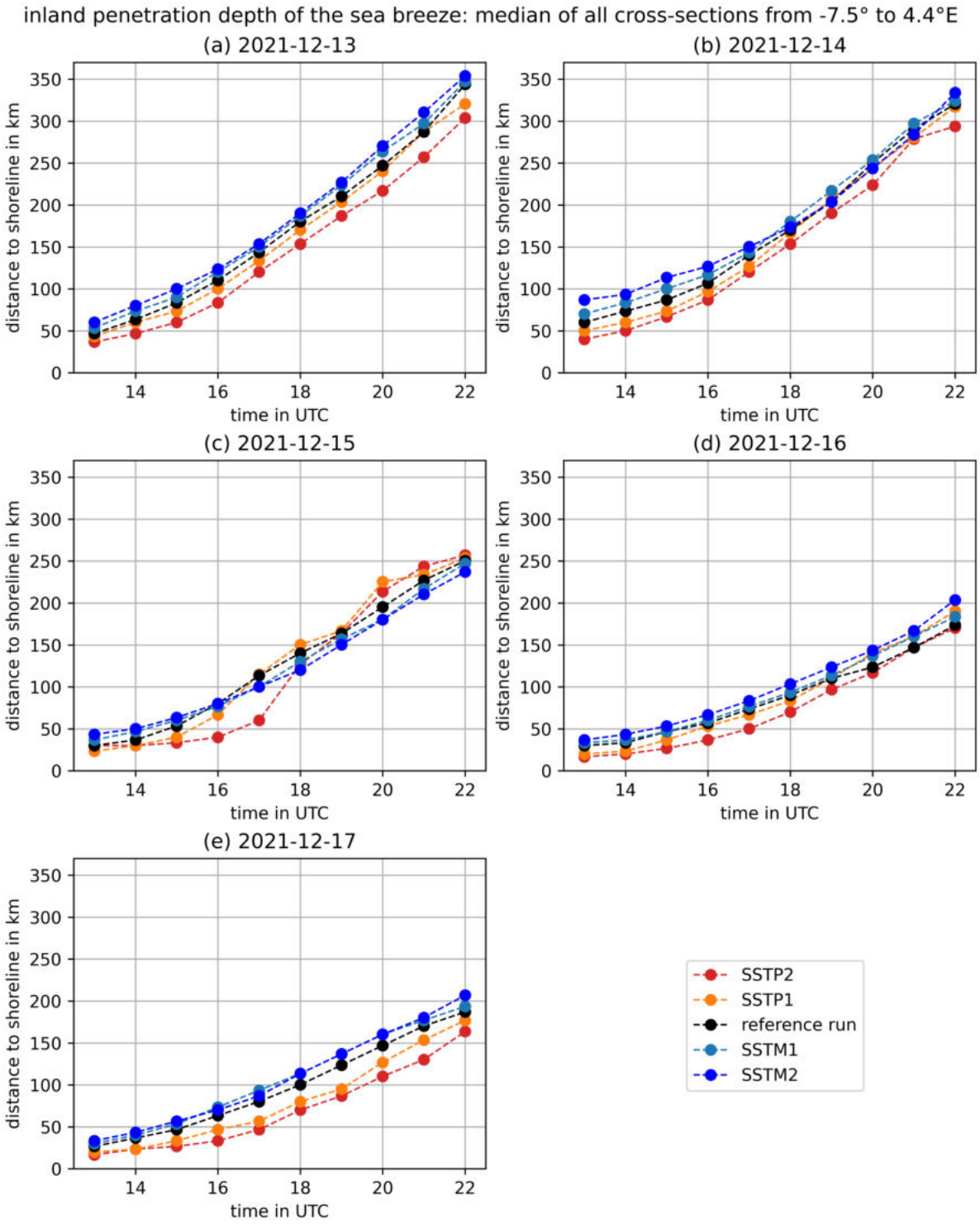

Figure 5.38: *Median inland penetration distance of the SBF between −7.5° and4.4°E (Ivory Coast to West Nigeria) for each day of the case study and for the reference run and the different SST experiments.*

reference run and the SSTP1 experiment, the distance of the SBF to the shoreline shows a higher variability at 19 UTC (Figure 5.39b and d). North of the Ivorian Gulf, in the SSTP1 run, the

distance of the SBF is in particular further inland compared to the reference run and the SSTM1 run at 19 UTC (compare 5.39b, d and f). A similar behaviour can be found in the Bight of Benin. This can be related to cold pools, which already form at 14 UTC in these regions at the SBF in the SSTP1 experiment and the reference run. At 14 UTC, the inland penetration distance is still higher for the experiments with decreased SSTs. But in the evening, the merged structures of the SB and the cold pool propagate faster inland than the SBF. Therefore on can find the deepest inland penetration distance in regions with the highest frontal cold pool activity: this appears in the Ivorian Gulf and the Bight of Benin in the runs with increased SSTs.

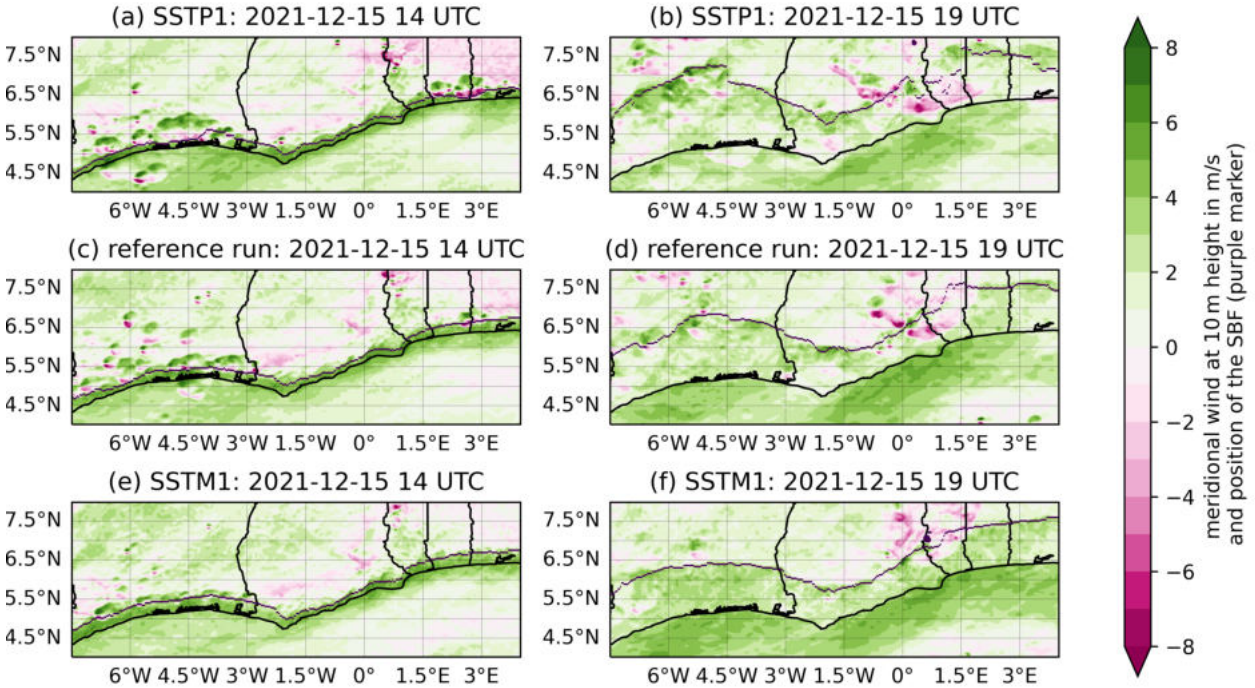

Figure 5.39: 10 m *meridional winds at 14 and 19 UTC (columns) on 15 December 2021 for the SSTP1-, the reference and the SSTM1-run (rows). The maps show the Guinea Coast and the adjacent Atlantic Ocean from Ivory Coast to West Nigeria.*

The median of the inland penetration depth of the cross-sections between −7.5° and 4.5°E shows a similar inland propagation speed in all runs. The impact of the variability in the monsoon winds and the cross-shore pressure gradient force due to the SST change cannot be directly observed. Still, these factors can influence the SB.

5.3.5 Influence of the SST on the height of the sea breeze

Figure 5.40 shows the median of the sea breeze (SB) height for all the cross-sections in the case study area in West Nigeria (3.5° to 3.9°E). In general, there are no consistent SST-dependences visible.

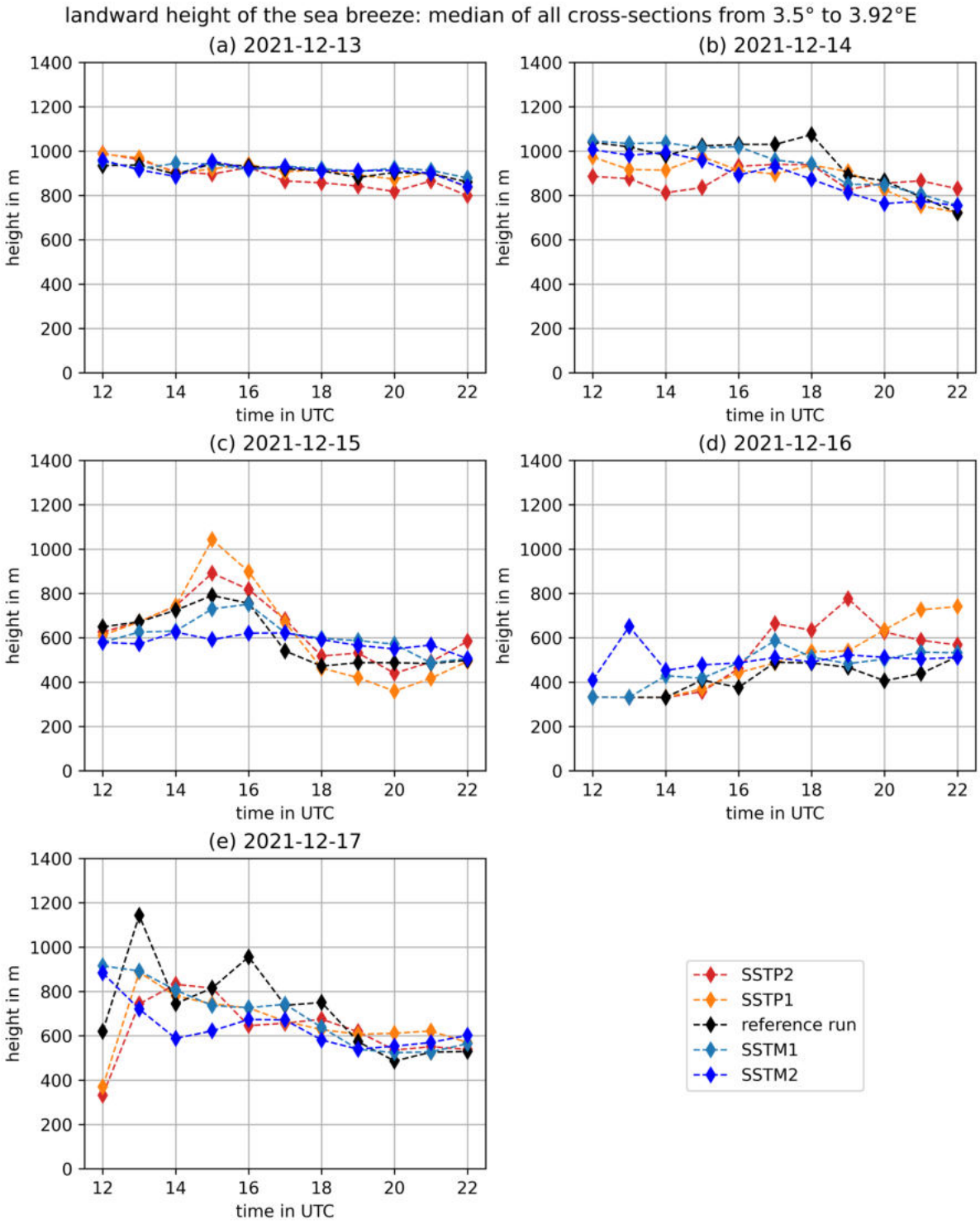

Figure 5.40: *Landward Sea Breeze height, one plot for every day of the simulation period. The depicted height is the median of the heights calculated in each cross-section between* 3.5° *and* 3.92° *E in the case study area in West Nigeria.*

During the first day (Figure 5.40a), the median of the SB height is very similar in all of the simulation runs. A minor tendency of the SB height to decrease about 100 m to 200 m during this

day can be observed. On 14 December, the SB is shallower for the experiments with increased SSTs until 14 UTC (Figure 5.40b). Both in the SSTP1 and SSTP2 experiment, the monsoon flow is weaker over land compared to the other simulations (compare the Hovmöller diagrams in Figure 5.32d to 5.35d in the afternoon on 14 December 2021). The case study in Chapter 5.2.8 has already shown, that the SB height is strongly reduced in an opposing flow. On 15 December 2021, the SBC develops in a Harmattan flow (compare the Hovmöller diagrams in Figure 5.32d to 5.35d on 15 December 2021). In all experiments, the SB height at 12 UTC is between 300 m and 400 m lower compared to the height at a similar daytime in the monsoon flow (compare Figure 5.40c at 12 UTC to Figure 5.40a and b at 12 UTC). While the SB height stays almost constant in the SSTM2 experiment during the day, all other simulations show a strong increase in height, peaking between 15 and 16 UTC and strongly reducing height in the early evening. This behaviour corresponds to the formation of a cold pool at the SBF. In the reference run and in SST experiments with increased SSTs, the updraft at the intersect of the SB flow and the off-shore cold pool outflow is increased (now shown), leading to even higher SB height values compared to the reference run. Figure 5.37b illustrates why the SB height decreases strongly in later hours: the northerly outflow of the cold pool has a lower depth than the SB. The averaged SB height is therefore lower for these time steps.On 16 and 17 December 2021, the SB height behaves rather similarly in all simulations. On the morning of 17 December, the SB detection algorithm locates the SBF close to the coast, therefore the mean height is determined from a few data points only, leading to many outliers.

Figure 5.41 shows the median of the landward SB height from all cross-sections between the Ivory Coast (−7.5°E) to West Nigeria (4.5°E). Similar to the median height of the SB in the case study in West Nigeria described before, the SB height has no clear dependency on the SSTs. Only on 15 December, higher SSTs cause a larger SB depth, most likely due to convective processes related to cold pools at the SBF (Figure 5.39) A major difference can be found in the intercomparison of the subplots 5.40b,c,d and 5.41b,c,d: The SB is shallower in the case study in West Nigeria. These dates cover the monsoon flow as well as the Harmattan period. Previous analysis shows that the height of the SB is mainly controlled by the embedding wind field. As the median takes parts of the Gulf of Guinea into account, which are not or only weakly affected by the Harmattan burst (for example Ivory Coast), the median of the SB height for the full coastline has larger values than the one for the case study in West Nigeria.

5.3.6 Influence of the SST on the SB velocity

The comparison of the Hövmöller diagrams between the SST experiments and the reference run shows an increased wind speed in the 10 m winds for runs with lower sea surface temperatures (SSTs) during the last three days: compare figures 5.20d, and 5.32d to 5.35d. The Hovmöller diagram of the SSTP2 run shows calm wind (white shading) whereas the SSTM2 run has a higher along-transect velocity (green shading in the area where the SB occurs). In Figure 5.42, the median of the mean SB velocity is presented for all experiments in the case study area in West Nigeria (averaged perpendicular cross-sections between 3.5° and 3.9°E). The mean SB velocity is calculated from the averaged onshore winds of all vertical levels between the surface and level 48 between the shoreline and the SBF. Level 48 is approximately 2800 m above ground over the ocean. A layer of this height is in the middle of the shallow overturning circulation. The SBF is determined with the SBF identification algorithm.

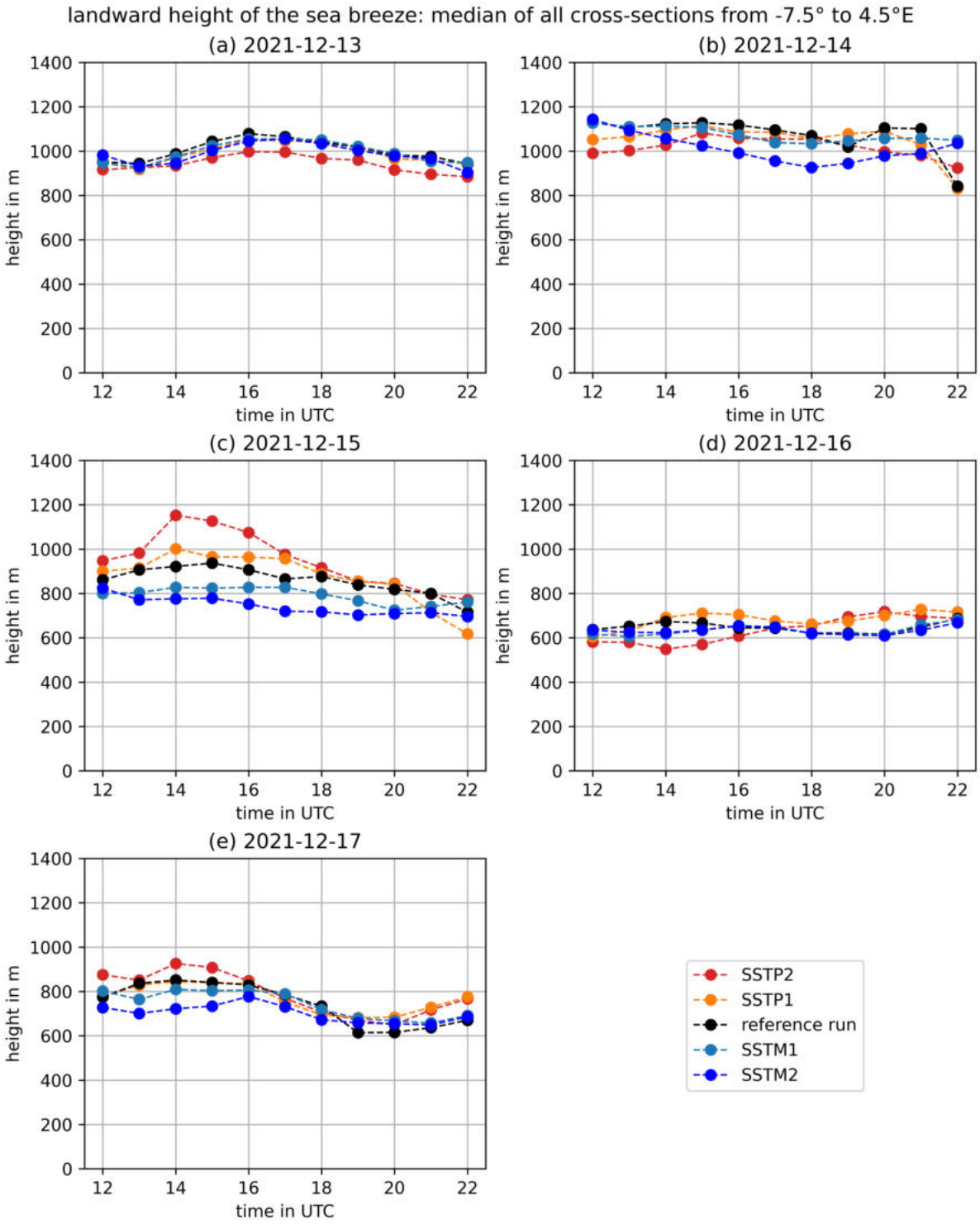

Figure 5.41: *Sea breeze height, one plot for every day of the simulation period. The depicted height is the median of the SB heights calculated for each cross-section between* $-7.5°$ *and* $4.5°E$.

All simulations show in general an analogue behaviour: The mean SB wind speed increases during the day and reaches its maximum between 14 and 19 UTC. Later, the mean velocity decreases

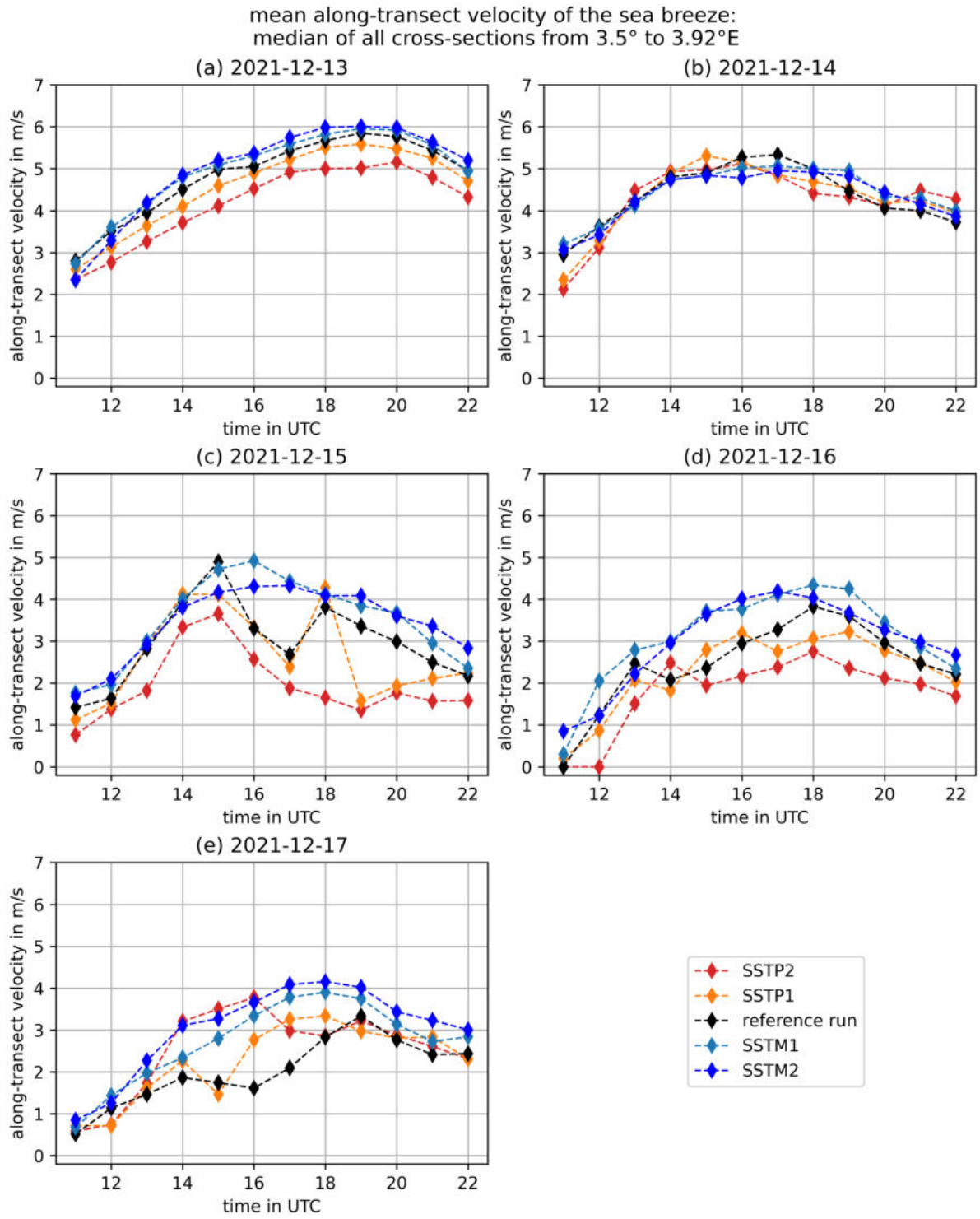

Figure 5.42: *Averaged velocity of the sea breeze, one plot for every day of the simulation period. The depicted velocity is the median of the averaged SB velocity calculated in each cross-section between* 3.5° *and* 3.92° *E.*

again. The embedding flow also influences the mean velocity in the SST experiments: In the monsoon period on 13 and 14 December, the mean SB velocity reaches 4.5 $\mathrm{m\,s^{-1}}$ to 6 $\mathrm{m\,s^{-1}}$ whereas

it ranges between 2.5 m s^{-1} and 4.5 m s^{-1} on 16 and 17 December in the Harmattan period.

On the first day of the simulation (Figure 5.42a), the SST dependency of the mean SB velocity is very clear: a lower the SST leads to a higher mean along-transect velocity of the SB. This result shows the immediate response of the SB on an SST change within the spin-up period. On the second day, there is no clear SST dependency on the mean SB velocity apparent (Figure 5.42b). On 15 December, the mean SB velocity suddenly decreases at 15 UTC in the reference run and the experiments with increased SSTs. This is related to the formation of a cold pool at the SBF (Figure 5.42c). Here, the SB velocity is reduced by the opposing flow of the cold pool outflow. Depending on the development of the merged front of the SB and the cold pool outflow, the SBF detection algorithm might jump to the cold pool front. This happens in the SSTP1 run and the reference run at 18 UTC. Consequently, the mean SB velocity increases suddenly as the cold pool outflow has a higher velocity than the SB (Figure 5.16 and explanation in Chapter 5.2.5). Except for this anomalous behaviour due to cold pool formation, the mean SB velocity is again higher for cooler SSTs. On 16 and 17 December, the SB develops late in the day and stays a few hours close to the shoreline. Therefore, the average is taken over a small area only which can lead to errors. Still, the trend of higher mean SB velocity is present for lower SSTs.

During the five days of the simulation period, the mean SB velocity can differentiate up to 2 m s^{-1} between the simulation with the lowest and the highest SST in the case study in West Nigeria.

Figure 5.43 shows the median of the mean SB velocity calculated in the perpendicular transects from the Ivory Coast to West Nigeria ($-7.5°$ to 4.5°E). The mean SB velocity shows a similar trend compared to the case study: in the period of the monsoon flow in the first two days, the median of the mean SB velocity is larger than during the last three days, where a Harmattan surge impacts the eastern parts of the Gulf of Guinea. The daily cycle of the SB velocity is also visible in the large-scale average. In Figures 5.43a, c and d the SB velocity differs especially in the afternoon and evening between the simulations. The median of the cross-sections along the shoreline from $-7.5°$ to 4.5°E reproduces the difference of up to 2 m s^{-1} in the mean velocity of the SB between the SSTP2 and SSTM2 simulations found in the case study. However, there is a large spread of the mean SB velocity in Figure 5.43 (not shown). This large spread results likely from the large variability of the SB velocity along the coast since the spread of the SB velocity in the case study in West Nigeria is smaller (not shown). The local dependency of the mean SB velocity (on the SSTs) is thus an interesting subject for future studies.

Figure 5.44 shows the 90th percentile of the SB velocity for the case study in West Nigeria. Overall, the 90th percentile of the SB velocity shows a similar daily cycle to the mean of the SB velocity. However, during the first day of the simulation, the 90th percentile velocity increases stronger during the daytime. On the second day, the 90th percentile velocity slope is also slightly increased. The median of the 90th percentile SB wind speed along the coast from West Nigeria until Ivory Coast is depicted in Figure 5.45. It shows in general higher velocities compared to the case study in West Nigeria. This is expected due to variations in the embedding wind field along the coast. In the full-coastal average, the mean SB wind velocity peaks between 15 to 17 UTC and thus 1 h to 2 h before the full-coastal 90th percentile of the SB velocity (Figure 5.43a,b,d and 5.45a,b,d). In most of the times, the 90th percentile SB velocity has higher values for colder SSTs.

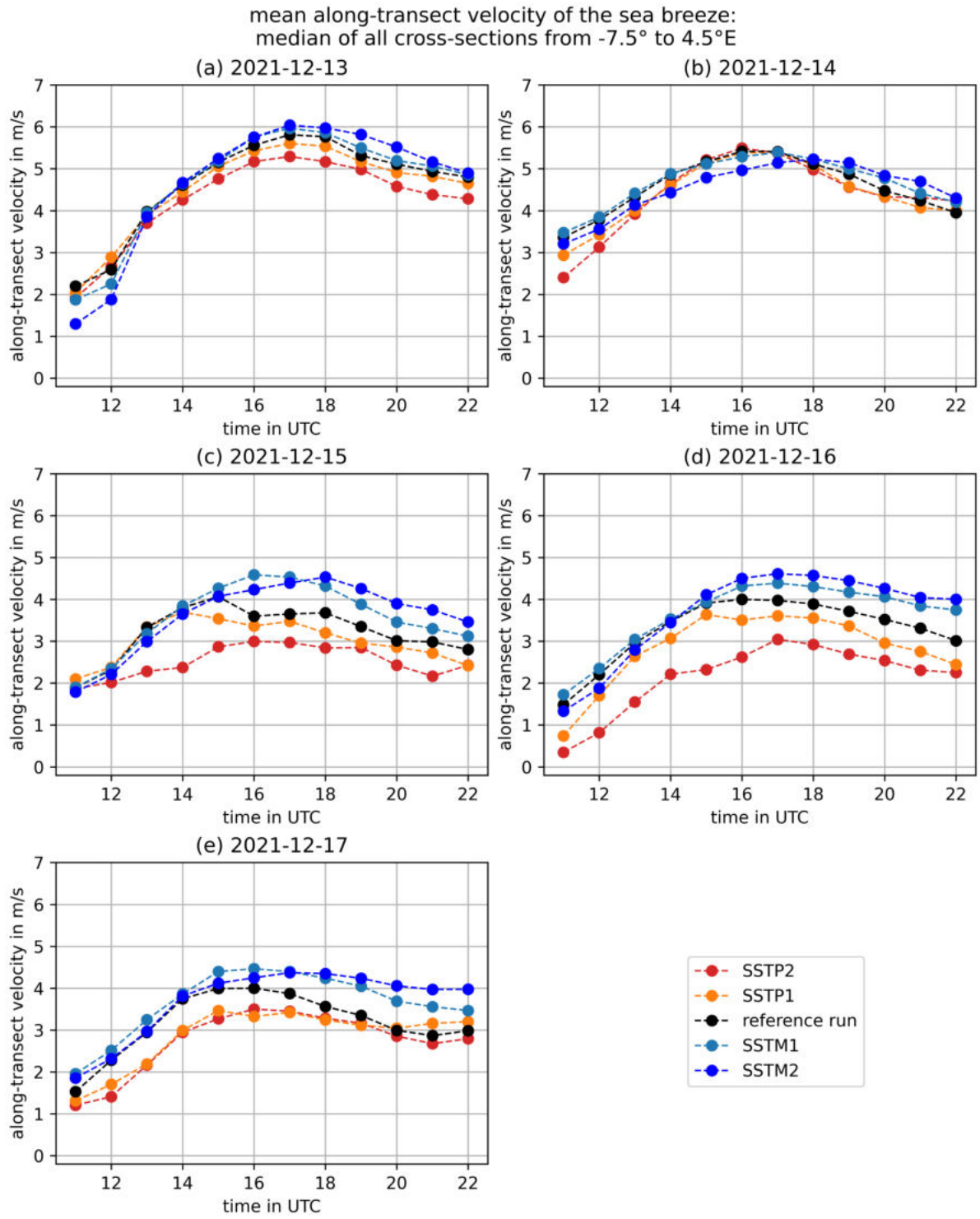

Figure 5.43: *Averaged velocity of the Sea Breeze, one plot for every day of the simulation period. The depicted velocity is the median of the averaged SB velocity calculated in each cross-section between* $-7.5°$ *and* $4.5°E$.

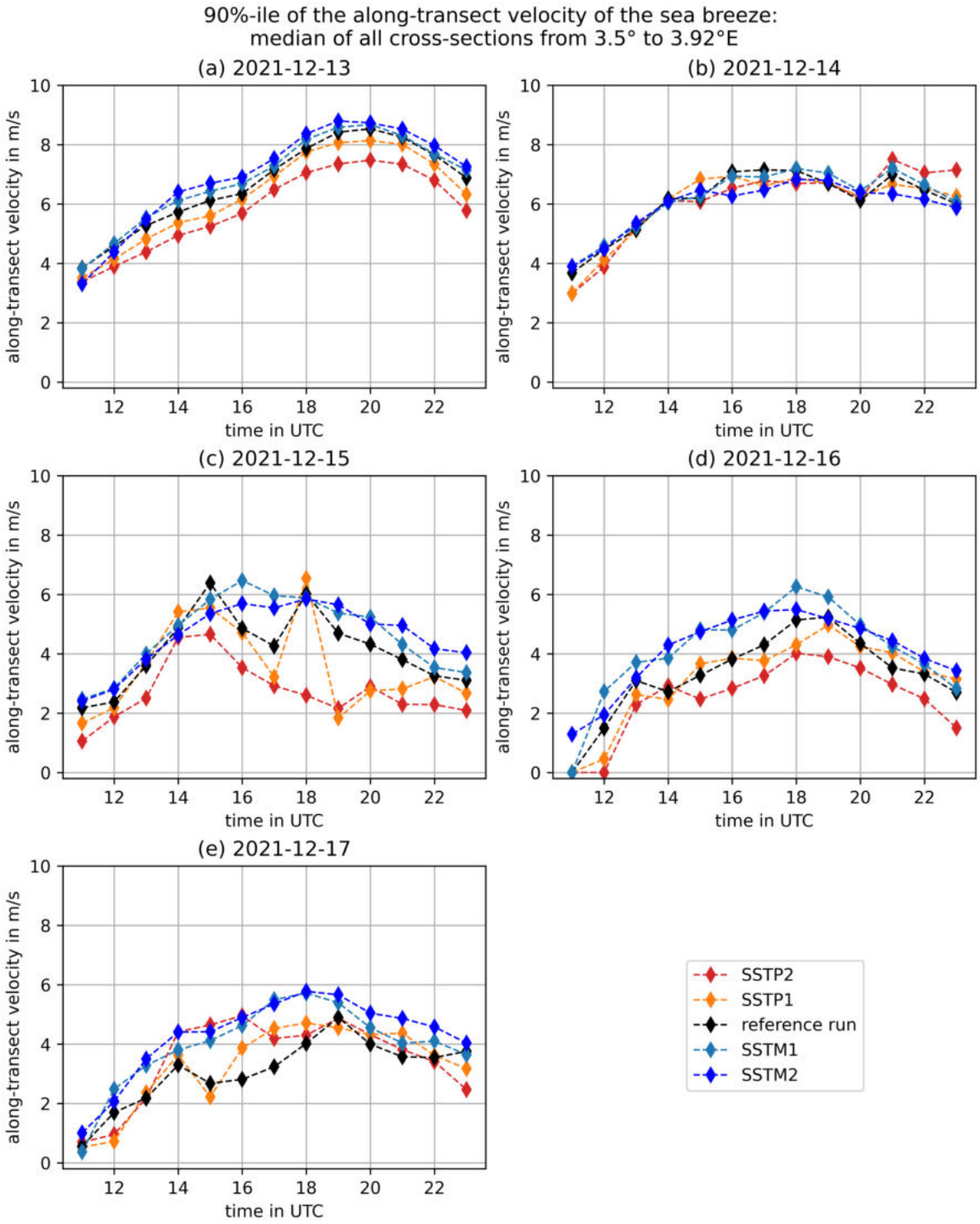

Figure 5.44: *90th percentile of the velocity of the Sea Breeze, one plot for every day of the simulation period. The depicted velocity is the median of the 90th percentile SB velocity calculated in each cross-section between* 3.5° *and* 3.92°*E.*

5.3.7 Chapter summary

Changes in the SST influence the air temperature and humidity over the ocean and to a lesser extent the atmosphere over land. Adjustment processes to the modified SSTs are found to take

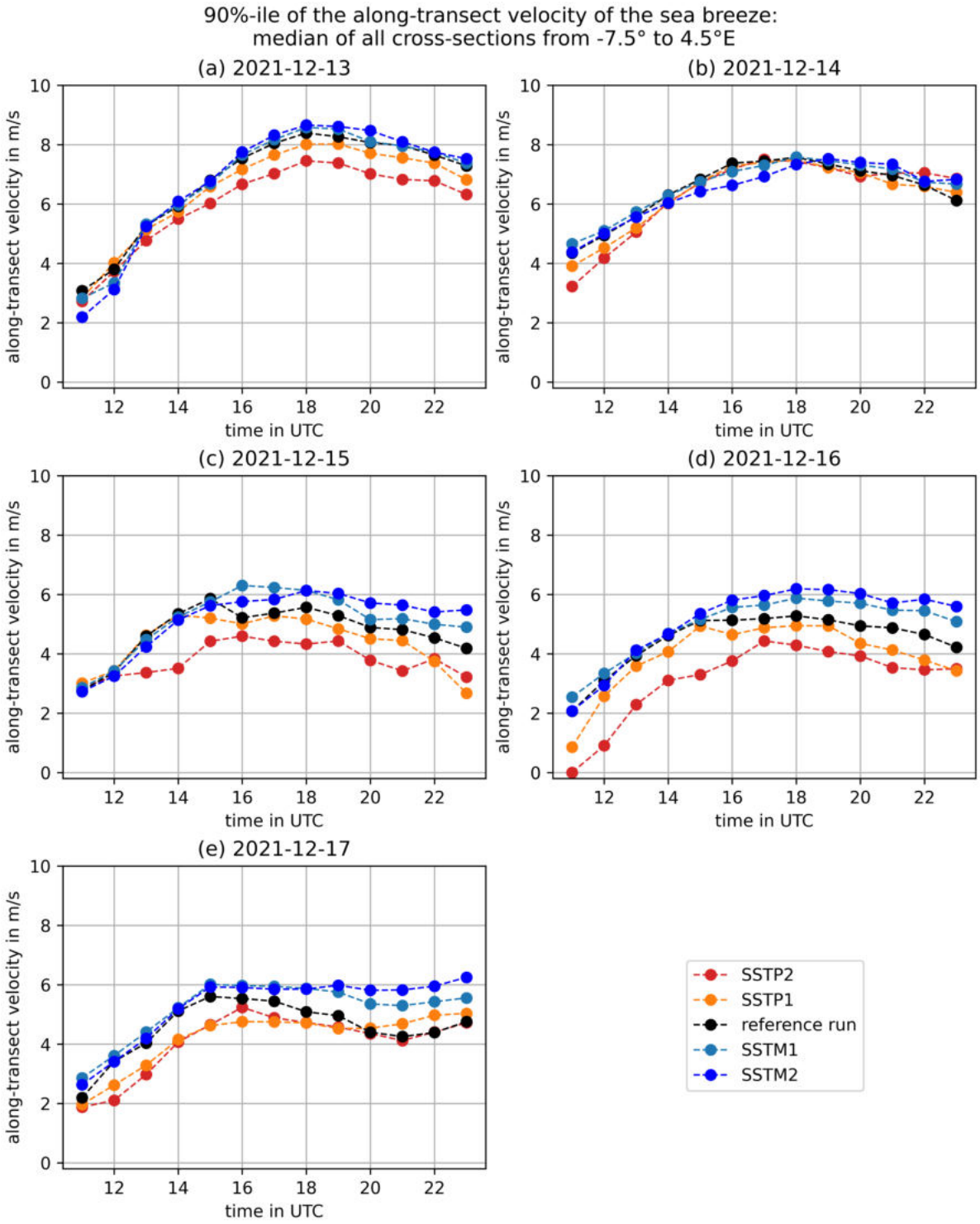

Figure 5.45: *90th percentile of the velocity of the Sea Breeze, one plot for every day of the simulation period. The depicted velocity is the median of the 90th percentile SB velocity calculated in each cross-section between* $-7.5°$ *and* $4.5°E$.

24 h to 34 h in the atmospheric boundary layer. The SST changes also affect the large-scale circulation of the WAM, in which the LSB is embedded. A higher SST leads to a decrease in

the monsoon winds, an increase in the Harmattan winds and a southward shift of the ITD. The LSB responds to increased SSTs with a decreased inland penetration distance and wind speed. For the SB height, no consistent SST dependence was found. The formation of cold pools at the SBF can modify these relations. For example, the increase in inland penetration distance due to lower SSTs can still be smaller compared to experiments with increased SSTs where cold pool density currents merge with the SB. The formation of cold pools at the SBF was suppressed for experiments with lower SSTs. The sensitivity of the SLB on SST changes is revealed to be complex and multifaceted.

6 Discussion

The land–sea breeze (LSB) determines near-surface wind fields in the near-coastal areas in the Gulf of Guinea to a large extent. Studies of Guedje et al. (2019) in Benin show an occurrence of the sea breeze (SB) all year around. In November and December, the SB is detected statistically on 60% of the days. The land breeze (LB) appearance also peaks in December with a recurrence in 80% of the days. Despite the high occurrence frequency of this local wind system and the well-known impact on local thunderstorm development, fog formation, air quality impact and its interrelation to coastal precipitation, the LSB is still sparsely investigated in the Gulf of Guinea (Miller et al., 2003). Further investigations on the characteristics of the LSB in the Gulf of Guinea are needed to better understand the impact of this wind system. The poor data availability due to the limited amount of weather stations in tropical West Africa poses an additional challenge for investigating the SB (Fink et al., 2017). Therefore, simulations performed with numerical weather prediction models are especially valuable to analyse the LSB, as they provide a 3D inside into the formation and development of the winds. The impact of the sea surface temperature (SST) on the LSB is only sparsely investigated. Different case studies in Brazil, England and the US found very different responses of the SB to SSTs. In the Gulf of Guinea, where high seasonal, intra-annual and strong short-time SST changes occur, the impact of the SST variability on the LSB has not been investigated yet, to the best of the author's knowledge.

This thesis project addresses this issue and investigates the impact of the SST on the LSB with sensitivity experiments: First, the Gulf of Guinea is simulated with the numerical weather prediction model ICON in a period from 13 to 17 December, thus in the season of the year with the highest LSB occurrence. The precipitation rates in these five days are below 10 mm along the Gold Coast and in the western part of the Bight of Benin and below 2 mm in the hinterland more than 2° North of the coastline (Figure 4.2). This period is chosen to investigate the LSB unaffected by persisting storms and precipitation to get an insight into the convective activity of the SB which can initiate thunderstorms and precipitation. In the first part of the data analysis in the results Section 5.2 the LSB is analysed in the reference run. In the second part, the derived characteristics are compared with the LSB characteristics in sensitivity SST experiments. These simulations are initialized with an equal atmospheric and land surface setup but have increased or decreased SSTs by 1 K or 2 K. The atmosphere and the ocean are thus not in equilibrium, similar to a sudden surface cooling event in the near-coastal ocean. The analysis of the air temperature and the specific humidity shows, that an equilibrium state is again reached after one day for the SST experiments with increased SSTs and after 33 h after initialization in the SST experiments with decreased SSTs. The SST experiments were named by the applied SST variation: the simulation with 2 K increased SSTs was called the 'SSTP2' run ('P2' stands for 'plus 2 K') whereas the simulation with 1 K decreased SST was called 'SSTM1' standing for 'minus 1 K'.

The sea breeze (SB) and the land breeze (LB) are identified in an analysis of vertical cross-sections arranged perpendicular to the shoreline. The cross-sections depict the along-transect wind speed, the vertical wind speed and the virtual potential temperature profile. Depending on the location and the date of the simulation, cross-shore onshore winds develop between 9 and 14 UTC. The emergence of these winds coincides in time and location with the formation of a density current: A layer of denser cooler marine air moves inland where the well-mixed boundary layer deepens due to solar heating. This density current is the SB. It expends offshore and landwards during the

daytime, increasing in wind speed. With the ceased solar heating of the land surface, an inversion layer forms at the land surface during the late evening, increasing in depth during the nighttime. The SB winds still propagate further inland but detach from the surface. Now, two scenarios are possible: either, the SB weakens in the following hours and dissipates or it increases further in strength, peaking around 925 hPa height in the along-transect velocity. This transformation from the SB into a nocturnal low-level jet (NLLJ) can be observed in the first two days of the simulation period in the reference run.

A few hours after sunset, when the atmosphere over the land is cooled below the temperature of the atmosphere over the ocean, shallow weak offshore winds can emerge over land between the shoreline and a distance of 100 km to 200 km inland. The persistence of these winds depends highly on the embedding flow in the reference run: in a strong opposing flow, these winds are suppressed. This happens on 14 and 15 December 2021 in the reference run in a case study in West Nigeria (transects perpendicular to the shoreline between 3.5° and 3.9° E are averaged). The offshore winds have a depth of barely 200 m over land and do not cross the shoreline. Due to the elevated orography in the coastal regions, these offshore winds are very likely a combination of katabatic winds and an LB. In an embedding offshore flow due to a Harmattan surge, as it is present on 16 and 17 December in the case study in West Nigeria, the combined katabatic flow and LB can reach a depth of 500 m and cross the shoreline with a frontal structure. In the reference run, this wind system propagates over 50 km off-shore before it dissolves when the land surface and atmosphere aloft heat after sunrise. The depth values of the LB are in good agreement with the study of Guedje et al. (2019). The climatology of low-level wind regimes in Benin characterises the LB as a shallow circulation, not reaching 600 m depth, which can be observed in wind roses at 6 UTC.

In the reference run, the SB occurs all along the coastline in the Gulf of Guinea on all days of the simulation period. It is visible on 10 m wind maps and in perpendicular transects generated for each longitude along the almost zonal coastline from the Ivory Coast until West Nigeria. A comparison of the reference run to the ERA5 reanalysis dataset reveals a high accordance of the 10 m winds in both data sets, not only in the vicinity of the shoreline but in general. A time-delayed onset of the SB in the ERA5 data can be related to the more than six times coarser grid spacing of the ERA5 data compared to the performed ICON simulations in this thesis. In the ERA5 data, the LB signal is not visible, also most likely due to the too-coarse grid resolution. Besides the good accordance of the 10 m winds between the reference run and the ERA5 dataset, the ICON simulation exhibits the advantage of resolving both the SB and the LB on a grid which allows a detailed analysis of the characteristics of these local wind systems.

The inland penetration distance of the SB is analysed with a sea breeze front (SBF) identification algorithm, which was designed and implemented in this thesis. It detects the SBF at the closest landward distance to the shoreline, where the horizontal gradients of the boundary layer depth and the mean horizontal wind velocity in the lowest four model levels above the surface level coincide in exceeding defined thresholds. The inland penetration distance of the SB is analysed in a case study in West Nigeria (average from 3.5° to 3.9° East). The results are compared to the median distance to the shoreline of all cross-sections from the Ivory Coast until West Nigeria (−7.5° to 4.5° East). The statistical evaluation of all these 400 perpendicular transects along the shoreline would have been impossible without the SBF identification algorithm.

The inland propagation distance of the SB in West Nigeria is analysed from 10 UTC until 22 UTC for the five days of the simulation period. For each day, the inland penetration distance increases slowly from the initialisation of the SBC until 16 to 17 UTC. At later times, the SB propagates faster inland. This result is in agreement with the theory of the development stages of the SB formulated by Clarke (1984): When the early mature stage of the SB begins with the decline in insolation, the decay of atmospheric turbulences leads to a faster inland propagation of the SB.

The day-to-day variations in the inland penetration distance, however, are very large: The distance of the SBF to the shoreline in the afternoon and the evening on 13 and 14 December is nearly double the distance of the SBF to the shoreline on 16 and 17 December 2021. The median inland penetration depth along the full coastline from Ivory Coast to West Nigeria shows a similar behaviour: At 20 UTC, the median distance exceeds 200 km on 13 and 14 December. On 15 December, it reaches about 160 km inland, whereas on 16 and 17 December, the sea breeze is closer than 130 km to the shoreline. Parker et al. (2017) mentioned an inland propagation of 60 km in 6 h and reports afternoon showers related to convective processes at the SBF up to 100 km inland. **?** found an inland penetration distance at 18 UTC reaching 250 km in a study based on ERA5 data in the Gulf of Guinea. These values are in agreement with the inland penetration depths found in the reference run. These day-to-day differences result most likely from differences in the large-scale surface flow: On the first two days of the simulation, the near-surface winds along the whole shoreline of the research area are determined by the shallow south-westerly, thus onshore, monsoon winds. The SB emerges within the shallow monsoon winds and occurs as a signal of increased onshore winds in the vicinity of the shoreline. Aloft of the monsoon winds at around 1500 m, a return flow of the shallow overturning circulation flows oceanward. The lower edge of this flow shows strong day-to-day variations. The return flow of the sea breeze circulation, forming aloft of the SB, adds to these winds. Since the height of the SB is lower than the monsoon flow, the return flow of the SB lies also lower than the return flow of the shallow overturning circulation. A sketch in Figure 5.13 illustrates how the SBC impacts the background flow. Both in cross-sections and Hovmöller diagrams, the SB is seen to propagate far inland in the following hours, reaching up to 300 km inland before midnight. While the along-transect wind velocity at 975 hPa is found to decrease around 19 UTC, the onshore winds at 925 hPa increase in strength and propagate further inland. The maximum inland extent of these onshore winds is the location of the ITD, calculated by the position of the 14 °C dew point temperature (shown in the Hovmöller diagram in Figure 5.20). The characteristics of the increased wind at 925 hPa agrees with the description of the nocturnal low-level jet (NLLJ) by Parker et al. (2017). A transformation of the SB during the nighttime is very likely when the winds are detached from the surface by a nighttime inversion and accelerated towards a heat low (Rácz and Smith, 1999). On 15 December 2021 in the reference run, the shallow monsoon flow is displaced by a northerly, thus off-shore, Harmattan wind. In the case study in Nigeria, the SB is already developed when the Harmattan winds reach the vicinity of the coastline. On 16 and 17 December, the SB develops in an off-shore flow. Under these conditions, the SB extends faster off-shore than on-shore in the reference run. Until 15 to 16 UTC, the SBC stays close to the shoreline. In the late afternoon, the median of the SBF position moves slower inland compared to the first three days. In these dates, no transformation into an NLLJ is visible in the Hovmöller diagrams. Also, the ITD position is shifted closer to the shoreline. In the case study in West Nigeria, the SB winds already reach the ITD at 22 UTC, a transformation in an NLLJ is thus not possible. The day-to-day variations

of the inland penetration distance and the strength of the circulation are very strong in the different environments of embedding flow and vertical wind shear. It seems likely that this sheared environmental flow of the onshore monsoon winds and the offshore overturning circulation return flow aloft enhance the SBC. Lu et al. (2006) agrees that the SB development favours a weak shear environment. However, Pearson et al. (1983) found no correlation of vertical shear to the inland penetration depth.

The comparison of the SST experiments and the reference run reveals an SST dependence of the inland propagation distance of the SBF. Again, a case study in West Nigeria is compared to the median of the inland penetration depth of all cross-sections from the Ivory Coast until West Nigeria. Both studies show very similar behaviour. The simulations show most of the time the following relation: the lower the SST, the deeper the inland penetration distance. The inland propagation speed of the SBF is similar in the different simulations within each day. This leads to the conclusion, that the SSTs mainly affect the onset of the SBC. From theory, it is known that the SBC forms due to the atmospheric temperature gradient between the land and the adjacent ocean. In the nighttime, the land surface is cooler than the ocean surface, thus the lower atmosphere over land is also cooled below the temperature of the adjacent marine air. After sunset, the incoming solar radiation increases the temperatures of the land surface stronger than those of the ocean surface. The atmosphere aloft the land is warmed from the land surface. When the air temperature over land exceeds the air temperature over the ocean, the cross-shore temperature gradient results in a cross-shore pressure gradient force which induces the SB (Miller et al., 2003). In case of a lower SST and thus a lower air temperature over the ocean, the temperature of the atmosphere over the land exceeds the temperature of the marine air earlier on the day. Thus, the SB develops earlier. And therefore it extends earlier inland compared to the simulations with higher SSTs. Higher SSTs on the other hand cause a higher marine air temperature which is exceeded later in the day by the temperature of the atmosphere over the land, thus the SBC is initialized to a later time in the day. This hypothesis is also confirmed by the comparison of the onset times of the SB in the reference run and the SST experiments. The difference of the inland penetration distance in the SSTP2 run and the SSTM2 run can exceed 50 km.

Indirect effects on the inland penetration distance are imposed by the influence of the near-surface winds. Cooler SSTs induce stronger monsoon winds in the SST experiments. The analysis of the large-scale overturning circulation of the West African Monsoon system also shows a weakening of the Harmattan winds and a shift of the ITD away from the shoreline in the simulations with decreased SSTs. The analysis of the SBC dependence on the embedding wind field in the reference run described in the previous paragraphs shows, that an opposing embedding flow limits the inland penetration depth while an onshore embedding flow supports the inland penetration. Thus, an increased monsoon flow in the experiments with cooler SSTs could increase the inland penetration velocity. Another indirect effect can be imposed by the increased atmospheric land-sea temperature gradient in SST experiments with decreased SSTs. A higher temperature gradient could lead to a higher pressure gradient force and thus to a stronger SB inland propagation velocity. Both effects would result in an increased spread of the inland penetration distances during the day. This is not consistently visible in the data. The bottom line of this analysis is thus, that indirect effects of the SST influence the inland penetration distance only marginally in comparison to the direct effect of the SST variation on the onset time of the SBC.

On 15 December 2021, the third day of the simulation period, the stated relation deeper inland penetration distance for lower SSTs reverses in the afternoon and evening. This behaviour is visible in the case study in West Nigeria and the median of the inland distance of the SBF to the shoreline from all cross-sections between the Ivory Coast and West Nigeria. On the third day of the simulation period, the monsoon winds are weakened in the western parts of the coast and displaced by Harmattan winds in the east of the Gulf of Guinea by around midday. An analysis of the 10 m wind maps, the along-transect wind velocities, the virtual potential temperature profile and the specific cloud water, rain and water vapour content revealed the formation of cold pools in the afternoon at the SBF along large sections of the coastline. Due to the increased convergence of the SB and embedding flow at the SBF an increased convective activity results. This induces strong precipitation near the SBF which evaporates by falling towards the ground taking energy from the surrounding air. This cooled air is denser than the surrounding atmosphere and sinks towards the surface, spreading in the radial direction as a density current (Zuidema et al., 2017). The outflow of these cold pools spreads with a faster velocity compared to the SBF propagation speed in the ICON simulations. The ICON simulations in this thesis project show a decreased convective activity in the SST experiments with lower SSTs. In the case study in West Nigeria, no cold pools are formed at the SBF on 15 December 2021, thus the SB penetrates as described in the paragraphs before inland. In the SST experiments with increased SSTs, the SBs develop later in the morning and have therefore in the early hours a smaller inland penetration depth compared to the SSTM2 run. Between 14 and 16 UTC, cold pools form at the SBF. The density current of the cold pool and the density current of the SB merge. The schematic in Figure 5.37(b) visualises the merged structure of the SB and the cold pool. As the landward outflow of these cold pools propagates faster inland than the SBF, the inland penetration distance of these new fronts soon overtakes the ones from the runs without cold pools. From the perspective of the near-surface winds, the cold pool density current propagating inland is very similar to that of the SB density current. Thus it is reasonable to define the new SBF at the front of the cold pool in cases where the cold pool merges with the SB.

The height of the LSB shows a high day-to-day variation but a very similar behaviour in the inter-comparison of the different simulations for each day. For the SB, the averaged height between the shoreline and the SBF is calculated using the wind reversal criteria of Wexler (1946): He defines the SB height at the vertical level where the onshore SB winds reverse to the offshore return flow of this circulation. In all simulations, the averaged height of the SB shows higher values when the SBC is embedded in the monsoon flow: the height of the SB lies between 900 m and 1200 m for all simulations. This is in good accordance with the analysis of Coulibaly et al. (2019), who found the SB to extend up to 1500 m or less in a climatological analysis for Cotonuo (Benin) in December. On 16 December 2021, the SB height decreases to values between 500 m and 700 m height in all experiments. The opposing Harmattan flow results thus in a shallower SB. As already mentioned in the paragraph of the first research question, the LB height behaves oppositely: A supporting Harmattan flow increases the depth and strength of the LB whereas an opposing monsoon flow can extinguish the LB in the simulations.

The only large difference in the SB height between the SST experiments occurs on 15 December 2021 in the case study in West Nigeria. This coincides with the period, where cold pools emerge at the SBF. The SSTM2 run shows an almost constant height during this day. In the SSTM2 simulation, no cold pools are formed at the SBF. The other simulations show a strongly increased

SB height from 14 to 16 UTC, thus in the time where the cold pools form. An analysis of the cross-sections reveals, that this increased height results from convective processes close behind the SBF. In the early evening, the SB height of all simulations is strongly reduced compared to the SSTM2 run. Since the density current of the cold pool moving ahead of the former SBF is shallower than the SB, the overall height of the merged cold pool and SB density currents is decreased. Except for this effect, no SST dependency could be found in the comparison of the reference run and the SST experiments. This result agrees with Steyn (1998), who found that the height of the SB depends on the surface-layer turbulent fluxes of sensible heat and momentum, but states that the SB height is independent of the temperature difference between the land and the ocean.

The diurnal cycle of the mean SB velocity, computed between the shoreline and the SBF, shows an increase in velocity from the emergence of the circulation until 15 to 17 UTC and a decreasing velocity in later hours. The 90th percentile of the SB peaks one to two hours later, thus around sunset or shortly afterwards. In general, a high sensitivity of the mean SB velocity to the embedding flow has turned out. In a case study in West Nigeria during the period of onshore monsoon winds, the SB velocity is up to $3\,\mathrm{m\,s^{-1}}$ higher than during the Harmattan surge. This dependency on the environmental flow agrees with studies from Simpson and Britter (1980), who found a reduction of the SB flow velocity of -0.59_{geostr} due to the opposing geostrophic flow.

The variation of the mean SB velocity up to $2\,\mathrm{m\,s^{-1}}$ due to SST variations is therefore an important factor. The general dependency can be summarised as in the following: Warmer SSTs cause a lower mean SB velocity whereas cooler SSTs increase the mean SB velocity. A similar behaviour can be found in the 90th percentile SB velocity.

Cross-sections in the reference run and all SST-experience show convection due to low-level convergence at the SBF during mid-day. Additionally, convective processes are observed ahead of the SB over land from mid-day until the late afternoon. On the third day of the simulation period, when the monsoon wind is displaced by a Harmattan wind in the eastern part of the Guinea Coast, the convective activity is found to be particularly high at the SBF. The higher frontal activity might be related to a stronger low-level convergence. A case study in West Nigeria on 15 December 2021 shows, how a cold pool intensifies during the passage of an SBF and decays afterwards. The formation of cold pools at the SBF has a large impact on the properties of the SBC: The merged structures of the cold pool outflow and the SB exhibit an increased inland propagation velocity, a decreased density current height and higher velocities within the density current forming out of the cold pool outflow and the SB. The case study on 15 December 2021 has also shown, that the new front of the system moves also frontal-like in large areas inland. The comparison of the reference run to the SST experiments also shows, that the formation of cold pools at the SBF can impact a large area along the shoreline. Interestingly, the inland penetration distance and the height and mean velocity of the SB show in particular differences between the SSTM2 run and the experiments with increased SSTs: In the case study in West Nigeria, no cold pools form in the SSTM2 run. In the SSTM1 run, the cold pool intensity, evaluated on the wind velocity of the cold pool outflow, is weak in comparison to the reference run. This analysis leads to the conclusion, that the increase in the SSTs over three days leads to an intensified cold pool formation whereas decreased SSTs impede or prevent the formation of cold pools. These interesting results need to be analysed on their universality in future studies. Additionally, the

amount of precipitation related to cold pools formed at the SBF needs to be investigated, since the local precipitation caused by frontal processes of the SB impacts the local community.

7 Conclusion and outlook

The land–sea breeze (LSB) is a thermally-driven circulation and is present all year around in the Gulf of Guinea (Guedje et al., 2019). Due to its influence on wind, air quality and precipitation, the LSB greatly influences the environment and the living conditions of countries along the Guinea Coast (Miller et al., 2003). The LSB is highly dependent on its local environment, for example on the embedding wind field and the thermal gradient between the land and the ocean (Crosman and Horel, 2010). This thesis is the first study investigating in detail the impact of sea surface temperatures (SSTs) on the LSB. In a research period from 13 to 17 December 2021, the atmosphere over the Gulf of Guinea and the Guinea Coast is modelled with the numerical weather prediction model ICON. The impact of the SSTs on the LSB is investigated with SST sensitivity experiments, where the SST was uniformly increased or decreased by 1 and 2 K.

The following paragraph summarises the results of the thesis by answering the research questions presented in Section 3.

Can the ICON model realistically reproduce the LSB in the chosen configuration?
The formation of the SB in the hours after sunrise, the intensification of the near-surface winds during mid-day, the increased inland propagation velocity after a reduction of atmospheric turbulences in the afternoon and a dissipation of the sea breeze (SB) in the nighttime observed in the reference run performed with ICON show similar behaviour to the SB described in the literature. The reference run also shows a good agreement of in the surface winds with the reanalysis data ERA5.

How far does the SB penetrate inland and what atmospheric mechanisms control this distance?
The inland penetration distance of the SB is found to be highly dependent on the embedding flow: in a period of opposing Harmattan winds, the SB reaches less far inland compared to a monsoon wind period. The acceleration of the SB in the late evening and the transformation into a nocturnal low-level jet is found to be dependent on the distance of the sea breeze front (SBF) to the intertropical discontinuity (ITD): the maximum inland penetration distance of the SB is found to be limited by the ITD position.

How does the inland penetration distance of the SB depend on the SSTs?
The SST experiments have shown that lower SSTs lead to a deeper inland penetration distance. The differences between the different simulations can reach up to $30\,\mathrm{km\,K^{-1}}$. The main reason for this difference is the time delay in the onset of the SBC for higher SSTs. Higher SSTs cause a warmer marine atmosphere, therefore it takes a longer time for the air temperature over land to exceed that of the adjacent marine air. This relation can be modified when strong convective activity triggers cold pool formation at the SBF. The density current originating from the outflow of the cold pool has a higher propagation velocity compared to the SB. Therefore, the front of the merged SB and cold pool outflow can exceed the inland penetration depth of simulations with cooler SSTs where no cold pools are created at the SBF.

How does the height of the LSB depend on the SSTs?
The height of the SB is found to be predominantly independent of the SST. Still, the SST in-

directly influences the SB height by affecting the formation of cold pools at the SBF. Frontal convective processes related to a cold pool formation can lead to an increased height during the emergence of the cold pool. When the shallow outflow of a cool pool is developed at the SBF, the merged structure of the SB and the cold pool is found to be lower in height compared to the pure SB. In general, there is a large dependency of the SB height on the embedding flow. In Harmattan periods, the SB height in the simulations lies between 500 m and 700 m, whereas it reaches 900 m to 1200 m when embedded in the shallow monsoon flow.

How do circulation characteristics (mean and maximum wind speed) of the SB depend on the SST?
The comparison of the SST experiments and the reference run show a higher mean wind speed within the SB and a higher 90th percentile of the mean wind speed within the SB for experiments with decreased SSTs and vice versa. This SB velocity difference between the coolest and the warmest SST experiment can exceed $2\,\mathrm{m\,s^{-1}}$. This impact is comparable to the influence of the embedding flow on the mean wind speed within the SB, which changes the mean and 90th percentile up to $3\,\mathrm{m\,s^{-1}}$ in the simulations.

Does the formation of convective clouds related to frontal processes at the sea breeze front depend on the SST?
Low-level convergence and convective processes at the SBF are present in the reference run and all SST experiments during the simulation period. On the Harmattan days, increased frontal activity has been noted which leads to an increased cold pool formation or strengthening at the SBF. A case study in West Nigeria shows a strengthening of a cold pool during the passage of an SBF. The density current emerging at the cold pool outflow shows a lower height, faster velocity and higher inland propagation speed than the SB. The cold pool outflow thus modifies the SB characteristics, when both structures merge. The seaward outflow of the cold pool can also interrupt the inflow of the SB near the coast. The comparison of the reference run and the SST experiments shows an increased cold pool development in the reference run and the SST experiments with higher SSTs. In the SST experiments with decreased SSTs, the cold pools formed in the case study are weaker in wind speed and radial propagation velocity. In the SSTM2 experiment, the cold pool formation was inhibited in a case study in West Nigeria. Hence, the SST impacts the formation of convective clouds at the SBF.

The results of this master's thesis show that the SST impacts the LSB in the Gulf of Guinea by changing its inland penetration depth, wind velocity and convective activity at the front. Since this work is the first detailed investigation of the SST impact on the LSB in this area, it leaves a wide field of open questions. In the following paragraphs, interesting future projects based on this master's thesis are illustrated.

The analysis of the large-scale circulation in the SST experiments shows increased (decreased) near-surface wind at the southern boundary in the SST experiments with increased (decreased) SSTs. These effects are very likely driven by the imposed SST discontinuity at the boundary of the simulation area. For future analyses including a publication of this work, the southern boundary of the first nest should be set farther south to prevent boundary effects in the second nest. In the current simulation setup, the southern boundaries are set to 5° South (second nest at 3° South). The boundary wind effects can be seen from this southern boundary up to 3° North.

Therefore I suggest a southern boundary for the first nest at 13° South while leaving the southern boundary of the second nest at 3° South.

Another task is a further adjustment of the SBF identification algorithm. While the algorithm detects the SB very well in a shallow monsoon flow, the identification of the SBF in a Harmattan surge, where frontal convective activity was largest, leads to inconsistencies: The landward outflow of the cold pool overtakes the SB and therefore forms a new front ahead of the following SB. The algorithm should be adapted to identify this new front as the SBF, for the reason that the surface winds cannot be differentiated as belonging to a cold pool or the SB. Since this algorithm is a useful new tool in SB research using numerical models, the code shall be provided to the community.

The sensitivity experiments performed in this thesis project change the SST uniformly at the initialisation of the simulation while keeping it constant afterwards to allow the atmosphere to adapt. It would be interesting to perform a simulation with daily updated SSTs during a short-time SST-cooling event triggered by Saharan dust. For this purpose, the ICON model needs to be adapted to allow a daily SST update. Another option would be a series of one-day simulations, initialized with a time difference of one day between the runs. Each simulation can be initialized with the up-to-date SSTs. For consistency, the output of the first run can be passed to the second run and so on. This analysis would allow an insight into the SST impact in a past realistic cooling event. The outcome can be compared to the more general results of the sensitivity experiments performed in this thesis to better understand the response of the SB to a constantly changing SST.

This thesis shows that the SST has a major impact on the SB characteristics in the Gulf of Guinea. These results are found in a setup where the SSTs of the whole ocean are changed uniformly, somewhat analogous to intra-annual SST variability. Still, the analysis of the OSTIA dataset shows that the short-time SST variations in December often occur, especially to the north of the equator. In future studies, it would be important to investigate the impact of a local cooling event in the near-coastal ocean on the LSB. What is the critical off-shore extent of a cooled or warmed ocean surface to impact the SB? A partial cooling or warming of the ocean surface implies SST gradients, which can affect the winds and induce atmospheric circulations above the ocean. This thesis also shows that the LSB is very sensitive to a change in the embedding wind field. The analysis of the LSB sensitivity to SST gradients and the horizontal extension of the SST anomaly will provide valuable insights for forecasting the LSB in the Gulf of Guinea.

It would be very interesting to investigate the variability of the sea breeze characteristics along the coast. Are there locations where the SB cannot extend inland so far or appears weaker or stronger than in other locations when the SSTs are increased or decreased? With the implemented SBF detection algorithm, such data can be easily generated. This analysis requires additional model runs in different seasons and years to allow a statistical analysis of the coastal variability of the SB. This analysis can identify locations which may experience a changing SB due to climate change. A detailed risk and benefit assessment of the impacts of the SB can point out locations, where the SBC enables good living conditions due to, for example, associated SB precipitation for farming or atmospheric cooling due to the inflow of marine air as well as potential zones of increased risk due to, for example, extreme precipitation in a context of global climate warming.

Another important project would involve a detailed analysis of the cold pool formation at the SBF. In which locations do cold pools occur more often and why? Is there a relation between warmer SSTs and the precipitation amount in cold pools due to increased inland moisture transport with the SB? A second detection algorithm for cold pools could be implemented to investigate the occurrence time and position of cold pools compared to the passage of the SBF. This analysis could be continued to investigate case studies where an SB coincides with extreme precipitation events in coastal areas. Numerical simulations could provide insight into the moisture and energy fluxes transferred from an SB to such a storm. A better understanding of these extreme events can give decision-makers the necessary information to take action to protect the local population from natural disasters.

The research field of the SBC in the Gulf of Guinea is an important subject because it is a meteorologically interesting region where we still don't fully understand the processes and their mechanisms. The work of this thesis project reveals the SST dependence of the major characteristics of the LSB over land in a case study in December 2021. The investigation of the characteristics of the LSB over the ocean is even more challenging due to the limited data availability. A research campaign in the tropical Atlantic could deliver valuable atmospheric and oceanic information, investigating also the SST variability which is especially during the minor upwelling season, barely understood.

8 Appendix

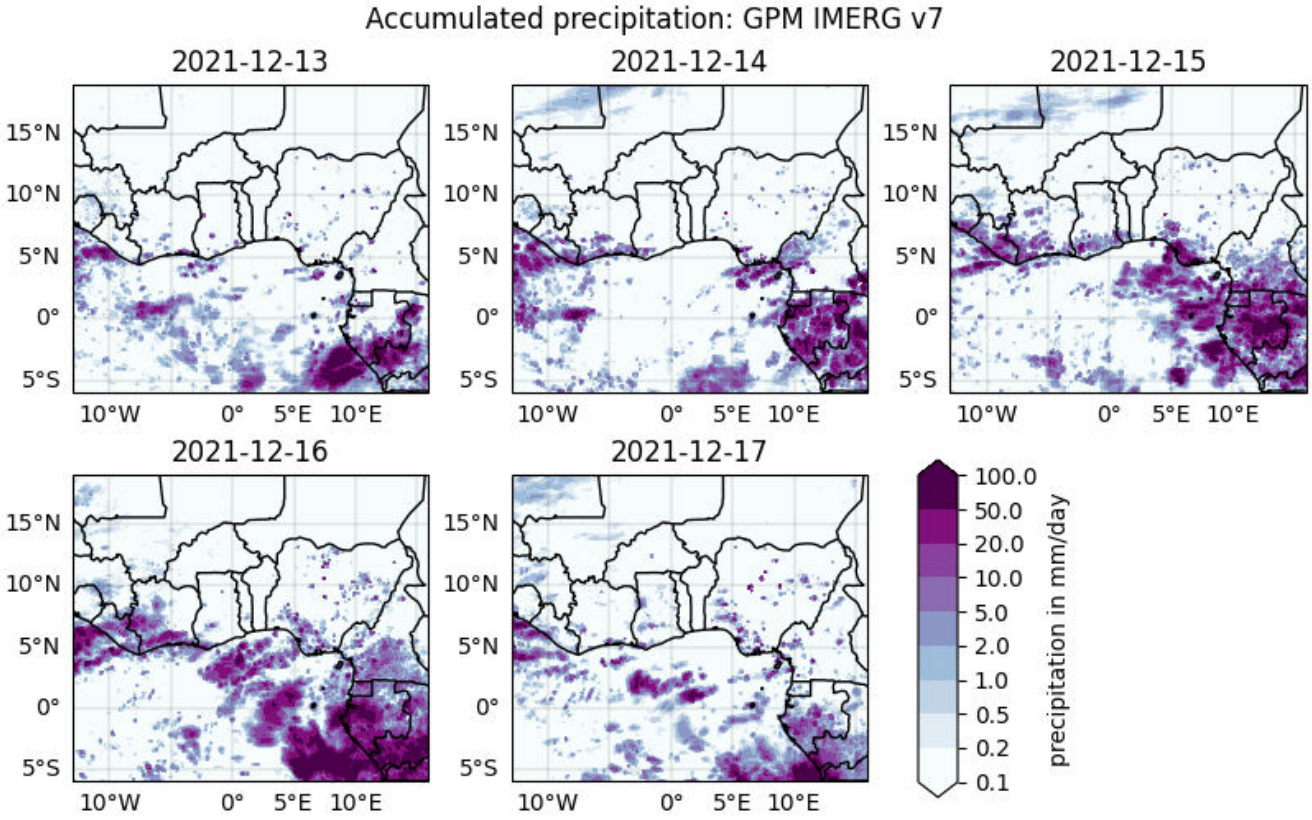

Figure 8.1: *Accumulated precipitation (GPM IMERG v6) and SST (OSTIA) in the period from 13 to 18 December 2021.*

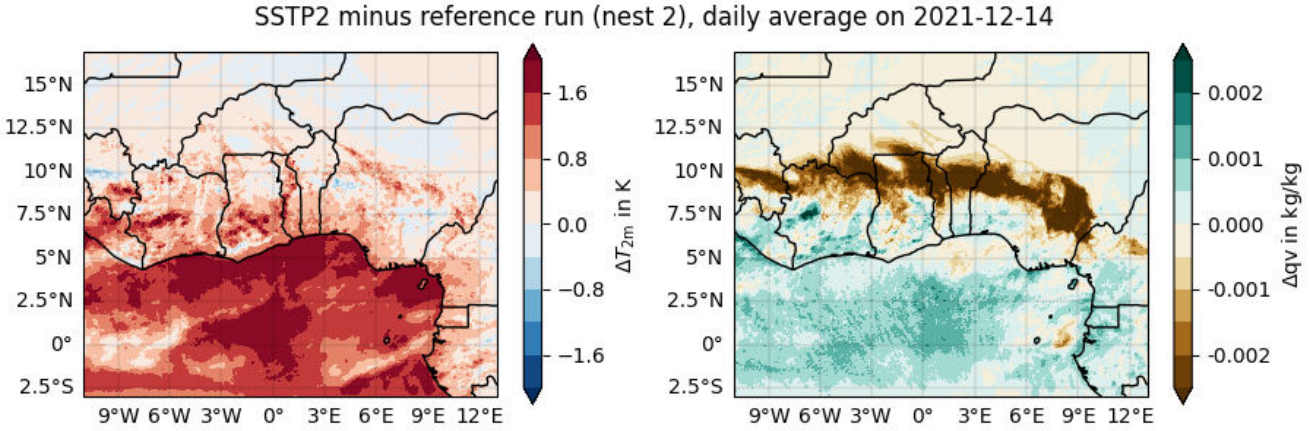

Figure 8.2: *Differences between the SSTP2 experiment and the reference run in the second nest in the air temperature and the specific humidity at* 2 m *height.*

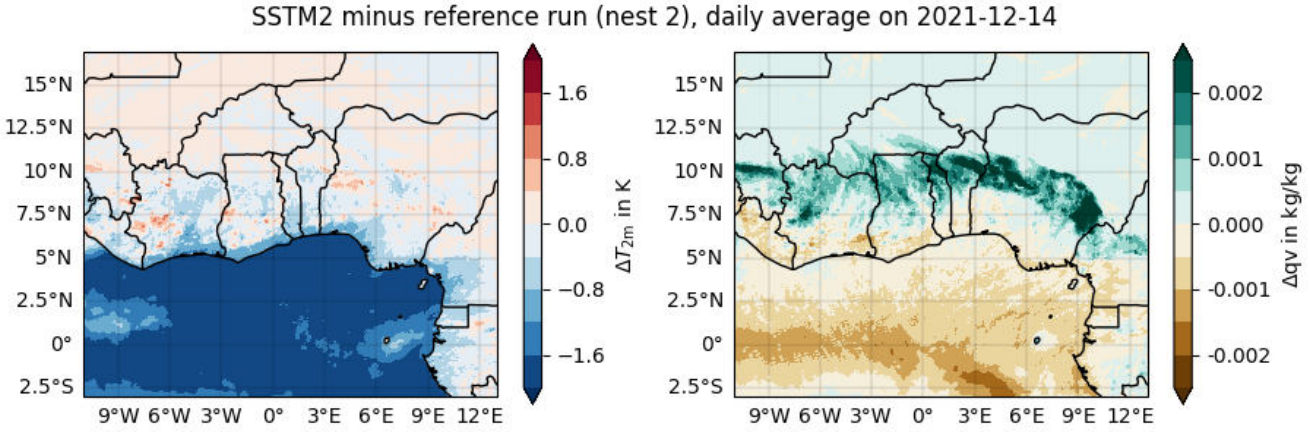

Figure 8.3: *Differences between the SSTM2 experiment and the reference run in the second nest in the air temperature and the specific humidity at* 2 m *height.*

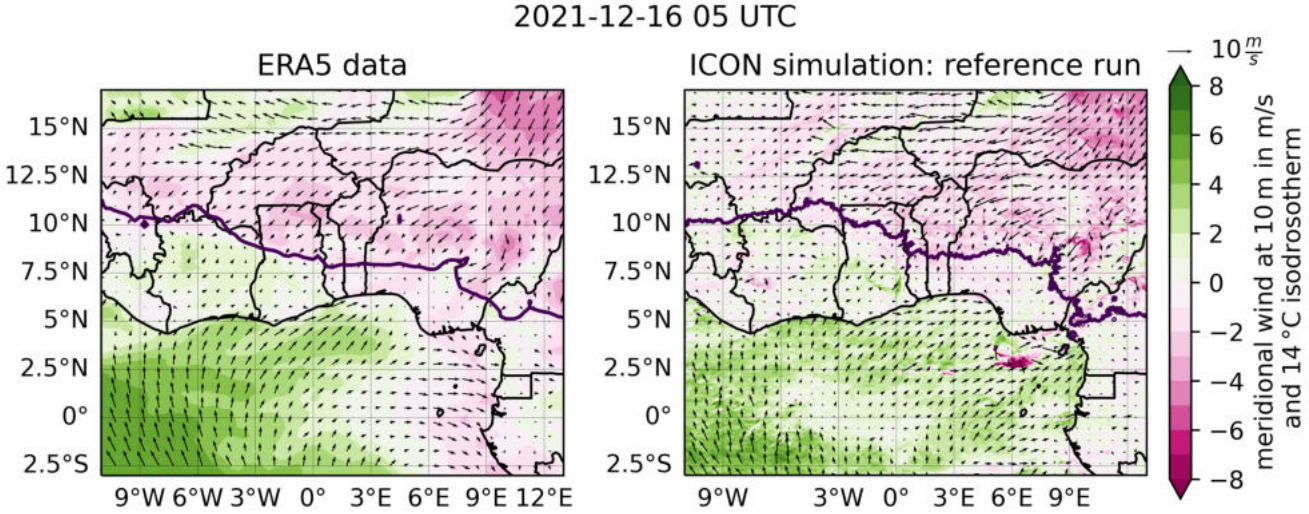

Figure 8.4: *Comparison of the ERA5 dataset and the ICON reference run on 16 December 2021 at 5 UTC. Both graphics show arrows of the* 10 m *wind speed and direction and the* 10 m *meridional wind in the contours.*

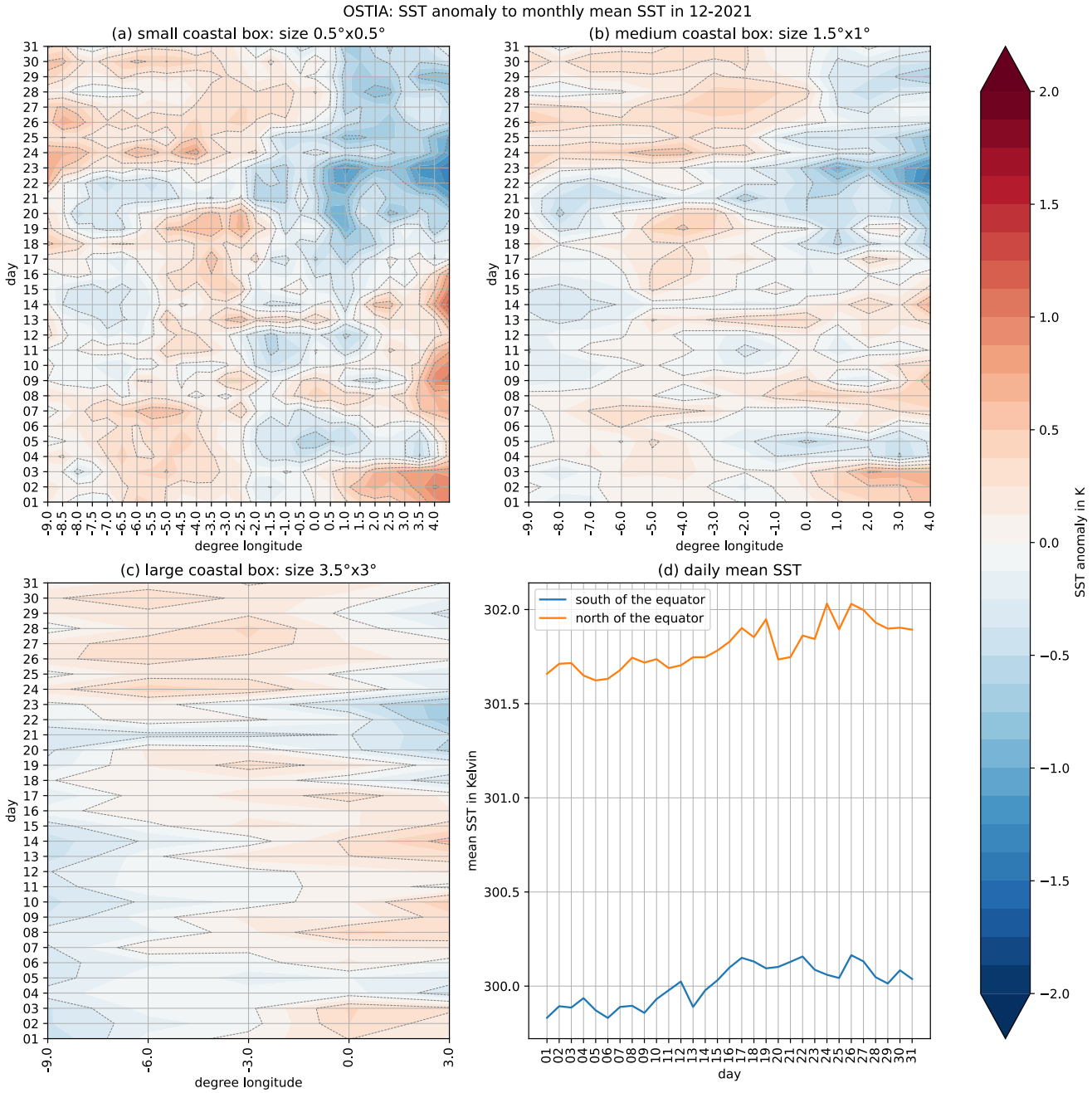

Figure 8.5: *Hovmöllerplots for the near-coastal daily SST changes are analysed on three lengths scales: small (0.5°×0.5°), middle (1.5°×1°), large (3.5°×3°). The boxes are presented in Figure 5.3. The contour lines in (a)-(c) indicate SST anomalies in* 0.25 K *steps. Subplot (d) shows the larger-scale mean SST in the area of Figure 5.3: The blue curve depicts the mean SST south of the equator in the research area while the orange curve takes only the ocean SST north of the equator within the research area.*

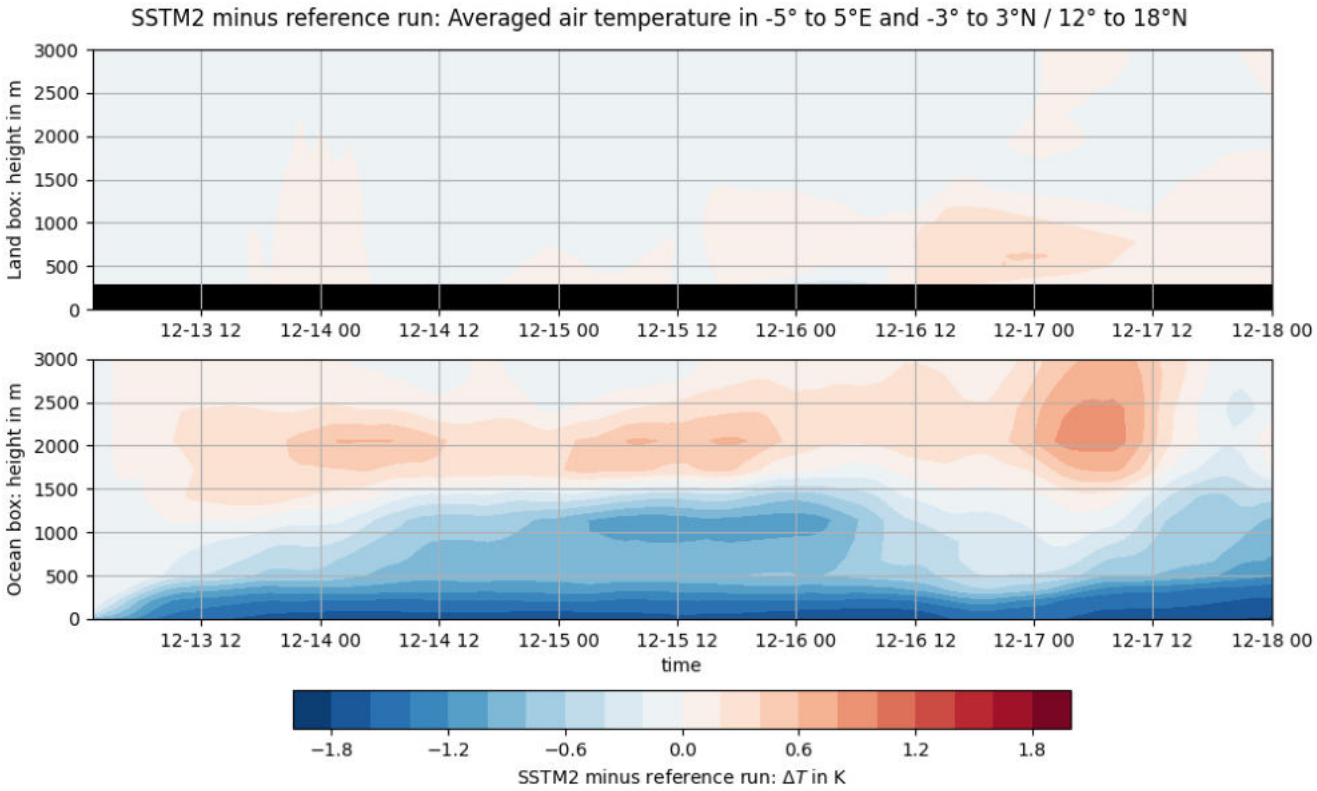

Figure 8.6: *Spinup of the SSTM2 experiment: Differences between the SSTM2 run and the reference run. The box over the sea extends from* $-5°$ *to* $5°E$ *and from* $-3°$ *to* $3°N$*. The box over the land covers an area from* $-5°$ *to* $5°E$ *and from* $11°$ *to* $17°N$*. Time series of the averaged air temperature anomaly in the lowest* $3\,\mathrm{km}$ *of the atmosphere over land (upper plot, black area indicates the orographic height) and ocean (lower plot).*

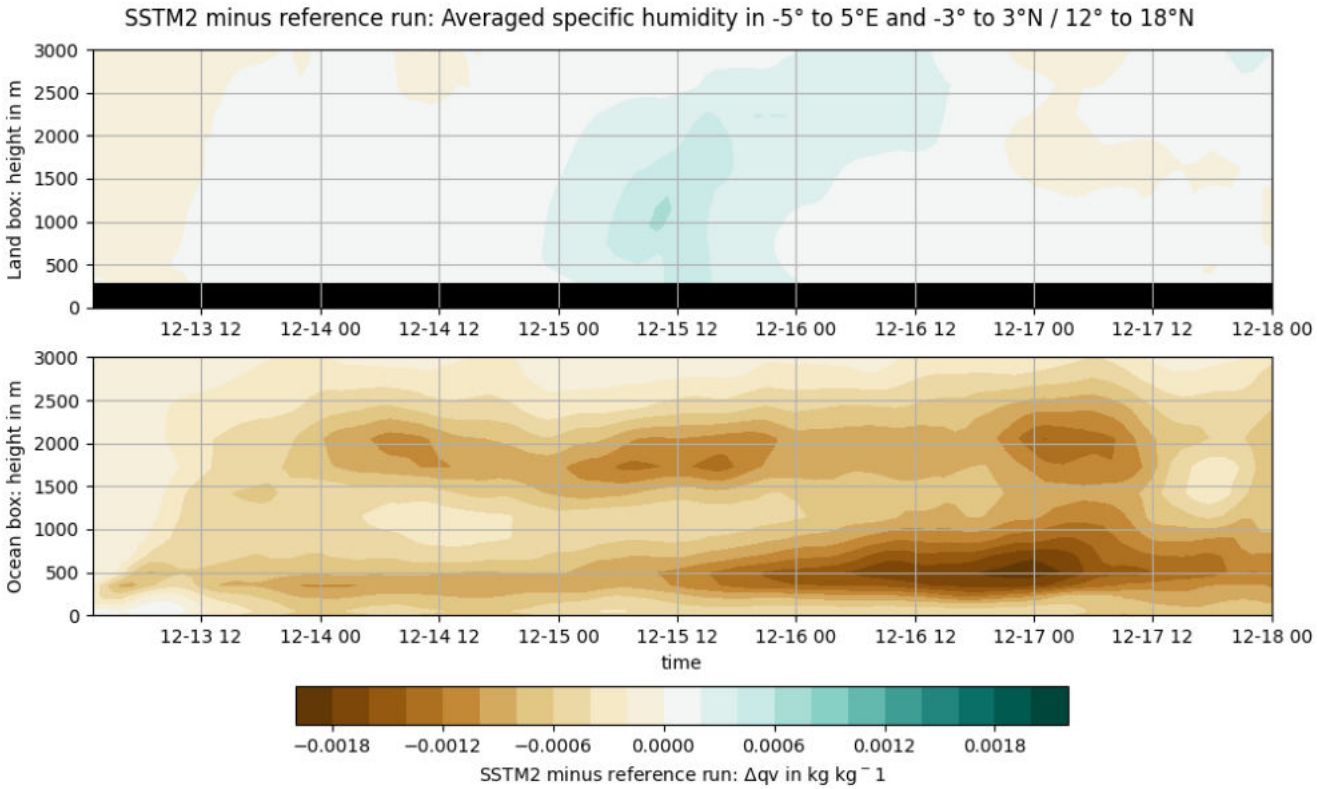

Figure 8.7: *Spinup of the SSTM2 experiment: Differences between the SSTM2 run and the reference run. The box over the sea extends from* $-5°$ *to* $5°E$ *and from* $-3°$ *to* $3°N$*. The box over the land covers an area from* $-5°$ *to* $5°E$ *and from* $11°$ *to* $17°N$*. Time series of the averaged specific humidity anomaly in the lowest* $3\,\mathrm{km}$ *of the atmosphere over land (upper plot, black area indicates the orographic height) and ocean (lower plot).*

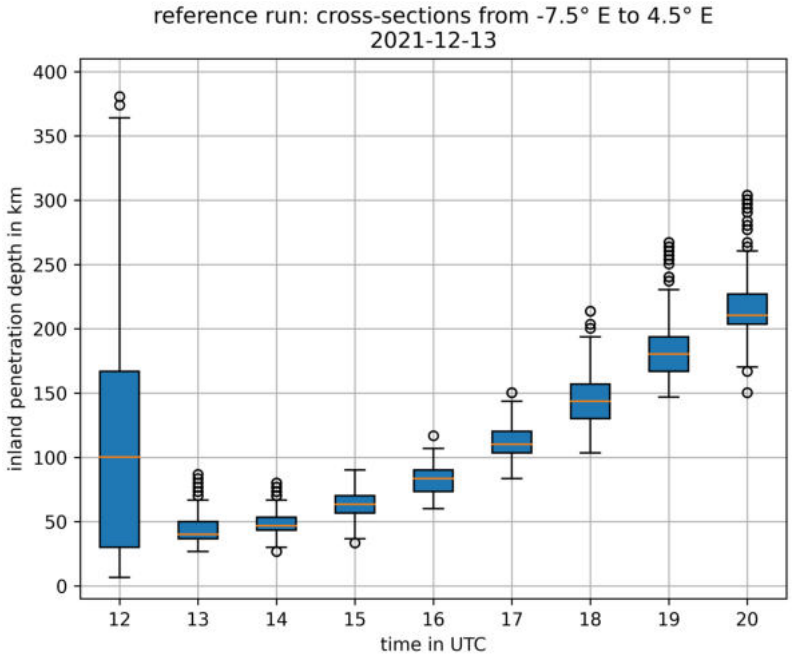

Figure 8.8: *Hourly median of the inland penetration distance of the SB along all cross-sections from −7.5° to 4.5° E on 13 December 2021. The box extends from the first quartile to the third quartile. The whiskers extend from the box to the farthest data point lying within the 1.5 of the inter-quartile range.*

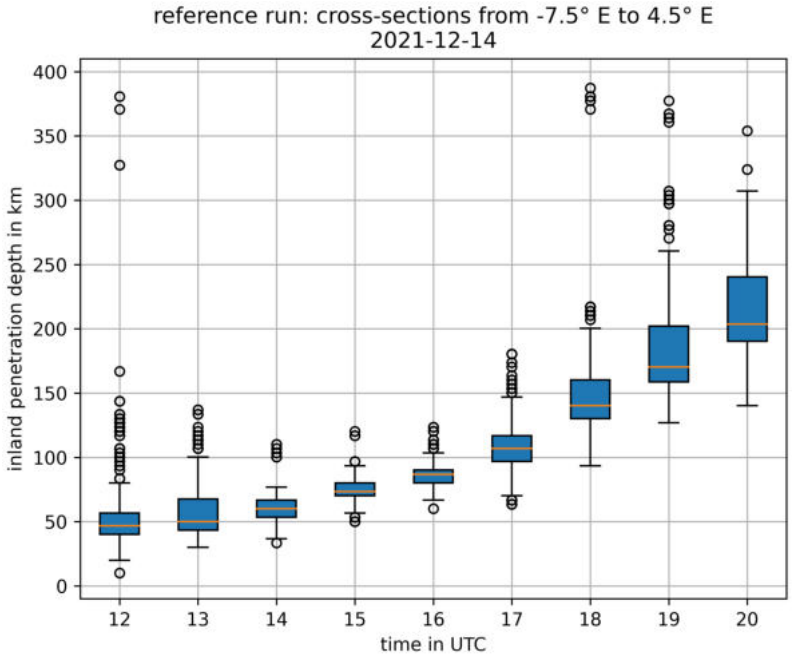

Figure 8.9: *Hourly median of the inland penetration distance of the SB along all cross-sections from −7.5° to 4.5° E on 14 December 2021. The box extends from the first quartile to the third quartile. The whiskers extend from the box to the farthest data point lying within the 1.5 of the inter-quartile range.*

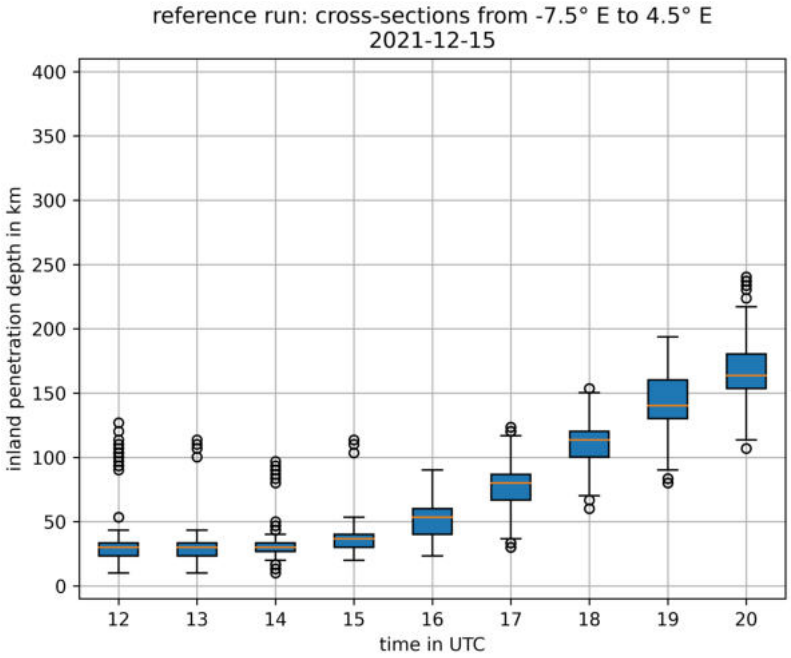

Figure 8.10: *Hourly median of the inland penetration distance of the SB along all cross-sections from −7.5° to 4.5° E on 15 December 2021. The box extends from the first quartile to the third quartile. The whiskers extend from the box to the farthest data point lying within the 1.5 of the inter-quartile range.*

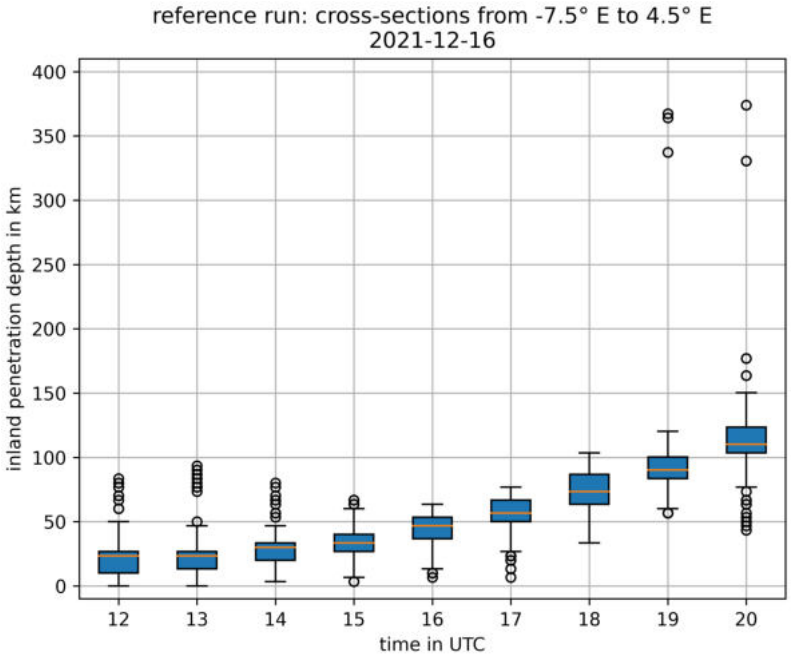

Figure 8.11: *Hourly median of the inland penetration distance of the SB along all cross-sections from −7.5° to 4.5° E on 16 December 2021. The box extends from the first quartile to the third quartile. The whiskers extend from the box to the farthest data point lying within the 1.5 of the inter-quartile range.*

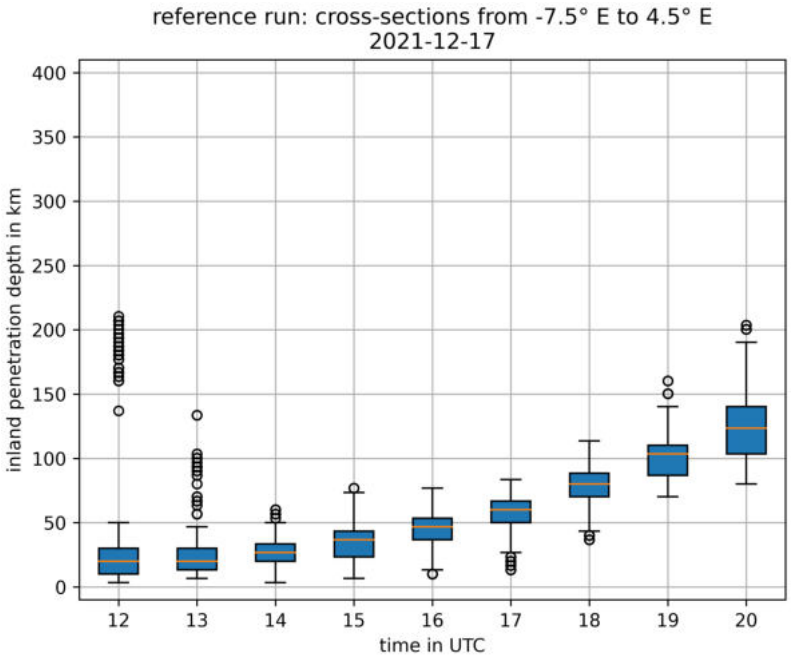

Figure 8.12: *Hourly median of the inland penetration distance of the SB along all cross-sections from* $-7.5°$ *to* $4.5°$ *E on 17 December 2021. The box extends from the first quartile to the third quartile. The whiskers extend from the box to the farthest data point lying within the 1.5 of the inter-quartile range.*

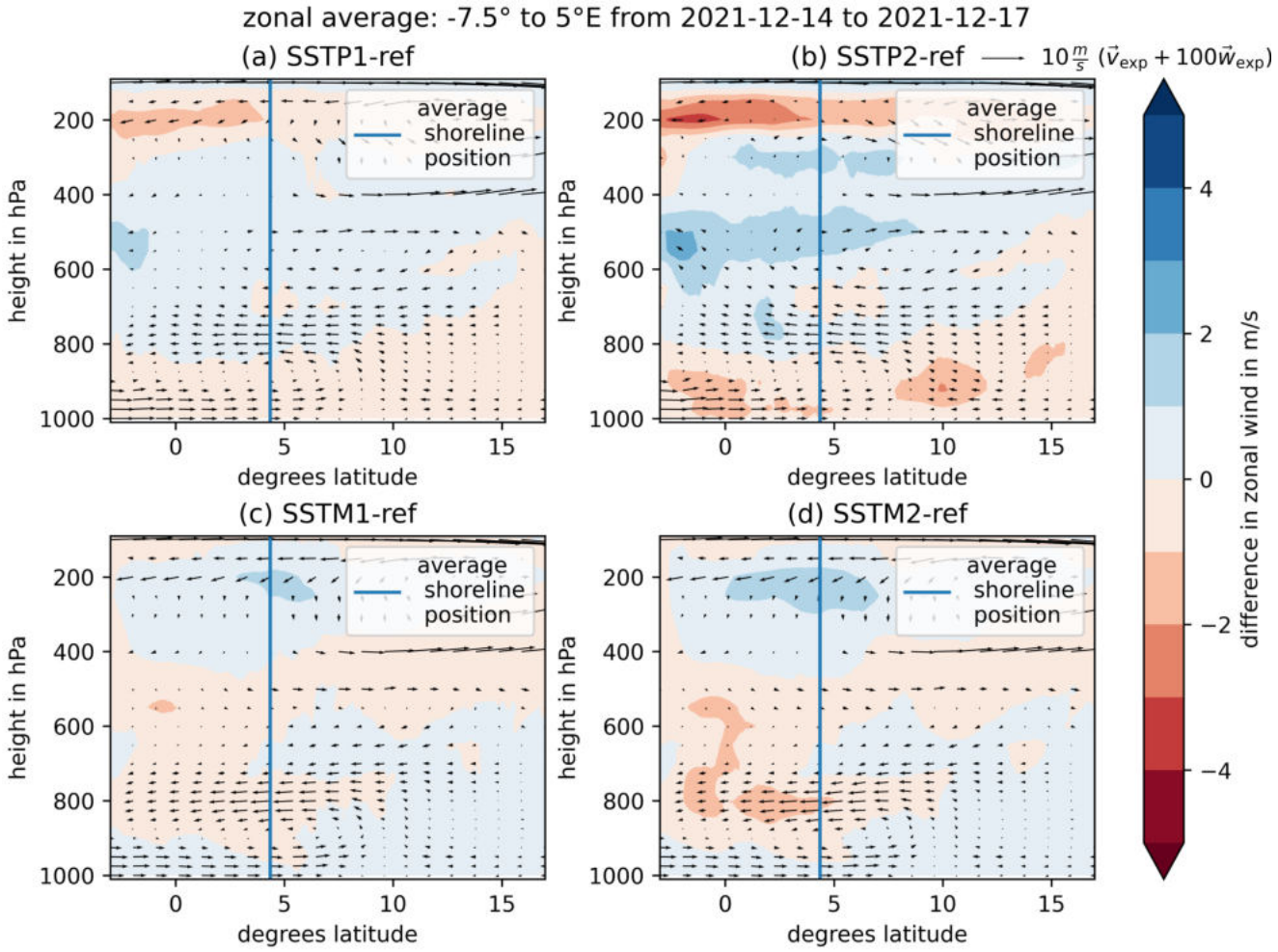

Figure 8.13: *Comparison of the zonal wind velocity of the SST experiments to the reference run. The graphic compares the mean zonal wind component from a zonal mean between 7.5° and 5°E averaged from 14 to 17 December 2021. Red shading indicates increased easterly winds and blue shading increased westerly wind velocity in the SST experiment compared to the reference run.*

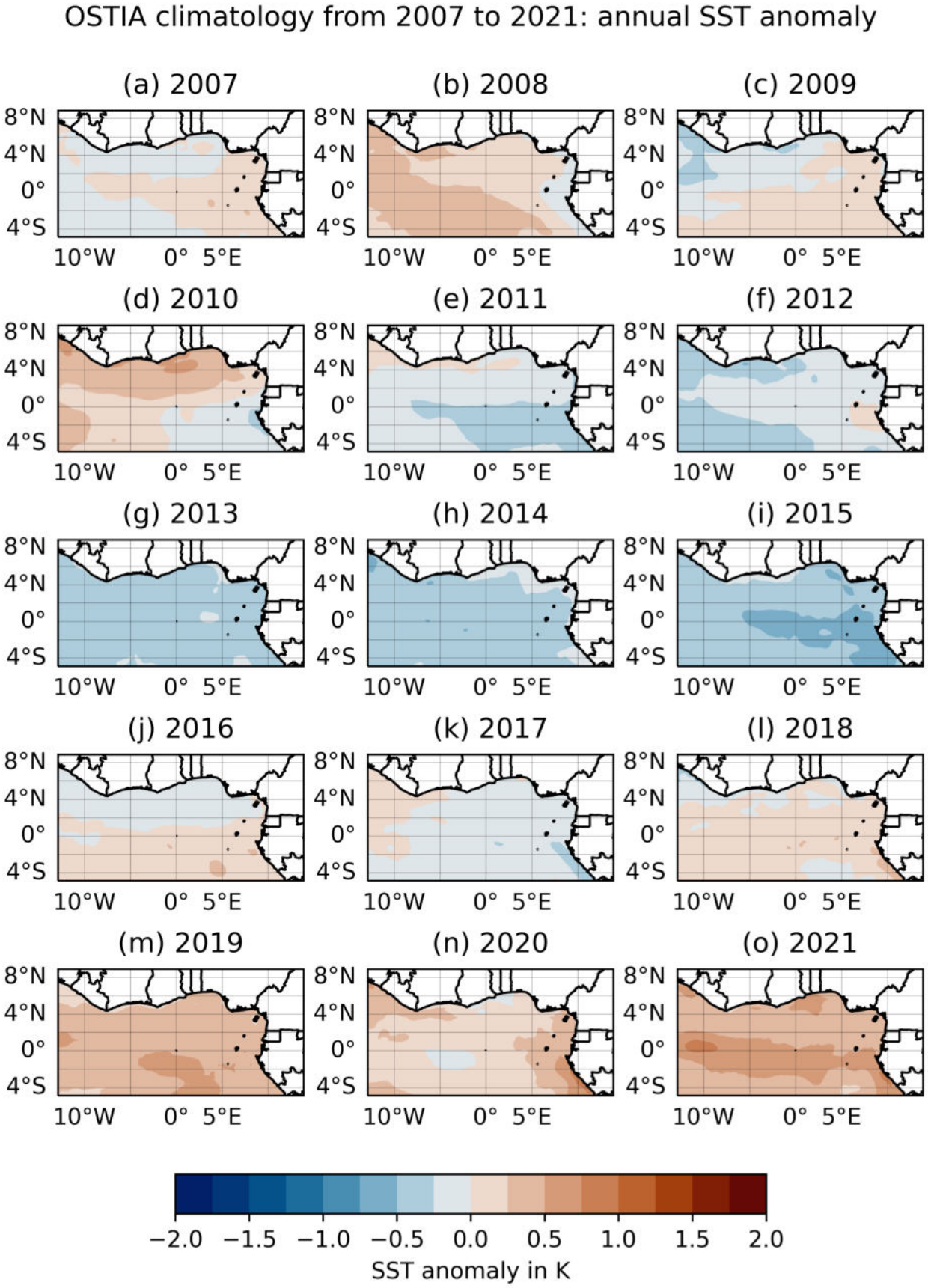

Figure 8.14: *OSTIA climatology: SST anomaly for every year from 2007 to 2021 (mean annual SST minus climatological mean).*

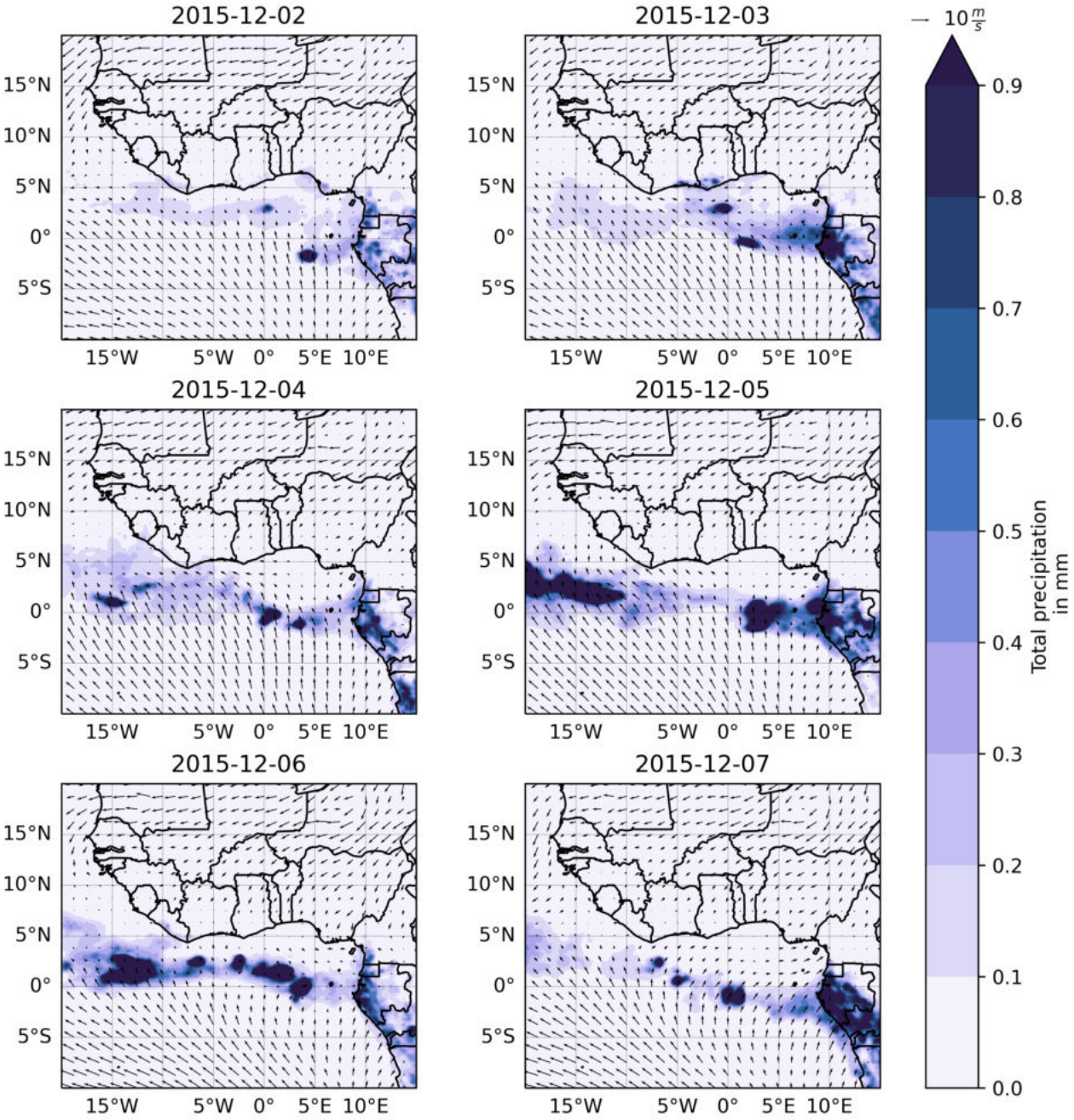

Figure 8.15: *ERA5 data:* 10 m *wind and total precipitation.*

List of Figures

List of Tables

References

Ali, K. E., K. Y. Kouadio, E. P. Zahiri, A. Aman, A. P. Assamoi, and B. Bourles, 2011: Influence of the gulf of guinea coastal and equatorial upwellings on the precipitations along its northern coasts during the boreal summer period. *Asian Journal of Applied Sciences*, **4**, 271–285, doi: 10.3923/ajaps.2011.271.285.

Amekudzi, L., W. A. Atiah, M. Maranan, A. H. Fink, and P. Knippertz, 2023: A process-based validation of gpm imerg and its sources using a mesoscale rain gauge network in the west african forest zone. *JOURNAL OF HYDROMETEOROLOGY*, **21**, doi:10.1175/JHM-D-19-0257.s1, URL https://doi.org/10.1175/JHM-D-19-0257.s1.

Amemou, H., V. Koné, A. Aman, and C. Lett, 2020: Assessment of a lagrangian model using trajectories of oceanographic drifters and fishing devices in the tropical atlantic ocean. *Progress in Oceanography*, **188**, 102 426, doi:10.1016/J.POCEAN.2020.102426.

Avellaneda, N. M., N. Serra, P. J. Minnett, and D. Stammer, 2010: Response of the eastern subtropical atlantic sst to saharan dust: A modeling and observational study. *Journal of Geophysical Research: Oceans*, **115**, 8015, doi:10.1029/2009JC005692, URL https://onlinelibrary.wiley.com/doi/full/10.1029/2009JC005692https://onlinelibrary.wiley.com/doi/abs/10.1029/2009JC005692https://agupubs.onlinelibrary.wiley.com/doi/10.1029/2009JC005692.

Bosson, K., A. Aman, E. Toualy, and S. Arnault, 2023: The surface guinea current variability from satellite data. *Regional Studies in Marine Science*, **64**, 103 045, doi:10.1016/j.rsma.2023.103045, URL https://doi.org/10.1016/j.rsma.2023.103045.

Brandt, P., M. Claus, R. J. Greatbatch, R. Kopte, J. M. Toole, W. E. Jo, and C. W. Böning, 2016: Annual and semiannual cycle of equatorial atlantic circulation associated with basin-mode resonance. *Journal of Physical Oceanography*, **46**, 3011–3029, doi:10.1175/JPO-D-15-0248.1, URL https://journals.ametsoc.org/view/journals/phoc/46/10/jpo-d-15-0248.1.xml.

Brandt, P., and Coauthors, 2023: Physical processes and biological productivity in the upwelling regions of the tropical atlantic. Copernicus Publications, 581-601 pp., doi:10.5194/os-19-581-2023.

Camberlin, P., M. Kpanou, and P. Roucou, 2020: Classification of intense rainfall days in southern west africa and associated atmospheric circulation. *Atmosphere 2020, Vol. 11, Page 188*, **11**, 188, doi:10.3390/ATMOS11020188, URL https://www.mdpi.com/2073-4433/11/2/188/htmhttps://www.mdpi.com/2073-4433/11/2/188.

Caniaux, G., H. Giordani, J. L. Redelsperger, F. Guichard, E. Key, and M. Wade, 2011: Coupling between the atlantic cold tongue and the west african monsoon in boreal spring and summer. *Journal of Geophysical Research: Oceans*, **116**, doi:10.1029/2010JC006570.

Clarke, R. H., 1984: Colliding sea-breezes and the creation of internal atmospheric bore waves: two-dimensional numerical studies. *Aust. Met. Mag.*

Coulibaly, A., B. J. Omotosho, M. B. Sylla, A. Coulibaly, and A. Ballo, 2019: Characteristics of land and sea breezes along the guinea coast of west africa. *Theoretical and Applied Climatology*, **138**, 953–971, doi:10.1007/s00704-019-02882-0.

Crosman, E. T., and J. D. Horel, 2010: Sea and lake breezes: A review of numerical studies. *Boundary-Layer Meteorology*, **137**, 1–29, doi:10.1007/s10546-010-9517-9.

de Coëtlogon, G., S. Janicot, and A. Lazar, 2010: Intraseasonal variability of the ocean - atmosphere coupling in the gulf of guinea during boreal spring and summer. *Quarterly Journal of the Royal Meteorological Society*, **136**, 426–441, doi:10.1002/qj.554.

Deser, C., M. A. Alexander, S. P. Xie, and A. S. Phillips, 2010: Sea surface temperature variability: Patterns and mechanisms. *Annual Review of Marine Science*, **2**, 115–143, doi:10.1146/annurev-marine-120408-151453.

DeYoung, C., and C. Evans, 2024: 1.3 - a preliminary assessment of the hrrr's ability to predict the great lakes lake-breeze front and marine atmospheric boundary layer. URL https://ams.confex.com/ams/104ANNUAL/meetingapp.cgi/Paper/430738.

Djakouré, S., P. Penven, B. Bourlès, V. Koné, and J. Veitch, 2017: Respective roles of the guinea current and local winds on the coastal upwelling in the northern gulf of guinea. *Journal of Physical Oceanography*, **47**, 1367–1387, doi:10.1175/JPO-D-16-0126.1.

Donlon, C. J., M. Martin, J. Stark, J. Roberts-Jones, E. Fiedler, and W. Wimmer, 2012: The operational sea surface temperature and sea ice analysis (ostia) system. *Remote Sensing of Environment*, **116**, 140–158, doi:10.1016/J.RSE.2010.10.017.

Dragaud, I. C. D. V., M. S. da Silva, L. P. de Freitas Assad, M. Cataldi, L. Landau, R. N. Elias, and L. C. G. Pimentel, 2019: The impact of sst on the wind and air temperature simulations: a case study for the coastal region of the rio de janeiro state. *Meteorology and Atmospheric Physics*, **131**, 1083–1097, doi:10.1007/s00703-018-0622-5.

Ekman, and V. Walfrid, 1905: On the influence of the earth's rotation on ocean-currents. *Almqvist & Wiksells boktryckeri, A.-B.,*.

environment facility (GEF), G., 2020: Strategic country cluster evaluation: Sahel and sudan-guinea savanna biomes.

Evan, A. T., D. J. Vimont, A. K. Heidinger, J. P. Kossin, and R. Bennartz, 2009: The role of aerosols in the evolution of tropical north atlantic ocean temperature anomalies. *Science*, **324**, 778–781, doi:10.1126/SCIENCE.1167404.

Fink, A. H., H. Paeth, V. Ermert, S. Pohle, and M. Diederich, 2010: I-5.1 meteorological processes influencing the weather and climate of benin.

Fink, A. H., and Coauthors, 2017: Meteorology of tropical west africa: The forecasters' handbook, first edition. edited. chapter 1.

Flohn, H., 1969: Local wind systems. world survey of climatology. *Elesevier, Amsterdam.*

Foltz, G. R., and M. J. McPhaden, 2008: Impact of saharan dust on tropical north atlantic sst. *Journal of Climate*, **21**, 5048–5060, doi:10.1175/2008JCLI2232.1, URL https://journals.ametsoc.org/view/journals/clim/21/19/2008jcli2232.1.xml.

Franchito, S. H., T. O. Oda, V. B. Rao, and M. T. Kayano, 2008: Interaction between coastal upwelling and local winds at cabo frio, brazil: An observational study. *Journal of Applied Meteorology and Climatology*, **47**, 1590–1598, doi:10.1175/2007JAMC1660.1.

Gentemann, C. L., P. J. Minnett, and B. Ward, 2009: Profiles of ocean surface heating (posh): A new model of upper ocean diurnal warming. *Journal of Geophysical Research: Oceans*, **114**, doi:10.1029/2008JC004825.

Good, S., and Coauthors, 2020: The current configuration of the ostia system for operational production of foundation sea surface temperature and ice concentration analyses. *Remote Sensing*, **12**, doi:10.3390/rs12040720.

Guedje, F. K., A. V. Houeto, E. B. Houngninou, A. H. Fink, and P. Knippertz, 2019: Climatology of coastal wind regimes in benin. *Meteorologische Zeitschrift*, **28**, 23–39, doi:10.1127/metz/2019/0930.

Hamilton, R. A., and J. W. Archbold, 1945: Meteorology of nigeria and adjacent territory.

Hardman-Mountford, N. J., and J. M. McGlade, 2003: Seasonal and interannual variability of oceanographic processes in the gulf of guinea: An investigation using avhrr sea surface temperature data. *International Journal of Remote Sensing*, **24**, 3247–3268, doi:10.1080/0143116021000021297.

Hatchett, B. J., M. L. Kaplan, N. J. Nauslar, C. M. Smith, and K. Nelson, 2020: Slope winds. *Encyclopedia of Wildfires and Wildland-Urban Interface (WUI) Fires*, 922–930, doi:10.1007/978-3-319-52090-2_209, URL https://link.springer.com/referenceworkentry/10.1007/978-3-319-52090-2_209.

Hersbach, H., and Coauthors, 2020: The era5 global reanalysis. *Quarterly Journal of the Royal Meteorological Society*, **146**, 1999–2049, doi:10.1002/qj.3803.

Holton, J. R., and G. J. Hakim, 2013: *An introduction to dynamic meteorology*. 94-99 pp.

Hsu, S. A., 1984: Sea-breeze-like winds across the north wall of the gulf stream: an analytical model. *Journal of Geophysical Research*, **89**, 2025–2028, doi:10.1029/JC089IC02P02025.

Huaman, L., C. Schumacher, A. H. Fink, and E. Buttitta, 2023: 2820 wileyonlinelibrary.com/journal/qj q. *J R Meteorol Soc*, **149**, 2820–2837, doi:10.1002/qj.4533, URL https://rmets.onlinelibrary.wiley.com/doi/10.1002/qj.4533.

Huffman, G. J., D. T. Bolvin, D. Braithwaite, K. Hsu, R. Joyce, P. Xie, and S.-H. Yoo, 2015: Nasa global precipitation measurement (gpm) integrated multi-satellite retrievals for gpm (imerg). *Algorithm theoretical basis document (ATBD) version*, **4**, –30.

Hummels, R., M. Dengler, and B. Bourlès, 2013: Seasonal and regional variability of upper ocean diapycnal heat flux in the atlantic cold tongue. *Progress in Oceanography*, **111**, 52–74, doi:10.1016/J.POCEAN.2012.11.001.

Ji, H. E., S. H. Lee, and H. W. Lee, 2013: Characteristics of sea breeze front development with various synoptic conditions and its impact on lower troposphere ozone formation. *Advances in Atmospheric Sciences*, **30**, 1461–1478, doi:10.1007/s00376-013-2256-3.

Jouanno, J., F. Marin, Y. D. Penhoat, J. M. Molines, and J. Sheinbaum, 2011: Seasonal modes of surface cooling in the gulf of guinea. *Journal of Physical Oceanography*, **41**, 1408–1416, doi:10.1175/JPO-D-11-031.1.

Kok, J. F., and Coauthors, 2017: Smaller desert dust cooling effect estimated from analysis of dust size and abundance. *Nature Geoscience*, **10**, 274–278, doi:10.1038/NGEO2912.

Lafore, J. P., and Coauthors, 2011: Progress in understanding of weather systems in west africa. *Atmospheric Science Letters*, **12**, 7–12, doi:10.1002/asl.335.

Lau, K. M., and K. M. Kim, 2007: Cooling of the atlantic by saharan dust. *Geophysical Research Letters*, **34**, doi:10.1029/2007GL031538.

Lindzen, R. S., and S. Nigam, 1987: On the role of sea surface temperature gradients in forcing low-level winds and convergence in the tropics. *Journal of the Atmospheric Sciences*, **44**.

Lombardo, K., E. Sinsky, J. Edson, M. M. Whitney, and Y. Jia, 2018: Sensitivity of offshore surface fluxes and sea breezes to the spatial distribution of sea-surface temperature. *Boundary-Layer Meteorology*, **166**, 475–502, doi:10.1007/s10546-017-0313-7.

Lu, D., L. White, R. S. Reddy, P. J. Croft, and J. M. Medlin, 2006: Numerical simulation of sea and bay breezes in a weak shear environment. *Meteorol Atmos Phys*, **94**, 153–165, doi:10.1007/s00703-005-0176-1.

Luo, B., P. J. Minnett, P. Zuidema, N. R. Nalli, and S. Akella, 2021: Saharan dust effects on north atlantic sea-surface skin temperatures. *Journal of Geophysical Research: Oceans*, **126**, e2021JC017 282, doi:10.1029/2021JC017282, URL https://onlinelibrary.wiley.com/doi/full/10.1029/2021JC017282https://onlinelibrary.wiley.com/doi/abs/10.1029/2021JC017282https://agupubs.onlinelibrary.wiley.com/doi/10.1029/2021JC017282.

Maranan, M., A. H. Fink, and P. Knippertz, 2018: Rainfall types over southern west africa: Objective identification, climatology and synoptic environment. *Quarterly Journal of the Royal Meteorological Society*, **144**, 1628–1648, doi:10.1002/QJ.3345, URL https://onlinelibrary.wiley.com/doi/full/10.1002/qj.3345https://onlinelibrary.wiley.com/doi/abs/10.1002/qj.3345https://rmets.onlinelibrary.wiley.com/doi/10.1002/qj.3345.

Markowski, P., and Y. Richardson, 2010: *Mesoscale meteorology in midlatitudes*. Wiley-Blackwell, 407 pp.

May, R. M., and Coauthors, 2024: Metpy: A python package for meteorological data. URL Unidata/MetPy, doi:10.5065/D6WW7G29.

McFee, B., M. McVicar, and D. Faronbi, 2024: librosa/librosa: 0.10.2. URL https://zenodo.org/records/4923181, doi:10.5281/ZENODO.4923181.

Merchant, C. J., O. Embury, P. L. Borgne, and B. Bellec, 2006: Saharan dust in nighttime thermal imagery: Detection and reduction of related biases in retrieved sea surface temperature. *Remote Sensing of Environment*, **104**, 15–30, doi:10.1016/J.RSE.2006.03.007.

Merle, J., 1980: Seasonal heat budget in the equatorial atlantic ocean. *Journal of Physical Oceanography*, **10**, 464–469, doi:10.1175/1520-0485(1980)010, URL https://journals.ametsoc.org/view/journals/phoc/10/3/1520-0485_1980_010_0464_shbite_2_0_co_2.xml.

Miller, S. T., B. D. Keim, R. W. Talbot, and H. Mao, 2003: Sea breeze: Structure, forecasting, and impacts. *Reviews of Geophysics*, **41**, doi:10.1029/2003RG000124.

Milton, S., A. Diongue-Niang, B. Lamptey, C. Bain, C. Birch, and P. Bougeault, 2016: Numerical weather prediction over africa. *Meteorology of Tropical West Africa: The Forecasters' Handbook*, 380–422, doi:10.1002/9781118391297.CH10, URL https://onlinelibrary.wiley.com/doi/full/10.1002/9781118391297.ch10https://onlinelibrary.wiley.com/doi/abs/10.1002/9781118391297.ch10https://onlinelibrary.wiley.com/doi/10.1002/9781118391297.ch10.

Minnett, P. J., M. Smith, and B. Ward, 2011: Measurements of the oceanic thermal skin effect. *Deep-Sea Research Part II: Topical Studies in Oceanography*, **58**, 861–868, doi:10.1016/J.DSR2.2010.10.024.

Mitchell, T. P., and J. M. Wallace, 1991: The annual cycle in equatorial convection. *Journal of Climate*, **5**.

Moore, D., P. Hisard, J. McCreary, J. O'Brien, J. Picaut, J.-M. Verstraete, and C. Wunsch, 1978: Equatorial adjustment in the eastern atlantic. *Geophysical Research Letters*.

Nicholls, R., S. Hanson, C. Herweijer, N. Patmore, S. Hallegatte, J. Corfee-Morlot, J. Chateau, and R. Muir-Wood, 2007: Ranking of the world's cities most exposed to coastal flooding today and in the future. URL www.oecd.org.

Nicholson, S. E., 2009: A revised picture of the structure of the "monsoon" and land itcz over west africa. *Climate Dynamics*, **32**, 1155–1171, doi:10.1007/s00382-008-0514-3.

Office, M., 2015: Cartopy: a cartographic python library with a matplotlib interface. URL https://scitools.org.uk/cartopy.

Ogawa, S., W. Sha, T. Iwasaki, and Z. Wang, 2003: A numerical study on the interaction of a sea-breeze front with convective cells in the daytime boundary layer. 635-651 pp.

Parker, D. J., and Coauthors, 2017: Meteorology of tropical west africa: The forecasters' handbook, first edition. edited, chapter 4.

Patrick, A. H. Fink, and H. V. Besler, 2003: Ghana dry zone und dahomey gap: Ursachen fÜr eine niederschlagsanomalie im tropischen westafrika achtung: Der hier abgedruckte text kann in editorialen details vom originaltext abweichen. 375-393 pp.

Pearson, R. A., G. Carboni, and G. Brusasca, 1983: The sea breeze with mean flow. *Quarterly Journal of the Royal Meteorological Society*, **109**, 809–830, doi:10.1002/qj.49710946209.

Perez, G. M., and M. A. S. Dias, 2017: Long-term study of the occurrence and time of passage of sea breeze in são paulo, 1960–2009. *International Journal of Climatology*, **37**, 1210–1220, doi:10.1002/joc.5077.

Porson, A., D. G. Steyn, and G. Schayes, 2007: Sea-breeze scaling from numerical model simulations, part i: Pure sea breezes. *Boundary-Layer Meteorology*, **122**, 17–29, doi:10.1007/s10546-006-9090-4.

Prill, F., D. Reinert, D. Rieger, G. Zängl, D. Rieger, and F. Prill, 2022: Icon tutorial. *J*, doi:10.5676/DWD, URL www.dwd.de.

Pu, Z., and E. Kalnay, 2018: *Numerical Weather Prediction Basics: Models, Numerical Methods, and Data Assimilation*, 1–31. Springer Berlin Heidelberg, doi:10.1007/978-3-642-40457-3_11-1.

Rast, S., 2018: Using and programming icon-a first introduction.

Raymond, D. J., 1995: Regulation of moist convection over the west pacific warm pool. *Journal of Atmospheric Sciences*, **52**, 3945 – 3959, doi:10.1175/1520-0469(1995)052<3945:ROMCOT>2.0.CO;2, URL https://journals.ametsoc.org/view/journals/atsc/52/22/1520-0469_1995_052_3945_romcot_2_0_co_2.xml.

Rotunno, R., 1983: On the linear theory of the land and sea breeze. *Journal of the Atmospheric Sciences*, **40**, 1999–2009.

Rácz, Z., and R. K. Smith, 1999: The dynamics of heat flows. *Quarterly Journal of the Royal Meteorological Society*, **125**, 225–252, doi:10.1002/qj.49712555313.

Sanogo, S., A. H. Fink, J. A. Omotosho, A. Ba, R. Redl, and V. Ermert, 2015: Spatio-temporal characteristics of the recent rainfall recovery in west africa. *International Journal of Climatology*, **35**, 4589–4605, doi:10.1002/JOC.4309, URL https://onlinelibrary.wiley.com/doi/full/10.1002/joc.4309https://onlinelibrary.wiley.com/doi/abs/10.1002/joc.4309https://rmets.onlinelibrary.wiley.com/doi/10.1002/joc.4309.

Schumann, EH, Illenberger, WK, Goschen, and WS, 1991: 1991algoabaywindssajs. *S. Afr. J. Sci*, **87**, 202–207.

Schunke, J., P. Laux, J. Bliefernicht, M. Waongo, W. Sawadogo, and H. Kunstmann, 2021: Exploring the potential of the cost-efficient tahmo observation data for hydro-meteorological applications in sub-saharan africa. *Water (Switzerland)*, **13**, doi:10.3390/w13223308.

Simpson, J. E., 1969: A comparison between laboratory and atmospheric density currents. *Quarterly Journal of the Royal Meteorological Society*, **95**, 758–765, doi:10.1002/qj.49709540609.

Simpson, J. E., 1987: *Gravity Currents - In the Environment and the Laboratory*. Ellis Horwood Limited, 15-27 pp.

Simpson, J. E., 1994: *Sea breeze and local winds*. cambridge university press.

Simpson, J. E., and R. E. Britter, 1980: A laboratory model of an atmospheric mesofront. *Quarterly Journal of the Royal Meteorological Society*, **106**, 485–500, doi:10.1002/qj.49710644907.

Simpson, J. E., D. A. Mansfield, and J. R. Milford, 1977: Inland penetration of sea-breeze fronts. *Quarterly Journal of the Royal Meteorological Society*, **103**, 47–76, doi:10.1002/qj.49710343504.

Soares, P. M., F. Johannsen, D. C. Lima, G. Lemos, V. A. Bento, and A. Bushenkova, 2024: High-resolution downscaling of cmip6 earth system and global climate models using deep learning for iberia. *Geoscientific Model Development*, **17**, 229–259, doi:10.5194/GMD-17-229-2024.

Sohou, Z., V. Koné, Y. C. Da-Allada, S. Djakouré, B. Bourlès, V. Racape, G. Degbe, and C. Adje, 2020: Seasonal and inter-annual onset sea surface temperature variability along the northern coast of the gulf of guinea. *Regional Studies in Marine Science*, **35**, doi:10.1016/j.rsma.2020.101129.

Souza, A. J., and Coauthors, 2021: Coastal upwelling limitation by onshore geostrophic flow in the gulf of guinea around the niger river plume. *Frontiers in Marine Science | www.frontiersin.org*, **1**, 607 216, doi:10.3389/fmars.2020.607216, URL www.frontiersin.org.

Steyn, D. G., 1998: Scaling the vertical structure of sea breezes.

Sungmin, O., U. Foelsche, G. Kirchengast, J. Fuchsberger, J. Tan, and W. A. Petersen, 2017: Evaluation of gpm imerg early, late, and final rainfall estimates using wegenernet gauge data in southeastern austria. *Hydrology and Earth System Sciences*, **21**, 6559–6572, doi:10.5194/hess-21-6559-2017.

Sweeney, J. K., J. M. Chagnon, and S. L. Gray, 2014: A case study of sea breeze blocking regulated by sea surface temperature along the english south coast. *Atmospheric Chemistry and Physics*, **14**, 4409–4418, doi:10.5194/acp-14-4409-2014.

van de Giesen, N., R. Hut, and J. Selker, 2014: The trans-african hydro-meteorological observatory (tahmo). *WIREs Water*, **1**, 341–348, doi:10.1002/wat2.1034.

Wallace, J., T. Mitchell, and C. Deser, 1989: The influence of sea-surface temperature on surface wind in the eastern equatorial pacific: Seasonal and interannual variability. *Journal of Climate*, **2**.

Wexler, R., 1946: Theory and observations of land and sea breezes. 272-287 pp.

Wissmeier, U., R. K. Smith, and R. Goler, 2010: The formation of a multicell thunderstorm behind a sea-breeze front. *Quarterly Journal of the Royal Meteorological Society*, **136**, 2176–2188, doi:10.1002/qj.691.

Zuidema, P., G. Torri, C. Muller, and A. Chandra, 2017: A survey of precipitation-induced atmospheric cold pools over oceans and their interactions with the larger-scale environment. *Surveys in Geophysics 2017 38:6*, **38**, 1283–1305, doi:10.1007/S10712-017-9447-X, URL https://link.springer.com/article/10.1007/s10712-017-9447-x.

Zängl, G., D. Reinert, P. Rípodas, and M. Baldauf, 2015: The icon (icosahedral non-hydrostatic) modelling framework of dwd and mpi-m: Description of the non-hydrostatic dynamical core. *Quarterly Journal of the Royal Meteorological Society*, **141**, 563–579, doi:10.1002/qj.2378.

9 Acknowledgements

Special thanks go to my supervisors Prof. Dr. Peter Knippertz and Prof. Dr. Andreas Fink from the Atmospheric Dynamics group at IMKTRO at KIT, who supervised me during my work. Thank you for giving me the support and freedom to shape my work according to my interests. I would also like to thank you for the exciting, lively and enthusiastic discussions in the meetings. Special thanks go to Pr. Dr. Andreas Fink for proposing this project and giving me the opportunity to write my master's thesis in the research field of ocean-atmosphere interactions, which I love so much.

A special thanks to my supervisor, Dr. Bethany Jane Woodhams, for her enthusiasm for my thesis project and for spending a lot of time discussing the physical and meteorological properties of the sea-land breeze and guiding me through the jungle of meteorological notation. Thank you for the helpful instructions on setting up and running the ICON simulations. You have given me the opportunity to learn a lot. Thank you for believing in the Sea Breeze identification algorithm all along. A very special thank you for reading through my thesis and continuing to mentor me even after moving to England. Thank you for being there for me beyond the project and supporting me in my enthusiasm for sea and wind. It has been a privilege and a pleasure to work with you.

I would also like to thank all the IMK group members working on campus south for creating a warm and friendly atmosphere for work and lunch. Thanks to Dr. Jannik Wilhelm for taking the time to introduce me to GitLab. Thanks to Dr. Raffael Aellig who gave me the opportunity to participate in a research campaign in Gabon. It is a pity that the campaign could not take place in the end. I would like to thank all the other Master and Bachelor students in my office for the great time during my thesis.

A special thanks goes to my sister and my parents, who have always supported me during my studies and my thesis. It means so much to me that you have given me a lot of freedom and expect nothing more from me than to live my life the way that makes me happy. To my partner and friends, thank you for not only making my life great, but also for supporting me throughout my studies.

This work was performed on the HoreKa supercomputer funded by the Ministry of Science, Research and the Arts Baden-Württemberg and by the Federal Ministry of Education and Research. I acknowledge support by the state of Baden-Württemberg through bwHPC. I acknowledge the use of imagery from the NASA Worldview application
(https://worldview.earthdata.nasa.gov), which is part of the NASA Earth Observing System Data and Information System (EOSDIS). I also acknowledge the use of MetPy (May et al., 2024), librosa (McFee et al., 2024), cartopy (Office, 2015).